

UNIVERSITY COLLEGE LONDON



Modelling and Experiments of Microchannels Incorporating Microengineered Structures

by

Alberto Cantu-Perez

A thesis submitted in partial fulfillment for the
degree of Doctor of Philosophy

in the

Faculty of Engineering
Chemical Engineering Department

January 2011

Declaration of Authorship

I, Alberto Cantu-Perez, declare that this thesis titled, ‘Modelling and Experiments of Microchannels Incorporating Microengineered Structures’ and the work presented in it are my own. I confirm that:

- This work was done wholly or mainly while in candidature for a research degree at this University.
- Where any part of this thesis has previously been submitted for a degree or any other qualification at this University or any other institution, this has been clearly stated.
- Where I have consulted the published work of others, this is always clearly attributed.
- Where I have quoted from the work of others, the source is always given. With the exception of such quotations, this thesis is entirely my own work.
- I have acknowledged all main sources of help.
- Where the thesis is based on work done by myself jointly with others, I have made clear exactly what was done by others and what I have contributed myself.

Signed:

Date:

“A good life is inspired by love and guided by knowledge.”

Bertrand Russell

UNIVERSITY COLLEGE LONDON

Abstract

Faculty of Engineering
Chemical Engineering Department

Doctor of Philosophy

by [Alberto Cantu-Perez](#)

Microreaction technology was conceived, thanks to the advances on microfabrication by the semiconductor industry. The first applications of microchannels used for performing reactions date back to the early nineties. Since then, many conferences dedicated to this topic are held worldwide such as the International Microreaction Technology Conference (IMRET) or the International Conference on Microchannels and Minichannels. The small dimensions of the microchannels lead to very high heat and mass transfer rates, reactions are therefore performed very efficiently on these devices. However, the small dimensions of the channels lead to high pressure drops. In addition, microchannels are very susceptible to clogging. This thesis studies the effect of different microchannel configurations in terms of mixing, mass transfer, residence time distribution and reaction. The objective is to design microreactors which incorporate different structures which make them efficient in terms of heat/mass transfer, but do not have the issue of high pressure drop and channel blockage.

Acknowledgements

I would like to thank all the people that somehow have helped or inspired my doctoral studies.

I would like to thank my supervisor Professor Asterios Gavriilidis. His passion for research and the constant look for perfection taught me a few things, not only academically but in life as well. I feel truly lucky of being one of his students.

Dr. Paola Lettieri deserves a special thanks as well. As the advisor of my Mphil thesis, her insight into the quality of my research was very helpful for the rest of my PhD studies.

I would like to thank also my friends at UCL. Some of the best times in my life I had them in London. Mr. Contantino (aka Mr. Constantinoupoli), Pinche Miguelito, Shane (P...) Morrin, Chandni from the 3rd floor. The people from the “Fire door keep shut room”. And last but certainly not least, las “chicas del CAPE” Giovanna, Melanie y Eria who deserve special mention. We had wonderful times on coffee breaks and on fridays @ ULU. One of the things I will miss the most about london is the chats we had those times.

I would also like to thank my parents Rosalva y Antonio. I doubt I could have better parents than them. They have always made an effort to make me feel loved. It has been an honor to be their son and I will consider myself lucky if I could be half as good a parent as they have been.

Lastly and most importantly I would like to thank Gaby (aka La Reyna). She has loved me and supported me for so many years that I feel indebted. To her I dedicate this thesis.

*Para la Reyna, que me ha apoyado en esta aventura
incondicionalmente. . .*

Contents

Declaration of Authorship	1
Abstract	3
Acknowledgements	4
List of Figures	10
List of Tables	16
Symbols	17
1 Introduction	21
2 Literature Survey	25
2.1 Mixing in Microchannels	25
2.1.1 Convective Micromixers	26
2.1.2 Distributive Micromixers	29
2.2 Residence Time Distributions	33
2.2.1 Pulse Experiment	34
2.2.2 Step Experiment	35
2.2.3 RTDs on Microchannels	36
2.2.3.1 Measuring RTDs in Microchannels	38
2.2.4 Conversion	39
2.2.4.1 Influence of RTD on Multiple Reactions	40
2.3 Mass Transfer	42
2.3.1 Fundamentals of Mass Transfer	42
2.3.2 Mass Transfer Coefficients	42
2.3.3 Physical Models	43
2.3.3.1 Film Theory	43
2.3.3.2 Penetration Theory	44
2.3.3.3 Surface Renewal	44

2.3.3.4	Graetz-Nusselt Problem	45
2.3.4	Mass transfer measurements	45
2.3.5	Mass transfer over reactive surfaces	48
3	Effects of Flow Ratio and Injection Location on the Performance of the Staggered Herringbone Micromixer	51
3.1	Introduction	51
3.2	Theoretical Methodology	53
3.2.1	Description of Mixer Geometry	53
3.3	Methods for Hydrodynamic Characterisation	54
3.3.1	Velocity Field	54
3.3.2	Particle Tracking	55
3.4	Methods for Mixing Characterisation	58
3.4.1	Mixing Length Based on Stretching Histories	58
3.4.2	Percentage of Mixing based on Nearest Neighbour Analysis	60
3.4.3	Mixing length from Striation Thickness Calculations	62
3.5	Results and Discussion	63
3.5.1	Qualitative Analysis	63
3.5.1.1	Flow Ratio 1:1	64
3.5.1.2	Flow Ratio 1:5	65
3.5.1.3	Flow Ratio 1:10	68
3.5.2	Quantitative Analysis	69
3.5.2.1	Percentage of Mixing based on the Nearest Neighbour Analysis	69
3.5.3	Striation Thickness	72
3.5.4	Stretching Histories	74
3.5.5	Scaling-up vs. Scaling-out	77
3.6	Conclusions	79
4	Residence Time Distributions in Microchannels: Comparison between Channels with Herringbone Structures and a Rectangular Channel	81
4.1	Introduction	81
4.2	Theoretical Approach	82
4.2.1	Numerical Particle Tracking Method	82
4.2.2	Analytical Method	84
4.3	Experimental Details	88
4.3.1	Set-up Description	88
4.3.2	Data Analysis	91
4.4	Results and Discussion	93
4.4.1	RTD from Particle Tracking and Hydrodynamic Model	93
4.4.1.1	Effect of Pe	98
4.4.1.2	Influence of Geometrical Parameters of Grooves	98
4.4.2	RTD from Experiments and Particle Tracking Model	101
4.5	Conclusions	103

5	Residence Time Distributions in Microstructured Plate Reactors	107
5.1	Introduction	107
5.2	Experimental Details	107
5.3	Numerical Methods	108
5.4	Results and Discussion	110
5.5	Conclusions	116
6	Mass Transfer and CO_2 Absorption in Microstructured Channels	118
6.1	Introduction	118
6.2	Theoretical Methodology	119
6.3	Description of Microchannel Configurations	119
6.4	Numerical Procedure for Mass Transfer Calculations	120
6.4.1	Simplification of Numerical Procedure via Turbulent Theory Concepts	122
6.4.2	Description of Model System for mass transfer evaluation (CO_2 Absorption) using 2D model	126
6.5	Results and Discussion	131
6.5.1	Study of Mass Transfer to Boundaries with a CFD/Particle Tracking Model	131
6.5.1.1	Effect of Channel Geometry on Concentration Profiles and Reactant Conversion	131
6.5.1.2	Calculation of Mass Transfer Coefficients	134
6.5.2	Study of Mass Transfer to Boundaries with Simplified 2D Model	135
6.5.3	Comparison of Mass Transfer Coefficients with Literature	137
6.5.4	Modelling of CO_2 absorption with Simplified 2D model	141
6.6	Conclusions	145
7	Hydrodynamics Studies in a Layered Herringbone Channel	147
7.1	Introduction	147
7.2	Experimental Methodology	148
7.2.1	Description of Microchannel Configurations	148
7.2.2	Evaluation of Mixing	150
7.3	Theoretical Methodology	153
7.3.1	Numerical Procedure for Mixing and RTD Studies	153
7.4	Results and Discussion	156
7.4.1	Residence Time Distributions	156
7.4.2	Mixing	159
7.5	Conclusions	169
8	Hydrodynamics and Reaction Studies in a Layered Herringbone Channel	170
8.1	Introduction	170
8.2	Experimental Methodology	171
8.2.1	Description of Reactors	171

8.2.2	Description of Model Reaction	171
8.3	Theoretical Methodology	173
8.3.1	Theoretical Approach for RTD Calculations	173
8.3.1.1	Numerical Particle Tracking Method	174
8.3.1.2	ADEM Model Parameters from Hydrodynamic Data	175
8.3.2	Calculation of D_{eff} with Turbulent Theory	176
8.3.3	Theoretical Calculation of Reaction Yields	177
8.4	Results and Discussion	179
8.4.1	Residence Time Distributions	179
8.4.2	Theoretical and Experimental Reactor Performance for a Consecutive Reaction	179
8.4.3	Comparison of ADEM Model Parameters Obtained from CFD/Particle Tracking and Hydrodynamic Data	184
8.5	Conclusions	187
9	Conclusions and Future Work	189
A	Particle Tracking Algorithm Implemented in Matlab	193
B	Further Calculations for Residence Time Distributions	228
C	Example for Experimental RTD calculations with Fourier Trans- form	233
D	Geometry Configuration for Layered Herringbone Channel	237
E	Derivation of mixing time equation	240
	Bibliography	242

List of Figures

2.1	Mixing principles for microfluidic devices [80]	27
2.2	Overview of the flow regimes and ranges of Reynolds number in laminar T-mixer flow with 1:1 mixing ratio, $Sc=3000$. T600x300x300 μm . Bottom: Mixing quality α_m is determined at a constant length $l = 5d_h$ of the mixing channel here $l = 2000\mu m$ [80]	28
2.3	Parallel micromixers: a) T-mixer, b) Y-mixer, c)parallel lamination, d)hydrodynamic focusing in [117]	29
2.4	Mixing mechanism based on split and recombination [41]	30
2.5	Other mixer geometries.	31
2.6	Mixer geometries containing grooves placed on one or more microchannel walls	34
2.7	Transforming the experimental C_{pulse} into the E curve. [88]	35
2.8	Information obtainable from a step experiment. [88]	36
3.1	Staggered herringbone mixer [143]	53
3.2	Cross-sectional images for a mixing ratio of 1:1 with particles initially located on the right of the channel (M1:1R). a) Particle tracking with no diffusion equation (3.1). b) Particle tracking with random walk diffusion equation (3.2)	57
3.3	Relevant distances for nearest neighbour analysis calculations	62
3.4	Cross-sectional particle distributions for striation thickness measurement	64
3.5	Cross-sectional images for configuration M1:1C (see table 3.2). a) initial conditions, b) end of 1st cycle, c) end of 2nd cycle, d) end of 3rd cycle, e)end of 4th cycle, f)end of 5th cycle. $Re = 7.16 \times 10^{-3}$	67
3.6	Cross-sectional images for the first 5 cycles a)M1:5R b)M1:5C. $Re = 7.16 \times 10^{-3}$	68
3.7	Cross-sectional images for the first 5 cycles a)M1:10R b)M1:10C $Re = 7.16 \times 10^{-3}$	70
3.8	Coefficient of variance as a function of number of cycles for various mixing ratios and injection configurations (see table 3.2).	71
3.9	Percentage of mixing vs. the number of cycles for all cases, calculated with the nearest neighbour analysis method.	72
3.10	Evolution of the striation thickness over the mixer length for all cases.	74
3.11	Particle positions and stretching values after 1 cycle, for a uniform array of 4100 particles.	75

3.12	Graph with the geometric mean λ_m and λ_{90} (conservative) vs. the number of cycle.	76
3.13	Comparison of mixing lengths for the striation thickness, nearest neighbour analysis and stretching methods for all configurations . . .	77
3.14	Plot of the mixing time for the M1:1R configuration in a staggered herringbone micromixer and a T-mixer as a function of the scaling up factor. $Pe = 10^5$	78
4.1	A) Geometry of the staggered herringbone channel. B) Geometry of the symmetric herringbone channel. Fluid travels from left to right.	83
4.2	Dimensionless RTD of particle tracking methods and analytical solutions for a cylindrical channel. a) Convection model vs. particle tracking simulation. b) Dispersion model vs. particle tracking with random walk simulation, $Pe = 150$	85
4.3	Picture of the experimental set up used for RTD studies.	90
4.4	Comparison of the RTD for the staggered herringbone channel obtained from the particle tracking method with random walk diffusion and the model of axial dispersion exchanging mass with a stagnant zone (ADEM) for cycles 5th, 15th and 25th (7.6, 22 and 38cm). The parameters of the model were calculated using particle tracking results for the 15th cycle. Channel dimensions are shown in table 4.1, $Pe \approx 10^4$ $Re \approx 10^1$	94
4.5	a)Residence time distribution in the rectangular channel from particle tracking with random walk diffusion. at 2cm and 6.2 cm. b) Residence time distribution in the staggered herringbone channel from particle tracking with random walk diffusion at 2cm and 6.2 cm. The dimensions of the channel are $w= 200 \mu m$, $h=85 \mu m$. $Pe \approx 10^4$ $Re \approx 10^1$	96
4.6	Dimensionless RTD for a rectangular microchannel and the staggered herringbone microchannel from a particle tracking method with random walk diffusion. The dimensions of the channel are $w= 200 \mu m$, $h=85 \mu m$ for both channels and the groove parameters are: $g_w = 50\mu m$, $g_d = 31\mu m$, $r_w = 50\mu m$. $Pe = 10^2$ $Re \approx 10^1$	99
4.7	Residence time distribution from particle tracking with random walk for a channel with staggered herringbone structures for $Pe = 10^4$ and $Pe = 10^5$. Channel dimensions $w=2mm$, $h=0.71mm$, groove width is 0.7mm width and 0.18mm depth. $Re \approx 10^1$ for both cases.	100
4.8	Normalised tracer concentration at the inlet and outlet for the staggered herringbone channel at 22 cm for three separate experiments. $Pe = 10^4$ $Re \approx 10^1$	102

4.9	Dimensionless experimental residence time distributions for a rectangular channel and channels with symmetric and staggered herringbone structures for $Pe \approx 10^4$. The dimensions of the channels are listed in table 4.1. The distance of measurement from injection location is 22 cm.	103
4.10	Comparison of the dimensionless residence time distributions obtained from experiments and from the particle tracking with random walk diffusion method for a) a rectangular channel b) staggered herringbone channel c) symmetric herringbone channel. The dimensions of the channels are listed in table 4.1. The distance of measurement from injection is 22cm. For all cases $Pe \approx 10^4$	105
4.11	Dimensionless experimental residence time distributions for a rectangular channel and a channel with symmetric and staggered herringbone structures for $Pe \approx 10^3$. The dimensions of the channels are listed in table 4.1. The distance of measurement from injection location is 22 cm.	106
5.1	a)Picture of the assembled and disassembled reactor with straight channels. b) Sheet geometries employed for RTD measurements. "Straight " has channels with hydraulic diameter 0.7 mm, "Straight " 1.07 mm and "Zig-Zag" has channels with hydraulic diameters 0.75 mm and 0.84 mm (for 5 and 9 shims respectively).	109
5.2	Picture of the experimental set up used for RTD studies.	110
5.3	Comparison of experimental vs. numerical RTDs for a rectangular cross section channel. Width=14mm, height=2.46mm.	111
5.4	Dimensionless RTDs for two reactor geometries at different flowrates. a) Straight 1, b) Straight 2.	112
5.5	Dimensionless RTDs for two reactor geometries at different flowrates. a) Zig-zag, b) Rectangular cross section channel.	114
5.6	Dimensionless RTDs for the zig-zag geometry with 5 and 9 shims ($d_H=0.75\text{mm}$ and 0.84mm respectively) for a flowrate of 2 ml/min.	115
5.7	Dimensionless variance of the RTDs for all geometries as a function of residence time.	116
6.1	Geometries considered for the numerical analysis of mass transfer to a reacting wall. The arrows indicate the direction fo the flow	120
6.2	Experimental falling film microreactor used in Ziegenbalg et al. [170] and simulated here.	128
6.3	a) Schematic view of the falling film microreactor. b) Enlarged view of the computational domain considered for the CFD calculations	129
6.4	Cross-sectional reactant concentrations and reactant conversion at different lengths for a rectangular, staggered 1-peak herringbone AA, flow inversion and staggered 2-peak herringbone channel AB (see figure 6.1). Infinitely fast reaction at the top wall. $Pe \approx 10^4$	133

6.5	Cross-sectional concentrations at different lengths for the geometry shown in figure 6.1b (BB structure). In this case it is not alternated with the standard herringbone structure shown in figure 6.1a. $Pe \approx 10^4$.	134
6.6	a) Mixing cup concentration at different lengths for all geometries. b) Sherwood number at different lengths. $Pe = 10^4$. Note that 1 cycle is approximately $\frac{z}{h} = 17$	136
6.7	A) Vertical velocity (u_y) and eddy diffusivity (E_D) as a function of channel vertical coordinate for the staggered herringbone channel (AA). The reactive wall is located at a channel height of $85 \mu m$. $Pe = 10^4$	137
6.8	a) Sherwood number vs. dimensionless length comparison 3D particle tracking with 2D eddy diffusivity. b) Sherwood number vs. $\frac{z}{PeH}$	138
6.9	Developing boundary layer over a reactive plate. a) Development of a boundary layer in a uniaxial flow. b) Simplified model of the simultaneous growth of axial and transverse concentration boundary layers over a reactive boundary. [77]	139
6.10	Sherwood number (6.23) vs. $Pe_{trans} = \frac{u_{trans}H}{D}$. Values from Kirtland et al. [77] are approximated from their reported figure 8a. In this work $B_1 = 0.8075$, whereas in Kirtland et al. [77] $B_1 = 0.6429$	141
6.11	Maps of the vertical velocity on the cross-section of a staggered herringbone channel (see figure 6.1a). a) 1 st half cycle. b) 2 nd half cycle. Then numbers I to VII indicate regions where different expression for E_D are calculated as described in the text. Flowrate 6.72 ml/min . Note that the computational domain for the Pseudo 3D model is from $600 \mu m$ to $1200 \mu m$.	143
6.12	Eddy diffusivity (E_D) as a function of channel height for the seven different regions shown in figure 6.11	144
6.13	NaOH conversion for the falling film microreactor for different inlet liquid flowrates and CO_2 fractions. Experimental conversions were taken from [170]	144
7.1	Schematic of layered herringbone channel and corresponding experimental structures. The dimensions of the structures can be seen in table 7.1, (see appendix C) for details of the experimental chips.	149
7.2	Geometries studied to compare the mixing behaviour of the layered herringbone channel	151
7.3	Computational domains of the geometries studied for mixing characterisation.	154
7.4	Experimental and numerical RTD for the glass layered herringbone configuration and comparison with a rectangular channel. $Pe = 10^4, Re = 10^1$	156
7.5	Cross-sectional picture obtained with confocal microscopy. a) Entrance of herringbone section, b) 1.5th cycle.	157
7.6	Normalised fluorescence intensity profiles as a function of channel depth for top and bottom channels.	158

7.7	Residence time distribution comparison between experiments and particle tracking for the acrylic layered herringbone channel. a) $Pe = 3 \times 10^3$ b) $Pe = 3 \times 10^4$. Flowrates were 2 and 0.2 ml/min. The diffusion coefficient of the dye used was $1.3 \times 10^{-9} m^2/s$	160
7.8	Cross-sectional particle distribution profiles after 5 cycles for the layered herringbone (left) and the floor herringbone structure (right)	161
7.9	Percentage of mixing calculated via the nearest neighbour analysis .	162
7.10	Vertical z-velocity at the top channel/groove interface (x-y plane) for the layered (a) and floor (b) herringbone configuration.	163
7.11	a) Experimental cross-sectional mixing pictures obtained by confocal microscopy at three different lengths. b) Simulated mixing pictures at three different lengths. $Pe = 10^4$	164
7.12	A) Experimental mixing pictures for the glass layered herringbone channel obtained by microscopy. The picture is seen from the top of the reactor. $Pe = 10^4$	165
7.13	Streamlines inside a $600 \times 300 \mu m$ (width x height T-mixer) for different Reynolds numbers. In the centre of each figure is the main channel and left and right are the inlets.	166
7.14	Mixing quality for the different geometries evaluated experimentally via the Villermaux-Dushman reaction. Theoretical mixing evaluation was done with particle tracking methods and the nearest neighbour analysis at a fixed residence time of 550ms.	168
8.1	Experimental and fitted fluorescence kinetic curves for the reaction of epinephrine in NaOH 1M.	173
8.2	Dimensionless RTD for a layered herringbone and a rectangular channel for two different Peclet numbers a) $Pe=12500$, $Re=12.5$ b) $Pe=1250$, $Re=1.25$. The dimensions of the simulated channels are shown in table 8.1	180
8.3	Experimental concentration of the intermediate in a consecutive reaction for a layered herringbone and a rectangular channel reactor.	181
8.4	Rescaled experimental concentration of the intermediate in a consecutive reaction for a layered herringbone and a rectangular channel reactor.	182
8.5	Theoretical concentration of the intermediate in a consecutive reaction for a layered herringbone and a rectangular channel reactor. a) with reactants unmixed before the reactor inlet, b) with reactants premixed before the reactor inlet.	183
8.6	Residence time distributions for the layered herringbone channel for a flowrate of 4 ml/min. RTDs were obtained by CFD/Particle tracking methods and with the ADEM model with the parameters fitted from the particle tracking data or from the hydrodynamics obtained from CFD calculations.	184

8.7	Theoretical intermediate THI concentration for the reaction (8.1) as a function of EP conversion for the layered herringbone and for the rectangular channel. The RTDs needed for the calculation of concentrations were obtained by the ADEM-CFD/Particle tracking, ADEM-Hydrodynamics and the CFD/Particle tracking methods.	186
B.1	Magnitude of axial velocity as function of channel width for two different channel heights.	228
B.2	Experimental comparison of inlet and outlet of the reactor with different experimental points.	229
B.3	Magnitude of axial velocity as function of channel width for two different channel heights.	230
B.4	Experimental comparison of inlet and outlet of the reactor with different experimental points.	230
B.5	Experimental comparison of inlet and outlet of the reactor with different experimental points.	231
B.6	Experimental comparison of inlet and outlet of the reactor with different experimental points.	232
C.1	Example of an RTD obtained by deconvolution from inlet and outlet impulse-response data. The convoluted signal $E(t) * Inlet(t)$ is also included to assess the validity of the convolution process.	234
D.1	Layers used to fabricate the glass layered herringbone channel. a) shows the top layer with the inlet and outlet ports. b) shows the layer with the main channel, two of these are used: one above and one below the herringbone layer. c) shows the herringbone layer that goes in between the main channels. d) is the bottom layer used for sealing.	238
D.2	Order of stacking of the layers for the glass layered herringbone channel	239

List of Tables

3.1	Mixer dimensions and fluid properties	54
3.2	Initial locations of particles for mixing simulations	56
3.3	Cross-sectional images for configuration M1:1R (see table 3.2). The left column represents the simulation where no diffusion is considered the centre are the experimental results from [143] and the right column is the simulation with $D = 2 \times 10^{-12} \text{m}^2/\text{s}$	66
3.4	Estimated mixing length as the necessary length to achieve 85% mixing via the nearest neighbour analysis technique.	72
3.5	Estimated mixing lengths with the average striation thickness for all mixing configurations.	73
4.1	Dimensions of microchannel geometries and fluid properties	86
4.2	Reactant conversion for a first order reaction and pressure drop in a staggered herringbone and a rectangular channel.	98
4.3	Influence of groove's geometrical parameters on the variance of the RTD.	99
6.1	Values of h at 298 K	127
6.2	Physical parameters used in the model	128
6.3	Dimensions for the computational domain of the falling film microreactor	130
6.4	Sherwood numbers for different values of Pe_{trans} obtained with two different values of γ_{trans} and with the 2D simplified model	140
7.1	Dimensions of the different geometries studied. Peclet number for al studies was $Pe = 10^4$	148
7.2	Dimensions of the different geometries studied.	158
8.1	Dimensions of the different geometries studied.	171
8.2	Parameters for the model of axial dispersion exchanging mass with a dead zone (ADEM) obtained by two different approaches.	185

Symbols

symbol	name	unit
a	Specific stretch	-
A	Surface area	m^2
B_0	Geometry dependent constant	
B_1	Geometry dependent constant	
C	Concentration	kg/m^3
C^*	Concentration on the stagnant zone	kg/m^3
C_s	Concentration at the surface	kg/m^3
C_{cup}	Mixing cup concentration	kg/m^3
COV	Coefficient of variance	-
d_H	Hydraulic diameter	m
d_i	Distance between particles	m
d_{mean}	Mean distance between particles	m
d_x	Distance between particles on the x axis	m
d_y	Distance between particles on the y axis	m
d_z	Distance between particles on the z axis	m
d_{xz}	Diagonal distance between particles	m
D_{ax}	Axial dispersion coefficient	m^2/s
E	Residence time distribution	1/s
E_{tw}	Residence time distribution measured through the wall	1/s
E_D	Eddy diffusivity	m^2/s
f	Fraction of volume subject to plug flow	-

F	Cumulative residence time distribution	-
F	Molar flow	mol/s
g	Geometry dependent constant	-
g	Acceleration due to gravity	m^2/s
g_d	Groove depth	m
g_w	Groove width	m
H	Height of channel	m
H	Henry's constant	$\frac{mol}{l \cdot atm}$
h	Height of channel	m
h_i	Parameters for gas solubility calculations	-
I	Current used in the limiting current technique	amp
I	Intensity of light for RTD measurements	-
I	Solution ionic strength	-
J	Mass flux across a boundary	$\frac{kg}{m^2 \cdot s}$
k	Reaction constant	-
k	Mass transfer coefficient	m/s
K	Mass transfer coefficient between the flowing volume and the stagnant zone	m/s
K	Overall mass transfer coefficient	m/s
K_L	Mass transfer coefficient on the liquid side	m/s
l	Liquid film thickness	m
l_1	Diffusion length for eddy diffusivity calculations (lagrangian)	m
l_2	Diffusion length for eddy diffusivity calculations (eulerian)	m
L	Length	m
\vec{l}	Stretching vector	-
p	Groove asymmetry	-
P	Pressure	Pa
n	Number of tanks	-
n	Reaction order	-
n_i	Moles of species i	-

N	Mass flux	$\frac{kg}{m^2s}$
N	Total number of particles	
Q	Flowrate	m^3/s
r	Reaction rate	$\frac{mol}{m^3 \cdot s}$
r_w	Ridge width	m
R	Tube radius	m
R_y	Correlation of the velocity of particles y distant apart	-
R_ξ	Correlation of the velocity of a particle at an instant with that of the same particle ξ seconds after	-
$RMSE$	Root mean square error	-
$s(t)$	Striation thickness	m
$\bar{s}t$	Average striation thickness	m
t	time	s
\bar{t}	Mean residence time	s
t_m	Mean residence time	s
T	Temperature	C
T	Time period	s
u	Mean velocity	m/s
u_b	Bubble velocity	m/s
U_m	Mean velocity	m/s
\vec{U}	Velocity vector	m/s
v	Volumetric flowrate	m^3/s
v_g	Vertical velocity on the groove	m/s
V	Vessel volume	m^3
Var	Variance	s^2
W	Channel width	m
w	Channel width	m
w_i	Weight factor for striation i	-
\bar{x}	Mean conversion	-
\vec{x}	Vector with particle positions	-

$x(t)$	Conversion at time t	-
y	Axial coordinate	m
y_i	Molar fraction	-
z_i	Valence for component i	-
δ_x	Penetration distance	
δ	Lyapunov exponent	
ΔP	Pressure drop	Pa
Γ	Gamma Function	-
γ	Surface tension	
$\dot{\gamma}$	Shear rate	
λ_m	Geometric mean of stretching values	-
μ	Viscosity	$Pa \cdot s$
ρ	Density	kg/m^3
σ	Standard deviation	s
σ_θ	Dimensionless standard deviation	-
θ	Dimensionless time	-
θ	Groove angle	-
τ	Average residence time	s
ξ	Random number with zero mean and unit variance	-

Chapter 1

Introduction

The chemical engineering field faces many challenges in today's changing world. The need for environmentally friendly processes is fundamental. Global issues such as the greenhouse effect and the supply of energy are driving the industry towards more efficient processes in terms of energy and raw material consumption. Microprocess engineering emerged as a branch in the chemical engineering field in the mid 90's. It offers a way to address some of these challenges in the near future.

The advances in microfabrication techniques for the semiconductor industry made possible the birth of microreaction technology. The first microreactors were usually built using photolithography and etching procedures [50]; however, other techniques were quickly adopted such as LIGA methods (Lithography, Electroplating and Molding), laser machining and soft lithography [165]. Microreactors exploit the fact that on the micrometer range, heat and mass transfer are intensified. This implies that isothermal conditions can easily be attained, which can result in greater conversions and selectivities. Although microchannels have been successfully used for analytical purposes [106], large scale production can be achieved by increasing the number of reactors, a concept known as scale-out or numbering-up, without the need of a pilot plant. This capability of microreactors have attracted

the attention of industries such as the pharmaceutical and fine chemical where the time it takes for a product to reach the market is critical [127].

Although the small dimensions of the channels lead to very high heat and mass transfer rates which, are certainly wanted characteristics in reactors, they also lead to high pressure drops and they are more susceptible to clogging. In addition, fluid flow in microchannels is laminar, therefore, mixing mechanisms relying on turbulence are absent and different microchannel configurations are needed to improve both mixing and mass transfer. In this thesis, several microstructures incorporated inside microchannels are studied in terms of mixing, mass transfer and residence time distributions (RTDs). The use of these structures can help in applications where mixing and mass transfer is a challenge, for example with liquids characterised by low diffusivities and/or high viscosities. The designs studied here can also be used to increase the dimensions of the channels to alleviate the problems with high pressures drops and clogging, without compromising the performance of the device in terms of mixing, RTD and mass transfer.

Chapter 2 includes a relevant background of the research efforts in the three main topics of this thesis: mixing, residence time distributions and mass transfer. In Chapter 3 the performance of the staggered herringbone micromixer [143] is analysed numerically for different flow ratios and injection locations. Three different techniques are used for the evaluation of the mixing length. In addition, areas of good and bad mixing within the microchannel are identified. This information can be used for different applications such as mass transfer to boundaries (studied in chapter 6).

Chapter 4, presents an experimental and numerical investigation on residence time distributions for channels with staggered and symmetric herringbone structures. These are compared to a rectangular channel with the same dimensions. The effect of flowrate and the groove geometrical parameters were studied. It was found that

at high Peclet numbers (high flowrate) the effect of the herringbone structures on the RTD was significant. However, at low Peclet numbers the differences reduced. An analysis of the effect of the groove geometrical parameters on the variance of the RTD showed that a groove angle of $\theta = 45^\circ$, depth of $g_d = 31\mu m$ and width $g_w = 50\mu m$ was close to the optimum. Chapter 5 presents a similar study on residence time distributions on microstructured plate reactors incorporating rectangular and zig-zag channels.

Chapter 6 focuses on the effect of different microstructures placed inside the microchannels on mass transfer to a wall. The performance of the staggered herringbone structure studied by Kirtland et al. [77] in an instantaneous reaction occurring at a microchannel wall is compared to a proposed alternated herringbone and a flow inversion structure. The geometries proposed were found to give bigger mass transfer coefficients and therefore stronger performance. The alternated herringbone was found to have the best performance, as not only the mass transfer coefficient was the highest, but it also had moderate pressure drops. A simplified model to replace the stirring effect of the herringbone structures with an enhanced diffusion coefficient was used to simulate the absorption of CO_2 in a falling film microreactor with herringbone structures on the microchannel floor. The agreement between simulations and experiments was satisfactory.

Chapter 7 presents mixing and residence time distribution studies in a layered herringbone channel. The proposed geometry is similar to the staggered herringbone channel. A plate with open-through herringbone structures is placed in the middle of two rectangular channels. This geometry allows for the use of single set of herringbones for two channels without compromising its performance in terms of efficient heat and mass transfer.

Chapter 8 focuses on the numerical and experimental investigation of a first order consecutive reaction in the layered herringbone geometry as compared to a

standard rectangular channel. Experimental residence time distributions for the layered herringbone channel were fitted to a model of axial dispersion exchanging mass with a dead zone. It was found that an approximation of the model parameters could be found exclusively with hydrodynamic data of the channel obtained from computational fluid dynamics. These efforts, eliminate the need of computing the RTD either numerically or experimentally. Reaction performance was found to be stronger on the layered geometry than on the rectangular one.

Chapter 9 presents the concluding remarks of this thesis along with major contributions of this work and future areas of research. Additional information about programming codes and calculations can be found on the appendices.

Chapter 2

Literature Survey

2.1 Mixing in Microchannels

Mixing is a fundamental operation in many chemical applications. Heat and mass transfer, chemical reactions and separations are all influenced by the mixing quality. Mixing efficiency in microchannels is determined by diffusion and convection mechanisms. Since flow within microchannels is predominantly laminar, mixing was usually achieved by diffusion mechanisms, either by reducing the dimensions of the channels or the size of the fluid layers [51, 78]. Mixing by diffusion is usually assessed by the Fourier number:

$$F_o = \frac{Dt}{d^2} \quad (2.1)$$

where D is the fluid diffusivity, t is the contact time and d is the characteristic dimension. Good mixing is achieved for $F_o > 0.1$ and complete mixing for $F_o > 1.0$; for channels in the order of hundred of microns the mixing time can be greater than hundred of seconds. Another commonly used number to characterize mixing is the Peclet number:

$$Pe = \frac{Ud}{D} \quad (2.2)$$

where U is the fluid velocity. For high Peclet numbers, convection is the phenomenon that dominates the mixing process [117]. For liquid phase reactions with high Peclet numbers mixing is a challenge, since even the small dimensions of the channels cannot overcome the small diffusion constants of liquids and consequently their long mixing times. Micromixers were created in order to get over this problem, their main objective being to increase the interfacial area and decrease the diffusion path [63].

Mixers can be classified as active or passive depending on the force that causes the mixing. Active micromixers use the disturbance of an external force such as pressure, temperature or electrokinetics for the mixing process, while passive micromixers do not require an external force, relying only on diffusion or chaotic advection [117]. Since active micromixers rely on moving parts or external fields, they are usually harder to operate than passive micromixers; for this reason many applications have been presented for the latter.

Hessel et al. [63] and Nguyen and Wu [117] have presented extensive reviews on micromixing. A chart showing the principal mixing mechanisms is shown in figure 2.1 [80]. In the following sections the principal types of mixing mechanisms will be discussed.

2.1.1 Convective Micromixers

Convective micromixers are the ones that use secondary flows usually present at high flowrates to enhance mixing. Several approaches have been used to enhance mixing at high Reynolds numbers. Wang et al. [157] investigated the effect of an arrangement of obstacles in the channel on mixing quality. They found that

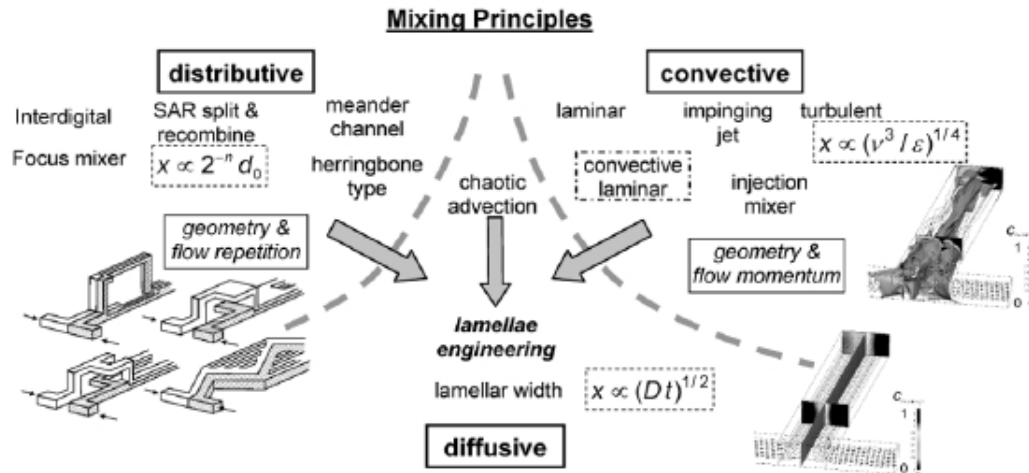


FIGURE 2.1: Mixing principles for microfluidic devices [80]

mixing could be greatly improved by the introduction of asymmetric obstacles. It was also found that at small Reynolds numbers flow recirculation was absent and mixing quality was poor. Ménégaud et al. [107] studied the effect of zig-zag shaped microchannels on mixing quality. For a constant Peclet number of 2600, the Reynolds number was varied. It was found that recirculation patterns and therefore improved mixing were only found at a critical Reynolds number higher than 80. Improved mixing has also been found in 90° bends [81], in curved channels [98] and in serpentine microchannels [98]. All these geometries are relative complex to fabricate or require a large footprint; in addition, relative high Reynolds numbers ($Re > 10^2$) are needed to improve the mixing performance. However, it has been shown that a simple T-mixer can have great mixing characteristics at intermediate Reynolds numbers [21, 42, 82, 164]. Six different regimes have been identified; their mixing characteristics can be found in figure 2.2

For $Re < 10$ the flow is laminar with straight streamlines, and mixing occurs mainly via diffusion. For $10 < Re < 130$ the straight laminar flow is disturbed and a pair of symmetric vortices appears at the T-junction. As the Reynolds number increases further ($130 < Re < 240$), fluid starts to switch sides and lamella thickness is reduced. Mixing efficiency starts to increase as can be seen in the

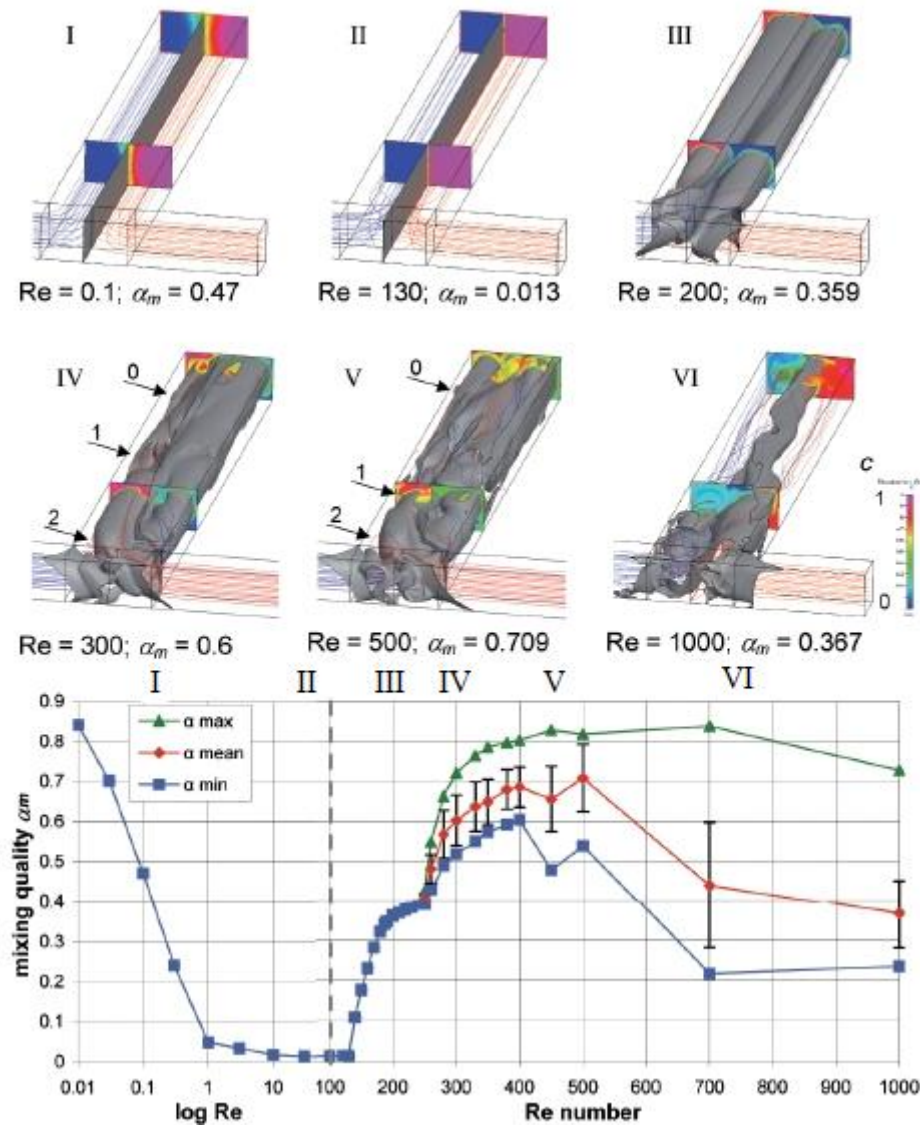


FIGURE 2.2: Overview of the flow regimes and ranges of Reynolds number in laminar T-mixer flow with 1:1 mixing ratio, $Sc=3000$. $T600 \times 300 \times 300 \mu m$. Bottom: Mixing quality α_m is determined at a constant length $l = 5d_h$ of the mixing channel here $l = 2000 \mu m$ [80]

bottom of figure 2.2. At a Reynolds number between 240 and 400 a transient behaviour occurs and pulsating flow is observed. For this reason a constant mixing quality for a given channel length is not observed and an average needs to be obtained as shown in figure 2.2. At $400 < Re < 500$ pulsating flow is still observed, however this is characterised by a higher frequency. On this regime the mixing quality reaches a maximum. Finally for $Re > 500$ the mixing quality decreases, regular pulsation is absent and although there is chaotic motion, fluids

are segregated.

2.1.2 Distributive Micromixers

The lamination of fluid streams is probably the simplest way of achieving fast mixing. Decreasing the diffusion path and increasing the contact surface can greatly reduce the mixing time. The most basic design is known as the ‘T-mixer’ or the ‘Y-mixer’ where two fluid streams flow parallel to each other (see figure 2.3a and b). In this case mixing relies only on diffusion and the channel length can be prohibitively long. Alternative ways of improving this design are by including obstacles on the channel [163], throttling the channel entrance [51] by hydrodynamic focusing [78] (see figure 2.3d) and by increasing the number of fluid streams (see figure 2.3c).

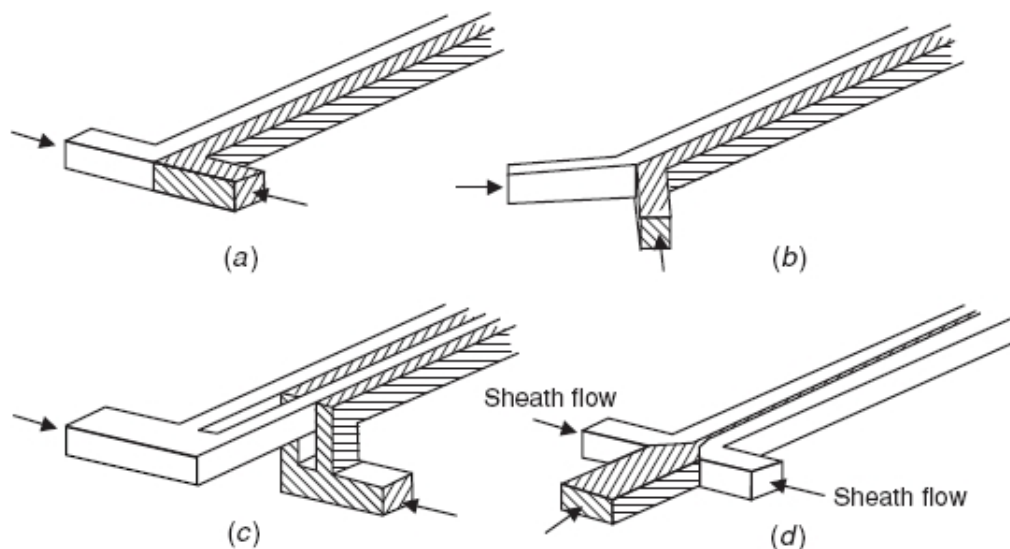


FIGURE 2.3: Parallel micromixers: a) T-mixer, b) Y-mixer, c)parallel lamination, d)hydrodynamic focusing in [117]

Multilamination micromixers also fall under the category of distributive mixing. The idea behind multilamination is to decrease the size of the fluid elements so that the thickness of fluid layers are small enough for the rate of diffusion to be significant. Since diffusion time is proportional to the square of the diffusion

distance, reducing lamella thickness result in a reduction of mixing times. This concept has been used for improving mixing in a number of publications [19, 62, 71, 79].

Another kind of distributive micromixers relies on the repeated stretching and folding of fluids, reducing fluid thickness therefore accelerating diffusion. Split and recombine (SAR) mixers fall in this category. The idea is to split a bi- or multi-layered stream perpendicular to the lamella orientation and recombine them. This mixing technique is displayed graphically in figure 2.4. Mixing is greatly increased because the repetition of various SAR units increases the interfacial area exponentially [132].

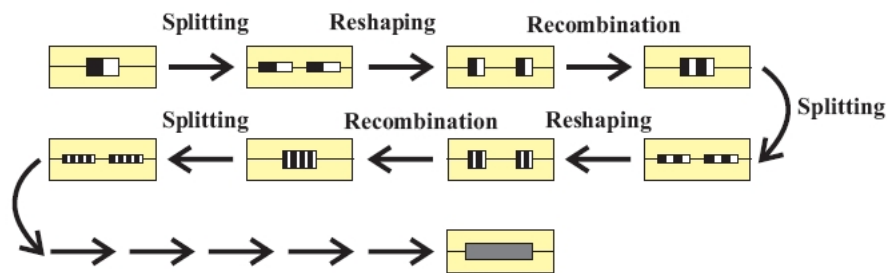


FIGURE 2.4: Mixing mechanism based on split and recombination [41]

Chen et al. [32] studied a ‘tear drop’ micromixer and compared its performance with an ‘F’ mixer geometry shown in figure 2.5a and b respectively. A theoretical model for the mixing evaluation of folding flow type of mixers was suggested in MacInnes et al. [104] and it was used to compare the geometries. It was found that the ‘F’ mixer needed considerable lower pressure drop for a given mixing time than the ‘tear drop’ mixer. However it is important to consider that the analysis was done for specific geometric parameters and does not necessarily imply that the ‘F’ mixer is inherently better than the ‘tear drop’ mixer. Other ways of splitting and recombining the flow to improve mixing characteristics are shown in figure 2.5c [54, 59, 112, 133].

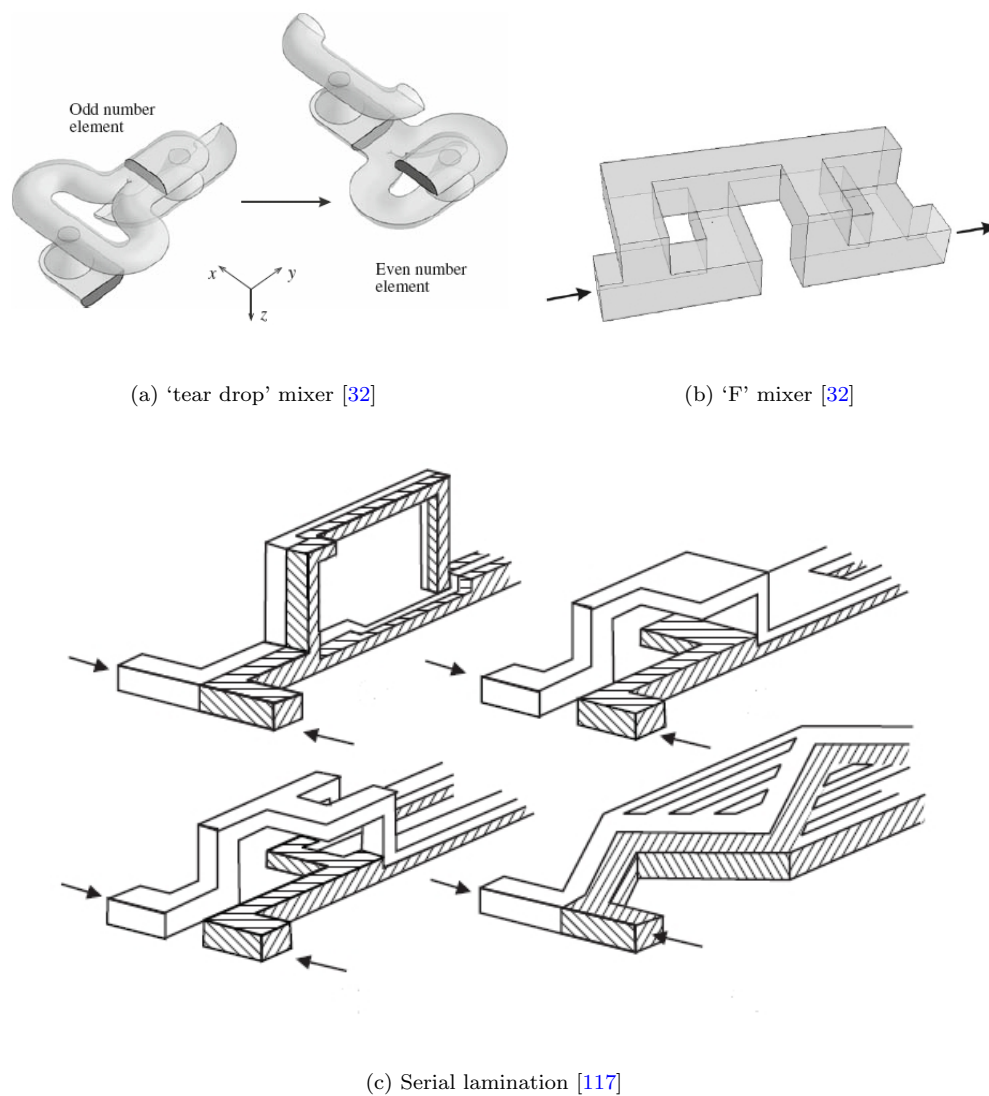


FIGURE 2.5: Other mixer geometries.

Another approach for the stretching and folding of fluid layers is to include rib structures on the microchannel walls. Johnson et al. [72] reported a micromixer with diagonal grooves ablated at the microchannel floor. They found that the grooves were able to induce lateral transport of material, reducing diffusion distance and consequently decreasing mixing time. Groove dimensions were optimised to improve mixing and reduce axial dispersion. Stroock et al. [143] proposed the staggered herringbone mixer (SHM) which consists of a series of asymmetric chevrons patterned on the microchannel floor (see figure 2.6a). The position of

the asymmetry changed every half cycle creating a pair of counter-rotating vortices that resembled the blinking vortex model proposed by Aref [9]. Mixing was greatly improved compared to an unstructured channel; it was found that mixing time scaled with the logarithm of Pe ($\frac{ud}{D}$) rather than linearly, yielding mixing times in the order of centimeters rather than meters.

Numerous investigations have been made regarding the optimization of the SHM parameters. Wang et al. [158] studied the impact of the groove aspect ratio on the performance of the SHM with the help of CFD simulations and particle tracking algorithms. They found that as the groove aspect ratio increased the flow pattern became less regular and the length necessary to generate one complete recirculation decreased exponentially. Yang et al. [166], also found that the groove depth is one of the most important factors dominating the mixing performance. According to their results the flow rate within the grooves plays a major role on the mixing behaviour of the SHM and that this is affected by the aspect ratio of the groove and the asymmetry index. The results presented by Aubin et al. [12] seem to confirm this finding, they showed that deeper and wider grooves reduced the maximum striation thickness more rapidly hence the mixing length is reduced. Also Bennett and Wiggins [17] showed that the fluid transportation within the groove, ditch mixing as they call it, plays a key role in the performance of the mixer, and they found that the short legs of the grooves could be removed without significant detriment on the mixing performance. Camesasca et al. [25] found that instead of having the grooves arranged in half cycles where the degree of asymmetry switches between two values, a non periodic arrangement could lead to an improvement on mixing compared to the original SHM design. Howell et al. [70] combined diagonal grooves with herringbones on the top and bottom of the channel. They found through experiments and computational fluid dynamics that mixing was more efficient on their design as compared to the SHM design by Stroock et al. [143].

Modifications to the geometries originally proposed by Johnson et al. [72] and Stroock et al. [143] have also been considered. Kim et al. [76] presented the barrier embedded micromixer (BEM) (see figure 2.6b). Chaotic mixing is achieved by a periodic perturbation on the velocity field caused by the insertion of barriers on the top wall and slanted grooves on the bottom. Whereas the flowfield under the effect of the slanted grooves is characterised by one elliptic point, the insertion of the barriers create two elliptic points and one hyperbolic point where stretching and folding is significant [76]. Yang et al. [167] designed a circulation disturbance micromixer (CDM) which is similar to the barrier embedded micromixer. Slanted grooves are ablated at the bottom and a zig-zag barrier on the top wall splits the helical flow induced by the grooves (see figure 2.6c). Numerical simulations showed that the CDM had the strongest mixing performance as compared to the BEM and the SHM. Mixing was found to be dependent on the number of zig-zag barriers per given length. Experiments confirmed the validity of numerical simulations.

2.2 Residence Time Distributions

Since Danckwerts [38] introduced the idea of a residence time distribution (RTD), it has remained as one of the fundamental concepts in the chemical engineering field. All major textbooks in chemical reaction engineering discuss it at some level. Danckwerts [38] provided the RTDs for plug flow and completely mixed reactors. However, deviation from these ideals are often encountered. Fluid bypass, recirculation and stagnation regions will have an impact on the RTD and they usually lower the performance not only of chemical reactors but heat exchangers and packed columns as well [88]. Since fluid elements take different routes within the reactor and there is a distribution of velocities, the fluid elements take different times to reach the end of the reactor. The distribution of these times is the RTD denoted with the letter E in this thesis with units of $time^{-1}$. The RTD is usually

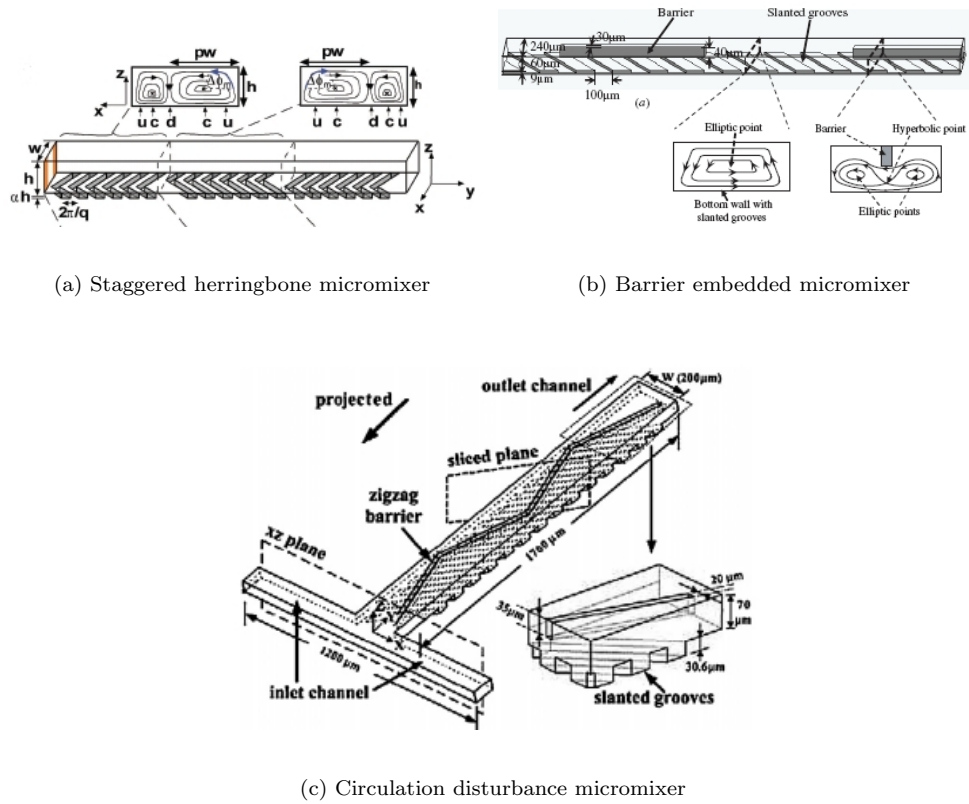


FIGURE 2.6: Mixer geometries containing grooves placed on one or more microchannel walls

measured by injecting an inert tracer at the inlet of the reactor and then measuring its concentration at the outlet. There are a number of ways for introducing the tracer, the most common being as a pulse or a step.

2.2.1 Pulse Experiment

If a quantity of M units of tracer is introduced into the vessel and the concentration of the tracer is recorded as a function of time at the outlet of the vessel, then the mean and the area of the curve can be found from [88]:

$$Area = \int_0^{\infty} C dt \approx \sum_i C_i \Delta t_i = \frac{M}{v} \quad (2.3)$$

$$\bar{t} = \frac{\int_0^{\infty} tC dt}{\int_0^{\infty} C dt} \approx \frac{\sum_i t_i C_i \Delta t_i}{\sum_i C_i \Delta t_i} \quad (2.4)$$

The residence time distribution $E(t)$ can be obtained simply by dividing the concentration C_{pulse} by the quantity $\frac{M}{v}$ as shown in figure 2.7. The RTD in dimensionless form E_{θ} measured in dimensionless time $\theta = t/\bar{t}$ is obtained from:

$$E_{\theta} = \bar{t}E = \frac{V}{M}C_{pulse} \quad (2.5)$$

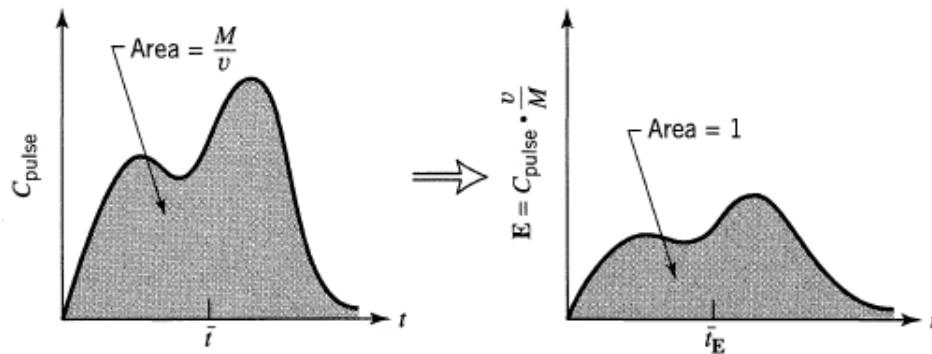


FIGURE 2.7: Transforming the experimental C_{pulse} into the E curve. [88]

2.2.2 Step Experiment

Consider now that a fluid is flowing through a vessel with a flowrate v and at time $t = 0$ the stream is switched to one with a tracer concentration C_{max} . The concentration C_{step} as a function of time would look as shown in figure 2.8. The dimensionless form of the C_{step} curve is usually called the F curve where the tracer concentration rises from zero to unity [88].

The step experiment is usually easier to perform than the pulse one. And since $F = \int E dt$ the RTD can be obtained by differentiating $E = \frac{dF}{dt}$.

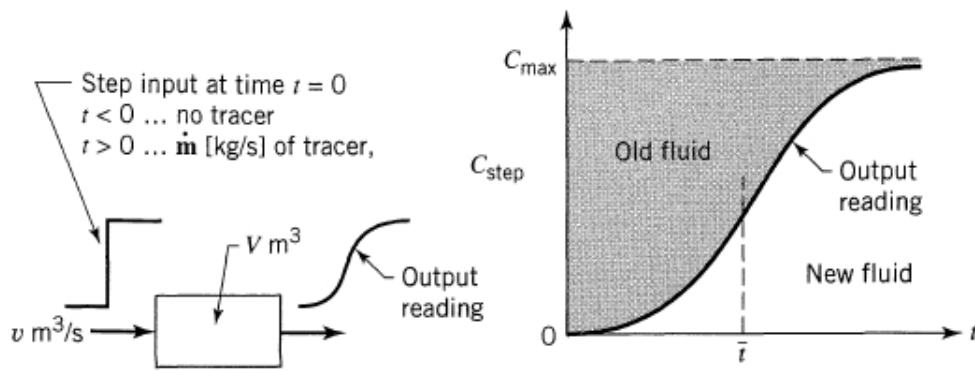


FIGURE 2.8: Information obtainable from a step experiment. [88]

2.2.3 RTDs on Microchannels

Microchannels usually exhibit laminar flow. At this regime, mixing occurs only by molecular diffusion and the RTD can be broad at very low and very high radial Peclet numbers [88]. Residence time distributions in microchannels with Taylor (segmented gas-liquid) flow have been studied by various investigators both theoretically and experimentally [56, 128, 129, 150]. Due to the recirculation patterns generated in the liquid slugs the microchannel acts as a series of batch reactors where a small amount of dispersion is present due to the communication of adjacent slugs by a thin liquid film. Salman et al. [128] studied the effect of different parameters on the RTD of a Taylor flow microreactor. It was found that increasing the Peclet number, ($Pe = \frac{u_b d}{D}$) the Capillary number ($Ca = \frac{\mu u_b}{\gamma}$) or the slug length increased the spread of the RTD. Trachsel et al. [150] measured the RTD experimentally for gas-liquid flow and compared it with the case of single phase flow, demonstrating that the variance of the RTD for gas-liquid flow was lower than for the single phase case.

For single phase flow Adeosun and Lawal [1] showed theoretically that microstructured packed bed configurations exhibit a narrower RTD as compared to a simple microchannel. Bošković and Loebbecke [20] investigated the RTD of three different split-and-recombine micromixers by fitting an empirical model to experimental

data. It was found that for all cases the RTD became narrower by increasing the flow rate due to the formation of secondary flows causing chaotic advection.

Aubin et al. [13] quantified the effect of microchannel aspect ratio on the RTD and the axial dispersion coefficient. They found that for a fixed cross-sectional area and throughput the RTD was narrower as the aspect ratio decreased (channel height/channel width=0.05-1). The axial dispersion coefficient was found to increase asymptotically with increasing aspect ratio. It was recommended that microchannels should be designed with an aspect ratio in order to obtain narrow RTD and minimise dispersion. Hornung and Mackley [69] measured experimentally the residence time distributions in disc-shaped plastic multiple capillary reactors. By fitting their data to Taylor's axial dispersion model it was shown that a single capillary 10m long displayed near plug flow characteristics. The multiple capillary reactor also presented plug flow characteristics, but with a deviation from Taylor's model due to variations in channel diameter.

Stroock et al. [143] proposed a chaotic mixer which consisted of staggered herringbone structures patterned on the floor of the microchannel. It was shown that this staggered herringbone mixer minimised dispersion at high Peclet numbers compared to a rectangular microchannel. Several articles have characterised the mixing behaviour of the staggered herringbone mixer [6, 11, 12, 25, 58, 73, 74, 93, 99, 158, 162, 166]. However, only few studies characterise its residence time distribution and its possible use to minimise dispersion. Stroock and McGraw [144] presented an approximate analytical model, called "lid-driven cavity mode", that mimics the effect of the grooves on the flow behaviour. They found that the patterned geometry (the microchannel floor with the grooves) can be replaced by a flat wall with an effective slip boundary condition representing the movement of the fluid caused by the grooves. The convection of massless particle tracers was used to characterise the flow behaviour. A comparison of the distribution of tracers at several cross sections along the microchannel with experimental results

showed that the model represented well the mixing characteristics of the staggered herringbone microchannel. They also presented RTD results for the staggered herringbone microchannel with different degrees of asymmetry and compared them to that of a rectangular microchannel. It was shown that all the channels with herringbone structures had a narrower RTD than the rectangular microchannel. Aubin et al. [12] using particle tracking confirmed that the RTD of the staggered herringbone microchannel approaches that of plug flow. They further observed that neither the groove depth nor the number of grooves per cycle affected the RTD significantly, in contrast with the groove width. These analyses are valid in the limit of $Pe \rightarrow \infty$ since particle tracking considers only the movement of the particles by convection. However, as the characteristic dimension of the microchannel decreases so does Pe and the assumption that convection dominates over diffusion is no longer valid. In this case, for mixing applications diffusion would be beneficial, while from the RTD point of view diffusion may be detrimental. The RTD is not properly accounted for with a pure particle tracking method because the volume of the grooves may appear to be dead space, while in reality, material will seep out from the grooves by diffusion creating a long tail in the RTD. A particle tracking algorithm that includes the effect of diffusion like the one considered in this thesis is more appropriate.

2.2.3.1 Measuring RTDs in Microchannels

Residence time distributions are usually obtained by injecting an inert tracer at the channel inlet and measuring its concentration at the outlet. Different approaches for the tracer introduction and the recording of the outlet concentration have been presented for microchannels. Günther et al. [57] used a T-junction along with computer controlled syringe pump switching for the introduction of the tracer and a LED-photodiode system for the measurement of tracer concentration. Trachsel et al. [150] injected the tracer as a Dirac-delta pulse by a piezoelectrically

actuated membrane and recorded its concentration by fluorescence microscopy. Bošković and Loebbecke [20] injected the tracer with an HPLC valve and recorded its concentration by an in-house made UV-vis flow-through cell. Lohse et al. [100] described a novel method for the determination of the RTD based on the optical activation of a caged fluorescence dye. Tracer concentration was determined by fluorescence microscopy. This method allows for the determination of RTD without the need of measuring the inlet signal because the inlet is ensured to be a Dirac-delta pulse. In this thesis a LED-photodiode array is used for the experimental measurement of RTDs. More details of this method can be found in chapter 4

2.2.4 Conversion

The ultimate goal of measuring the residence time distribution is to be able to characterise reaction performance (conversion) with it. However, there are other factors that have an impact on reaction conversion [88].

- Reaction kinetics
- Earliness or lateness of mixing
- Whether the fluid behaves as a macro or micro fluid

A microfluid is characterised by complete mixing at the molecular level, i.e. individual molecules are free to move. This condition is typical of gases and liquids with low viscosity. On the other hand, in a macrofluid, molecules are grouped together in packets. Solid particles and viscous liquids are typical examples of macrofluids. Since there is no interaction between molecules in a macrofluid, each packet behaves as a batch reactor. The mean conversion is given by [45]:

$$\bar{x} = \int_0^{\infty} x(t)E(t)dt \quad (2.6)$$

where \bar{x} is the mean conversion and $x(t)$ is the conversion of each element at time t . For first order reactions $x(t) = e^{-kt}$ where k is the reaction constant.

The earliness and lateness of mixing also affects reaction conversion. When the reaction order is greater than one ($n > 1$) late mixing increases conversion, for $n < 1$ early mixing increases conversion. One of the advantages of having the RTD is that for first order reactions the kinetics and the RTD are the only information needed for the calculation of the conversion. The issue of microfluid/macrofluid and the earliness and lateness of mixing does not play a role. For reaction orders different than one, a flow model like the ones described before in this section is needed. Equations for the conversion of a reactor subject to the axial dispersion or the tank in series model can be found in Fogler [45], Levenspiel [88]. However, the knowledge of the RTD is important not only to identify a model suitable for the reactor, it can also provide upper and lower bounds to the reaction conversion.

2.2.4.1 Influence of RTD on Multiple Reactions

Both mixing efficiency and RTDs play an important role on the product composition in multiple reactions. For series reactions, when an intermediate is the desired product, a plug-flow contacting pattern would give the best results. Since microchannels deviate from the idealised plug flow behaviour, characterising the extent of mixing and the residence time distribution in microchannels is an active field of study. Different mixing principles and geometries have been studied such as the traditional T-mixers [21, 42, 82, 164], multilamination [19, 40, 62, 84] and split and recombine geometries [32, 54, 87, 104, 112, 122, 132]. Residence time distributions have also been measured in different microchannel configurations such as T-mixers [2, 57, 100], micromixers based on different principles such as chaotic

advection and split and recombine [1, 12, 20, 26], capillaries [69] and in gas/liquid flow [56, 128, 129, 150].

The influence of mixing on the product distribution in multiple reactions has been studied in microchannels. Aoki et al. [7] investigated the effect of lamination width, reaction constants and reaction orders on the conversion and yield in multiple reactions using computational fluid dynamics. It was shown that the lamination width greatly affected the yield of the desired product. In most cases the complete mixing of the reactants at the inlet gave the highest yield. However, when both the reaction order and the rate constant for the reaction producing by-products are higher than those of the reaction with the desired product, a large lamination width gave higher yields than a perfectly mixed inlet condition. This is because the higher order reaction is more affected by reactant concentrations and it will only proceed where the reactants are well mixed. When the lamination width is increased, the region where reactants are well mixed decreases and the reaction with lower order (in this case the desired reaction) is favored. In an extension to that study Aoki et al. [8] introduced two dimensionless numbers that characterise the effect of geometric design of fluid segments on product yield and selectivity. The ratio of reaction rate to diffusion rate (Damköhler number), allows to determine whether the reaction proceeds under reaction controlled conditions regardless of the shape of the fluid elements. The aspect ratio of the diffusion lengths in both directions (width and height) was also studied. It was found that the arrangement of the fluids in rectangular fashion in the cross-section gave higher yields, especially when the aspect ratio is high.

The effect of type of flow and hence the RTD in multiple reactions has been studied by Levien and Levenspiel [92]. They analysed the product distribution for a series reaction for four different flow regimes: plug flow, laminar flow, power-law and mixed flow. It is found that deviation from plug flow behaviour results in a detrimental effect on the intermediate yield. However, even the worst case of

non-newtonian fluid gave better results than a Newtonian fluid in mixed flow. In Chapter 8 the conversion of an intermediate in a series reaction is studied in a layered herringbone channel.

2.3 Mass Transfer

2.3.1 Fundamentals of Mass Transfer

There are two ways of describing mass transfer in a system: by Fick's law of diffusion, which uses the diffusion coefficient, or by the use of mass transfer coefficients. Although the approach with Fick's law (coupled with convection and reaction as necessary) is more fundamental, often the use of mass transfer coefficients greatly simplifies the analysis without compromising the results. In this section, the most relevant mass transfer models will be presented along with attempts of measuring mass transfer coefficients in different systems.

2.3.2 Mass Transfer Coefficients

Mass transfer coefficients are often used in experimental approaches since it is an easy way to arrange the results and develop correlations. If we would like to know the mass transfer rate from a well mixed solution to an interface, we would expect that the rate of mass transferred is proportional to the concentration difference and the surface area [35]:

$$(\text{rate of mass transferred}) = k(\text{interfacial area})(\text{concentration difference}) \quad (2.7)$$

If both sides are divided by the area, the mass transfer flux can be expressed as:

$$N_i = k(c_i - c) \quad (2.8)$$

where N_i is the flux at the interface, c_i is the concentration at the interface and c is the concentration at the bulk (average concentration away from the interface). This relationship shows that a large value of k indicates fast mass transfer just in the same way that a higher reaction constant indicates a faster chemical reaction. Therefore the mass transfer coefficient can be thought of as a velocity of diffusion.

2.3.3 Physical Models

2.3.3.1 Film Theory

The simplest model that one can use for the calculation of mass transfer coefficients is the film theory. Mass transfer is assumed to happen between the bulk and a hypothetical stagnant film near the interface [35]. The solute is assumed to be highly diluted so that the diffusion perpendicular to the interface can be neglected. From this theory, the mass transfer coefficient can be calculated as:

$$k = \frac{D}{l} \quad (2.9)$$

where l is an unknown liquid film thickness, D is the diffusion coefficient and k is the mass transfer coefficient. This theory says that the mass transfer coefficient is proportional to the diffusion coefficient and independent of fluid velocity. The dependence of the mass transfer coefficient on other factors (like fluid velocity) is lumped in the unknown film thickness l .

2.3.3.2 Penetration Theory

The penetration theory suggested by Higbie [64] assumes a thick film generated by the flow where mass transfer occurs via diffusion. The mass transfer coefficient on this model is obtained from:

$$k = \sqrt{\frac{Dv_{max}}{\pi L}} \quad (2.10)$$

where v_{max} is the maximum velocity and L is the length of the region of study. This model predicts a variation of the mass transfer coefficient with the diffusion coefficient of $k \propto D^{\frac{1}{2}}$ as opposed to the prediction of the film theory of $k \propto D$. These two predictions tend to bracket the experimental results [35].

2.3.3.3 Surface Renewal

The surface renewal theory proposed by Danckwerts [36] predicts the same relation between the mass transfer coefficient and the diffusion coefficient as the penetration thickness theory; however, the physical picture is more realistic. It considers mass transfer between two regions: an interfacial and a well mixed region. The volume of the interfacial region is constantly being replaced by volume elements in the well mixed region. The mass transfer coefficient is given by

$$k = \sqrt{\frac{D}{\tau}} \quad (2.11)$$

where τ is the average residence time for an element in the interfacial region. Just as the film thickness l in the film theory is unknown, the average residence time τ also is unknown.

2.3.3.4 Graetz-Nusselt Problem

The Graetz-Nusselt problem is used often for the prediction of mass transfer coefficients in circular tubes. This model considers mass transfer across a wall in a tube subject to laminar flow. The model assumes a fixed wall concentration. The mass transfer coefficient averaged over the tube length L expressed as a Sherwood number is given by [35]:

$$Sh = \frac{3^{\frac{1}{3}}}{\Gamma(\frac{4}{3})} \left(\frac{dv}{\nu}\right)^{\frac{1}{3}} \left(\frac{\nu}{D}\right)^{\frac{1}{3}} \left(\frac{d}{L}\right)^{\frac{1}{3}} \quad (2.12)$$

where Γ is the gamma function and v is the fluid velocity. Similar expressions for the Sherwood number for different systems subject to laminar flow such as mass transfer on a flat plate, between two immiscible cocurrent streams, on a falling liquid film or between flat parallel plates can be found in [139].

2.3.4 Mass transfer measurements

Gas absorption in hollow fibres have received a lot of attention since the pioneering work by Qi and Cussler [124]. Most of the work done in hollow fibres has considered the absorption of CO_2 in NaOH. However water [96, 125] and amine solutions have also been used [126, 159]. A review of CO_2 absorption in hollow fibres with different solvents has been presented by Li and Chen [95]. Qi and Cussler [124] obtained mass transfer coefficients for the absorption coupled with chemical reaction of CO_2 in NaOH. Their experimental results were in good agreement with the correlation proposed by Sieder and Tate [137] and the theoretical result from equation (2.12). However, this agreement is misleading, because the conditions are not consistent with the heat transfer analysis of Sieder and Tate [137]. For instance, in Qi and Cussler [124] only one third of the membrane is porous which should reduce the mass transfer coefficient. Furthermore, the coefficient should

also increase with the presence of a chemical reaction. Kreulen et al. [85] absorbed CO_2 in hollow fiber membranes with water-glycerol mixtures. They found that their experimental results were in accordance with the prediction of equation (2.12) and the Sieder and Tate [137] correlation. Moulin et al. [111] measured the transfer of oxygen to water by means of hollow fiber membranes. A comparison between the mass transfer between straight and helically coiled membranes was done. It was found that coiled membranes had Sherwood numbers between 2 and 4 times greater than for straight ones. Secondary flows induced by Dean vortices were responsible for the increase in mass transfer. Their results for straight membranes were in accordance with equation (2.12)

Mass transfer has also been heavily studied for catalytic reactions in monoliths. Holmgren and Andersson [68] have studied CO oxidation in monoliths both experimentally and theoretically via CFD. A correlation for the Sherwood number was proposed that predicted values higher than the ones obtained from analytical calculations. Balakotaiah et al. [14] presented a new model for the analysis of catalytic reactions in monoliths. The proposed model has been compared to the two-dimensional model and the widely used one-dimensional two-phase model. It was found that the proposed model is the simplest way of characterising qualitatively surface catalysed reactions. Balakotaiah and West [15] solved the convection-diffusion equation for laminar flow in a duct of arbitrary shape with an infinite reaction at the wall. It was shown that the exit conversion depends mainly on the Peclet number and that a universal curve of conversion vs. Pe can be drawn for all geometries.

The oxygen transfer to an aqueous medium has been subject of study due to its importance in aerobic bioprocesses [27, 105, 120, 151]. There are several ways of measuring the oxygen transfer rate, Gogate and Pandit [52] gives an overview of the different methods available. The most common way is to measure the oxygen concentration in the liquid side with an oxygen sensitive electrode. Also

the oxygen concentration in the liquid can be measured by monitoring its reaction with sodium sulfite [61]. A procedure for calculating mass transfer coefficients for the oxygenation of water in hollow fiber membranes was developed by Ahmed and Semmens [3]. In their study deoxygenated water was pumped from a closed reservoir to the channels. Inside the channels was a bundle of hollow fibers where oxygen was being pumped. The concentration of oxygen was measured in the reservoir by means of an oxygen electrode. The overall mass transfer coefficient was found by plotting $\ln\left(\frac{C^*}{C^*-C_1}\right)$ vs. t and measuring the slope of the line. Since the membranes were hydrophobic, mass transfer in the membrane and in the gas side can be neglected and $\frac{1}{K} = \frac{1}{k_L}$. Two assumptions were considered in the calculation: the response time of the oxygen probe is fast enough to monitor the change in oxygen concentration; the oxygen concentration in the reservoir changes slowly compared to the concentration in the module.

A simple way of calculating mass transfer coefficients is by the limiting current technique. An extensive discussion of the technique can be found in Tobias et al. [149], here a brief description is included. Direct current through a liquid is maintained through a flow of electron from the ions in the liquid to the electrode surface. The mass transfer coefficient can be related to the current measured by:

$$k = \frac{I}{A \cdot c \cdot F} \quad (2.13)$$

where F is the Faraday constant, c is the bulk concentration of the species, A is the surface area for mass transfer, I is the current and k is the mass transfer coefficient. This technique has been used by Burns and Jachuck [23] for the calculations of mass transfer coefficients in a spinning disc reactor. Shrivastava et al. [136] have used it for the evaluation of different geometries at increasing mass transfer coefficients for water filtration applications. They found for all the geometries studied that $Sh \propto Pe^{\frac{1}{3}}$ in accordance to the prediction by the Graetz-Nusselt

theory. Li et al. [94] studied both theoretically and experimentally the effect of net spacers in mass transfer by means of the limiting current method. It was found that mass transfer coefficients obtained experimentally were in good agreement to the ones obtained by CFD. Furthermore the variation of the Sherwood number was also in accordance with the Graetz-Nusselt equation. Kirtland et al. [77] calculated theoretically the mass transfer coefficients for the staggered herringbone channel. It was found that flow pattern generated by the herringbones can be described by a modified Graetz behaviour where the Sherwood number can be calculated by $Sh = B_0 Pe^{\frac{1}{3}}$ in the developing region and $Sh = B_0 Pe_{trans}^{\frac{1}{3}}$ for the asymptotic region. where $Pe_{trans} = \frac{u_{trans}H}{D}$, u_{trans} is the horizontal transverse velocity and H is the height of the channel.

2.3.5 Mass transfer over reactive surfaces

Mass transfer to reactive surfaces in microchannels is of great relevance due to its applications in surface catalysed reactions [75, 156], electrochemical reactions [31, 33, 34, 44] and biological applications [18, 102, 114, 138]. The delivery of material from the bulk to the reactive surface is important to increase the yield or the efficiency in terms of material consumption.

The staggered herringbone channel has been shown to be effective at increasing mass transfer to boundaries. Kirtland et al. [77] simulated mass transfer on the top wall of a channel with floor staggered herringbone structures by tracking passive tracers over a range of Peclet numbers with an instantaneous reaction occurring at the top wall. They found that the staggered herringbone had a higher rate of mass transfer compared to a standard rectangular channel. It was also found that other geometries (symmetric herringbone and diagonal grooves) which do not produce a chaotic flow had mass transfer rates comparable to the herringbone

channel. The symmetric herringbone and the diagonal grooves generated sufficient transverse flow to remove the boundary layer growing in the channel ceiling. Although the performance of these structures leads to a significantly larger drop in the average concentration as compared to an unstructured rectangular channel, they still had a worst performance than the staggered herringbone case. This indicates that mixing in the bulk is not a necessary condition to achieve high mass transfer rates. Yoon et al. [168] described 3 methods to overcome mass transfer limitation to reactive surfaces: i) removing the depleted zone through multiple periodic outlets, ii) adding fresh reactants through multiple periodic inlets, or iii) inducing transverse convective motion with herringbone structures. It was found that approaches i) and ii) are better at improving the reactant conversion rate; however the space required for operation and the pressure drop is higher than approach iii). Golden et al. [53] used grooves for redirecting the flow and enhancing the delivery of molecules from the bulk to the reacting surface. Assay results showed an increase between 26-46% relative to a plain rectangular channel. Lopez and Graham [101] have shown that shear-induced diffusion in flowing suspensions can also enhance the mass transfer to boundaries. It was found that the most effective way to enhance mass transfer to a boundary was through a combination of herringbone structures and shear-induced diffusion. The herringbone structures were found to be effective at circulating fluid between the adsorbing wall and the bulk, whereas the shear-induced diffusion enhanced transport across the boundary layer.

Static mixers are commonly used to increase heat and mass transfer and avoid temperature and concentration gradients that are detrimental for reaction applications. However, mixers are not the best way of enhancing heat and mass transfer to a wall. For these applications flow inverters can give a better performance because they maximise the driving force by bringing material from the wall to the bulk and vice versa. They have been used in macroscopic equipment for increasing

heat transfer performance [115] and to obtain narrow RTDs [130, 153]. In chapter 6 mass transfer to a reactive surface is studied for herringbone and flow inversion structures and these are compared to a standard rectangular channel

Chapter 3

Effects of Flow Ratio and Injection Location on the Performance of the Staggered Herringbone Micromixer

3.1 Introduction

Several publications have been presented regarding the behaviour of the Staggered Herringbone Micromixer (SHM) under different conditions as shown in chapter 2; these investigations have been done with a flow ratio 1:1. However, in practice, the flow ratio is in general different because flowrates and concentrations of the different components to be mixed are usually different. In this chapter we shall consider the effects of various flow ratios and injection locations of the fluid on the performance of the SHM and its impact on the necessary mixing length.

Many of the methods to characterize mixing are based on the intensity of segregation concept proposed by Danckwerts [37]. The mixing quality can be assessed

by an index usually in terms of a standard deviation or variance of a sample that measures the degree of homogeneity of the system [67]. Stroock et al. [143] determined the amount of mixing by measuring experimentally the standard deviation of the intensity distribution of the tracer obtaining an index of 0.5 for complete segregated and 0 for complete mixed systems; Aubin et al. [11] tracked the positions of massless particles to characterise the behaviour of micromixers. They presented an approach of quantifying mixing by quadrant analysis dividing a mixer cross section in a finite number of cells, calculating the amount of particles in each cell and determining the degree of mixing by plotting the variance of particles in each cell at a given mixer length. This approach has also been used by Hobbs and Muzzio [65, 66, 67]; Aubin et al. [12] in a following paper presented the statistical technique called the nearest neighbour analysis. This method compares the distance between the particles in the sample to a uniform distribution of the same sample. A small variance indicates that the sample resembles a uniform array. They quantified mixing by dividing the variance of the distances between the sample and the uniform array at a certain time, over the variance at complete segregation. An alternative to this procedure is to use the coefficient of variance, COV, which is the standard deviation normalized by the mean [65]. Mixing can also be characterised by measuring the decrease in the average striation thickness [12, 47, 118]. However sometimes measuring this quantity may be difficult. An alternative to this procedure is to track fluid tracers through the mixer and compute the stretching of a fluid vector associated with each particle. The amount of intermaterial area generated by the flow is proportional to the rate of stretching of the particles [65, 67, 97, 146].

In this chapter mixing has been characterised by three methods: the nearest neighbour analysis, the reduction in the average striation thickness and the stretching histories. All of them give an estimation of the necessary mixing length.

3.2 Theoretical Methodology

3.2.1 Description of Mixer Geometry

The mixer geometry used in the calculations is based on the one presented by Stroock et al. [143], with asymmetric herringbones on the bottom of the channel, which create a pair of counterrotating vortices (see figure 3.1).

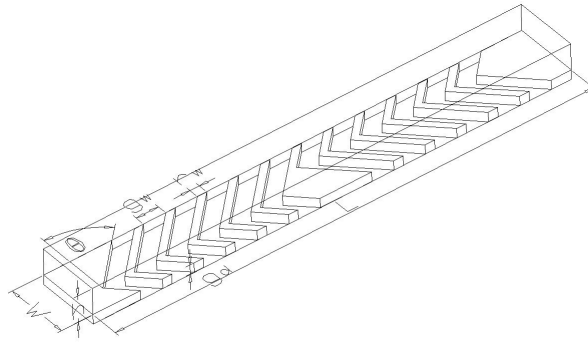


FIGURE 3.1: Staggered herringbone mixer [143]

The degree of asymmetry p is measured by the fraction of channel width occupied by the long arm of the herringbones. The peak of the herringbone switches its position every half cycle allowing to change the position of the vortices, creating a flow pattern similar to the blinking vortex model proposed by Aref [9]. The mixer consists of several mixing cycles where each cycle is composed of two sets of grooves with the centre of the asymmetry alternated (Figure 3.1). The channel width is $200 \mu m$ and the channel height is $85 \mu m$. The grooves are placed at an angle with respect to the axial direction. The full depth of the grooves is $30.6 \mu m$. Due to the repeating cycles, the velocity field in the axial direction can be assumed to be periodic and hence the velocity field in one mixing cycle can be obtained and reused repeatedly for successive cycles. Details of the mixer geometry and fluid properties are summarised in Table 3.1 below. Fluid properties are consistent with Stroock et al. [143] work. The direction of the flow is from left to right.

TABLE 3.1: Mixer dimensions and fluid properties

Staggered Herringbone Mixer	
Channel width W	200 μm
Channel height h	85 μm
Length per cycle	1.516mm
Number of grooves per cycle	12
Groove asymmetry p	2/3
Groove angle θ	45°
Groove depth g_d	30.6 μm
Groove width g_w	50 μm
Ridge width r_w	50 μm
Fluid properties	
Density	1200 kg/m^3
viscosity	0.067 $Pa \cdot s$
Mean velocity u	0.002 m/s
Diffusion constant	2x10 ⁻¹²
Pe	200000
Re	7.16x10 ⁻³

3.3 Methods for Hydrodynamic Characterisation

3.3.1 Velocity Field

The numerical calculations were performed with COMSOL Multiphysics 3.3, a commercial modelling software based on the finite element method that solves the Navier-Stokes and mass conservation equations simultaneously. The velocity field has been solved using periodic boundary conditions so that the velocity at the outlet boundary is equal to the inlet one, with a constant flow rate throughout the channel; additionally, no-slip boundary conditions have been applied to all walls. A mesh consisting of 30,712 number of elements and 156 256 degrees of freedom was used to execute the simulations and they were performed on Windows XP with Pentium IV 3.00 GHz CPU and 2 GB of RAM.

The species concentration and thus mixing performance, can be found by solving

the convection-diffusion equation coupled with the Navier-Stokes equation, however for liquid-liquid mixing with $Pe > 10^3$ numerical errors (often called numerical diffusion) attributed to the discretisation of the convective term in the convection-diffusion equation are likely to affect the results [131]. To avoid this problem, computing the trajectories of massless particles convected by the flow (with no diffusion) is commonly used to characterise mixing and it is a good approximation for flows with high Peclet numbers [11, 12, 158].

3.3.2 Particle Tracking

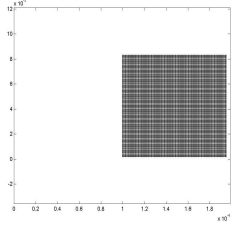
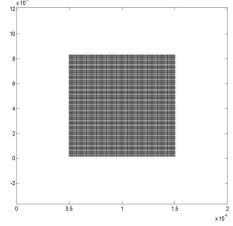
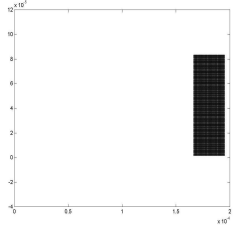
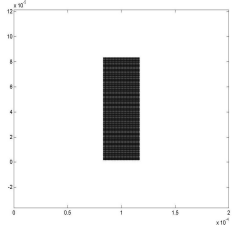
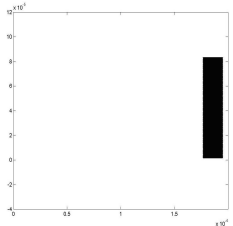
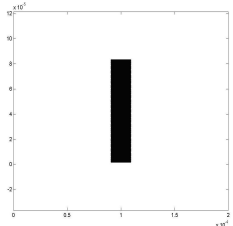
A particle tracking method was undertaken in order to assess the quality of mixing of the SHM under different operation conditions. 7872 massless particles are evenly distributed at the inlet, according to the initial conditions presented in Table 3.2. The locations of the particles are computed by integrating the equation of motion:

$$\frac{d\vec{x}}{dt} = \vec{U} \quad (3.1)$$

where \vec{x} is the vector with the positions of the particles, \vec{U} is the fluid velocity vector and t is time. A Matlab particle tracking algorithm (see appendix C) obtains the velocity at the position of the particle by interpolation (from the velocity field obtained from COMSOL) and gets its new position by solving equation (3.1) for a fixed time step, the positions of the particles are recorded and the procedure is repeated over a specified number of steps. This code is set so that the velocity field obtained for the first cycle could be used over many mixing cycles. A standard fourth order Runge-Kutta method with fixed time steps was used to get the solution.

The particle tracking algorithm described above can be modified so that the particles have a convective transport and a random diffusion step. This approach has

TABLE 3.2: Initial locations of particles for mixing simulations

Configuration ID	Mixing Ratio	Initial Location of Particles
M1:1R	1:1	
M1:1C	1:1	
M1:5R	1:5	
M1:5C	1:5	
M1:10R	1:10	
M1:10C	1:10	

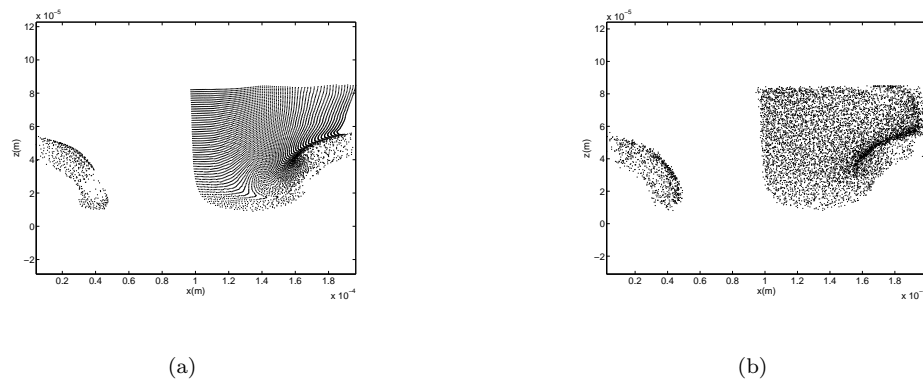


FIGURE 3.2: Cross-sectional images for a mixing ratio of 1:1 with particles initially located on the right of the channel (M1:1R). a) Particle tracking with no diffusion equation (3.1). b) Particle tracking with random walk diffusion equation (3.2)

been used before to approximate diffusion [77, 145]. Therefore equation (3.1) is modified and the particle trajectories are calculated with the following stochastic differential equation [49]:

$$d\vec{x} = \vec{U}dt + \sqrt{2Ddt}\vec{\xi} \quad (3.2)$$

where $\vec{\xi}$ is a vector with random numbers with zero mean and unit variance.

When a particle leaves one of the boundaries of the channel, it is reflected back to its previous position. Equation (3.2) approximates the solution to the convection-diffusion equation as the time step goes to zero. The positions of the particles at different lengths of the mixer are compared for the two particle tracking methods (with or without diffusion). It is shown in figure 3.2 that for high Peclet numbers the solution does not change significantly and that the assumption of no diffusion is adequate. Therefore equation (3.2) is not implemented for the rest of the calculations in this chapter.

3.4 Methods for Mixing Characterisation

3.4.1 Mixing Length Based on Stretching Histories

Several studies have revealed that mixing can be quantified by the evolution of the stretching of material elements in the flow [65, 67, 97, 146]. The amount of interfacial area between lamella, generated by the flow, is proportional to the amount of stretching the fluid experiences. Since the stretching is highly non-uniform [30, 113], there are particles that experience high and low stretching, representing regions of good and bad micromixing [97]. This is important when deciding the injection location of the fluids. The Matlab code described in the previous section is used to compute the positions of 4100 particles. In addition, the stretching of a vector \vec{l} associated with each particle is calculated by integrating equation (3.1) along with:

$$\frac{d(\vec{l})}{dt} = (\nabla \vec{U})^T \cdot \vec{l} \quad \vec{l}_{t=0} = \vec{l}_0 \quad (3.3)$$

The total accumulated stretching after some time is defined as:

$$\lambda = \frac{|\vec{l}|}{|\vec{l}_0|} \quad (3.4)$$

where each tracer has been assigned an initial vector $|\vec{l}_0|$. At the end of each cycle the geometric mean of the stretching values for all particles is computed:

$$\lambda_m = \left(\prod_{i=1}^N \lambda_i \right)^{\frac{1}{N}} \quad (3.5)$$

where N is the total amount of particles at the end of each cycle. If the flow is chaotic the stretching will grow exponentially and the stretching rate in a spatially periodic flow can be described with the specific stretch as defined in [65]:

$$a = \lim_{n \rightarrow \infty} \left[\frac{1}{n} \ln(\lambda_m) \right] \quad (3.6)$$

where n is the cycle number. The striation thickness reduction is equivalent to the length stretch [119]:

$$\lambda_m = \frac{l(t)}{l(0)} = \frac{s(0)}{s(t)} \quad (3.7)$$

where $l(t)$ and $l(0)$ are the lengths of a fluid element at time t and 0 respectively and $s(t)$ and $s(0)$ are the striation thicknesses at time t and 0. Therefore, if a is the specific rate of stretch, the striation thickness at any time can be calculated with:

$$s(t) = \frac{s(0)}{\lambda} = \frac{s(0)}{e^{at}} = s(0)e^{-at} \quad (3.8)$$

For a spatially periodic flow, the penetration distance due to molecular diffusion increases along the mixer length while the striation thickness is reduced from $s(0)$ to $s(t)$, according to the stretching function, a . The ratio of penetration distance to striation thickness evolves along the mixer length according to [119]:

$$\frac{\delta_x}{s(0)e^{-\delta t}} = \left[\frac{D}{(s(0))^2 2\delta} (e^{2\delta t} - 1) \right]^{\frac{1}{2}} \quad (3.9)$$

where δ_x is the penetration distance and δ is the Lyapunov exponent. For a spatially periodic system the specific stretch a is the direct analog of the Lyapunov exponent and equation (3.9) becomes [74]:

$$\frac{\delta_x}{s(0)e^{-at}} = \left[\frac{D\tau}{(s(0))^2 2a} (e^{2an_{mix}} - 1) \right]^{\frac{1}{2}} \quad (3.10)$$

Mixing is assumed to be complete when the penetration distance from molecular diffusion becomes equal to the striation thickness [119]. This happens when:

$$1 = \left[\frac{D\tau}{(s(0))^2 2a} (e^{2an} - 1) \right]^{\frac{1}{2}} \quad (3.11)$$

Rearranging equation (3.11), the number of cycles required for complete mixing is determined from:

$$n_{mix} = \frac{\ln \left(\frac{(s(0))^2 2a}{D\tau} + 1 \right)}{2a} \quad (3.12)$$

and the mixing length is:

$$y = n_{mix} L_{cycle} \quad (3.13)$$

3.4.2 Percentage of Mixing based on Nearest Neighbour Analysis

The nearest neighbour analysis method, described in Aubin et al. [12], estimates the distance between the tracer and the nearest particle placed in a uniformly distributed grid (see figure 3.3), this distribution is intended to represent the state of complete mixing where particles are present everywhere in the cross section. The distance d_i in figure 3.3 is obtained with the following expression:

$$d_i = \sqrt{((x_i - x_{np})^2 + (z_i - z_{np})^2)} \quad (3.14)$$

where (x_i, z_i) are the coordinates of the particles in the uniform distribution and (x_{np}, z_{np}) are the coordinates of the nearest particle tracer. Also d_{mean} which represents the mean distance between the central particle and the rest of the 8 particles in the uniform array can be defined as follows:

$$d_{mean} = \frac{2d_x + 2d_z + 2d_{xz}}{8} \quad (3.15)$$

where the distances d_x , d_z , and d_{xz} are shown in figure 3.3. A variance of d_i is computed as follows:

$$Var = \frac{\sum_{i=1}^N (d_i - d_{mean})^2}{N - 1} \quad (3.16)$$

where N is the number of particle tracers. If the value of d_i is less than d_{mean} , then a value equal to d_{mean} is assigned to d_i . In this case, uniform mixing is considered to have been achieved and results to a variance of 0 according to equation 3.16. To measure the degree of homogeneity the coefficient of variance (COV) is calculated as follows:

$$COV = \frac{Var}{d_{mean}} \quad (3.17)$$

Also the extent of mixing can be quantified by measuring the spatial distribution of the tracers in the cross-section. The tracers will be in a uniform array when the distances between the tracers and the particles in the uniform array is equal to d_{mean} . In this case the system is completely mixed. For other cases the degree of mixing can be thought of as the percentage of tracers that is already arranged in a uniform manner; thus, it is possible to calculate the mixing percentage as:

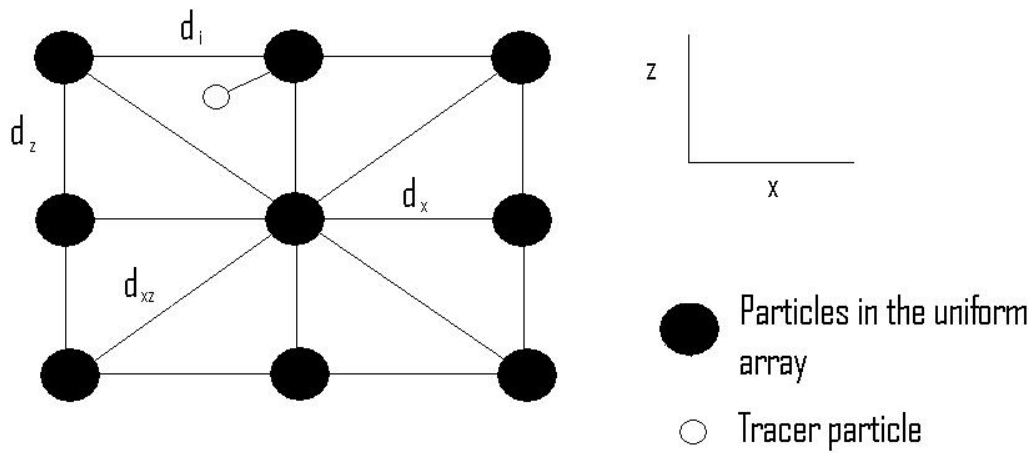


FIGURE 3.3: Relevant distances for nearest neighbour analysis calculations

$$\%mixing = \frac{N_{uniform}}{N} \quad (3.18)$$

where $N_{uniform}$ is the number of particles that have a distance to the nearest particle in the uniform array, less than or equal to d_{mean} .

3.4.3 Mixing length from Striation Thickness Calculations

The average striation thickness in a cross-section at the end of various cycles is measured by identifying patterns of striations in the particles. At the end of every cycle a snapshot of the plane $z - x$ and horizontal slices, j , of $5 \mu m$ thickness covering the central part of the cross-section, from $20 \mu m$ to $70 \mu m$, are taken. The positions of the particles are recorded within each slice of the mixer cross-section as shown in figure 3.4. The thickness of the striation, $st_{i,j}$ is measured by identifying the initial and final particle of the striation. If the horizontal separation of the particles is within $2.5 \mu m$, then it is considered that they belong to the same striation. In addition, the thickness of the spaces without particles has also been measured since it represents the other fluid being mixed. Since some striations are considerably bigger than others, calculating an arithmetic average may give

misleading results. To overcome this problem a weighted average is computed as follows:

$$w_i = \frac{st_i}{W} \quad (3.19)$$

$$\overline{st}_j = \sum_{i=1}^k w_i st_i \quad (3.20)$$

where w_i is the weight factor for striation i , st_i is the thickness of striation i , W is the width of the channel, k is the number of striations identified on the section and \overline{st}_j is the average striation thickness for section j . This procedure is repeated ten times from a height of 20 to 70 μm of the channel, and the average striation thickness for the whole cross section is taken as the arithmetic mean of \overline{st} for the ten sections:

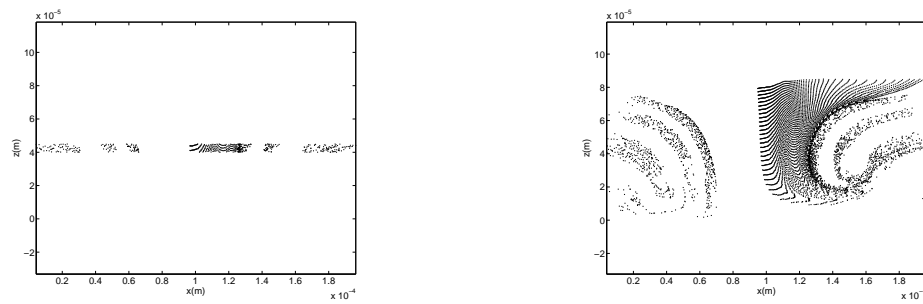
$$\overline{st} = \sum_{j=1}^{10} \overline{st}_j \quad (3.21)$$

After obtaining \overline{st} for different number of cycles an exponential curve can be fitted as described by equation (3.8). With the exponential factor a , the mixing length can be obtained with the procedure described in section 3.4.1.

3.5 Results and Discussion

3.5.1 Qualitative Analysis

In this section, the distribution of particles after a number of cycles is analysed for a mixing ratio of 1:1, 1:5 and 1:10. In addition two injection locations for each mixing ratio were also evaluated.



(a) Particles at the end of 3rd cycle at a height between 40 and 45 mm

(b) Particles at the end of 3rd cycle on the whole cross-section.

FIGURE 3.4: Cross-sectional particle distributions for striation thickness measurement

3.5.1.1 Flow Ratio 1:1

Table 3.3 compares the distributions of particles obtained from the two particle tracking methods described in section 3.3.2 for the first five cycles for a mixing ratio of 1:1 with the fluids flowing side by side. Experiments from Stroock et al. [143] are also shown for comparison. For configuration M1:1R (see table 3.2), it is clear that at the end of the first cycle some of the particles have been transported to the other side of the channel as can be seen on table 3.3. Figure 3.5, shows the distribution of particles after the first five cycles for configuration M1:1C. The fluid particles seem more uniformly distributed in the crosssection. As the particles are placed in the centre of the channel, a fraction of them is able to access the long leg of the groove, while the other fraction enters the short leg. Thus, particles are transported to both sides of the channel, enhancing what Bennett and Wiggins [17] called ditch mixing. By the end of the fifth cycle most of the particles in M1:1C are distributed randomly across the crosssection of the channel, while in M1:1R there is a high accumulation of particles on the centre.

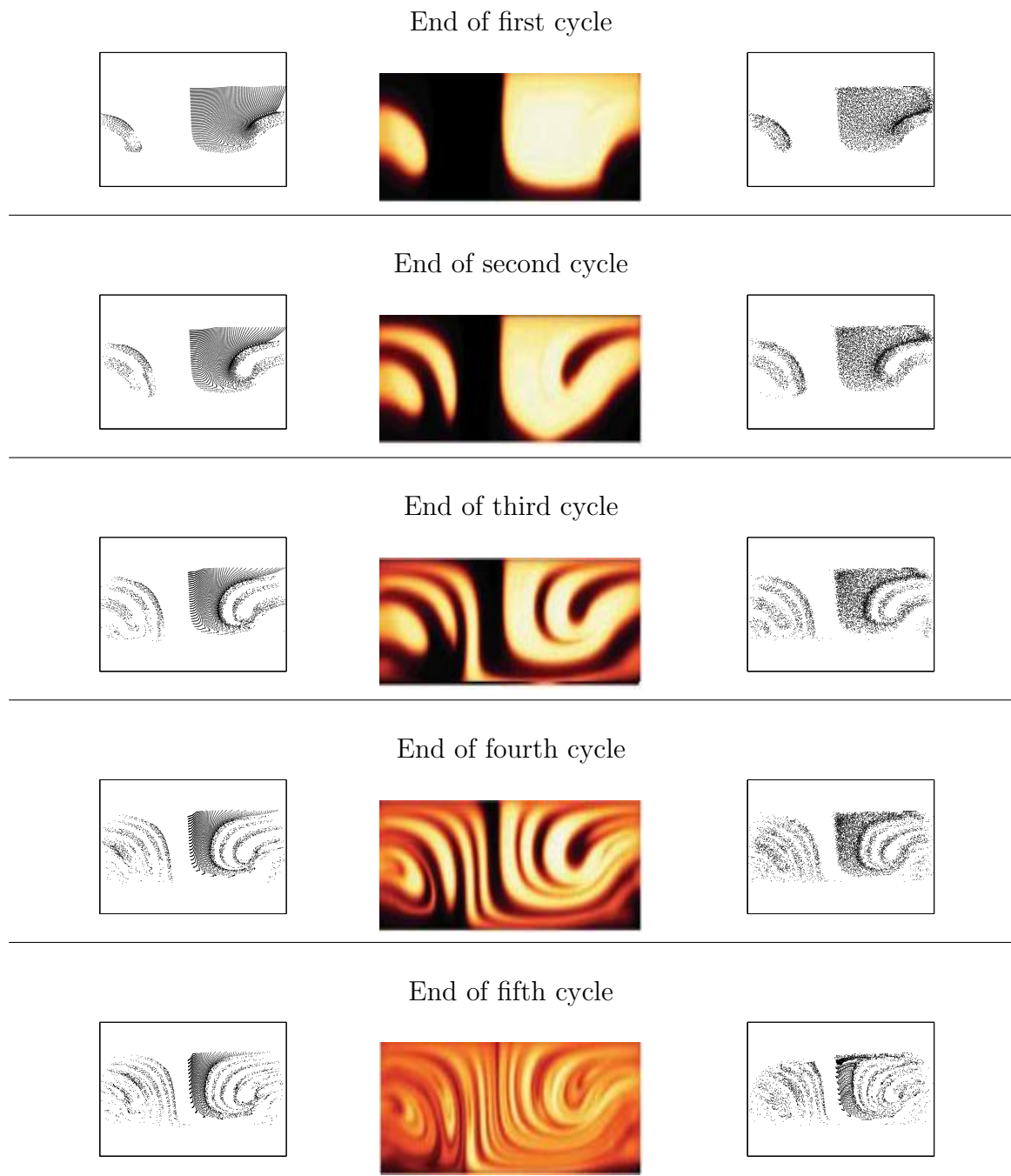
Table 3.3 also includes a comparison between both particle tracking methods and the experimental results from [143]. Although the simulation results are in good agreement with the experiments there are some discrepancies worth noting. In the

experimental results at the end of the third cycle on the bottom of the channel, there seems to be fluid from the left side of the channel traveling to the right side, the simulations are unable to capture this feature. Also the simulations seem to underestimate the mixing capabilities, while in the experiments at the end of the fifth cycle the concentration of the dye is somewhat uniform apart from the corners at the bottom, in the simulations there is still a high concentration of particles in the centre of the channel that has barely moved. The inclusion of diffusion to the particle tracking algorithm via the random walk procedure does not seem to improve a lot the difference. Even though it starts to capture the movement of fluid at the bottom of the channel from the left side to the right side, it still contains a high number of particles in the centre of the channel. Stroock and McGraw [144] presented an analytical model that closely resembles the SHM behaviour by replacing the grooves on the bottom by a slip boundary condition, the magnitude of the slip velocity was adjusted to achieve quality agreement with the experiments. Previous attempts to reproduce the SHM behaviour via CFD calculations have had the same problem of underestimating the stirring capacity of the mixer evidenced mainly by a high concentration of particles in the centre of the channel [11, 12, 73].

3.5.1.2 Flow Ratio 1:5

For configuration M1:5R, after five cycles (figure 3.6a) the particles seem to be rotating in one half of the channel with little communication with the other half, thus mixing is poor. After two cycles none of the particles have been able to reach the left side of the channel, instead they are all confined in a single striation. On the other hand, for M1:5C (figure 3.6b) the particles experience a great amount of transverse movement (particles are convected to both sides of the channels) thus mixing is greatly enhanced. At the end of the first cycle there are particles present on both sides of the channel and after 5 cycles there are lots of striations clearly

TABLE 3.3: Cross-sectional images for configuration M1:1R (see table 3.2). The left column represents the simulation where no diffusion is considered the centre are the experimental results from [143] and the right column is the simulation with $D = 2 \times 10^{-12} \text{m}^2/\text{s}$.



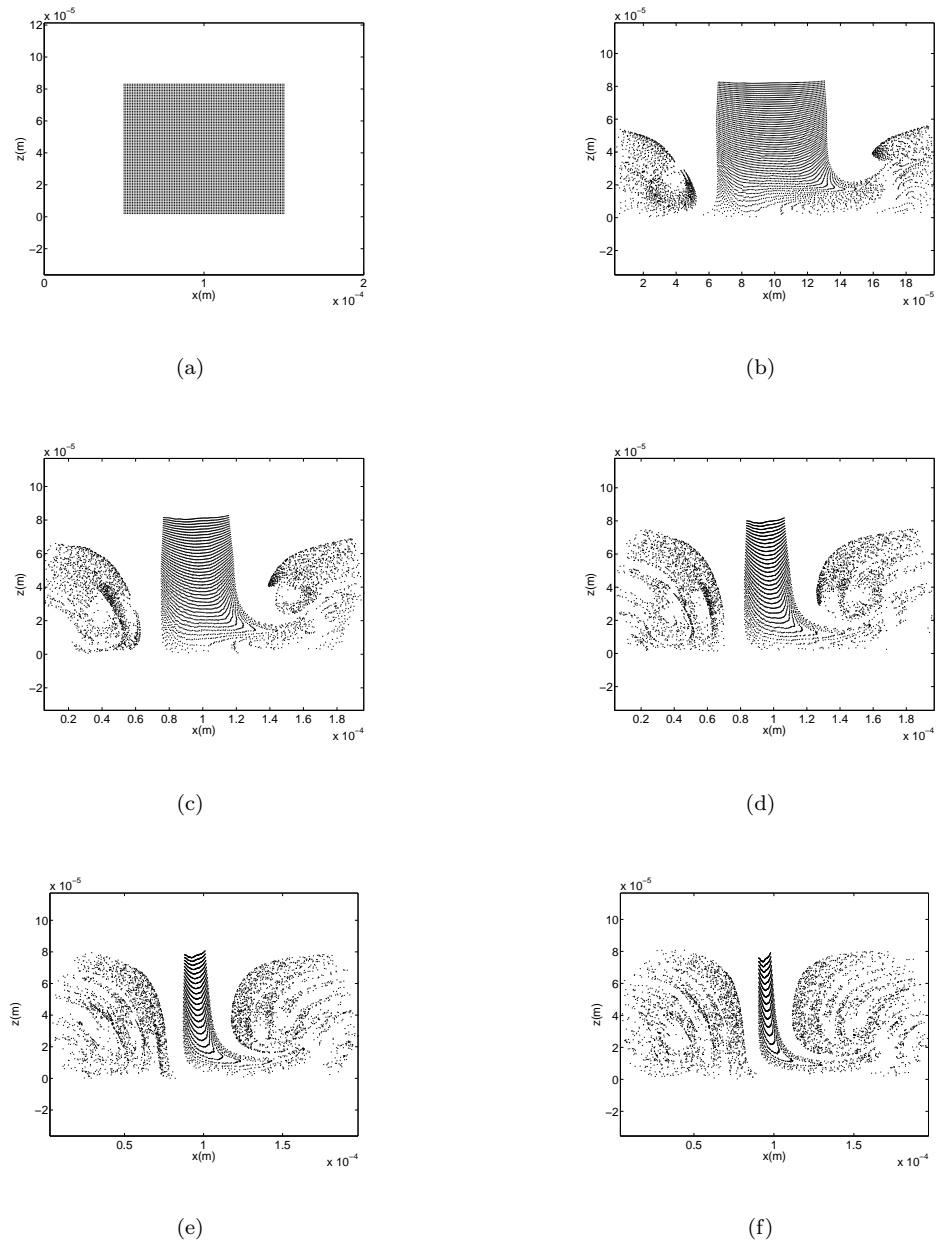


FIGURE 3.5: Cross-sectional images for configuration M1:1C (see table 3.2). a) initial conditions, b) end of 1st cycle, c) end of 2nd cycle, d) end of 3rd cycle, e) end of 4th cycle, f) end of 5th cycle. $Re = 7.16 \times 10^{-3}$.

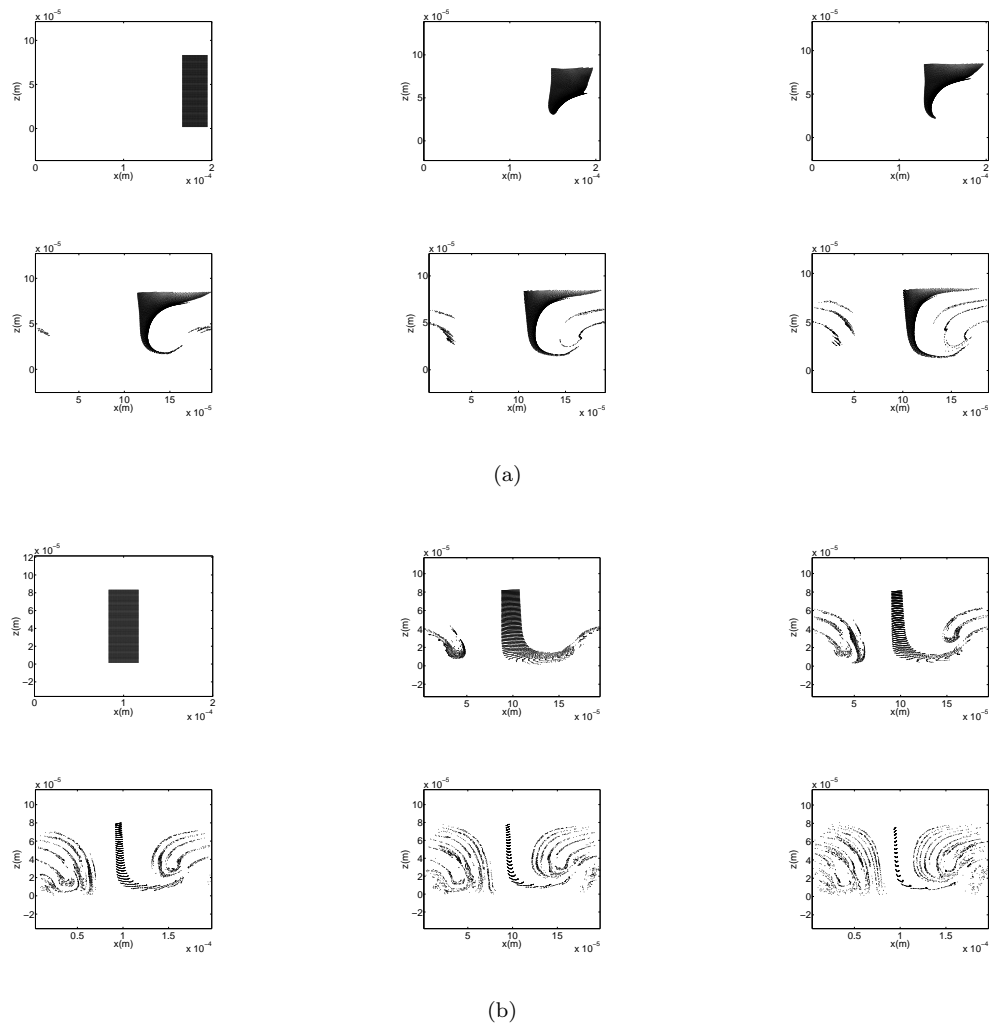


FIGURE 3.6: Cross-sectional images for the first 5 cycles a)M1:5R b)M1:5C.
 $Re = 7.16 \times 10^{-3}$.

identifiable. It is interesting to note, that the impact on mixing of the locations of the fluids is more important for M1:5R and M1:5C than for the first two cases (M1:1R, M1:1C).

3.5.1.3 Flow Ratio 1:10

M1:10R configuration is somewhat similar to the M1:5R and M1:1R cases. The particles exhibit very little transverse movement, and instead they experience a densification on the right side of the channel (figure 3.7a). However, M1:10R presents a poorer behaviour than the other two cases (table 3.3 and figure 3.6),

mainly because as the amount of particles is decreased (the flow ratio decreases), the particles take longer to reach the other side of the grooves thus experiencing little transportation to the left side of the channel. This is also the reason why the injection location is more important as the flow ratio decreases. After four cycles there are practically no particles on the left side whereas for M1:1R and M1:5R there were particles after one and three cycles respectively. Note that for M1:10R there are only 3 striations after 5 cycles whereas for the other cases it is difficult to count.

For M1:10C on figure 3.7b, mixing is greatly enhanced when the particles are on the centre of the channel. Just as in M1:1C and M1:5C the grooves are able to move the particles to both sides of the channel achieving almost a random distribution of the particles. M1:10C presents almost the same behaviour as M1:5C with the only difference that for the former the particles that remain in the centre are less, which is explained by the fact that the mixing ratio is smaller. The main difference in both cases is that for M1:10R the particles are being convected only in one half of the channel and there is little communication with the other half, while in M1:10C the particles are being transported by the grooves to both sides of the channel. In fact, it is evident from figures 3.5, 3.6b, and 3.7b, that the amount of particles that remains in the centre is reduced at the end of every cycle as these are transported to the sidewalls by the grooves.

3.5.2 Quantitative Analysis

3.5.2.1 Percentage of Mixing based on the Nearest Neighbour Analysis

In order to evaluate the quality of mixing, the coefficient of variance (COV) was computed by the method described in section 3.4.2. Figure 3.8, shows the COV for all mixing ratios versus the number of cycle. It shows that even before the fluid

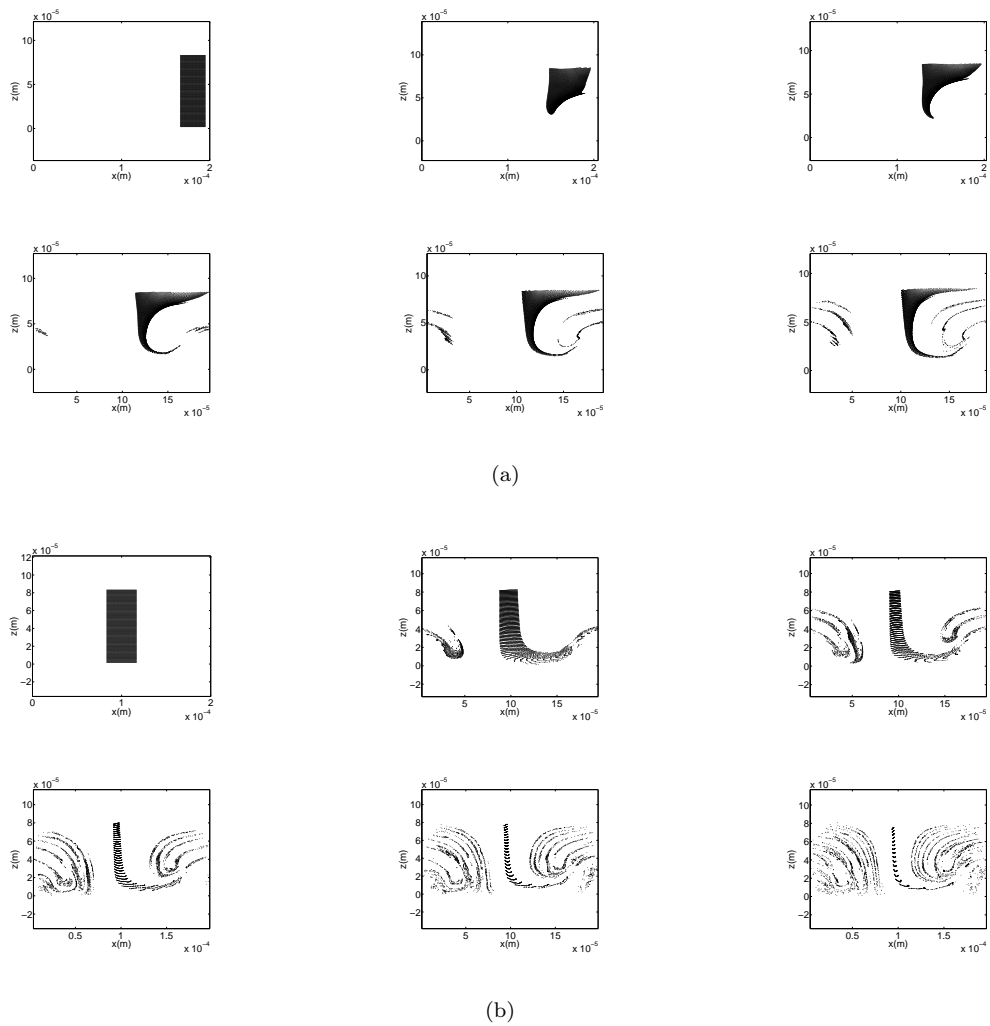


FIGURE 3.7: Cross-sectional images for the first 5 cycles a)M1:10R b)M1:10C
 $Re = 7.16 \times 10^{-3}$.

starts traveling along the channel, the initial COV decreases by placing one of the fluids in the centre because of the reduced distances between the initial positions of the particles and their uniform distribution. Albeit the mixing performance is better in M1:1C than in M1:1R, the differences are reduced as the fluid proceeds along the axial direction. For M1:5R and M1:5C the different injection locations have a greater impact than in M1:1R and M1:1C, the same is true for M1:10R and M1:10C. It is interesting to note that all cases show an exponential decrease on COV as found for chaotic flows [65, 74]. However for M1:5R and M1:10R, when the particles are on the side of the channel, the exponential decrease does not start until some of the particles have reached the other side of the channel, that is the

3rd and 4th cycles respectively, for the previous cycles the decrease is linear.

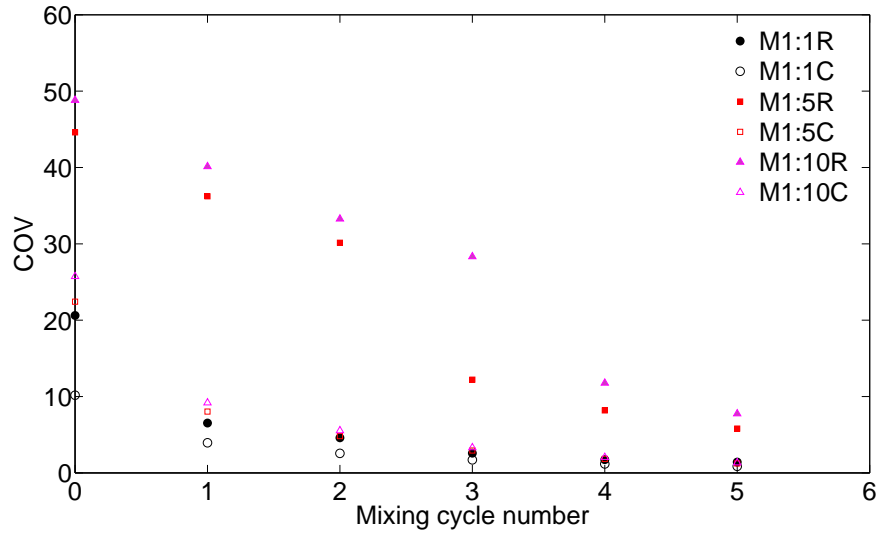


FIGURE 3.8: Coefficient of variance as a function of number of cycles for various mixing ratios and injection configurations (see table 3.2).

The percentage of mixing is calculated with equation (3.18) and the results for all cases are plotted in figure 3.9. If 85% of mixing is used as an arbitrary value to compare mixing and estimate a mixing length, for all cases, placing the particles in the centre of the channel resulted in a lower mixing length than its corresponding case with the particles on the side of the channel. It is important to note that the percentage of mixing seems to reach an asymptote. One of the reasons is that since diffusion is not included in the particle tracking algorithm, it is difficult to find particles near the channel walls. In addition when a particle leaves through one of the boundaries it is lost from the simulation, and this also contributes to not finding particles near the walls. The impact on the mixing length is more important for mixing ratios smaller than 1:1. Table 3.4 shows the estimated mixing length for all cases.

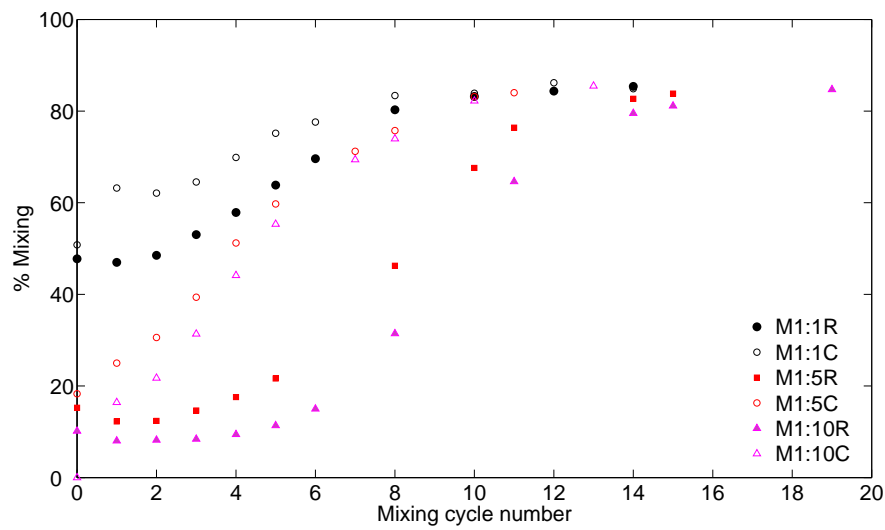


FIGURE 3.9: Percentage of mixing vs. the number of cycles for all cases, calculated with the nearest neighbour analysis method.

TABLE 3.4: Estimated mixing length as the necessary length to achieve 85% mixing via the nearest neighbour analysis technique.

Configura- tion	Mixing length for nearest neighbour analysis 85% mixing (m)
M1:1R	0.0181
M1:1C	0.0167
M1:5R	0.0258
M1:5C	0.0182
M1:10R	0.0288
M1:10C	0.0182

3.5.3 Striation Thickness

The evolution of the average striation thickness shows an exponential reduction for all cases (figure 3.10). The results show that case M1:1R, M1:1C, M1:5C, M1:10C, achieve practically the same average striation thickness after 5 cycles (between 10 and 12 μm). This is supported by the fact that they also have the same COV value (around 1.5). It is possible to calculate a mixing length with equations (3.8)-(3.13). The only parameter needed is the specific stretch a which can be estimated if the average striation thickness graphs are approximated to an exponential function. Then the parameter a is obtained by fitting the graph

to equation (3.8). Table 3.5 shows the values of the fitted parameter a and the corresponding mixing length for all cases. Just as in the COV analysis the striation thickness evolution for M1:5R shows two distinct behaviours one for the first three cycles characterised by a nearly constant decrease and another one for the rest of them that shows an exponential decrease, characteristic of chaotic flows. The parameter a was estimated according to the behaviour from the third cycle and the mixing length was calculated as the length necessary to achieve mixing as computed with equations (3.8)-(3.13) plus the length of the first three cycles. The mixing length for M1:10R is obtained in the same form as in M1:5R the only difference is that the exponential decrease is considered to start at the fourth cycle. The results obtained here agree with the ones presented by Aubin et al. [12]. They showed that for a groove depth $d_g = 0.35h$ and a mixing ratio of 1:1, an average striation thickness of $10 \mu m$ is obtained after 0.84cm. According to figure 3.10 and to equation (3.8) with $a = 0.44$ for a groove depth $d_g = 0.36h$ the length necessary to achieve a striation thickness of $10 \mu m$ is 0.8cm (around 5 cycles). The small differences may be explained by the fact that the groove depth considered in this work is bigger, therefore enhancing the striation thickness reduction. It should also be taken into account that the height of the channel in this work is $85 \mu m$ not $77 \mu m$ as in Aubin et al. [12].

TABLE 3.5: Estimated mixing lengths with the average striation thickness for all mixing configurations.

Con-figuration	Initial striation thickness (m)	Specific stretch (a)	Mixing time (s)	Mixing length (m)
M1:1R	1×10^{-4}	0.44	7.46	0.0149
M1:1C	7.5×10^{-5}	0.49	6.34	0.0126
M1:5R	8.4×10^{-5}	0.4	7.79	0.0155
M1:5C	7.5×10^{-5}	0.41	7.41	0.0148
M1:10R	8.8×10^{-5}	0.42	7.54	0.0150
M1:10C	8.4×10^{-5}	0.47	6.76	0.0135

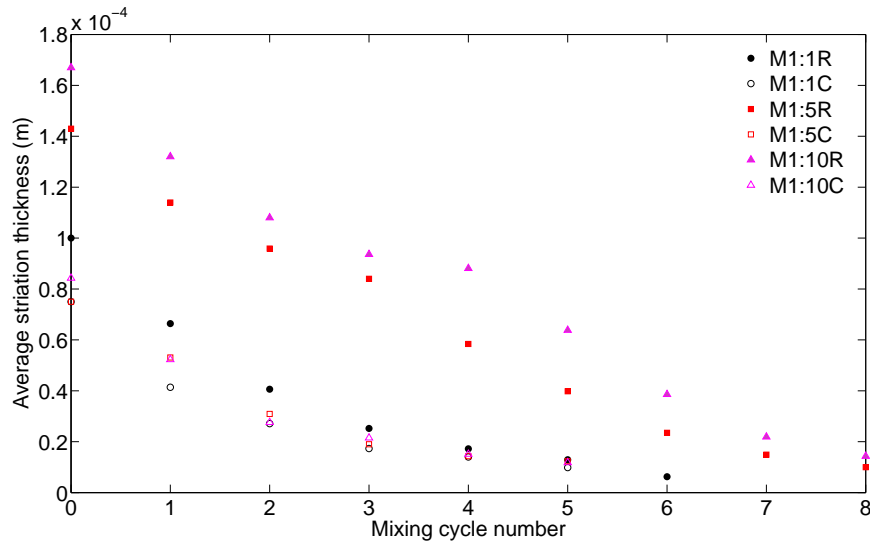


FIGURE 3.10: Evolution of the striation thickness over the mixer length for all cases.

3.5.4 Stretching Histories

The stretching histories for an array of 4100 particles placed uniformly in the whole crosssection at the inlet are computed according to section 3.4.1. The results after one cycle are shown in figure 3.11. The figure shows the locations of the particles and the diameter of the circles represent the relative value of the stretching. It can be seen that the regions with the highest stretching are near the peaks of the herringbones (at a channel width of 66 and 133 μm) and in the channel corners. Therefore, if particles are placed close to these regions they will converge quicker to a more uniformed distribution since the stretching (and intermaterial surface) will grow exponentially. If the particles are placed in the centre they will experience little amount of stretching as shown on figure 3.11 and supported by figures 3.5, 3.6b and 3.7b, where the particles that remain in the centre have barely moved since the original injection.

The advantage of placing the particles in the centre is that they will be transported by the grooves to the side walls of the channel, therefore they will be in the regions of highest stretching (good mixing). If a plot of $\ln(\lambda_m)$ vs. number of cycles is

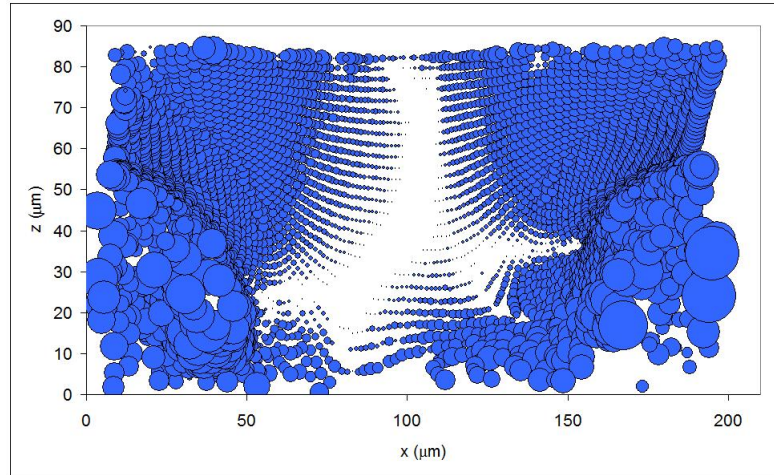


FIGURE 3.11: Particle positions and stretching values after 1 cycle, for a uniform array of 4100 particles.

made, the slope of the graph will be the specific stretch, a , according to equation (3.6) and the time and distance for complete mixing may be estimated by equations (3.12) and (3.13) respectively. Figure 3.12 shows this graph for all cases. If the specific stretch is obtained as the slope of the graphs then the mixing length would be 0.68 cm for M1:1R and 0.53 cm for M1:1C; this is a much lower value than the 1.3cm predicted by Stroock et al. [143] for $Pe = 2 \times 10^5$ (In this work $Pe = \infty$). If instead of using the geometric mean λ_m , which represents the value at which 50% of the particles have higher stretching values than the mean, a more conservative value is used, for example when 90% of the particles have higher stretching values than the mean (λ_{90}) [74], the mixing length would be 1.1cm for M1:1R which is closer to the 1.3cm predicted by Stroock et al. [143] and 0.70cm for M1:1C. It is important to note that for M1:5R and M1:10R only the points after the third and fourth cycle respectively were taken into account. Since there are two different behaviours as explained in sections 3.5.2.1 and 3.5.3 and according to equation (3.6) the specific stretch is calculated at long values of t , we have to disregard the first values that are not representative of the behaviour of the system and as in section 3.5.3 the total mixing length is calculated with equations (3.12) and (3.13) plus the length of the cycles disregarded.

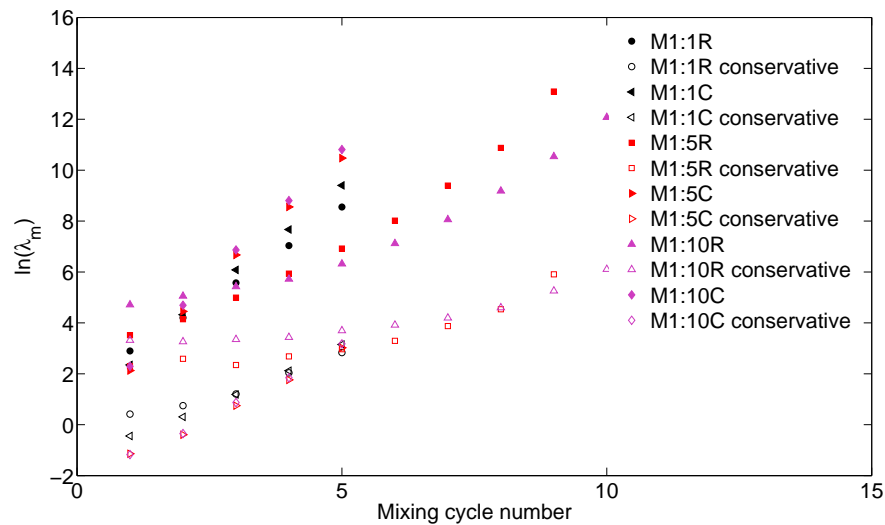


FIGURE 3.12: Graph with the geometric mean λ_m and λ_{90} (conservative) vs. the number of cycle.

Figure 3.13 shows a comparison of the mixing lengths obtained by the three different methods presented in this investigation. For the nearest neighbour analysis method, complete mixing is assumed at 85%; since diffusion is not considered, it is hard to find particles in the corners of the channel, and this is the reason why for all cases it is difficult to obtain a value above 85% of mixing, as shown in figure 3.9. The striation thickness and the nearest neighbour analysis methods agree well, within 13%. On the other hand, although the stretching histories show a lower mixing length for cases M1:1C, M1:5C and M1:10C compared to the corresponding cases with particles on the sides, the mixing length values can be as low as 50% of those predicted by the other two methods. It is hard to say which of the methods provide the most accurate prediction as they all have some drawbacks. The stretching histories method considers a geometric mean stretch at the end of each cycle, while in reality there is a log normal distribution [74]. On the other hand, the nearest neighbour analysis is not considering diffusion which will accelerate the degree of mixing and finally the striation thickness method is dependent of the capacity of identifying the striation patterns (which becomes more difficult after a few cycles). Therefore for design purposes it is recommended to use the

biggest of the three values.

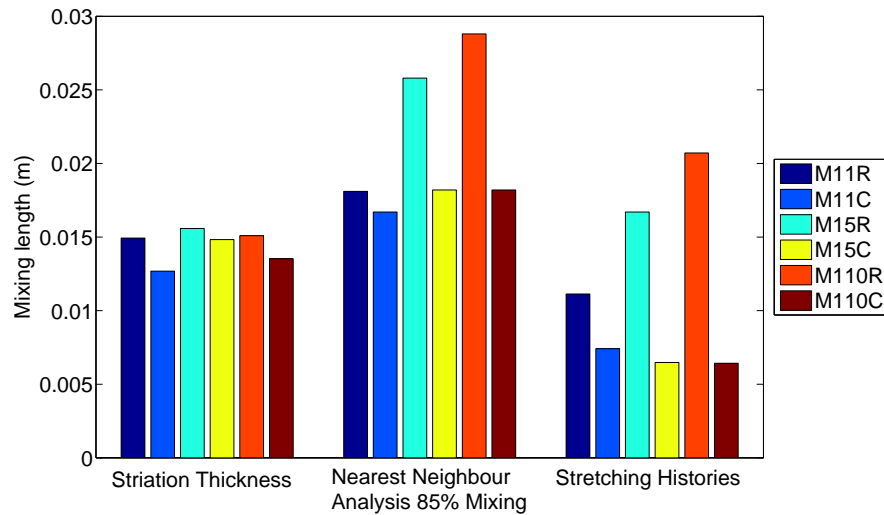


FIGURE 3.13: Comparison of mixing lengths for the striation thickness, nearest neighbour analysis and stretching methods for all configurations

3.5.5 Scaling-up vs. Scaling-out

The usual trend in microprocess technology is to achieve commercial production by increasing the number of parallel channels in the process (numbering up or scaling out) so that the benefits of working in the microscale (intensified mass transfer, large surface/volume ratio) are retained. However it is possible to scale up the staggered herringbone micromixer without a significant loss of its advantages. Say for example that all the dimensions of the channel are multiplied by a scaling factor of 10. If the pressure drop and all the fluid properties are kept constant then the average velocity in the channel will increase ten times according to the following:

$$U_{avg} \propto \frac{\Delta P \cdot h^2}{\mu L} \quad (3.22)$$

Therefore the residence time in each cycle is kept constant. The distribution of particles for this system after 5 cycles (not shown) is exactly the same as for the standard $200\ \mu\text{m}$ channel shown in figure 3.3 and therefore the striation thickness behaviour and the specific stretch a are the same as in figure 3.10 and table 3.5 respectively but with striations 10 times bigger. According to equation (3.12) if the specific stretch a and the diffusion coefficient D are kept constant then the mixing time is proportional to the natural logarithm of the initial striation thickness (which is a function of the geometry of the mixer). Figure 3.14 compares the mixing time for the M1:1R case with a standard T-mixer (where mixing is achieved only by diffusion), as a function of the scaling up factor. From figure 3.14, it can be seen that the mixing time for M1:1R grows linearly in a semi-log plot, while for the T-mixer grows to the square of the scaling factor. This result indicates that the dimensions of the staggered herringbone channel can be increased without a huge impact on mixing time. This has significant implications for pressure drops and throughput considerations.

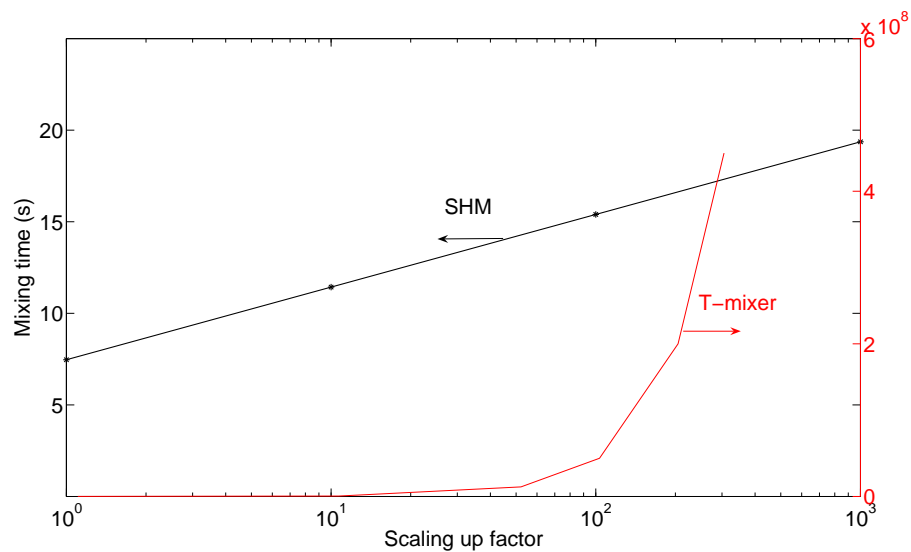


FIGURE 3.14: Plot of the mixing time for the M1:1R configuration in a staggered herringbone micromixer and a T-mixer as a function of the scaling up factor. $Pe = 10^5$.

3.6 Conclusions

The performance of the SHM under flow ratios of 1:1, 1:5 and 1:10 and two injection locations: on the centre and on the side of the channel, was investigated using numerical simulations and particle tracking. Mixing was characterised by three different methods: nearest neighbour analysis, striation thickness reduction and stretching histories. The results show that for all the flow ratios investigated, mixing is greatly enhanced by placing one of the fluids in the centre of the channel. The transverse movement of fluid is responsible for the improved mixing when the particles are placed in the centre. The grooves allow the transportation of material from the centre to the channel's walls. This is also supported by the calculation of the stretching histories, which show that the regions with the highest stretching (good mixing) are located on the sides of the channel. Therefore when the particles are placed in the centre, lower mixing lengths are obtained by all of the methods. The average striation thickness was found to decrease exponentially as a function of axial position as predicted for chaotic flows. When the particles were on the side of the channel and for mixing ratios higher than 1:1, it was found that the rate at which the striation thickness was decreasing was not constant. There is one rate that characterises the behaviour for the first few cycles, when the particles are still confined to the side of the channel where they were injected and another one for the behaviour thereafter, when the particles are all over the cross section. All three methods agree relatively well on the ranking of each case with respect to mixing length. They show that for all cases studied the ones that give the longest mixing length are the cases with the particles on the right of the channel. The mixing lengths obtained by the average striation thickness method agree well with the mixing length to achieve 85% mixing obtained from the nearest neighbour analysis. However, the results obtained from the stretching histories method are in general lower than with the other two methods. The highest mixing length should be selected for design purposes. Finally a scaling up study showed that the

mixing length increases with the logarithm of the scaling factor, so that a mixer scaled up by a factor of 1000 will increase its mixing time by less than 3 times.

Chapter 4

Residence Time Distributions in Microchannels: Comparison between Channels with Herringbone Structures and a Rectangular Channel

4.1 Introduction

In this chapter, the RTD for a rectangular channel is compared with that of channels with floor herringbone structures (structures on the bottom wall, see figure 4.1). Residence time distributions are obtained experimentally by means of a LED-photodiode array system and numerically by CFD simulations with particle tracking. The effect of geometrical parameters, herringbone symmetry and operational parameters on the RTD is investigated.

4.2 Theoretical Approach

Two different theoretical approaches were employed for the calculation of the RTD. The first one is completely numerical, relying on the solution of the Navier-Stokes equations and a particle tracking algorithm. The second one is based on a hydrodynamic model with adjustable parameters which are fitted using experimental or particle tracking data.

4.2.1 Numerical Particle Tracking Method

The channel with the staggered herringbone structure (fig 4.1A) is similar to the one proposed by Stroock et al. [143]. The channel is divided in cycles, each one consisting of twelve asymmetric grooves. The position of the asymmetry changes every half cycle. In figure 4.1B a schematic of a symmetric herringbone structure is presented. The grooves in both structures are placed at an angle $\theta = 45$ with respect to the channel width. The groove depth is 0.17mm, the groove width is 0.7mm and the ridge width is 0.3mm (measured along the axial direction). In addition to the herringbone floor channels, an unstructured rectangular channel is also considered. The widths of the channels are 2mm for all cases and their heights are 0.85, 0.81 and 0.71mm for the rectangular, symmetric and staggered herringbone channels respectively. All the above dimensions correspond to experimentally determined values of microchannels used in the experiments and are summarised in table 4.1. Due to the repeating cycles, the velocity field is assumed to be periodic and hence the velocity field in one cycle can be obtained and used repeatedly for successive cycles. The fluid properties of water were used for all simulations with density =1000kg/m³ and viscosity =0.001Pa.s.

The residence time distribution $E(t)$ can be calculated by solving the velocity field for the particular geometry and tracking the positions of massless particles

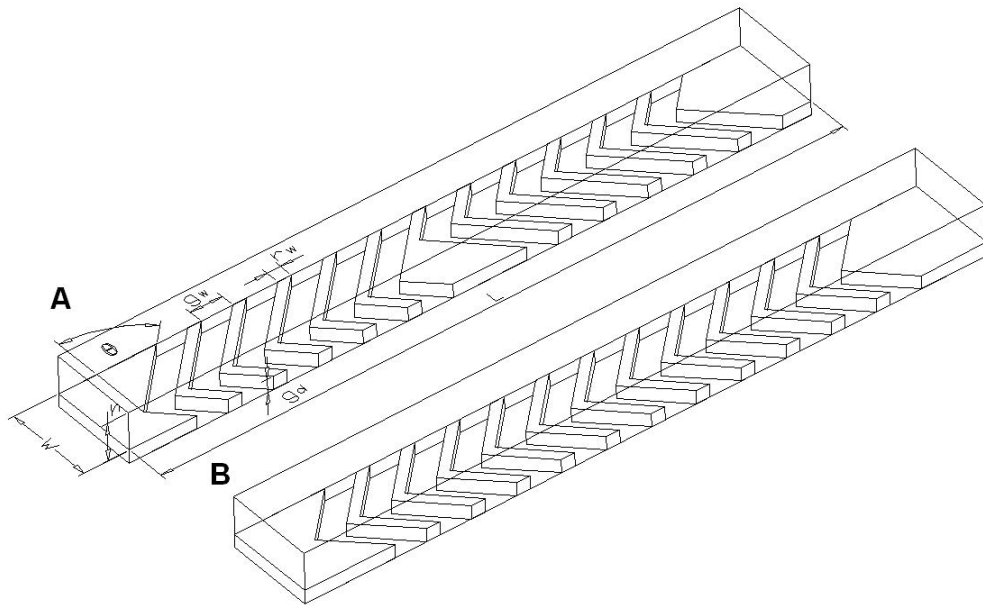


FIGURE 4.1: A) Geometry of the staggered herringbone channel. B) Geometry of the symmetric herringbone channel. Fluid travels from left to right.

convected by the flow. It has been shown by Levenspiel and Turner [91] that to obtain the correct RTD when the velocity profile at the injection and measurement point is not flat (for example in laminar flow) the number of particles introduced must be proportional to the velocity at each radial injection position and the measurement must be the mixing cup reading. For this reason 4400 particles are distributed proportionally to the axial velocity at the channel inlet. The procedure to compute the particle trajectories is described in chapter 3 sections 3.3.1 and 3.3.2. 34582 of tetrahedral mesh elements in the model were used and the simulations were run on Windows XP with Pentium IV 3.00 GHz CPU and 2GB of RAM.

Due to the stochastic nature of the particle tracking calculations an average of three runs is considered for all simulations yielding an error on the calculated mean residence time of $\pm 1.2\%$. Once the number of particles arriving at the channel exit, N_i , as a function of time interval, $\Delta t_i = t_{i+1} - t_i$, is obtained the RTD can be calculated from:

$$E(t_i) = \frac{N_i}{\sum_{i=1}^n N_i \Delta t} \quad (4.1)$$

where n is the total number of time intervals. The RTD in dimensionless form is obtained from:

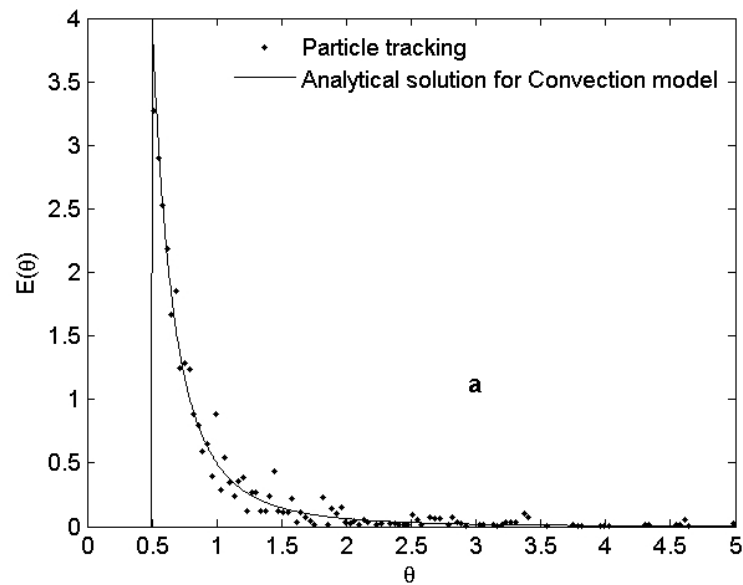
$$E(\theta_i) = t_m E(t_i) \quad (4.2)$$

where t_m is the mean residence time.

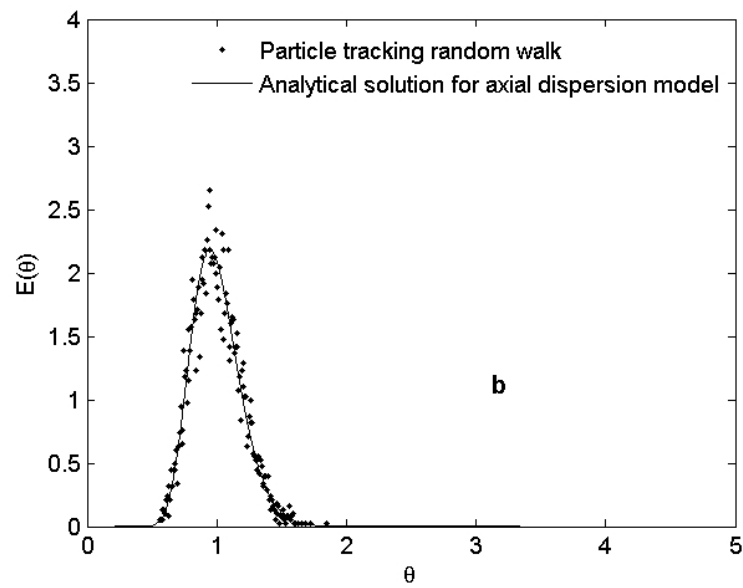
Figure 4.2 shows a comparison of both particle tracking methods (i.e. with or without random walk diffusion) with available analytical solutions for a $100\mu\text{m}$ diameter cylindrical channel with no diffusion (convective regime) [88] and with a diffusion constant of $D = 10^{-9}\text{m}^2/\text{s}$ for a $Pe=150$ ($Pe = \frac{ud}{D}$) [90]. Measurements are made at a dimensionless length of $L/d = 45$. The agreement of both methods with the analytical solutions is satisfactory. Particle tracking with random walk diffusion is used for all subsequent calculations, because it can incorporate the effect of mass transfer by diffusion in the RTD, while the standard particle tracking method is only valid in the limit of no diffusion or $Pe \rightarrow \infty$.

4.2.2 Analytical Method

Analytical expressions for the RTD for ideal reactors (CSTR, convective model, plug flow) are available in the literature. A comprehensive review of the flow system models for chemical reactors is given by Wen and Fan [160]. The axial dispersion model is commonly used to describe the behaviour in tubular reactors



(a)



(b)

FIGURE 4.2: Dimensionless RTD of particle tracking methods and analytical solutions for a cylindrical channel. a) Convection model vs. particle tracking simulation. b) Dispersion model vs. particle tracking with random walk simulation, $Pe = 150$.

TABLE 4.1: Dimensions of microchannel geometries and fluid properties

	Rectangular Channel	Staggered Herringbone Channel	Symmetrical herringbone channel
Channel width (w)	2 mm	2 mm	2 mm
Channel height(h)	0.84mm(±)2%	0.81mm(±)7%	0.71mm(±)7%
Length per cycle (L)	1.516 mm	1.516 mm	1.516 mm
Number of grooves per cycle	-	12	12
Groove width, g_w	-	0.7mm(±)2%	0.7mm(±)2%
Ridge width, r_w	-	0.3mm(±)2%	0.3mm(±)2%
Groove depth g_d	-	0.17mm(±)25%	0.17mm(±)16%
Groove Asymmetry	-	2/3	2/3
Groove Angle, θ	-	45°	45°
Fluid Properties			
Density	1000kg/m ³		
Viscosity	0.001Pa · s		

that deviate from plug flow and is characterised by a dispersion mechanism acting in the axial direction. The governing equation of this model is:

$$\frac{\partial C}{\partial t} = D_{ax} \frac{\partial^2 C}{\partial y^2} - U_m \frac{\partial C}{\partial y} \quad (4.3)$$

where C is the average concentration of the tracer, U_m is the mean axial velocity, y is the direction of the flow and t is time. Taylor [148] and Aris [10] provided analytical expressions for the determination of the axial dispersion coefficient in long cylindrical tubes. Ananthakrishnan et al. [5] and Levenspiel [88] provide useful charts for the limits of application of each expression. The axial dispersion model is not suitable for RTDs exhibiting long tails. In this case the axial dispersion model exchanging mass with a stagnant volume (ADEM) is more appropriate [28, 29, 86, 152]. It is expressed by the following system of differential equations:

$$D_{ax} \frac{\partial^2 C}{\partial y^2} - U_m \frac{\partial C}{\partial y} = f \frac{\partial C}{\partial t} + (1 - f) \frac{\partial C^*}{\partial t} \quad (4.4)$$

$$(1 - f) \frac{\partial C^*}{\partial t} = K (C - C^*) \quad (4.5)$$

where f is the fraction of the volume subject to plug flow with axial dispersion, C^* is the concentration in the stagnant zone and K is the mass transfer coefficient between the flowing volume and the stagnant zone. Estimating the model parameters by fitting the measured response signal $C_{out}(t)$ with the one calculated in the time domain $C_{calc}(t)$ is shown to give the most accurate results [43, 108]. Applying the Laplace transform to equations (4.4) and (4.5), the transfer function subject to open-open boundary conditions is [28]:

$$F(s) = \frac{2\beta^{\frac{1}{2}} \exp\left[\frac{1}{2}\left(Pe_L - \beta^{\frac{1}{2}}\right)\right]}{\left(Pe_L - \beta^{\frac{1}{2}}\right) - \left(Pe_L + \beta^{\frac{1}{2}}\right) \exp\left(-\beta^{\frac{1}{2}}\right)} \quad (4.6)$$

where:

$$\beta = Pe_L^2 + 4s\phi Pe_L t_m \quad (4.7)$$

$$\phi = f + \frac{G(1-f)}{t_m s(1-f) + G} \quad (4.8)$$

$$G = \frac{KL}{U_m} \quad (4.9)$$

$$Pe_L = \frac{U_m L}{D_{ax}} \quad (4.10)$$

where L is the length of the channel. By using the definition of the transfer function in the Fourier domain, which corresponds to the residence time distribution, $E(t)$,

in the time domain, the calculated output signal in the time domain is obtained from an inverse Fourier transform:

$$C_{calc}(t) = \mathcal{F}^{-1}[\mathcal{F}(E(t)) \cdot \mathcal{F}(C_{in}(t))] \quad (4.11)$$

The continuous Fourier transform and its inverse are approximated to a discrete Fourier transform by a fast Fourier transform using the Cooley-Tukey algorithm in Matlab. The model has three parameters: f , G and Pe_L which are obtained by minimising the root mean square error (RMSE) shown in equation (4.12).

$$RMSE = \left[\frac{\int_0^{2T} (C_{out} - C_{calc})^2 dt}{\int_0^{2T} (C_{out})^2 dt} \right]^{\frac{1}{2}} \quad (4.12)$$

where $2T$ is the time at which the tail of the distribution vanishes. The criterion for convergence is when the root mean square error (RMSE) is less than 0.1 [155]. The optimisation was done in Matlab using the *fminunc* function which uses the BFGS method.

4.3 Experimental Details

4.3.1 Set-up Description

The channels were fabricated on a plate of PMMA (Polymethylmethacrylate) (RS-components), 8cm x 8cm x 3mm by engraving (Roland EGX-400). The engraved PMMA plates were cleaned in an ultrasonic bath for 20 min using Decon 90 and dried with an air gun. To produce closed channels the plates were clamped, along with a top PMMA plate with feed-through holes, in a stainless steel jig and placed in an oven (Lenton WF30) for 10 min at 110 C (close to the PMMA softening

temperature) for bonding. The chips were allowed to cool slowly overnight and were ready to use the next day. The dimensions of the channels were measured with a profilometer (Veeco, Dektak 8) and are given in table 4.1.

A HPLC pump (Waters 510) was used for feeding deionized water to the chip (flowrates 0.5 and 1 ml/min). The tracer pulse (Parker Blue dye) was introduced by a 6-port sample injection valve (Rheodyne 7725(i)) equipped with 5 μ l sample loop and an internal position signal switch that indicates the time of injection. The piping among all components was Teflon 0.254mm ID. The hydraulic residence time in the tubing connecting the valve to the inlet of the chip was 1.5 and 7.6 s for flowrates of 0.5 and 0.1 ml/min respectively.

Tracer detection was performed by light absorption. Illumination was provided by two square LEDs (Kingbright L-1553IDT). To make sure that only light going through the desired channel area was collected, black tape was used to mask the neighbouring areas. To seal the system from ambient light it was placed in a dark box. The detection system was based on a linear diode array detector (TSL, 1401R-LF) which had 128 diodes each of dimensions 63.5 microns by 55.5 microns. This was driven using the manufacturer's recommended circuit. A scan of all diodes would take 1.28 ms and the interval between successive scans was 5.12 ms. Data from the sensor were collected using a National instruments PCI-6010 data acquisition card before being analysed and displayed on a computer using a program written in Labview. Every 100 ms the computer would average the previous two scans, calculate the absorbance for each diode and display the result. The absorbance of the tracer dye was found to be in accordance with the Beer-Lambert law. A digital signal from the injection valve was also acquired to allow the absorbance data time to be referenced to the time of injection.

In order to obtain the true RTD of the system, the mixing cup concentration must

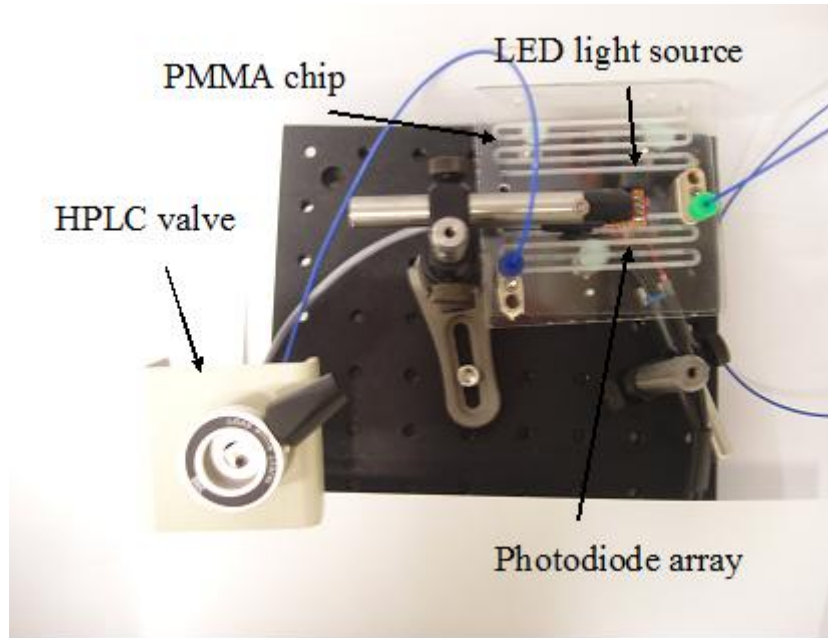


FIGURE 4.3: Picture of the experimental set up used for RTD studies.

be measured (flux-averaged concentration). However, through the wall measurements are usually the norm in experimental set-ups such as in this work. Levenspiel et al. [89] and Levenspiel and Turner [91] have shown that, when there is a spread in longitudinal velocity (such as in laminar flow), through the wall measurements will lead to distributions skewed towards the slower moving molecules. A correction for through the wall measurements was suggested [89] that is valid when interaction between streamlines is negligible. A picture of the experimental set up is shown in figure 4.3.

The diffusion coefficient of the dye in water was obtained experimentally in a rectangular channel 21cm x 2mm x 0.85mm, by first calculating the vessel dispersion number ($\frac{D_{ax}}{U_m L}$) by the following equation [90]:

$$\frac{D_{ax}}{U_m L} = \frac{1}{8} \left(\sqrt{8\sigma^2 + 1} - 1 \right) \quad (4.13)$$

where σ is the variance of the distribution obtained experimentally and L is the

length of the region of study. The relationship between diffusivity and axial dispersion coefficient for a rectangular channel with arbitrary aspect ratio is [39]

$$D_{ax} = D + \frac{h^2 U_m^2}{210D} g \quad (4.14)$$

where g is a number depending on the aspect ratio of the channel and is approximately 3.8 for the conditions presented here .

4.3.2 Data Analysis

The mean residence time can be calculated from the intensity data according to:

$$t_m = \frac{\sum_{i=1}^n t_i I(t_i) \Delta t_i}{\sum_{i=1}^n I(t_i) \Delta t_i} \quad (4.15)$$

where $I(t_i)$ is the intensity of light measured by the detector at each recorded time, Δt_i is defined as $t_{i+1} - t_i$ and is constant throughout the experiment. The variance may be calculated as follows:

$$\sigma^2 = \frac{\sum_{i=1}^n (t_i - t_m)^2 I(t_i) \Delta t}{\sum_{i=1}^n I(t_i) \Delta t} \quad (4.16)$$

which in dimensionless form is:

$$\sigma_\theta^2 = \frac{\sigma^2}{t_m^2} \quad (4.17)$$

The intensity measured at both the outlet and inlet is normalised to yield a normalised concentration:

$$\widehat{C}(t_i) = \frac{I(t_i)}{\sum_{i=1}^n I(t_i) \Delta t} \quad (4.18)$$

The input signal to the region of interest is not a perfect Dirac-delta impulse since the injected plug is dispersed by the capillary tube from the injection point to the inlet of the channel. The output concentration is then related to the input concentration and the RTD by the convolution integral [116].

$$C_{out}(t) = \int_0^t C_{in}(t-t') E(t') dt' \quad (4.19)$$

The convolution integral corresponds to multiplication in the frequency domain, therefore:

$$\mathcal{F}(C_{out})(t) = \mathcal{F}(E(t)) \cdot \mathcal{F}(C_{in}(t)) \quad (4.20)$$

The RTD is obtained by taking the inverse Fourier transform of equation (4.20).

$$E_{tw} = \mathcal{F}^{-1} \left(\frac{\mathcal{F}(C_{out}(t))}{\mathcal{F}(C_{in}(t))} \right) \quad (4.21)$$

where $E_{tw}(t)$ is the age distribution curve of the region of interest obtained from experimental data measured through the wall. The Fourier transform and its inverse were approximated by a fast Fourier transform as described earlier. Deconvolution is very sensitive to noise, therefore signal filters and curve smoothing were used [109]. The parameters of the filter and the curve smoothing were chosen so that the convolution of C_{in} with $E_{tw}(t)$ resulted in C_{out} . In addition it was checked that neither the mean residence time nor the variance changed as a result

of this procedure as suggested by Mills and Dudukovic [109]. The number of experimental points taken for C_{out} and C_{in} were always more than 2000 ($t=0.1s$) to avoid aliasing. In dimensionless form, the time and the RTD are:

$$\theta_i = \frac{t_i}{t_m} \quad (4.22)$$

$$E_{tw}(\theta_i) = t_m E_{tw}(t_i) \quad (4.23)$$

Since the RTD obtained was measured through the wall and transverse concentration profiles due to laminar flow are expected, a correction must be made in order to obtain the correct RTD. According to Levenspiel et al. [89] if both the inlet and outlet are measured through the wall the correct RTD may be obtained from:

$$E(\theta_i) = \frac{E_{tw}(\theta_i)}{\theta_i^2} \quad (4.24)$$

The results without this correction yield measurements which are skewed towards the right, resulting to higher average residence time and variance.

4.4 Results and Discussion

4.4.1 RTD from Particle Tracking and Hydrodynamic Model

Figure 4.4 shows the $E(t)$ curve obtained with the particle tracking method with random walk diffusion described in section 4.2.1 for a channel with staggered herringbone structures (see table 4.1 for dimensions) for $Re = 0.013$ and $Pe = 10^4$ at a distance of 7, 22 and 36cm (5th, 15th and 25th cycle) from channel entrance. It

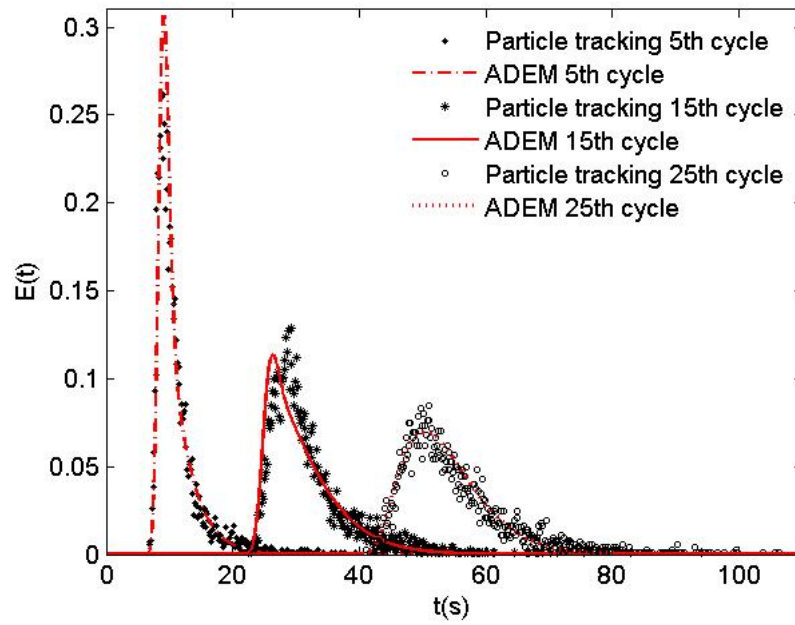


FIGURE 4.4: Comparison of the RTD for the staggered herringbone channel obtained from the particle tracking method with random walk diffusion and the model of axial dispersion exchanging mass with a stagnant zone (ADEM) for cycles 5th, 15th and 25th (7.6, 22 and 38cm). The parameters of the model were calculated using particle tracking results for the 15th cycle. Channel dimensions are shown in table 4.1, $Pe \approx 10^4$ $Re \approx 10^1$.

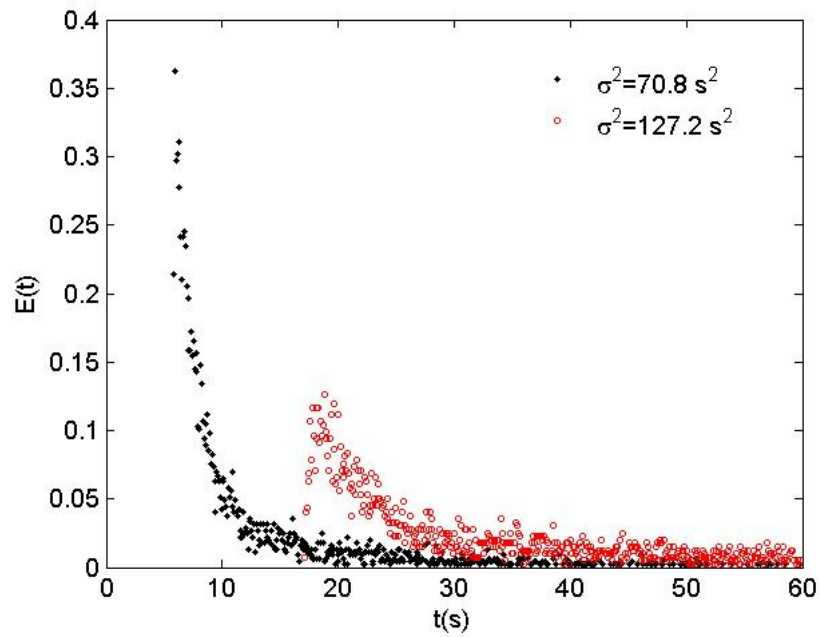
can be seen that the particles experience a high peak followed by a long tail which is due to particles trapped in the grooves that take longer time to get out of the system. Tracking the particles for a long time might be computational expensive. For this reason, a suitable hydrodynamic model would help predict the RTD for longer times. Hence, the RTD at the 15th cycle is fitted to the ADEM model as described in section 4.2.2 The values of the model parameters were calculated to be: $Pe_L = 597.7$, $G = 1.58$ and $f = 0.85$ with a mean residence time $t_m = 31.76s$ calculated with equation (4.15) replacing $I(t_i)$ with N_i .

It is worth noting that the hydraulic residence time $t'_m = V/v_o$ is 37.2s. This gives a ratio of t_m/t'_m of 0.85 which is consistent with the work of Aubin et al. [12] who found that for wide grooves ($75\mu m$) the ratio of the calculated residence time from particle tracking to the hydraulic residence time was 0.85. Furthermore, the volume fraction of the stagnant zone in the ADEM model $(1 - f) = 0.15$ is close

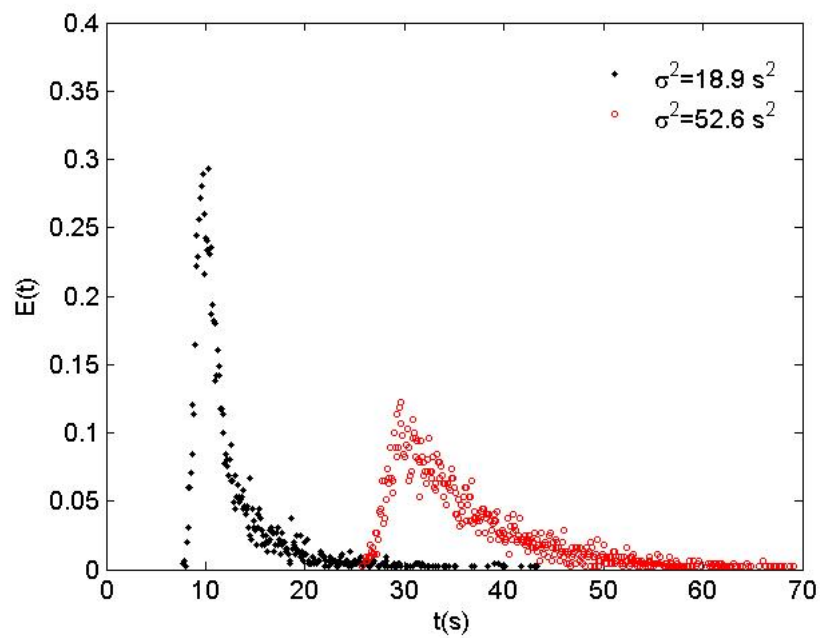
to the volume fraction of the channel occupied by the grooves which is 0.13. From these Pe_L and G the original model parameters (see equations (4.4) and (4.5)) are found to be: $D_{ax} = 2.29 \times 10^{-8} m^2/s$, $K = 0.052 s^{-1}$. Using these parameters, the RTD at different lengths (5th and 25th cycle) are calculated and are shown in figure 4.4. The agreement of the RTD prediction by the model at the 5th and 25th cycle is satisfactory.

In figure 4.5, RTDs obtained via particle tracking for a rectangular channel and a microchannel with staggered herringbone structures for $Pe \approx 10^4$ are shown. The microchannels are $200 \mu m$ wide and $85 \mu m$ deep for both the rectangular and the herringbone microchannel; the grooves are $50 \mu m$ wide and $31 \mu m$ deep. These dimensions are similar to those of Stroock et al. [143]. The dispersion experienced by the rectangular microchannel is higher than in the patterned microchannel as shown by the calculated variances. Note that variances are calculated by equation (4.16), where $I(t_i)$ is replaced by N_i . For the rectangular microchannel the calculated variances were 70.8 and $127.2 s^2$, for 2 and 6.2cm long microchannels respectively, while for the microchannel with staggered herringbones were 18.9 and $52.6 s^2$. The RTD for the rectangular microchannel is characterised by an early peak after 6 and 18 seconds at 2cm and 6.2 cm microchannel length respectively, followed by a long tail (typical of a pure convection model with no diffusion). The hydraulic residence time for these two positions is 11.27 and 33.0s respectively. On the other hand, for the microchannel with staggered herringbones, the peaks are located at 10 and 30s for the same microchannel positions (2 and 6.2 cm). The hydraulic residence time for these two positions is 12.2 and 35.5s respectively. These results show that the microchannel with staggered herringbones is able to reduce dispersion; the time where the peaks are obtained are closer to the hydraulic residence time. The results are in qualitative agreement with the experimental observations of Stroock et al. [143].

If we would like to have a similar RTD in the rectangular microchannel as in the



(a)



(b)

FIGURE 4.5: a) Residence time distribution in the rectangular channel from particle tracking with random walk diffusion. at 2cm and 6.2 cm. b) Residence time distribution in the staggered herringbone channel from particle tracking with random walk diffusion at 2cm and 6.2 cm. The dimensions of the channel are $w = 200 \mu\text{m}$, $h = 85 \mu\text{m}$. $Pe \approx 10^4$ $Re \approx 10^1$.

staggered herringbone one, we would have to decrease the size of the unstructured channel. One way of estimating the dimensions of a rectangular microchannel that behaves similar to a microchannel with herringbone structures would be to obtain an axial dispersion coefficient from the variance of the staggered herringbone microchannel distribution as shown in equation (4.13). Then, if the diffusion coefficient is known, the characteristic dimensions of a rectangular microchannel can be obtained for any aspect ratio with equation (4.14). This analysis showed that, keeping the aspect ratio constant $\frac{h}{w} = 0.425$, the dimensions of a rectangular microchannel, which has a similar variance as a 2mm wide staggered herringbone microchannel, would be 450 μm . One would expect that this procedure is not accurate enough since the RTD of the staggered herringbone microchannel cannot be correctly characterised by a simple axial dispersion model. However, we found that although the shape of the RTDs for the staggered herringbone and the rectangular microchannel was different, the conversion for first order chemical reaction was the same. Since the conversion for a first order chemical reaction is uniquely determined by the reaction constant and the RTD in the reactor, it provides a basis for comparing different RTDs. The mean conversion for a first order chemical reaction of the type $A \xrightarrow{k} B$ is given by:

$$\bar{x} = 1 - \int_0^{\infty} e^{-kt} E(t) dt \quad (4.25)$$

Table 4.2 shows the conversions and pressure drop for a rectangular microchannel with and without herringbone structures for a reaction constant $k = 0.1s^{-1}$. The results show that a rectangular channel with 2mm width has a conversion of 64.8% and a ΔP of 6700 Pa after 22 cm for $Pe = 10^4$ while the staggered herringbone channel achieved 68.8% with a ΔP of 6300 Pa for the same conditions. If the width of the rectangular microchannel is decreased to 450 μm , a conversion of 68.6% is achieved but with a pressure drop of $\Delta P = 29500$ Pa. For comparison,

a Kenics mixer with a diameter of 1.2mm (the hydraulic diameter of the rectangular channels considered was 1.2mm) and the same conditions considered for the rectangular channels would give a pressure drop of $\Delta P = 36343$ Pa [142].

TABLE 4.2: Reactant conversion for a first order reaction and pressure drop in a staggered herringbone and a rectangular channel.

	Conversion	$Pe = \frac{U_m d}{D}$	ΔP (Pa)
Plug flow	70.8 %	40000	-
Staggered herringbone channel 2mm wide	68.8 %	40000	6300
Rectangular channel 2mm wide	64.8 %	40000	6700
Rectangular channel 450 μm wide	68.6 %	9000	29500

4.4.1.1 Effect of Pe

Although the herringbone structures prove to be an efficient way to narrow the RTD at high Peclet numbers, for smaller Peclet numbers where mass transfer by diffusion plays a more important role, channels with and without herringbones have a similar RTD as shown in figure 4.6 for $Pe = 10^2$ (Pe was changed by changing the diffusion constant). In this case, radial mass transfer by diffusion is substantial and there is no need to have the herringbone structures to narrow the RTD. Furthermore, for the staggered herringbone channel, as the Peclet number increases the RTD remains unchanged as shown in figure 4.7. This result has been pointed out recently by Vikhansky [154] who showed that for a chaotic flow the RTD is practically independent of Pe . Such behaviour opens the possibility of increasing the velocity or the hydraulic diameter of the channels (increase Pe) without compromising its performance in terms of residence time distribution.

4.4.1.2 Influence of Geometrical Parameters of Grooves

A sensitivity analysis of the influence of the groove's geometrical parameters on the residence time distribution was carried out at a fixed length of 2.3 cm and

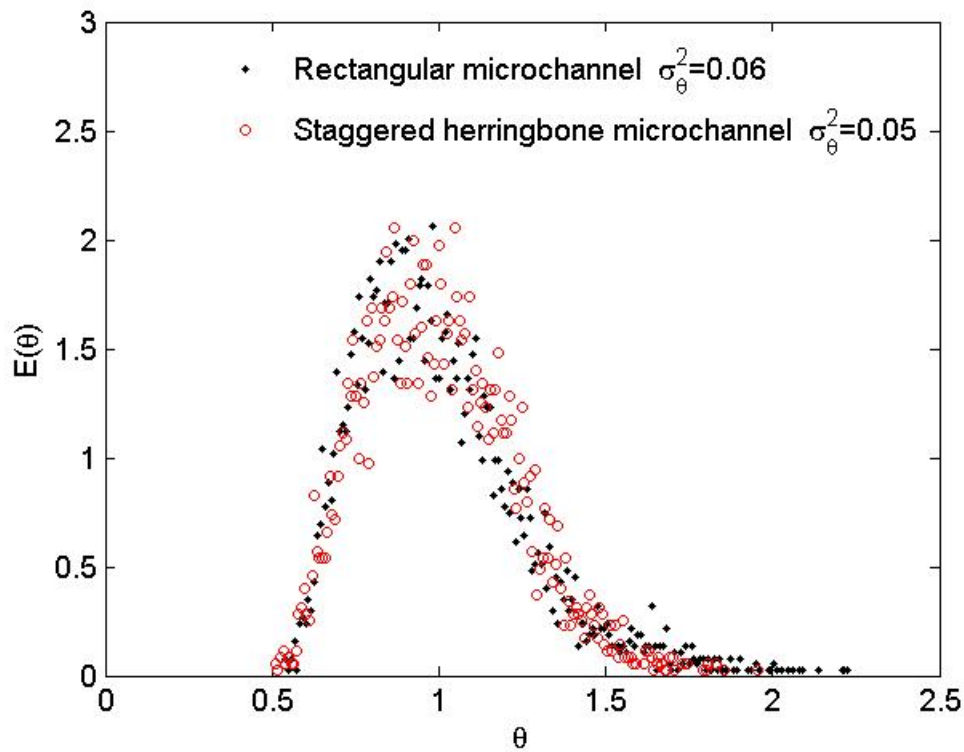


FIGURE 4.6: Dimensionless RTD for a rectangular microchannel and the staggered herringbone microchannel from a particle tracking method with random walk diffusion. The dimensions of the channel are $w = 200 \mu m$, $h = 85 \mu m$ for both channels and the groove parameters are: $g_w = 50 \mu m$, $g_d = 31 \mu m$, $r_w = 50 \mu m$. $Pe = 10^2$ $Re \approx 10^1$

the same fluid flowrate ($Pe \approx 10^4$, $Re \approx 10^1$). The dimensionless variances for all cases were estimated from an average of three simulations (with an error of less than 8%) and compared to the reference case with 45° groove angle, $31 \mu m$ depth and $50 \mu m$ width at a length of 2.3cm (15 cycles) and are shown in table 4.3.

TABLE 4.3: Influence of groove's geometrical parameters on the variance of the RTD.

	$\sigma_\theta^2 = 0.0654$	$\sigma_\theta^2 = 0.0206$	$\sigma_\theta^2 = 0.0194$
Influence of groove angle	$\theta = 30^\circ$	$\theta = 45^\circ$	$\theta = 60^\circ$
Influence of groove depth	$\sigma_\theta^2 = 0.0852$	$\sigma_\theta^2 = 0.0206$	$\sigma_\theta^2 = 0.0194$
	$g_d = 15 \mu m$	$g_d = 31 \mu m$	$g_d = 60 \mu m$
Influence of groove width	$\sigma_\theta^2 = 0.1113$	$\sigma_\theta^2 = 0.0206$	$\sigma_\theta^2 = 0.0517$
	$g_w = 30 \mu m$	$g_w = 50 \mu m$	$g_w = 70 \mu m$

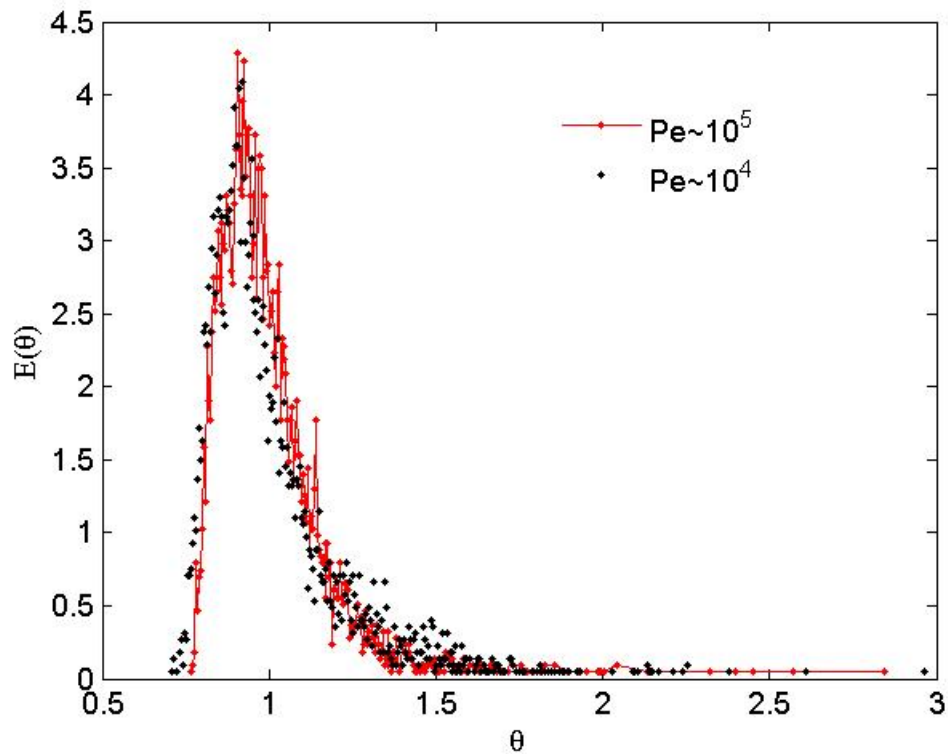


FIGURE 4.7: Residence time distribution from particle tracking with random walk for a channel with staggered herringbone structures for $Pe = 10^4$ and $Pe = 10^5$. Channel dimensions $w=2\text{mm}$, $h=0.71\text{mm}$, groove width is 0.7mm width and 0.18mm depth. $Re \approx 10^1$ for both cases.

At an angle of 30° and 60° the variances of the RTD are 0.0654 and 0.0194 respectively, compared to 0.0206 of the reference case. It seems that there is an optimum groove angle to maximise transverse fluid movement. In fact, for mixing which also is influenced by the transverse movement of fluids, and groove angle of 53° has been found to be optimal [6]. The analysis on the groove depth shows that the RTD exhibits a higher variance at low depth ($15 \mu\text{m}$) ($\sigma^2 = 0.0852$) compared to the reference case ($\sigma^2 = 0.0206$); at higher depths the variance remains nearly constant $\sigma^2 = 0.0199$ and $\sigma^2 = 0.0194$ for 43 and 60 microns depths respectively. This indicates that increasing the groove depth narrows the RTD, however there is a critical groove depth beyond which the RTD is no longer improved. The results by Aubin et al. [12] also show that increasing the groove depth does not affect the RTD significantly. The groove width has a significant impact on the RTD.

Both for wider and narrower grooves the distribution is worsened with respect to the reference case. Narrow grooves ($15 \mu\text{m}$ wide) give the highest variance for all cases studied ($\sigma^2 = 0.1113$) because they are unable to stir the fluid and force it to sample the whole cross-section. On the other hand, wide grooves stir the fluid efficiently as has been shown by Aubin et al. [12] and Lynn and Dandy [103]. However, although mixing is improved as the groove width is increased, the RTD is worse ($\sigma^2 = 0.0517$) with respect to the reference case, because of the increased volume of the grooves which could potentially increase dispersion by allowing a greater percentage of fluid to remain in the system for longer times. Results by Aubin et al. [12] also showed that narrow grooves have a detrimental effect on the RTD. However, they found that at wide grooves the RTD was improved. Reasons for this discrepancy may be because in this chapter mass transfer by diffusion was considered and the particles are able to leave the low velocity zones by diffusion.

4.4.2 RTD from Experiments and Particle Tracking Model

Residence time distributions have been obtained experimentally for a rectangular channel and channels with symmetric and staggered herringbone structures at a length of 22 cm with blue dye (Parker Quink) as a tracer. Figure 4.8 shows the normalised tracer inlet and outlet signal, \widehat{C}_{in} and \widehat{C}_{out} at $Pe \approx 10^4$, for three separate experiments, which were very similar (measured mean residence times where within 1.1%), indicating good reproducibility.

Since the injected plug is not a perfect pulse, the RTD needs to be obtained by deconvolution as discussed earlier. This procedure is accompanied by an increase in noise; for this reason signal filters and curve smoothing were applied. The convolution of the RTD and the inlet tracer signal reproduced exactly the outlet signal. RTDs for the three experimental devices are shown in figure 4.9. It is evident from this figure that the RTD for the rectangular channel is consistent

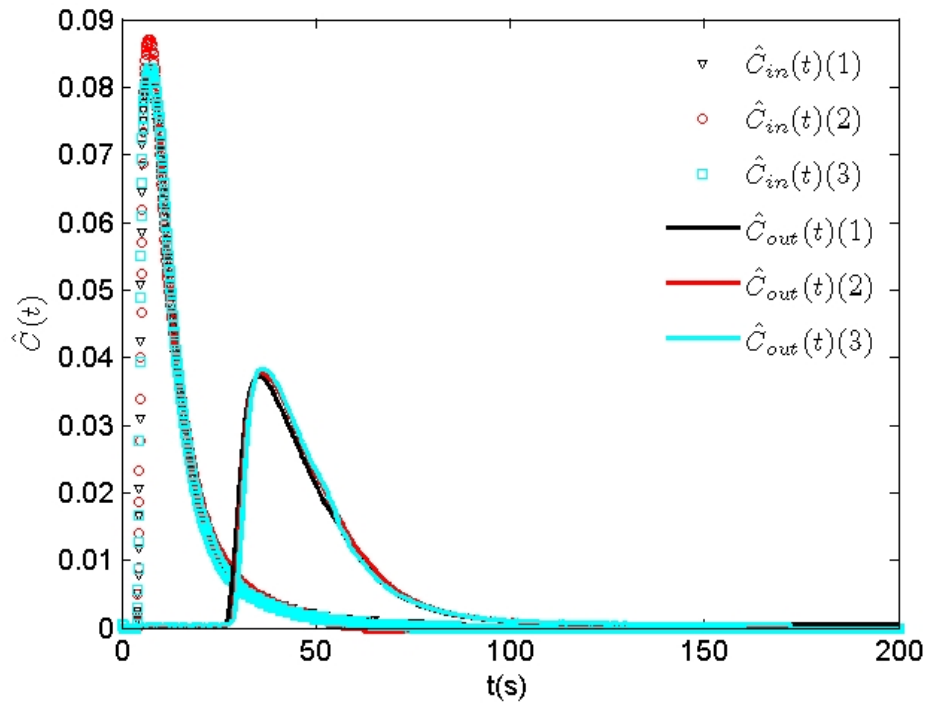


FIGURE 4.8: Normalised tracer concentration at the inlet and outlet for the staggered herringbone channel at 22 cm for three separate experiments. $Pe = 10^4$ $Re \approx 10^1$.

with the asymmetry of the convective model characterised by an early peak at half the mean residence time followed by a long tail. Furthermore the RTD of the channel with the staggered herringbone structures and the one with the symmetric ones are similar, which is consistent with the results obtained by Stroock and McGraw [144]. The dimensionless variance, σ_{θ}^2 , for the staggered and symmetric herringbone channels are 0.049 and 0.064 respectively much smaller than that of the rectangular channel (0.223). Although it has been shown that the symmetrical herringbone is a poor mixer [144], in terms of RTD it does a good job by achieving flow inversion through bringing material from the low to the high velocity zones and vice versa.

Figure 4.10 shows a comparison between the experimental results and the particle tracking with random walk diffusion. For all the channels considered the agreement was good. As was shown in section 4.1.1 for particle tracking, as the Pe number

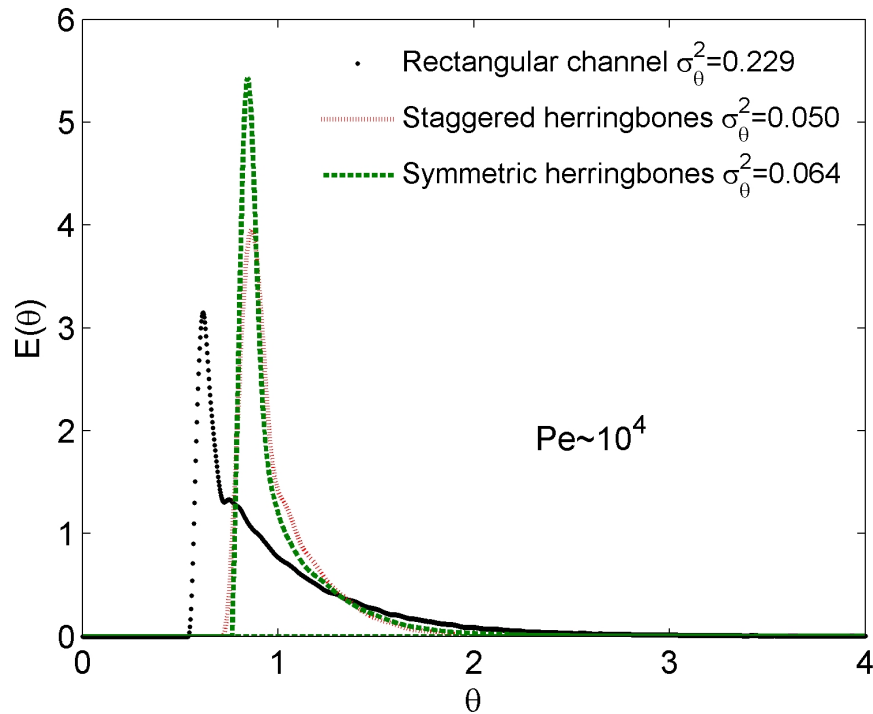


FIGURE 4.9: Dimensionless experimental residence time distributions for a rectangular channel and channels with symmetric and staggered herringbone structures for $Pe \approx 10^4$. The dimensions of the channels are listed in table 4.1. The distance of measurement from injection location is 22 cm.

decreases, mass transfer by diffusion plays an important role and the impact of using herringbone structures to narrow the RTD is reduced.

In figure 4.11, experimental RTDs for the three channel types are shown for a lower $Pe \approx 10^3$, obtained by decreasing liquid flowrate. The channels with herringbone structures still have a narrower RTD and lower variance (0.029, 0.033) than a rectangular channel (0.070), but the difference is not as great as in the case for $Pe \approx 10^4$ (compare with figure 4.9).

4.5 Conclusions

Residence time distributions were obtained numerically via particle tracking with random walk diffusion and experimentally for a rectangular channel and the results

were compared with a rectangular channel of the same dimensions with staggered and symmetric herringbone structures. Comparisons between RTDs obtained from simulations and experiments were in good agreement. Both simulations and experiments show that at high Peclet numbers, channels with herringbone structures have a narrower RTD than a rectangular channel. However, this difference is reduced as Pe decreases. Simulations also showed that at high Pe the RTD for the herringbone channels remains unaffected. This result opens the possibility of increasing the dimensions of the channel without compromising its performance in terms of narrow RTD. The RTD for the channels with herringbone structures can be fitted to an axial dispersion exchanging mass with a stagnant zone model (ADEM). This was shown to be helpful to describe RTDs at long lengths. An analysis of the effect of the groove geometrical parameters on the variance of the RTD showed that a groove angle of $\theta = 45^\circ$, depth of $g_d = 31\mu m$ and width $g_w = 50\mu m$ is close to the optimum. By calculating the conversion for a first order chemical reaction, it was shown that the dimensions of the channel with herringbones can be significantly increased relative to a plain rectangular channel without affecting its performance.

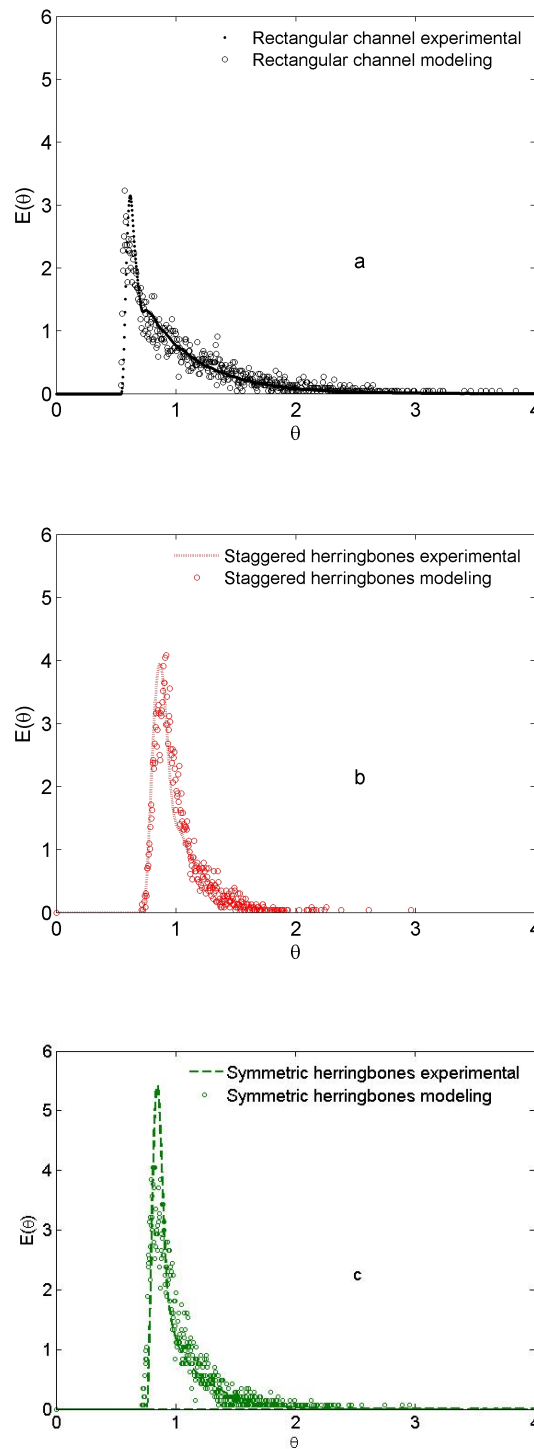


FIGURE 4.10: Comparison of the dimensionless residence time distributions obtained from experiments and from the particle tracking with random walk diffusion method for a) a rectangular channel b) staggered herringbone channel c) symmetric herringbone channel. The dimensions of the channels are listed in table 4.1. The distance of measurement from injection is 22cm. For all cases $Pe \approx 10^4$.

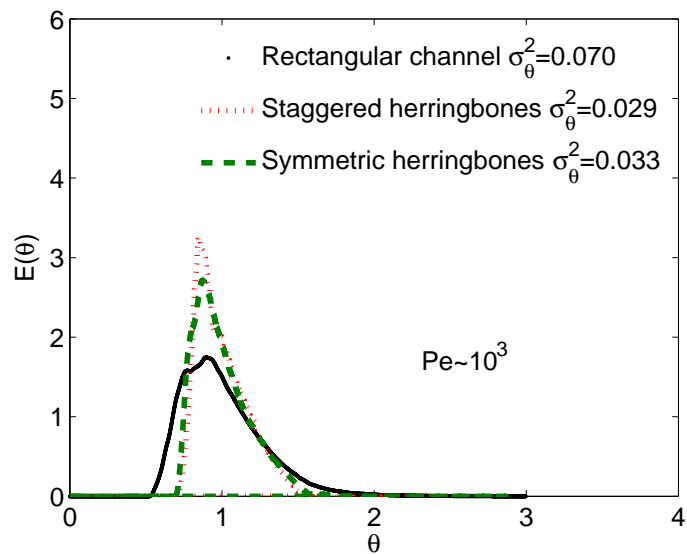


FIGURE 4.11: Dimensionless experimental residence time distributions for a rectangular channel and a channel with symmetric and staggered herringbone structures for $Pe \approx 10^3$. The dimensions of the channels are listed in table 4.1.

The distance of measurement from injection location is 22 cm.

Chapter 5

Residence Time Distributions in Microstructured Plate Reactors

5.1 Introduction

In this chapter, the RTD is measured experimentally for four different laminated microstructured plate reactor configurations containing straight or zig-zag channels. The residence time distributions are obtained by means of a LED-photodiode array system for five different flow rates. Variances as a function of residence time are obtained to compare the level of dispersion encountered. In addition RTDs are calculated via CFD and particle tracking methods to validate the experimental procedure.

5.2 Experimental Details

The reactors used in this study were provided by Chart Energy & Chemicals based on the ShimTec® technology. The reactor is comprised of a stack of microstructured stainless steel and copper sheets with etch-through features. The sheets have

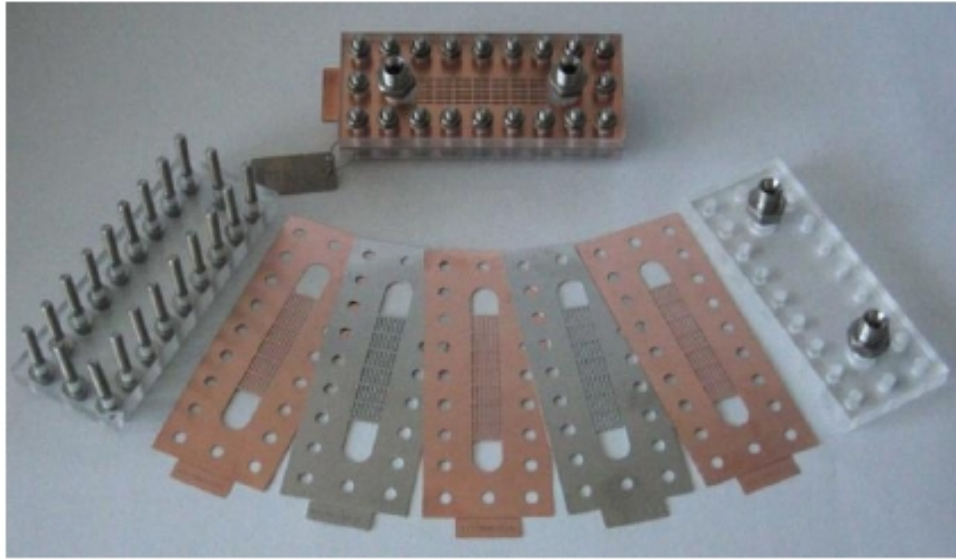
dimensions of 150x60mm. Channel depth and total volume of the reactor can be varied by stacking a different number of sheets. Closed channels are obtained by clamping the metal sheets with acrylic plates containing inlet and outlet ports. The copper sheets are placed alternating between the stainless steel ones to obtain better sealing (copper is a softer metal). The acrylic plates come in contact only with copper sheets. A picture of the assembled and disassembled reactor is shown in figure 5.1a, while in figure 5.1b sheets of straight channel and zig-zag configurations employed for the corresponding reactors are shown. In addition to the main channels (the etch-through features), additional non-etch-through features (seen as herringbones in figure 5.1b) are incorporated in the structure to promote communication between channels. The inlet and outlet ports in the original acrylic plates were moved to the sides so as to allow optical access for the RTD measurement. In addition to the stainless steel plate reactors, an acrylic rectangular cross section reactor with internal dimensions: width=14mm and height=2.46mm ($d_H=4.18\text{mm}$) was also considered for comparison purposes. The Reynolds and Peclet numbers for the various experiments and geometries, were in the range 0.4-6 and 300-5000 respectively.

The experimental set up to obtain the RTDs is the same as described in chapter 4 section 4.3.1. A picture of the experimental set up is shown in figure 5.2.

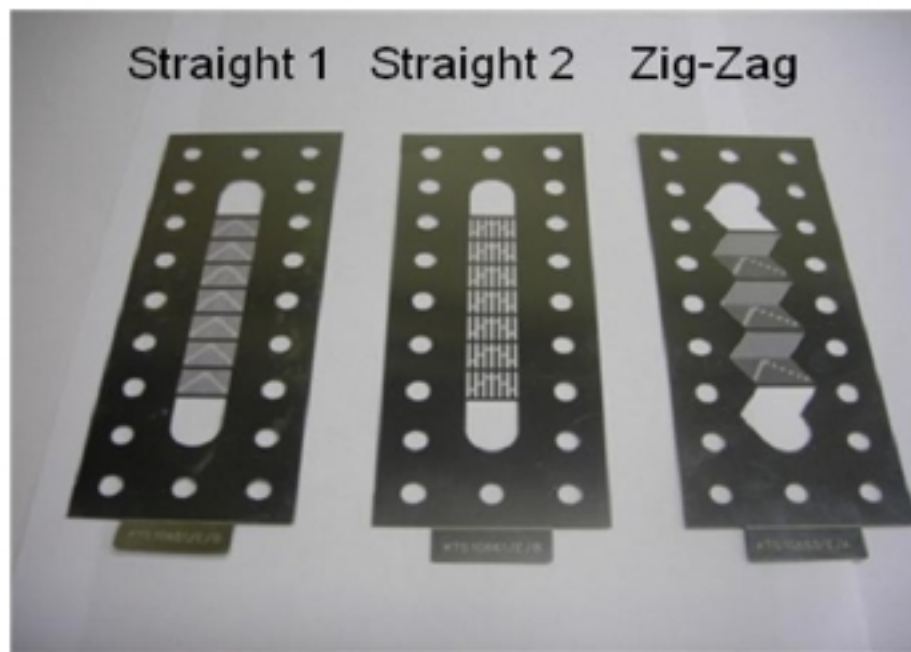
The analysis of the experimental data to obtain the residence time distributions is the same as the one shown in chapter 4 section 4.3.2.

5.3 Numerical Methods

In chapter 3 sections 3.3.1 and 3.3.2 a procedure to track the positions of massless particles was presented; this procedure is used here to obtain the RTD for a



(a)



(b)

FIGURE 5.1: a) Picture of the assembled and disassembled reactor with straight channels. b) Sheet geometries employed for RTD measurements. “Straight ” has channels with hydraulic diameter 0.7 mm, “Straight ” 1.07 mm and “Zig-Zag” has channels with hydraulic diameters 0.75 mm and 0.84 mm (for 5 and 9 shims respectively).

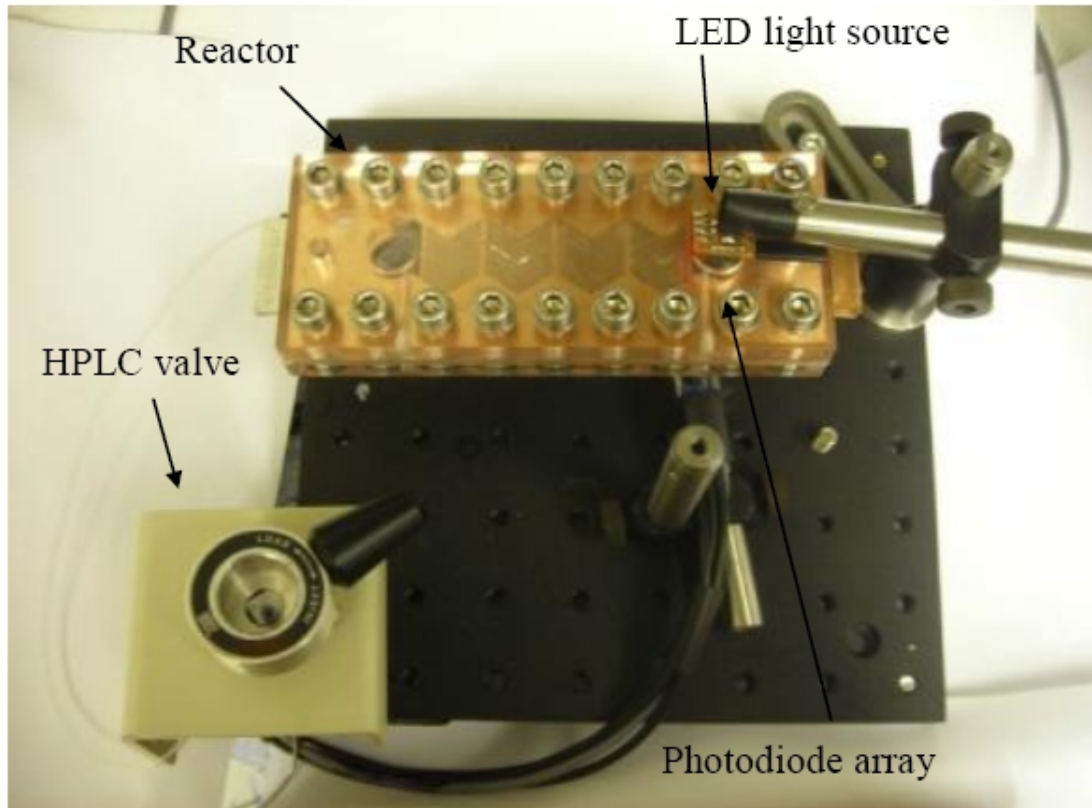


FIGURE 5.2: Picture of the experimental set up used for RTD studies.

rectangular slit with 14mm width, 2.46 mm height and 53mm length. 27222 tetrahedral mesh elements and 10^4 particles were used in the model. The simulations were run on Windows XP with Pentium IV 3.00 GHz CPU and 2GB of RAM.

5.4 Results and Discussion

Numerical calculations as discussed in section 5.3 were performed for the validation of the experimental procedure. Figure 5.3 shows the experimental and numerical RTDs for the channel with the simple rectangular slit. This geometry was chosen as it was the simplest to model. It can be seen that the agreement between the experiments and simulations is good and the experimental procedure is reliable.

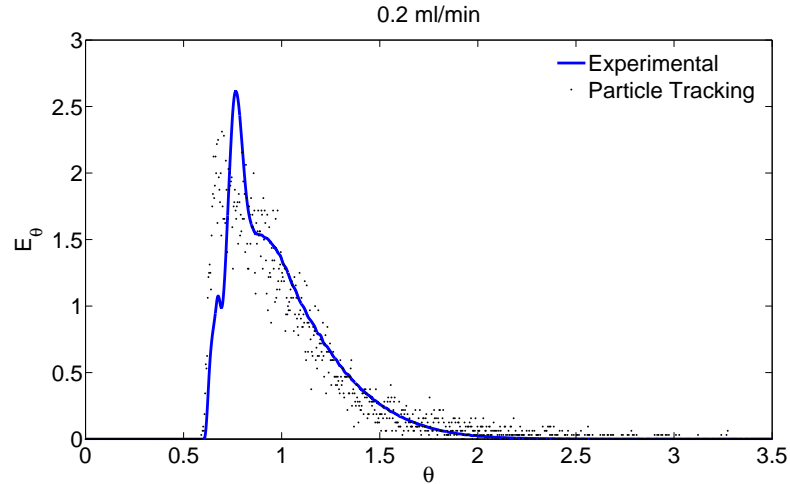
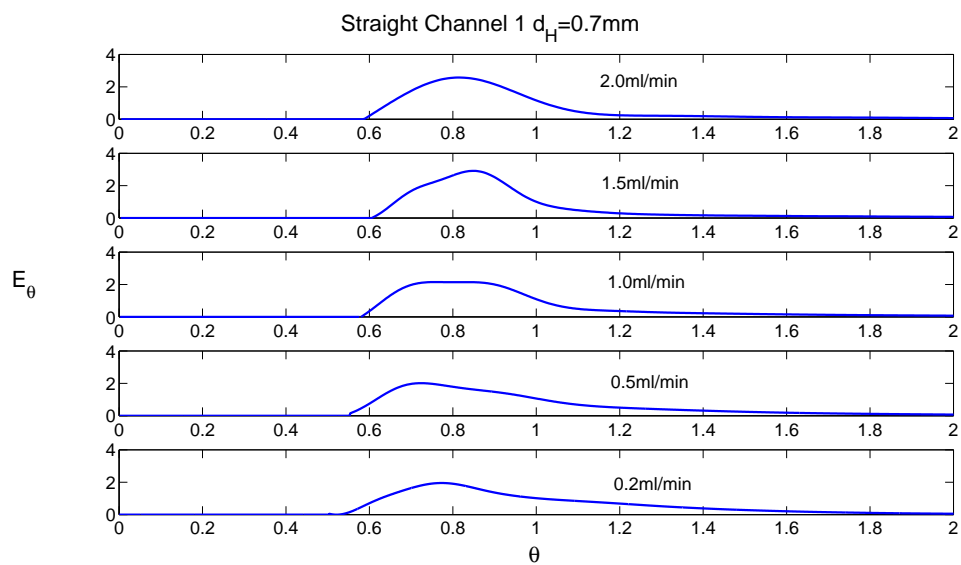


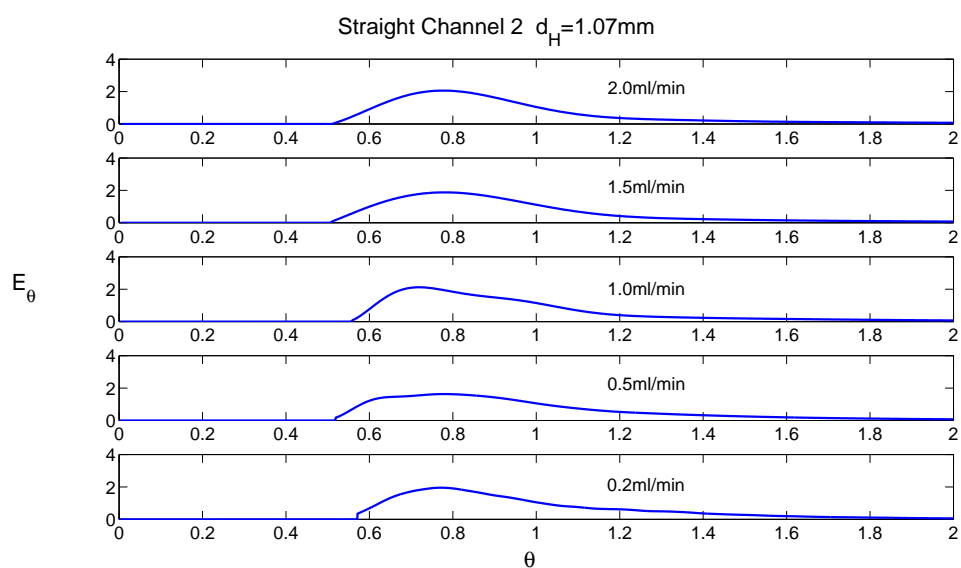
FIGURE 5.3: Comparison of experimental vs. numerical RTDs for a rectangular cross section channel. Width=14mm, height=2.46mm.

The residence time distributions for all geometries at five flowrates were obtained experimentally. Figure 5.4a shows the RTDs for the straight channel 1 geometry. The RTDs are characterised by a first appearance time close to 0.5. As the flowrate increases, the peak height of the distribution increases but it is not clear whether the RTD becomes wider with increasing flowrate. The same conclusions apply for the straight channel 2 geometry shown in figure 5.4b. Even though the channel with $d_H=0.7\text{mm}$ seems to lead to slightly narrower peaks than the one with $d_H=1.07\text{mm}$, it is not clear which structure has the narrowest residence time distribution.

The RTDs for the zig-zag channels and the rectangular slit channel are shown in figures 5.5a and 5.5b respectively. The first appearance time for the rectangular slit is close to 0.66, which is near to the theoretical value for parallel plates with no diffusion [116]. The effect of flowrate is very clear on this geometry. As the flowrate increases, the peak height of the distribution increases and the peak becomes more asymmetric. On the other hand, for the zig-zag channel, the distribution is more symmetric. Flowrate does not have a great impact on the RTD for this geometry. Even though there is a factor of 10 difference between the smallest and largest flowrate, there is not a big difference on the shape of the RTD. Recirculation



(a)



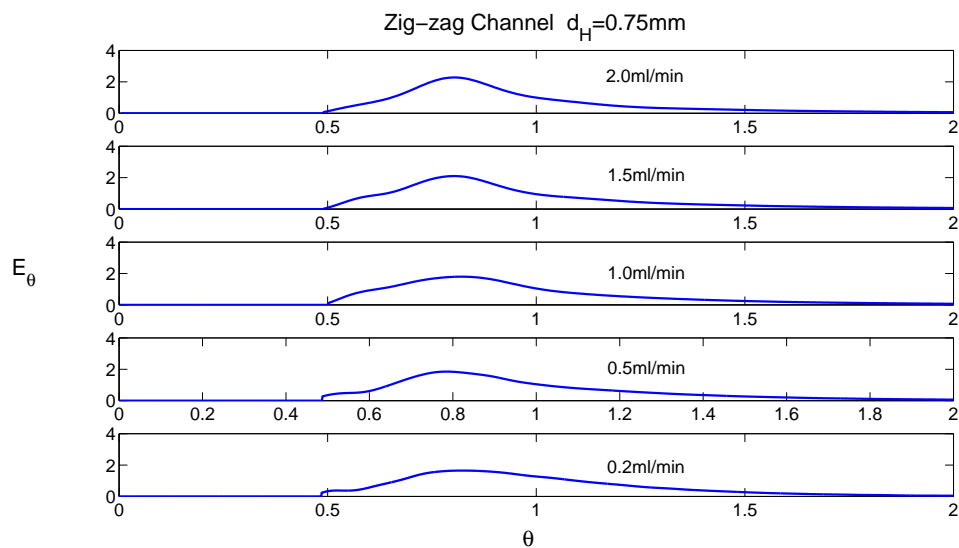
(b)

FIGURE 5.4: Dimensionless RTDs for two reactor geometries at different flowrates. a) Straight 1, b) Straight 2.

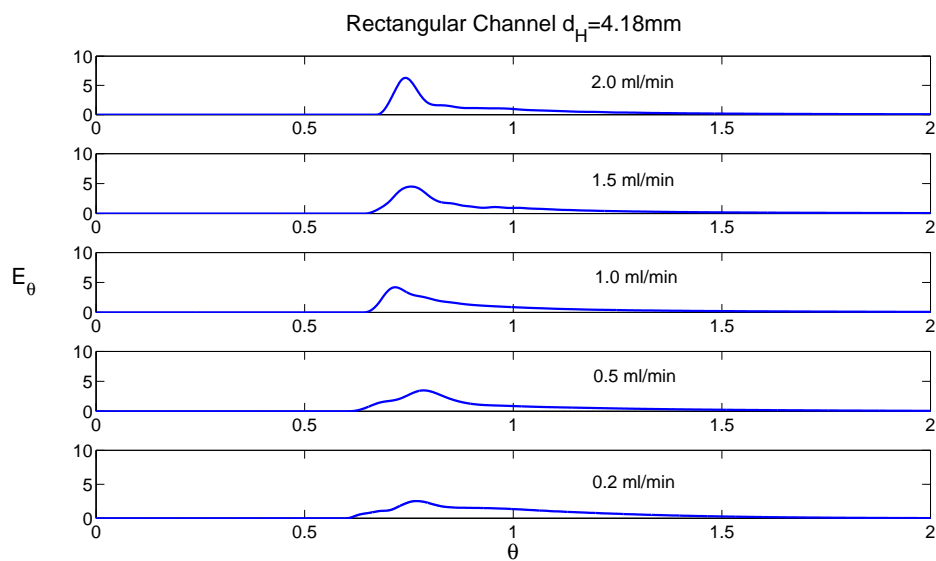
patterns which improve mixing have been shown to be present in zig-zag shaped microchannels at $Re > 80$ [107]. Saxena and Nigam [130] showed that secondary flows and low dispersion coefficients can be found in coiled tubes even at small Reynolds numbers (in the order of 10^1). The Reynolds numbers in our study are in the order of 10^0 - 10^1 and the presence of bends in the channels in conjunction with the non-etched-through features, may play a role in the generation of secondary flows, as the RTD is narrower for the channels with a zig-zag configuration as compared to straight ones. Overall, not only the zig-zag, but also the straight channel geometries showed a relative insensitivity of the flowrate on the RTD, as compared with the rectangular cross-section channel.

The number of shims for the zig-zag geometry was doubled to examine the impact of the hydraulic diameter of the reactor on the RTD. Figure 5.6 shows the dimensionless RTDs for the zig-zag geometries with 5 and 9 shims at a flowrate of 2 ml/min. It can be seen that the increase in the hydraulic diameter from 0.7 mm to 0.85 mm did not have a big impact on the RTD. The increase in the number of shims resulted in a decrease of fluid velocity due to the constant flowrate. However the Peclet number was relatively constant because the changes in velocity and hydraulic diameter compensated each other. Residence time distributions were found to be independent of Pe when secondary flows were present [26, 154]. The similar RTD results obtained for the zig-zag configuration for different Peclet numbers (varied by changing flowrate or hydraulic diameter) seem to indicate the presence of secondary flows even for the small Reynolds number tested.

Although the RTD graphs have the advantage of giving a qualitative idea of how narrow the distribution is, sometimes it is hard to tell which distribution is actually narrower. For this reason, the dimensionless variance of the RTD is plotted against mean residence time in figure 5.7. The figure indicates that the zig-zag geometry has the narrowest RTD. At small residence times (high flowrates) the differences in the variance of the geometries are large. However as the residence time is



(a)



(b)

FIGURE 5.5: Dimensionless RTDs for two reactor geometries at different flowrates. a) Zig-zag, b) Rectangular cross section channel.

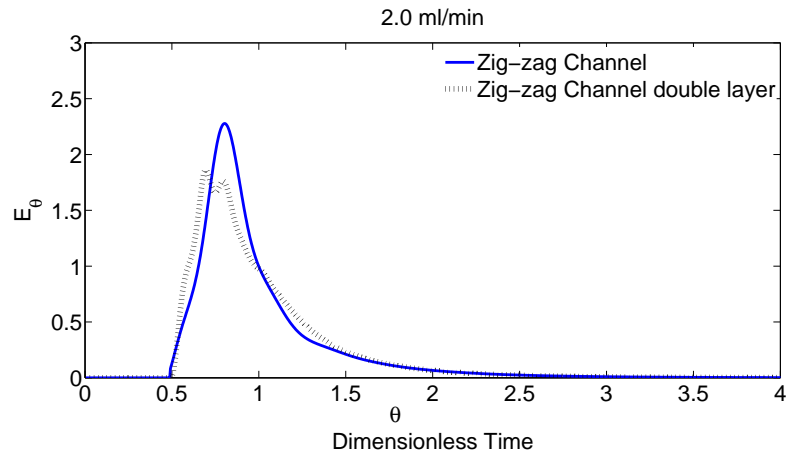


FIGURE 5.6: Dimensionless RTDs for the zig-zag geometry with 5 and 9 shims ($d_H=0.75\text{mm}$ and 0.84mm respectively) for a flowrate of 2 ml/min.

increased, the differences between the geometries diminish. This indicates that for the low flowrates studied here (small Pe), diffusion mechanisms are significant enough to homogenise the flow and minimise dispersion.

The structures with the worst behaviour were the rectangular slit and the straight 2 geometry. This result can be related to the fact that these geometries have the largest hydraulic diameter and convection will dominate over diffusion as compared with the other geometries. It is interesting to note however, that even though the rectangular slit has a hydraulic diameter nearly 4 times that of the straight 2 geometry, the variances of their RTDs are quite similar and the former even has a first appearance time closer to 1. It has been shown that at constant cross-sectional area and throughput, narrow RTDs can be obtained at low aspect ratios (depth/width) preferably lower than 0.3 [13]. The RTD narrows because as the aspect ratio decreases (the channels become wide and shallow) the maximum velocity decreases and the spread in the distribution of velocities is reduced. The aspect ratio for the rectangular slit channel studied was quite low (0.18). This is probably the reason why even though it had much larger hydraulic diameter, it had a comparable RTD with a microstructured channel with a lower hydraulic diameter but higher aspect ratio.

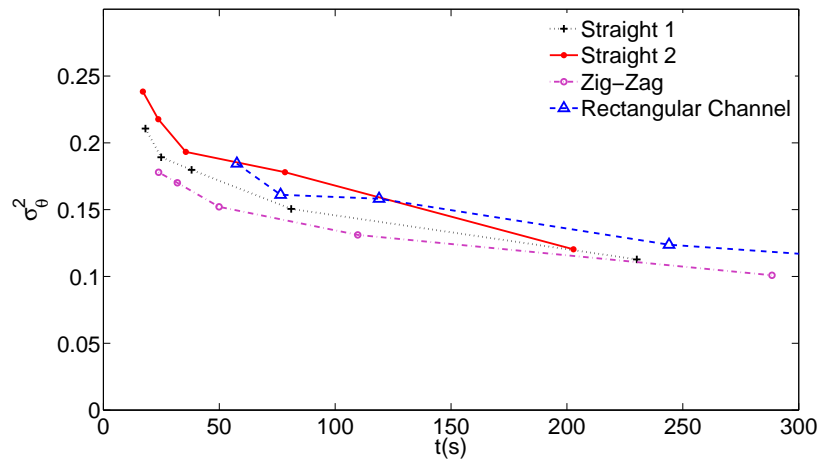


FIGURE 5.7: Dimensionless variance of the RTDs for all geometries as a function of residence time.

5.5 Conclusions

Residence time distributions for four different reactor configurations with straight and zig-zag channel geometries were investigated experimentally. Numerical calculations for a rectangular cross section channel were in good agreement with experimental results. The experiments indicated that using channels in a zig-zag configuration results in a narrower RTD than using straight ones. The calculated variance for the geometries showed that at high flowrates (low residence time) the zig-zag channel had narrower distribution than the rest of the geometries. However, as the flowrate decreased the differences in the RTDs were smaller. Secondary flows are thought to be responsible for the better performance of the zig-zag configuration. The number of channel layers was doubled for the zig-zag configuration without a detrimental effect on the RTD. This indicates that the reactor throughput can be increased without a significant impact on its performance. A rectangular cross section channel with hydraulic diameter of 4.18mm was found to have the widest RTD. However, even though the hydraulic diameter was nearly four times bigger than the rest of the geometries, the differences in the

RTDs were not large, and this was attributed to the low aspect ratio of the channel. Increasing the flowrate affected the RTD of the rectangular channel, while there was no significant effect for the microstructured reactors, and in particular the zig-zag geometry.

Chapter 6

Mass Transfer and CO_2

Absorption in Microstructured Channels

6.1 Introduction

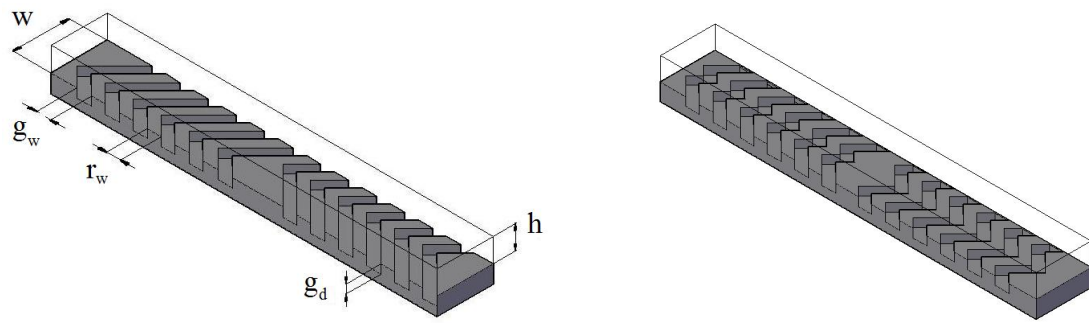
In this chapter, mass transfer to boundaries considering an instantaneous reaction at the top wall is analysed numerically via CFD and particle tracking methods for a staggered herringbone channel. The results are compared with a rectangular channel and to two proposed geometries: one based on the flow inversion concept and the other a modified herringbone channel. In addition a simplified two-dimensional model is proposed to simulate mass transfer to boundaries that uses the eddy diffusivity concept commonly used in turbulent theory. The use of herringbone structures to intensify the absorption of CO_2 in a falling film microreactor is investigated with a simplified two-dimensional model.

6.2 Theoretical Methodology

6.3 Description of Microchannel Configurations

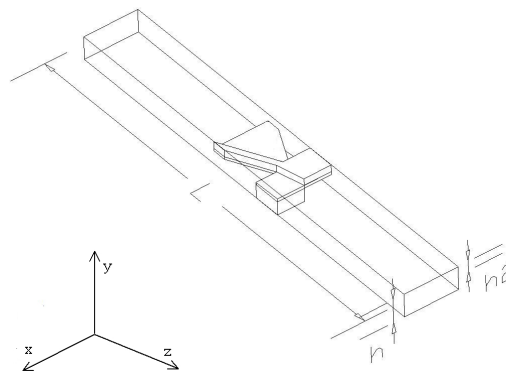
The herringbone structures considered on the microchannel floor are presented in figure 6.1a and are similar to the ones proposed by Stroock et al. [143]. The channel is divided in cycles, each one consisting of twelve asymmetric grooves. The position of the asymmetry changes every half cycle. The channel width is 200 μm and the channel height is 85 μm . The grooves are placed at an angle $\theta = 45^\circ$ with respect to the channel width. The groove depth is 31 μm , the groove width is 50 μm and the ridge width is 50 μm (measured along the axial direction). An alternative herringbone structure is shown in figure 6.1b. Instead of having one herringbone spanning the entire width of the channel, there are two herringbones, covering one half of the width each. Channel and groove dimensions are the same as in the staggered herringbone channel. Geometry A in figure 6.1a and B in 6.1b are combined to form an AB herringbone channel. On odd cycles, geometry 6.1a is used and on even cycles geometry 6.1b is used. Channels with AA structures are also considered and it is the staggered herringbone channel studied previously [77].

The flow inversion structure shown in figure 6.1c ($w = 200\mu\text{m}$, $h_1 + h_2 = 85\mu\text{m}$) has a structure in every cycle that splits the flow so that the fluid originally close to the top wall is transported to the bottom and vice versa. This transformation allows for the removal of the boundary layer for a reaction occurring at the top wall. In addition a rectangular channel with $w = 200\mu\text{m}$, $h = 85\mu\text{m}$ is also considered (not shown). For all structures the cycle length is $L = 1.5\text{mm}$ and the geometry is repeated periodically.



(a) Staggered 1-peak herringbone channel (A)

(b) Staggered 2-peak herringbone channel (B)



(c) Flow inversion geometry for reaction studies

FIGURE 6.1: Geometries considered for the numerical analysis of mass transfer to a reacting wall. The arrows indicate the direction for the flow

6.4 Numerical Procedure for Mass Transfer Calculations

The species concentration for a reaction occurring at the microchannel top wall can be found by solving the convection-diffusion-reaction equation coupled with the Navier-Stokes equation; however, for liquid-liquid mixing with $Pe > 10^3$ numerical errors (often called numerical diffusion) attributed to the discretisation of the convective term in the convection-diffusion equation are likely to affect the results

[131]. To avoid this problem, computing the trajectories of massless particles convected by the flow is commonly used [11, 12, 158].

The cross-sectional concentration gradient induced by an instantaneous reaction on the top wall can be calculated by solving the velocity field for the particular geometry and tracking the positions of massless particles convected by the flow. The particle algorithm, It was found that 10^5 particles were enough to ensure convergence of the calculated cross-sectional concentrations. The particles are distributed proportionally to the axial velocity at the channel inlet. This condition approximates the flux of solute through the inlet plane. The numerical procedure to compute the particles trajectories is described in chapter 3 sections 3.3.1 and 3.3.2.

The instantaneous reaction in the top wall is simulated by considering that when a particle touches the channel wall it reacts with a probability of 1. The $x y z$ position of the first crossing of the reactive wall for every particle is recorded (which indicates the position where the particle reacted). Subsequent crossing does not impact the concentration calculations. The information of whether a particle has reacted or not is kept so that cross-sectional concentrations are obtained at different lengths. The Sherwood number $Sh = \frac{k(z)H}{D}$ is calculated from the reacting flux across the boundary:

$$J(z) = k(C_s - C_{cup}) \quad (6.1)$$

where $J(z)$ is the reacting flux, k is the mass transfer coefficient, C_s is the reactant concentration at the reacting surface (zero in this case) and C_{cup} is the mixing cup concentration. The mixing cup concentration is calculated with the following equation:

$$C_{cup} = \frac{\int_0^Y \int_0^X C(x, y, z) u_z(x, y) dx dy}{\int_0^Y \int_0^X u_z(x, y) dx dy} \quad (6.2)$$

where u_z is the axial velocity as a function of (x, y) position. From a mass balance it can be shown that reactive flux can be expressed as:

$$J(z) = UH \frac{dC_{cup}}{dz} \quad (6.3)$$

Combining equation (6.1) and (6.3) with $Sh = \frac{k(z)H}{D}$ gives the following:

$$Sh(z) = \frac{d \ln C_{cup}}{d \frac{z}{PeH}} \quad (6.4)$$

The Sherwood number can therefore be viewed as the relative rate of change of C_{cup} with respect to the nondimensional number $\frac{z}{PeH}$ which is the inverse of the Graetz number. Concentrations are calculated by binning the particles in evenly spaced bins ($2\mu m$ squares) and dividing the number of particles that have not reacted over the total number of particles in each bin. The particles pass the relevant square bin at different times.

6.4.1 Simplification of Numerical Procedure via Turbulent Theory Concepts

The flow of gases or liquids can be classified as laminar or turbulent. In laminar flow, the layers of fluid slide over each other without mixing. The velocity field for simple geometries can be solved analytically such as the well known parabolic velocity profile in a round pipe. Transport of mass between layers occurs only by molecular diffusion. On the other hand, turbulence is characterised by random fluctuations of the velocity at any given point. Mass transfer in a turbulent flow

occurs when mass is transported by the mixing of eddies. A complete understanding of turbulent diffusion would require the knowledge of the size and motion of the eddies. Since this is extremely complex even with today's computational power, efforts have been directed to the statistical description of turbulence. Taylor [147] provided for the first time a statistical description of the nature of turbulence. He found that the scale of turbulence and its statistical properties can be given an exact interpretation if one considers the correlation between velocities at different points of the field. The diffusion of particles was shown to depend on the correlation R_ξ between the velocity of a particle at any instant (u_0), and that of the same particle ξ seconds after (u_ξ). R_ξ is defined as $R_\xi = \frac{u_0 u_\xi}{u_0^2}$ such that $R_\xi = 1$ when $\xi = 0$ and $R_\xi \rightarrow 0$ when ξ is large. If $\overline{y^2}$ is the mean square of the distance that the particles have diffused in time t , it was shown that:

$$\frac{1}{2} \frac{d}{dt} (\overline{y^2}) = \overline{y\dot{y}} = \overline{v^2} \int_0^t R_\xi d\xi \quad (6.5)$$

where $\overline{v^2}$ is the square of the mean velocity. If the time of diffusion is small so that R_ξ is 1 then equation (6.5) becomes:

$$\frac{1}{2} \frac{d}{dt} (\overline{y^2}) = \overline{v^2} t \quad (6.6)$$

If we define T as the time where $R_\xi = 0$ for all values of ξ greater than T then:

$$\overline{y\dot{y}} = \overline{v^2} \int_0^T R_\xi d\xi \quad (6.7)$$

From this equation it is possible to define a length l_1 such that:

$$l_1 \sqrt{\overline{v^2}} = \overline{v^2} \int_0^T R_\xi d\xi = \frac{1}{2} \frac{d}{dt} (\overline{y^2}) \quad (6.8)$$

So far the analysis was done in a Lagrangian manner, that is following the path of particles. An equivalent length defined in a Eulerian manner (where streamlines exist in a given space at one instant of time), which can be thought of as the average size of the eddies, can be defined as [147] :

$$l_2 = \int_0^H R_y dy \quad (6.9)$$

where R_y is the correlation of u at two points y distant apart. A plot of R_y against y represents the distribution of u along the y axis. R_y is obtained from:

$$R_y = \frac{\overline{u_y u_{y+\Delta y}}}{\bar{u}^2} \quad (6.10)$$

where \bar{u} is the average velocity between the two points. When Fick's law is applicable and the dispersion time is large the eddy diffusivity can be expressed as [135]:

$$E_D = \sqrt{\bar{u}^2} \int_0^H R_y dy \quad (6.11)$$

Since molecular diffusion takes place inside and between eddies, the transport of mass should include the effect of both molecular and turbulent diffusion. Since E_D is assumed to be independent of D the combined action of molecular and turbulent transport is considered to be additive and the effective diffusion coefficient can be calculated as [135]:

$$D_{eff} = E_D + D \quad (6.12)$$

An overall eddy diffusivity coefficient can be obtained by calculating the integral in equation (6.9) and multiplying by the average velocity as shown in equation

(6.11). Equation (6.11) gives a constant E_D for the whole channel and since we are interested in calculating mass transfer to a wall, it is important to get an accurate value of E_D close to it. Several publications have acknowledged the importance of getting an accurate value close to a wall [110, 134, 141]. In this work, to obtain E_D for the staggered herringbone channel AA, the fluid dynamics are first solved in Comsol Multiphysics as described in section 6.4. The solution is exported to Matlab where a code gets a value of the velocity in the vertical direction (u_y) averaged over the width. Rather than calculating an arithmetic average of the vertical velocity over the width, a weighted average according to the axial velocity is calculated (an analog of the mixing cup concentration):

$$u_y \Big|_z = \frac{\int_0^W u_y(x, y) u_z(x, y) dx}{\int_0^W u_z(x, y) dx} \quad (6.13)$$

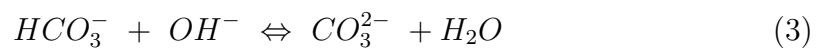
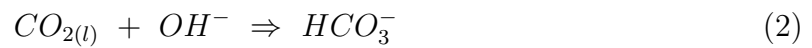
E_D was calculated as a function of channel vertical height, by changing the lower limit of the integral in equation (6.11) from 0 to y so that close to the reactive wall (when y is close to Y) we do not overestimate l_2 . This is done in order to capture the fact that the area of interest is between the specific vertical location and the reactive wall. In addition, the constant velocity $\sqrt{u^2}$ is replaced with $\overline{u_y}$ to account for the small velocities near the reactive wall. Equation (6.13) gives the weighted vertical velocity value at a given (y, z) coordinate. A simple arithmetic average over 120 values obtained at different z locations is done to obtain a single value of $\overline{u_y}$ that is valid for the whole channel cycle. With this procedure a function of $E_D(y)$ is obtained.

The possibility of using this procedure to replace the effect of the herringbone structures with a D_{eff} and reduce the model from a 3-dimensional geometry to a simpler 2D model will be investigated. This can greatly reduce the computation time and would allow to simulate more complicated geometries and reaction

schemes. Comparisons of 3D simulations with the simplified 2-dimensional approach are shown in the results section. In addition, the application of the 2D model for the modelling of CO_2 absorption falling film microreactors with and without herringbone structures is also considered.

6.4.2 Description of Model System for mass transfer evaluation (CO_2 Absorption) using 2D model

The absorption of CO_2 from a mixture of $CO_2 - N_2$ into an aqueous solution of NaOH in a microstructured mesh reactor was modelled in Comsol Multiphysics 3.5. The reaction steps occurring in this system are:



Reaction (1) represents the process of physical dissolution of gaseous CO_2 into the liquid solution. Equilibrium at the interface is described by Henry's law:

$$c_{CO_2}|_{interface} = HP_{CO_2} \quad (6.14)$$

where H is the equilibrium solubility of CO_2 in the liquid phase. The solubility of a gas into an electrolyte is dependent on the ionic strength of the solution. Hermann et al. [60] studied the effect of dissolved salts on the solubilities of gases and proposed the following empirical correlation:

$$\log\left(\frac{H}{H_{water}}\right) = -\sum_i (h_i + h_g) c_i \quad (6.15)$$

the parameters h_i are different for each of the ions present in the solution while h_g refers to the absorbed gas in the liquid phase, and are shown in table 6.1.

TABLE 6.1: Values of h at 298 K

i	Component	$h_i \text{ m}^3\text{kmol}^{-1}$
1	Na ⁺	0.1171
2	OH ⁻	0.0756
3	HCO ₃ ⁻	0.1372
4	CO ₃ ²⁻	0.1666
g	CO _{2(l)}	-0.0183

Since reaction (3) is significantly faster than reaction (2) the overall scheme is governed by reaction (2) which has second order kinetics. $r = k_{OH}c_{OH}c_{CO_2}$. The reaction constant was shown to change with temperature and ionic strength according to [123]:

$$\log(k_{OH}) = 11.916 - \frac{2382}{T} + 0.221I - 0.016I^2 \quad (6.16)$$

The solution ionic strength can be calculated from the ion concentrations and their valence as:

$$I = 0.5\sum_i c_i z_i^2 \quad (6.17)$$

the rest of the parameters used in the model are shown in table 6.2

A pseudo 3D model for the CO₂ absorption in a falling film microreactor (see figure 6.2) was presented in [4]. The same model is used in this chapter. A fully developed flow in a straight channel with constant fluid properties is assumed in

TABLE 6.2: Physical parameters used in the model

Parameter	Value	Reference
$D_{CO_2}^G$ (m^2/s)	1.855×10^{-5}	Cussler [35]
$D_{CO_2}^l$ (m^2/s)	$1.97 \times 10^{-9} (1 - 0.129c_{HO^-} - 0.261c_{CO_3^{2-}})$	Zanfir et al. [169]
$D_{OH^-}^l$ (m^2/s)	$1.7D_{CO_2}^l$	Zanfir et al. [169]
$D_{CO_3^{2-}}^l$ (m^2/s)	$D_{CO_2}^l$	Zanfir et al. [169]
μ_l ($Pa \cdot s$)	1.2×10^{-3}	Al-Rawashdeh et al. [4]
μ_g ($Pa \cdot s$)	1.69×10^{-5}	Cussler [35]
ρ_l (kg/m^3)	1040	Al-Rawashdeh et al. [4]
E_D (m^2/s)	$1 \times 10^{-9} - 2.2 \times 10^{-7}$	-

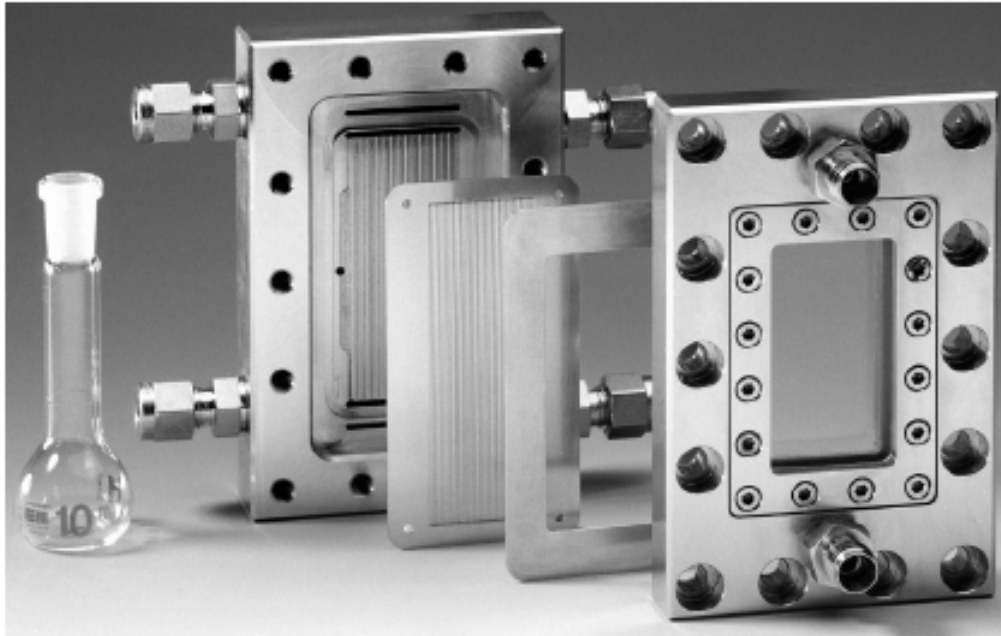
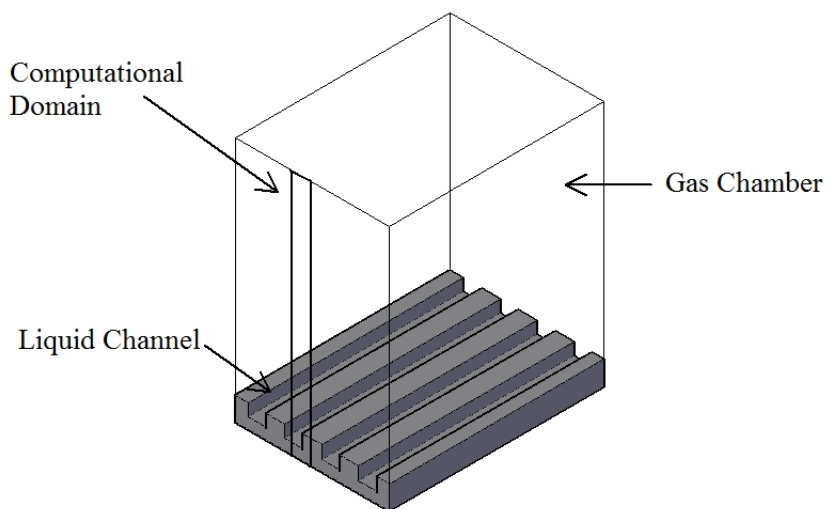


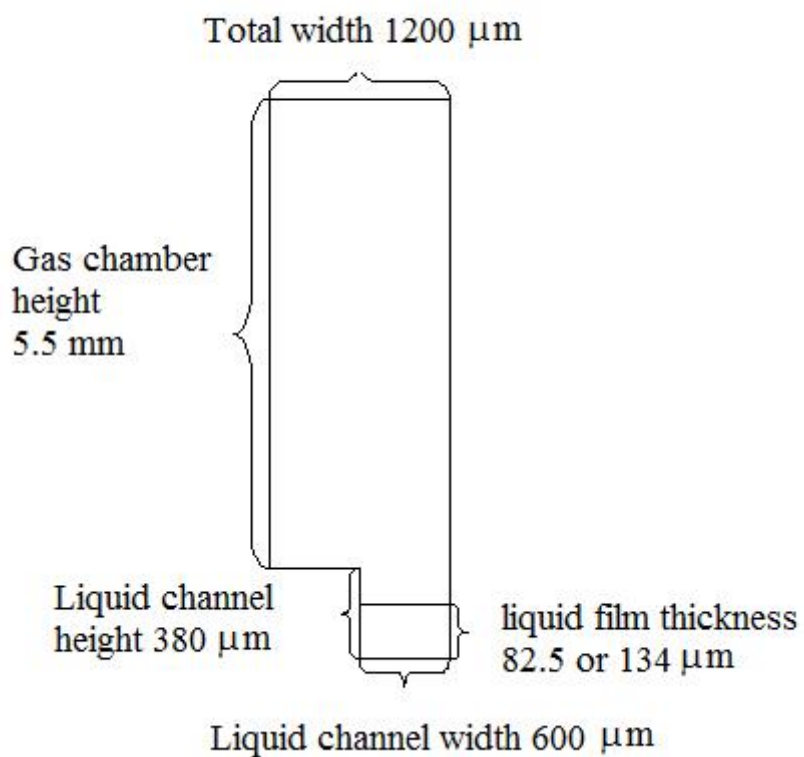
FIGURE 6.2: Experimental falling film microreactor used in Ziegenbalg et al. [170] and simulated here.

this model. The computational domain along with the dimensions used are shown in figure 6.3. Table 6.3 shows the dimensions of the computational domain.

With the assumption of constant fluid properties, the 3D Navier-Stokes equations characterising the velocity components reduce to a single 2D Poisson equation for the cross-sectional profile of the axial velocity component. In the liquid side the velocity distribution is driven only by gravity (no pressure gradient is applied) and is obtained by solving:



(a)



(b)

FIGURE 6.3: a) Schematic view of the falling film microreactor. b) Enlarged view of the computational domain considered for the CFD calculations

TABLE 6.3: Dimensions for the computational domain of the falling film microreactor

Component	Value
Gas chamber height	5.5mm
Liquid channel height	380 μm
Liquid film thickness	82.5 or 134 μm
Liquid channel width	600 μm

$$-\mu_l \left(\frac{\partial^2 v_l}{\partial x^2} + \frac{\partial^2 v_l}{\partial y^2} \right) = \rho_l g \quad (6.18)$$

where μ_l is the viscosity in the liquid side and v_l is the axial velocity component. At the channel walls no-slip boundary condition is applied ($v_l = 0$). For the symmetry boundaries a free-slip boundary condition is applied ($\nabla v_l = 0$). At the gas-liquid interface, continuity of the velocity and shear stress is assumed. The velocity distribution for the gas phase is obtained with the following equation

$$-\mu_g \left(\frac{\partial^2 v_g}{\partial x^2} + \frac{\partial^2 v_g}{\partial y^2} \right) = \frac{\partial P_g}{\partial z} \quad (6.19)$$

If the pH of the solution is kept above 11 all CO_2 is converted to CO_3^{2-} and the amount of HCO_3^- is negligible [4]. Therefore the only species of interest are OH^- , CO_3^{2-} and CO_2 . The concentration for all species both in the gas and liquid phase are governed by the advection-diffusion-reaction equations:

$$\frac{\partial c_i}{\partial t} + v \nabla c_i = D_i \nabla^2 c_i + r_i \quad (6.20)$$

where c_i , D_i , and r_i denotes the concentration, diffusion coefficient and reaction rate respectively. If axial diffusion is neglected, the 3D steady state equation can be replaced by a 2D transient equation with time representing the axial coordinate. This is why the model is called pseudo 3D. Zero flux boundary conditions are

applied to all species at the walls and symmetry faces ($\mathbf{n} \cdot \mathbf{D}\nabla\mathbf{c}_i = \mathbf{0}$ where this expression indicates that the derivative is taken in the direction normal to the boundary). For CO_2 at the gas-liquid interface the concentrations are governed by equilibrium according to Henry's law shown in equation (6.14) and due to mass conservation the flux at the liquid and gas phase should be equal ($J_g = J_l$). Although the experimental results that are used for comparison purposes were obtained in counter-current mode [170], the pseudo 3D simulations did not allow for this mode to be modelled and co-current mode had to be used instead. However, results from a 2D model showed that the flow arrangement did not have an impact on NaOH conversion for the conditions studied here (not shown).

6.5 Results and Discussion

6.5.1 Study of Mass Transfer to Boundaries with a CFD/- Particle Tracking Model

The ability of the geometries shown in section 6.1 to improve mass transfer to the top wall is analysed in this section. In section 6.5.1.1 a qualitative analysis of the effect of channel geometry on cross-sectional concentration is presented showing the cross-sectional concentrations for different channel lengths. In section 6.5.1.2 a quantitative comparison of the geometries is shown calculating the mixing cup concentrations and the mass transfer coefficients as a function of channel length.

6.5.1.1 Effect of Channel Geometry on Concentration Profiles and Reactant Conversion

Figure 6.4 shows the comparison of the cross-sectional reactant concentration profile for the rectangular channel, both herringbone channels (AA, AB) and the flow

inversion structure shown in figure 6.1 at different lengths. The results for the staggered herringbone channel are in good agreement with the literature [77]. For the staggered herringbone channel the boundary layer forming at the top wall is partially removed by the secondary flow induced by the grooves. However, it can be seen that the material boundary layer extends primarily towards the centre of the channel. This is consistent with mixing studies shown in Chapter 3, Section 3.5.4, where it was found that the relative amount of stretching at the centre of the channel was much smaller than at the sides of the channel. The zones with high stretching represent areas of good mixing. This indicates that the fluids are poorly mixed in the centre of the channel which leads to the growing of the boundary layer in that region. The AB channel shows a more uniform concentration than the AA one. The presence of the AB structures allows for the fluid in the centre to be moved to other parts of the channel, therefore the boundary layer present in the staggered herringbone channel is not present in this structure.

The results for the flow inversion structure show that this geometry is more efficient at removing the boundary layer than the staggered herringbone channel. At a length of $\frac{z}{h} = 640$ the cross-sectional concentration profile for the flow inversion structure is nearly uniform, whereas the staggered herringbone shows a boundary layer in the middle of the channel. However the AB channel shows the strongest performance (highest conversions) of the three geometries. It is interesting to note that the improved behaviour of the AB herringbone geometry is due to the synergy of the geometries involved (see figures 6.1a and 6.1b). The cross-sectional concentration for structure BB for $Pe = 10^4$ is shown in figure 6.5. It can be seen that the boundary layer grows close to the sides of the channels as opposed to the centre of the channel as in the AA geometry. On its own, geometry BB has worse performance than geometry AA. However, when the geometries are alternated the reaction performance is improved since the geometries are complementary: geometry AA is good at removing material from the sides of the channel, and

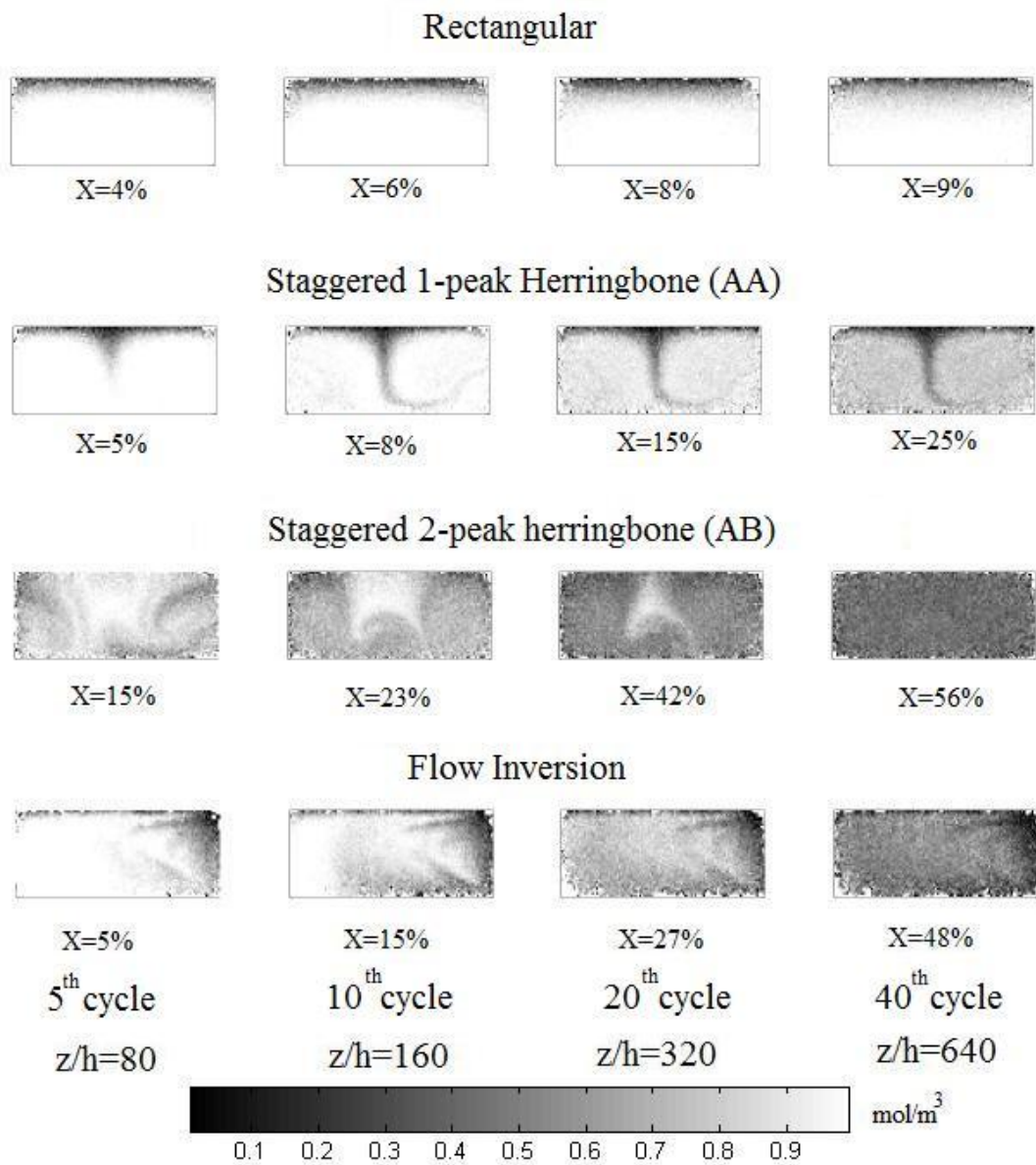


FIGURE 6.4: Cross-sectional reactant concentrations and reactant conversion at different lengths for a rectangular, staggered 1-peak herringbone AA, flow inversion and staggered 2-peak herringbone channel AB (see figure 6.1). Infinitely fast reaction at the top wall. $Pe \approx 10^4$.

geometry BB at removing it from the centre. The cross-sectional concentrations for geometry AB (see figure 6.4) show regions with no reacted fluid near the centre of the channel (seen as white background). The reason for this is because all the cross-sectional pictures were obtained at the end of a B structure, and the accumulated reacted material in the centre was already removed.

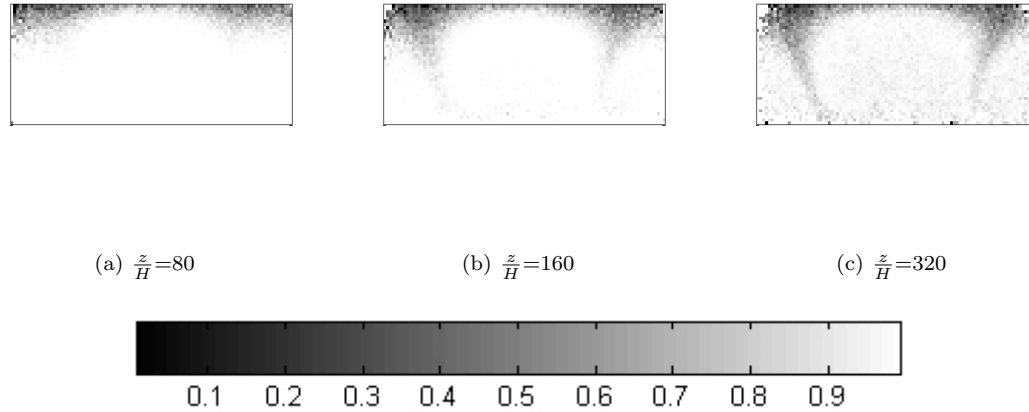


FIGURE 6.5: Cross-sectional concentrations at different lengths for the geometry shown in figure 6.1b (BB structure). In this case it is not alternated with the standard herringbone structure shown in figure 6.1a. $Pe \approx 10^4$.

6.5.1.2 Calculation of Mass Transfer Coefficients

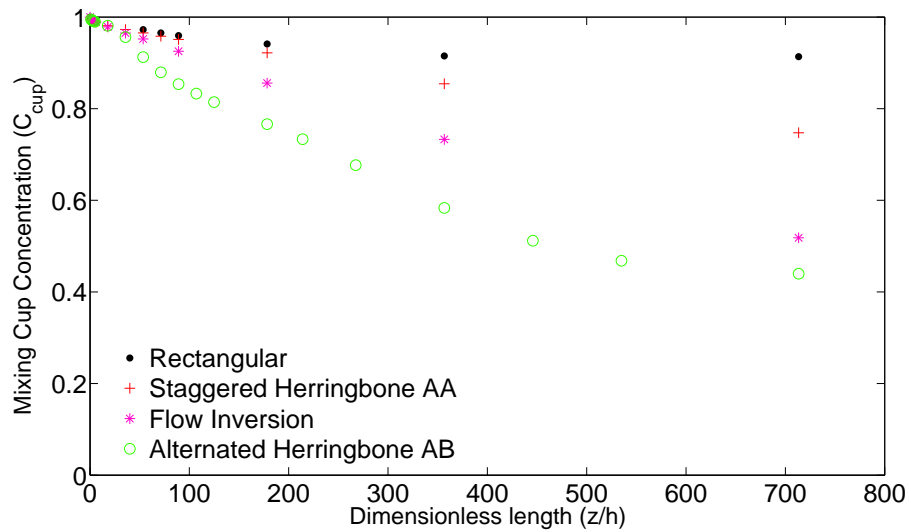
Figure 6.6, shows the mixing cup concentration calculated at different lengths for all geometries. The concentration decay for the flow inversion structure is much steeper than for the AA staggered herringbone channel, with the AB herringbone channel having the steepest gradient. This is further supported by the calculated Sherwood number (Sh) shown in figure 6.6b. For the staggered herringbone channel, the Sh achieves an asymptotic value of 8 at around $\frac{z}{h} = 20$. On the other hand, the flow inversion structure has nearly double Sh (ca. 17) than the one calculated for the staggered herringbone channel AA. It is not clear whether the alternated herringbone channel AB has reached an asymptotic value; however, for all the lengths studied the Sherwood number was about three times larger (ca. 30) the staggered herringbone AA and twice as much as the one calculated for the flow inversion structure. The alternated herringbone structure (AB) shows a sudden change in the behaviour of the Sherwood number with channel length. Before the end of the first cycle the behaviour is similar to the staggered herringbone channel. However, after the first cycle a sudden increase in the Sherwood number is seen. The reason for this is because at this channel length, instead of repeating geometry

A for the second cycle, geometry B is used and the mass transfer performance is improved. It is important to note that, although the Sherwood number for the flow inversion structure is higher than the staggered herringbone AA, the pressure drop is 2.5 times larger whereas the AB herringbone channel has a similar pressure drop as the staggered one. This result indicates that the alternated herringbone structure not only gives the strongest performance in terms of mass transfer, but also has a low pressure drop (even lower than a rectangular channel of the same dimensions).

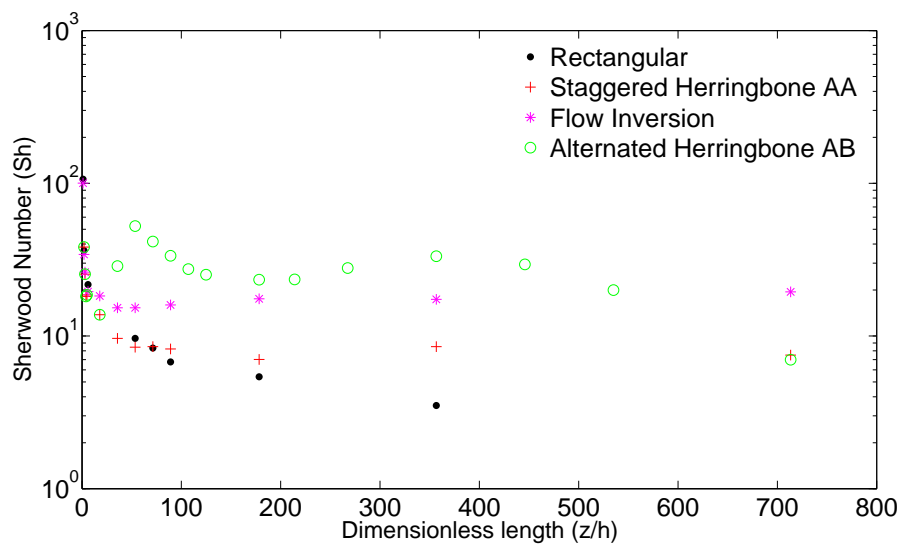
6.5.2 Study of Mass Transfer to Boundaries with Simplified 2D Model

In this section the eddy diffusivity discussed in section 6.4.1 is used to simplify the procedure to calculate the mixing cup concentrations and the mass transfer coefficients. Figure 6.7 shows the vertical velocity ($\overline{u_y}$) and eddy diffusivity (E_D) as a function of channel vertical coordinate (y), averaged over the cycle length for the staggered herringbone channel. It can be seen that the strongest stirring and therefore highest E_D is close to the channel floor at around 15 to 20 μm from the floor. This is consistent with the stretching calculations on chapter 3 section 3.5.4, where it was found that the highest stretching (highest stirring intensity) was localised close to the microchannel floor.

The mass transfer in the staggered herringbone channel AA can then be simulated in 2 dimensions (length and height) where the effective diffusion coefficient in the channel is calculated with equation (6.12). An 8th order polynomial is fitted to the graph of E_D vs. y . This equation is used as an input to the model in Comsol to allow D_{eff} to change as a function of vertical position. In figure 6.8a the Sherwood number as a function of channel dimensionless length for different values of Pe is plotted. From figure 6.8 it can be seen that the 2D and 3D simulations agree well



(a)



(b)

FIGURE 6.6: a) Mixing cup concentration at different lengths for all geometries. b) Sherwood number at different lengths. $Pe = 10^4$. Note that 1 cycle is approximately $\frac{z}{h} = 17$

for $Pe = 10^4$. Both the 3D particle tracking and the simplified 2D model agree well with previously reported data [77]. Kirtland et al. [77] showed that when the dimensionless length ($\frac{z}{h}$) is scaled with Pe ($\frac{z}{Pe h}$), all the curves collapse in the

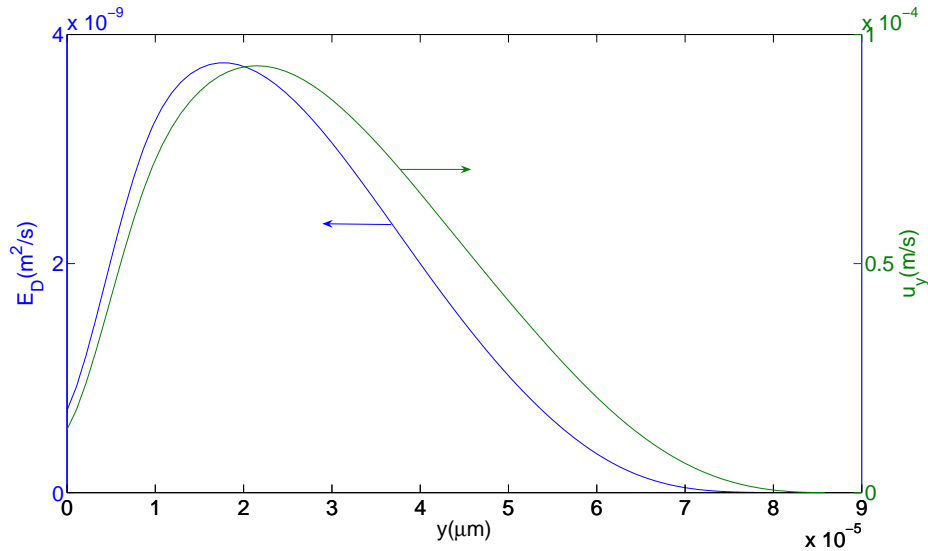
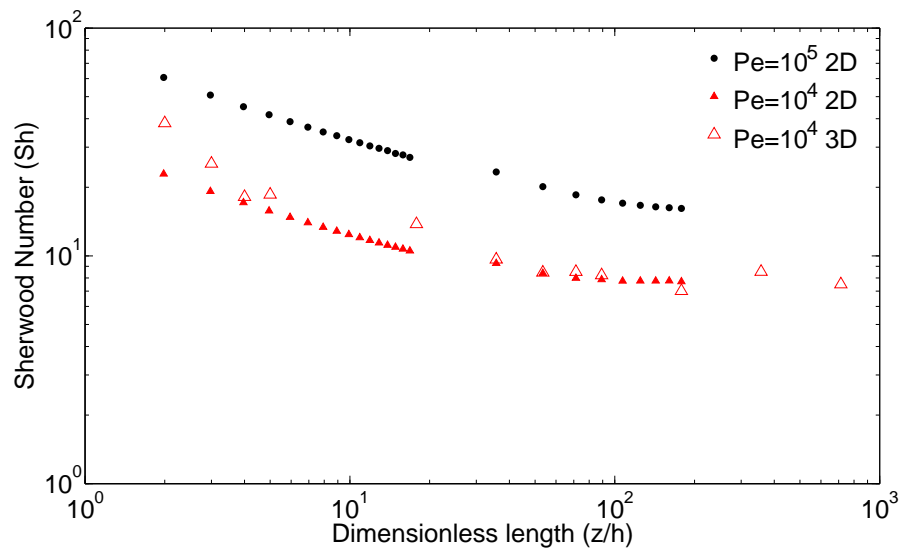


FIGURE 6.7: A) Vertical velocity (u_y) and eddy diffusivity (E_D) as a function of channel vertical coordinate for the staggered herringbone channel (AA). The reactive wall is located at a channel height of $85 \mu\text{m}$. $Pe = 10^4$

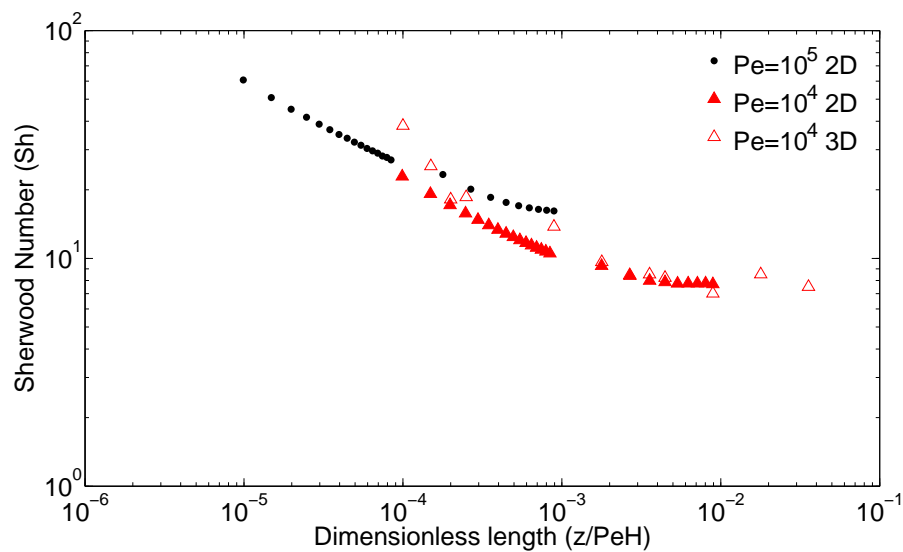
developing region. A plot of Sh vs. $\frac{z}{PeH}$ is shown in figure 6.8b. The data scale as $Sh \propto Pe^{\frac{1}{3}}$ in the developing region consistent with Kirtland et al. [77], before taking its asymptotic value which depends on Pe . The asymptotic Sh for this work is $Sh_{\infty} \approx 8$ while Kirtland et al. [77] finds $SH_{\infty} \approx 8.5$ for $Pe = 10^4$. Overall figure 6.8a demonstrates that the 2D simplified model which uses hydrodynamic data from CFD simulations is a reasonable substitute for full 3D particle tracking simulations in terms of the mass transfer behaviour of the staggered herringbone channel AA. Discrepancies at small $\frac{z}{h}$ are attributed to the stochastic nature of the CFD/particle tracking simulations. At low $\frac{z}{h}$ very small time steps are required for improved accuracy.

6.5.3 Comparison of Mass Transfer Coefficients with Literature

Kirtland et al. [77] extended the classic L ev eque problem of mass transfer to an infinite plate in a fully developed shear flow, to transverse velocity components of



(a)



(b)

FIGURE 6.8: a) Sherwood number vs. dimensionless length comparison 3D particle tracking with 2D eddy diffusivity. b) Sherwood number vs. $\frac{z}{PeH}$

a 3D flow in a rectangular duct (see figure 6.9a). The L ev eque problem is similar to a reactive wall of a duct since near the wall Poiseuille flow can be approximated by simple shear flow. In their analysis two different axial and transverse flows are assumed to interact with the reactive wall. Each of these develops its own

boundary layer (see figure 6.9b). The Sherwood number for uniaxial flow as a function of axial position for a single reactive wall is given by [77]:

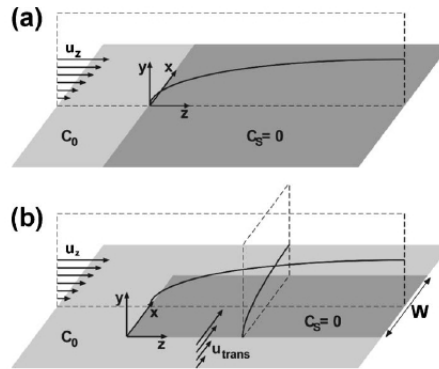


FIGURE 6.9: Developing boundary layer over a reactive plate. a) Development of a boundary layer in a uniaxial flow. b) Simplified model of the simultaneous growth of axial and transverse concentration boundary layers over a reactive boundary. [77]

$$Sh(z) = \frac{9^{-\frac{1}{3}}}{\Gamma(\frac{4}{3})} \left(\frac{H\dot{\gamma}}{U} \right)^{\frac{1}{3}} \left(\frac{z}{PeH} \right)^{-\frac{1}{3}} \quad (6.21)$$

where $\dot{\gamma}$ is the shear rate and Γ is the gamma function. As an approximation of the shear rate the value of $\dot{\gamma} = \frac{6U}{H}$ for flow between parallel plates is used. If L ev eque's analysis is used for the transverse flow in the vertical direction y , the growth of the transverse boundary layer is stopped after a distance of the order of the height (H). Equation (6.21) can be integrated with y as the independent variable (rather than z) from $y = 0$ to $y = H$ for an average flow speed U and a transverse velocity u_{trans} giving the asymptotic value for Sh :

$$Sh = \frac{3^{\frac{1}{3}}}{2\Gamma(\frac{4}{3})} \left(\frac{H}{H} \right)^{\frac{1}{3}} \left(\frac{H^2\dot{\gamma}_{trans}}{D} \right)^{\frac{1}{3}} \quad (6.22)$$

the dimensionless ratio $\frac{H\dot{\gamma}_{trans}}{u_{trans}}$ can be found by differentiating the transverse velocity with respect to y at the reactive wall. The transverse shear rate $\dot{\gamma}_{trans}$ is approximated by $\frac{u_{trans}}{H} = 0.547$ [77]. The value of $\dot{\gamma}_{trans}$ was also obtained by

differentiating the vertical velocity u_{trans} with respect to the vertical coordinate y near the reactive wall. The values for the Sherwood number obtained with the two values for $\dot{\gamma}_{trans}$ and the ones obtained from the 2D simplified model are shown in table 6.4.

TABLE 6.4: Sherwood numbers for different values of Pe_{trans} obtained with two different values of $\dot{\gamma}_{trans}$ and with the 2D simplified model

	Sh for $Pe_{trans} = 395$	Sh for $Pe_{trans} = 3950$
2D simplified model	7.71	16.14
$\dot{\gamma}_{trans} = \frac{u_{trans}}{H}$	5.93	12.78
$\dot{\gamma}_{trans} = \left. \frac{\partial u_{trans}}{\partial y} \right _{y=H}$	6.73	14.50

Regrouping terms, equation (6.22) reduces to:

$$Sh = B_1 Pe_{trans}^{\frac{1}{3}} \quad (6.23)$$

where $Pe_{trans} = \frac{u_{trans}H}{D}$ and B_1 is a geometry dependent constant. From equation (6.22) $B_1 = \frac{3^{-\frac{1}{3}}}{2\Gamma(\frac{4}{3})} \left(\frac{H\dot{\gamma}_{trans}}{u_{trans}} \right)^{\frac{1}{3}}$. Equation (6.23) with $\dot{\gamma}_{trans} = \frac{u_{trans}}{H}$ has been used to predict the asymptotic behaviour of Sh for different values of Pe_{trans} and it is compared with the results of the 2D simplified model presented in section 6.5.2 and the results reported by Kirtland et al. [77]. The value of u_{trans} used for the 2D model is the average value of u_y which can be obtain by integrating the curve u_y vs. y shown in figure 6.7 the results are shown in figure 6.10.

It can be seen from figure 6.10 that the prediction from the simplified 2D model agrees well with the modified Graetz behaviour proposed by Kirtland et al. [77] (differences within 30% between $B_1 Pe_{trans}^{\frac{1}{3}}$ and the 2D simplified model). In this case, the asymptotic value for Sh is dependent on Pe_{trans} (see equation (6.23)) whereas in the conventional Graetz behaviour Sh_{∞} is constant. This suggests that mass transfer coefficients can be obtained only by solving the velocity field and

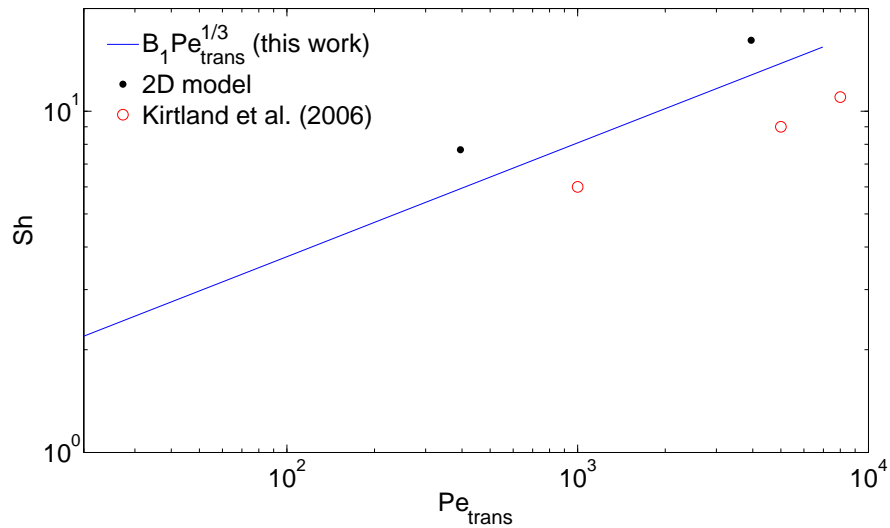


FIGURE 6.10: Sherwood number (6.23) vs. $Pe_{trans} = \frac{u_{trans}H}{D}$. Values from Kirtland et al. [77] are approximated from their reported figure 8a. In this work $B_1 = 0.8075$, whereas in Kirtland et al. [77] $B_1 = 0.6429$

obtaining a value of u_y . Such approach eliminates the need of calculations which can be computationally expensive specially for 3D geometries.

6.5.4 Modelling of CO_2 absorption with Simplified 2D model

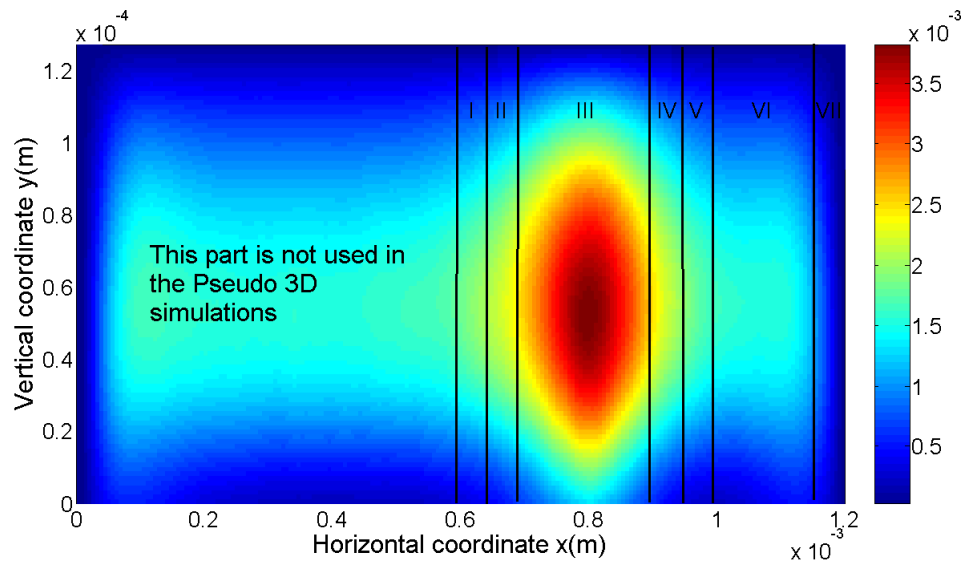
The absorption of CO_2 in 1M NaOH aqueous solution in a falling film microreactor was simulated with the pseudo 3D approach described in section 6.4.2. The effect of the herringbone structures in reaction conversion was incorporated via the eddy diffusivity approach described in section 6.4.1. The simulations are compared with experimental data reported in Ziegenbalg et al. [170]. Two different liquid flowrates per plate were considered (a plate has 16 channels) 1.68 ml/min and 6.72 ml/min which resulted in two different liquid film thicknesses (82.5 and 134 μm). For the case with no herringbones the model parameters are those described in section 6.4.2 and shown in table 6.2. For the herringbone channel case, the diffusion coefficients in the liquid side needs to be changed to effective diffusion coefficients that approximates the stirring effect of the grooves. In order to calculate the eddy

diffusivity, the vertical velocity (u_y) for the falling film geometry with herringbones on the liquid side, needed to be calculated as a function of channel height. Instead of averaging the vertical velocity over the width and the whole cycle length as described in section 6.4.1, in this case only a weighted average over the length of a half cycle was calculated because now only half of the microchannel is simulated (see figure 6.3). This gives two maps of the vertical velocity as function of channel x, y coordinates (see figure 6.11).

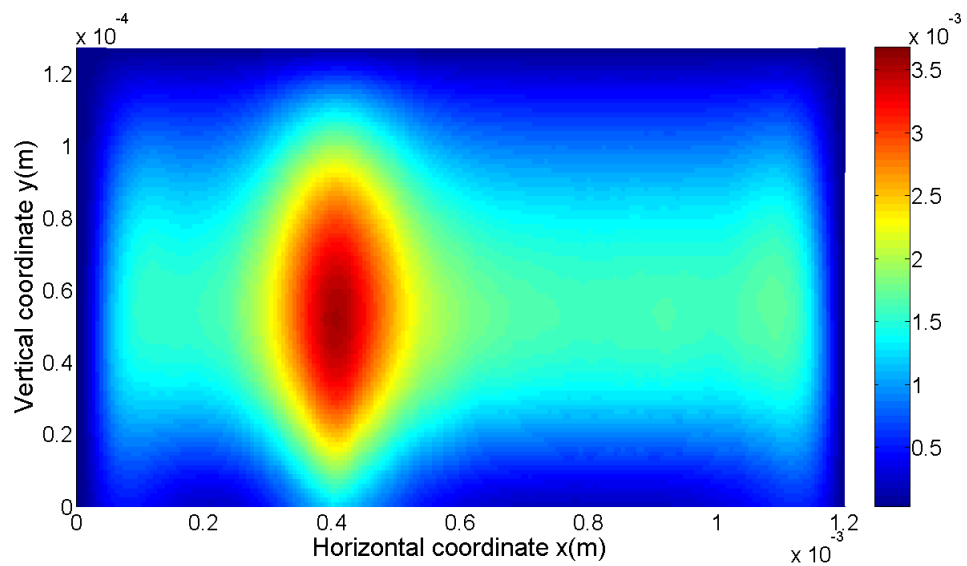
The profiles show a strong vertical velocity near the herringbone peak at 800 μm for the 1st half cycle and 400 μm for the 2nd half cycle. This suggests that at these points, the removal of reacted liquid is greater and the reaction rate would be higher. It has been shown experimentally that near the groove asymmetry the hydroxide conversion is higher [170]. Due to the large differences on the intensity of the vertical velocity, to calculate the eddy diffusivity, the width of the channel was divided in 7 regions where an equation for the vertical velocity (u_y) as a function of channel height is obtained for each region. The eddy diffusivity is calculated as discussed in section 6.4.1. The seven regions are shown in figure 6.11a, these divisions are important since the calculated eddy diffusivities are a function of vertical velocity; the more the number of regions, the more accurate the results. Figure 6.12 shows the eddy diffusivity curves for the seven different regions. As expected the values for region III show the highest value for E_D . On the other hand, region VII shows the smallest E_D .

Conversions obtained from the pseudo 3D simulation for both the normal and the grooved 1200 μm plate are compared with experimental results from [170] in figure 6.13 for different liquid flowrates and CO₂ inlet molar fractions ($y_{\text{CO}_2} = \frac{n_{\text{CO}_2}}{n_{\text{total}}}$ where n_i indicates moles of species i).

The molar flow ratio $F_{\text{CO}_2}/F_{\text{NaOH}}$ was constant for all simulations and equal to 0.4. The results from the simulations are in good agreement with the experimental



(a)



(b)

FIGURE 6.11: Maps of the vertical velocity on the cross-section of a staggered herringbone channel (see figure 6.1a). a) 1st half cycle. b) 2nd half cycle. Then numbers I to VII indicate regions where different expression for E_D are calculated as described in the text. Flowrate 6.72 ml/min. Note that the computational domain for the Pseudo 3D model is from 600 μm to 1200 μm .

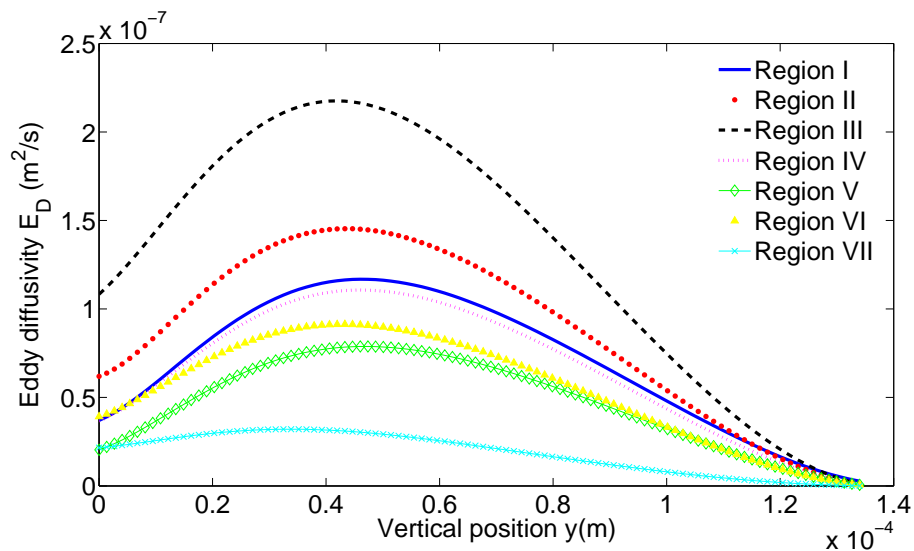


FIGURE 6.12: Eddy diffusivity (E_D) as a function of channel height for the seven different regions shown in figure 6.11

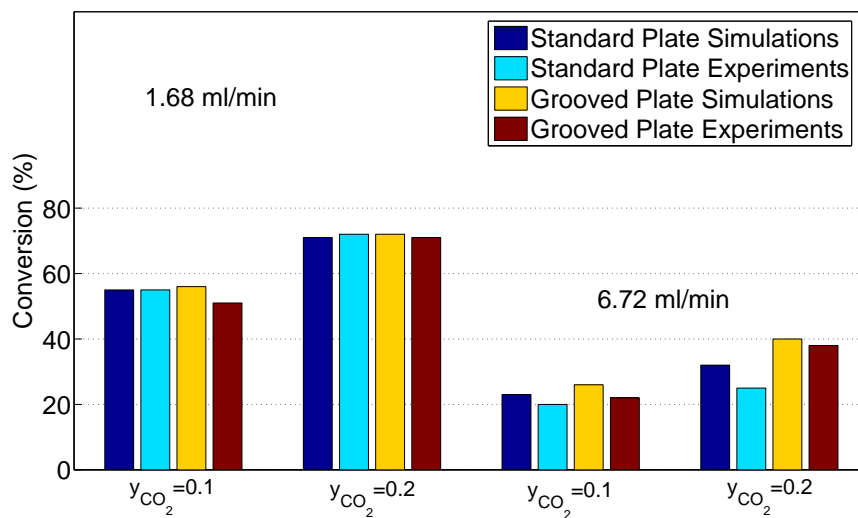


FIGURE 6.13: NaOH conversion for the falling film microreactor for different inlet liquid flowrates and CO_2 fractions. Experimental conversions were taken from [170]

data from the literature [170]. At low liquid flowrates (1.68 ml/min), the grooved plate does not make a major impact on NaOH conversion, conversions are similar to the ones obtained for the standard plate. However, at higher liquid flowrates (6.72 ml/min) the grooved plate shows a higher conversion than the standard plate. Higher conversions for both plates were found for low liquid flowrates due to increased residence time. Also, on both plates, an increase on y_{CO_2} resulted in an increase on conversion due to higher reaction rates (the reaction constant is a function of the concentration). The difference in the performance of the plates increased with increasing y_{CO_2} . Whereas the simulations showed the the conversion for the grooved plate was 11% higher than the normal plate at $y_{CO_2} = 0.1$, at $y_{CO_2} = 0.2$ it was 23% higher. Experimental conversions for the grooved plate were 15 and 52% higher respectively. This indicates that the grooved plate gives an improved advantage as compared to the standard plate at extreme conditions of high flowrate and high reaction rate (high y_{CO_2}) where the system is mass transfer controlled. The agreement between experiments and simulations for the grooved plate makes the eddy diffusivity concept an interesting approach for the simulation of complicated geometries.

6.6 Conclusions

Mass transfer to a reactive boundary has been investigated numerically for four different geometries: the staggered 1-peak (AA) and staggered 2-peak herringbone channel (AB), a flow inversion structure and a rectangular channel for comparison purposes. The results from the reaction studies indicate that the proposed alternated herringbone channel is more efficient at removing the depleted reactant fluid from the reaction zone than the other two geometries. Mass transfer coefficients were calculated for all geometries and showed good agreement with literature values [77]. The mass transfer coefficients for the AB herringbone channel

were higher at all lengths than the ones calculated for the flow inversion structure and the AA herringbone channel. The eddy diffusivity concept commonly used in turbulent theory was used to simplify the numerical calculations. It was found that the staggered herringbone channel can be modelled with a two-dimensional model with an eddy diffusion coefficient that approximates the stirring behaviour of the herringbones. The agreement between the Sherwood numbers calculated with 3D particle tracking simulations and the 2D model was satisfactory. The eddy diffusivity was also used for the modelling of CO_2 absorption with 1M NaOH in a falling film microreactor with herringbone structures. The modelling results are in good agreement with the experimental data of [170]. The results showed that the use of a grooved plate increased the NaOH conversion relative to a standard plate in cases where mass transfer was limited. This occurred at high flowrates and high reaction rates. Using this procedure greatly simplifies the calculations and opens the possibility of simulating more complex systems with multiple reactions occurring on surfaces and/or the bulk.

Chapter 7

Hydrodynamics Studies in a Layered Herringbone Channel

7.1 Introduction

In this chapter, a layered herringbone structured microchannel is investigated in terms of mixing and residence time distributions. In this geometry, a plate with see-through herringbone structures is placed in the middle of two rectangular channels (see figure 7.1a). The use of this plate allows for the use of a single set of herringbones for two channels, as opposed to the original design with one structure per channel. Mixing is studied in this configuration numerically with Comsol Multiphysics 3.5 and Matlab using particle tracking and experimentally with confocal microscopy and via the iodide-iodate reaction [48, 84, 121]. The layered herringbone microchannel is compared in terms of mixing with a $100 \times 300 \mu\text{m}$ silicon/glass T-mixer and a $400 \mu\text{m}$ capillary T-mixer.

7.2 Experimental Methodology

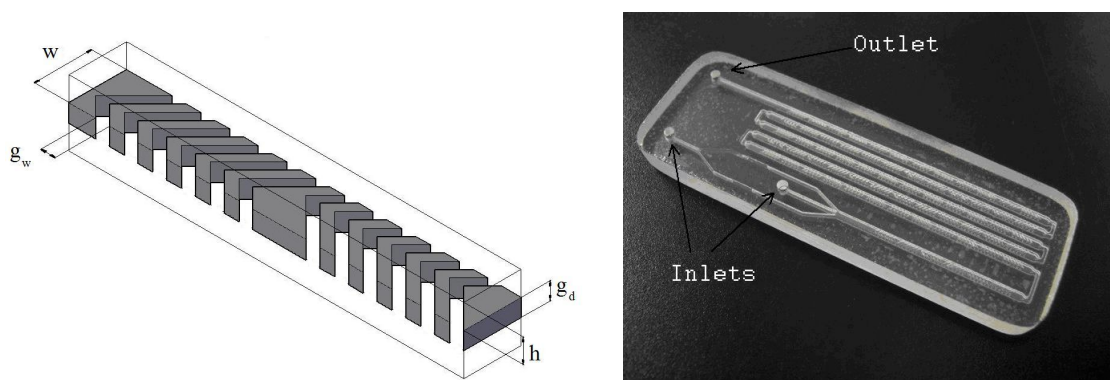
7.2.1 Description of Microchannel Configurations

The layered microchannel geometry considered in this chapter is shown in figure 7.1 b and c, while its dimensions are shown in table 7.1.

TABLE 7.1: Dimensions of the different geometries studied. Peclet number for all studies was $Pe = 10^4$

	Glass Layered Herringbone (mixing)	Acrylic Layered Herringbone (RTD)
Width (w)	1.2mm	2mm
Height (h)	510 μ m	1mm
Groove width (g_w)	300 μ m	500 μ m
Groove depth (g_d)	370 μ m	1mm
Ridge width (r_w)	300 μ m	500mm
Angle (θ)	45 \angle	45 \angle

It consists of two symmetric, top and bottom microchannels separated by a middle layer with see-through herringbone grooves. The chip has a total of five layers: the two rectangular channels, the see-through herringbone grooves and a top layer with two inlets and one outlet port (see appendix D). The staggered herringbone structures are similar to the ones considered by Stroock et al. [143]. The channel is divided in cycles, each one consisting of twelve asymmetric grooves. The position of the asymmetry changes every half cycle. It is important to note that the herringbones are not placed on the microchannel floor and the fluids flowing in top and bottom channels are able to communicate through these features. Also the first 7mm of the main channel immediately after the joining of the inlet channel does not contain any herringbone grooves (see mask in appendix D). A schematic of one cycle of the layered herringbone design is shown in figure 7.1a; figure 7.1b shows the chip fabricated in photo-structurable glass (FOTURAN) used in the mixing experiments. Devices fabricated with FOTURAN can have big aspect ratios as opposed to devices made from regular glass with chemical etching. The geometry



(a) Schematic of one cycle of the layered herringbone channel

(b) Picture of the glass chip employing a layered herringbone channel. The chip is 26x76mm.



(c) Picture of the acrylic chip employing a layered herringbone channel. The chip is 60x150mm.

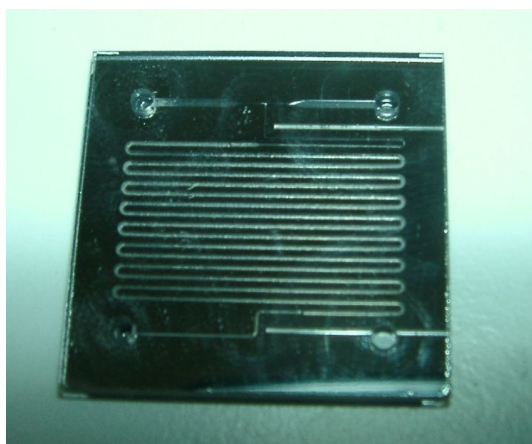
FIGURE 7.1: Schematic of layered herringbone channel and corresponding experimental structures. The dimensions of the structures can be seen in table 7.1, (see appendix C) for details of the experimental chips.

of the experimental chip is therefore closer to the one used in simulations. For RTD experiments, a chip similar to the one fabricated in glass was fabricated in acrylic by micromachining (see figure 7.1c). In addition to the layered herringbone channel a silicon/glass T-mixer fabricated by photolithography with $100\mu\text{m}$ width, $300\mu\text{m}$ depth and 2cm long. After the first 2cm the dimensions of the channel change to $600\mu\text{m}$ width, $300\mu\text{m}$ depth and 20cm long. A PEEK mixing tee with $500\mu\text{m}$ ID with a circular capillary $\frac{1}{16}$ " OD with $400\mu\text{m}$ ID and 30 cm long was also considered for mixing comparisons (see figure 7.2). A stainless steel housing was used to hold the silicon/glass mixer and provide access ports.

7.2.2 Evaluation of Mixing

Experimental mixing evaluation was performed by a confocal fluorescence microscope (Leica SP-2). A solution of acridine orange with concentration of $20\mu\text{M}$ with $D = 1 \times 10^{-9} \text{m}^2/\text{s}$ [46] in water was used as the fluorescent dye. The solution with acridine orange was mixed with an equal flowrate of deionized water. HPLC pumps (Waters 510 and Jasco PU-2080 plus) were used to inject the liquids to the different geometries tested. In order to get cross-sectional pictures of the mixing performance, picture slices taken in the plane x-z were stacked together and then an orthogonal view in Leica Confocal software was used to view the plane x-y.

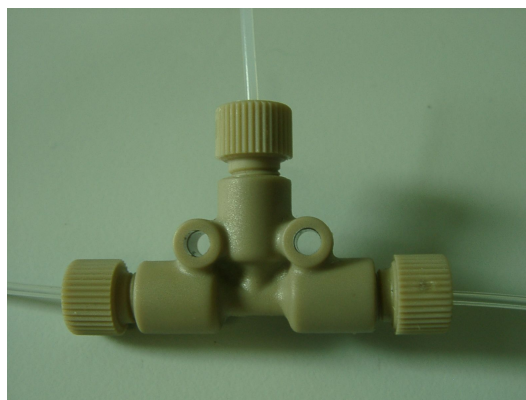
Mixing was also evaluated with the competitive-parallel iodide-iodate reaction (Villermoux-Dushman reaction) used for the quantification of mixing in continuously stirred reactors [48, 55]. These reactors contained a solution of I^- , IO_3^- and NaAc (sodium acetate) to which a strong acid was added. Mixing of these solutions results in the following two reactions:



(a) 100x300 μm (width x depth) silicon/glass mixer channel

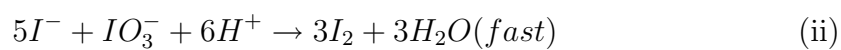
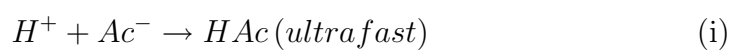


(b) 100x300 μm (width x depth) silicon/glass mixer channel with stainless steel holder



(c) Mixing tee with 500 μm ID holes and 400 μm ID capillaries

FIGURE 7.2: Geometries studied to compare the mixing behaviour of the layered herringbone channel



The neutralisation reaction is instantaneous and under perfect mixing all the acid will be consumed in the neutralisation process. However, when an excess of acid is

present or local deviations from the average concentration of acid due to imperfect mixing are present, iodine formation is possible. Therefore iodine concentration measured by UV-vis absorption can be used to quantify the extent of mixing. High iodine concentrations indicate poor mixing. The mixing ratio was 1:1 as opposed to the original work of Fournier et al. [48]. For this reason the concentrations of the solutions had to be modified in order to get detectable amounts of iodine. The solutions used were 1000 ml of 0.1374M *HCl*, 500 ml of 0.0319M *KI* in 1.33M of NaAc and 500 ml of 0.00635M *KIO₃* in 1.33M of NaAc. The use of these concentrations resulted in detectable amounts of iodine [40].

The solutions with *KI* and *KIO₃* were combined before the start of the experiment. The solutions were pumped to the mixers with a syringe pump (Cole Parmer 74900-35). Iodine formation was monitored offline with a UV-detector (Jasco UV-2075 Plus) at 352nm. If the time between experiment and measurement is long, the iodine formation cannot be strictly related to mixing performance [40], for this reason the time between experiments and measurement was always 2 minutes (which was the time to take enough sample for the lowest flowrate). This ensures that the results between samples could be compared, and also minimised the amount of iodine formation due to time delays. Deionised water was pumped to the UV-detector as a carrier fluid at 3 ml/min. A sample of 20 μ l was taken from the outlet of the reactor and injected with an HPLC valve to the deionised water stream. Absorption was recorded at 352nm as a function of time and the area under the chromatogram was used as the absorption value. High absorption values meant poor mixing characteristics, the inverse was taken so that high values were related to good mixing performance. An average of 5 measurements was used for repeatability.

Experimental residence time distributions were obtained as described in section 4.3 of chapter 4.

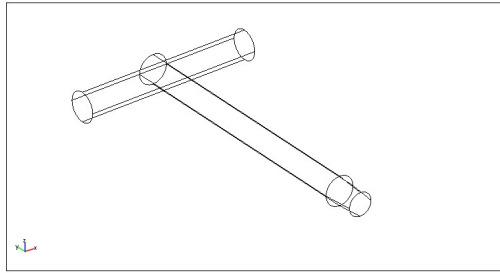
7.3 Theoretical Methodology

7.3.1 Numerical Procedure for Mixing and RTD Studies

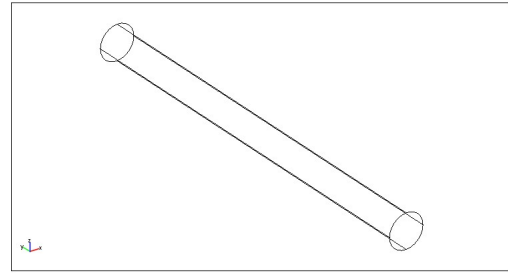
All the geometries described in section 7.2.1 have certain dimensions at the inlet part of the channel that then change for the rest of the channel. For this reason, two different computational domains were used for every geometry: one for the inlet and the other for the rest of the channel. Figure 7.3 shows the computational domains for the geometries described in section 7.2.1.

The Navier-Stokes equation and the continuity equation for the conservation of mass, are solved simultaneously with COMSOL Multiphysics 3.5 for the computational domains shown in figure 7.3. Figure 7.3a shows the computational domain for the inlet section of the capillary T-mixer with $400\mu m$ ID. This section comprises a volume of $2.9\ \mu l$ with a bore diameter of $500\mu m$. At the end of this section (after $500\mu m$), the diameter of the cylinder is reduced to $400\mu m$ to account for the transition from the mixing-tee to the main capillary. Figure 7.3b shows the computational domain used as the main channel for the capillary geometry (away from the inlet).

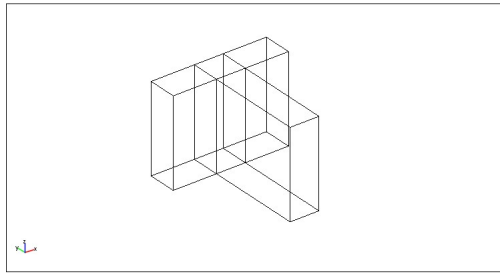
The computational domain for the silicon/glass T-mixer is shown in figure 7.3c and d. The computational domain is also split in two as in the capillary geometry. The first part (figure 7.3c) shows the T-junction whereas the second part (figure 7.3d) is the main channel where inlet effects have disappeared (vortex formation in the T-junction). The second geometry (main channel) for the silicon/glass T-mixer has two different dimensions; the original $100\mu m \times 300\mu m$ and after 2cm the geometry is changed to $600\mu m \times 300\mu m$. The reason for this is that this chip was originally designed to have a mixer section ($100\mu m \times 300\mu m$) and residence time section ($600 \times 300\mu m$).



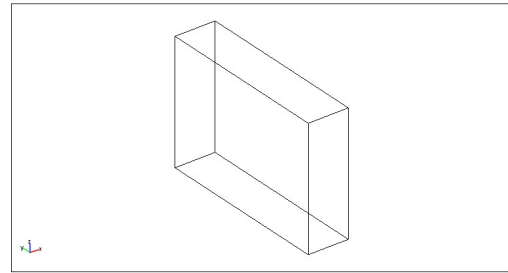
(a) Computational domain for the inlet section of the capillary T-mixer geometry.



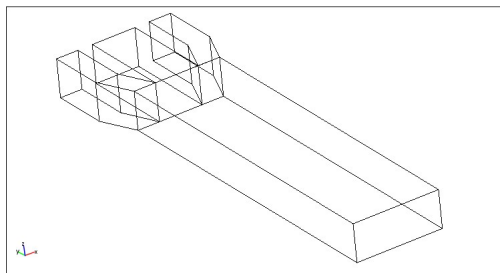
(b) Computational domain for the main channel section of the capillary T-mixer geometry.



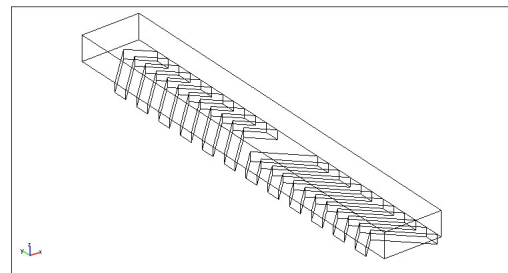
(c) Computational domain for the inlet section of the silicon/glass T-mixer geometry.



(d) Computational domain for the main channel section of the silicon/glass T-mixer geometry.



(e) Computational domain for the inlet section of the glass layered herringbone mixer geometry.



(f) Computational domain for the main channel section of the glass layered herringbone mixer geometry.

FIGURE 7.3: Computational domains of the geometries studied for mixing characterisation.

Finally, the computational domain for the layered herringbone channel is shown in figure 7.3e and f. The inlet section (figure 7.3e) shows the three inlets and the plain channel where no herringbones are present. Figure 7.3f shows the herringbone section of the channel which starts 7mm after the inlet. Note that due to symmetry and to reduce computational efforts, only half of the geometry has been simulated. A plane of symmetry can be defined at mid height of the herringbone grooves, and this way only one channel needs to be simulated. Note that for all computational domains only straight channels are simulated, bends have been ignored.

A fixed pressure was used as a boundary condition at the inlet and 0 Pa pressure for the outlet for all geometries. This boundary condition defines a parabolic profile at the inlets and outlets. In addition no-slip boundary conditions were applied to all walls. The simulations were run on Windows Vista with Pentium Dual-Core 3.00 G Hz CPU and 4GB of RAM. For all geometries the solution obtained was checked to be mesh independent. Particles trajectories are computed as described in chapter 3, sections 3.3.1 and 3.3.2.

4400 particles are distributed proportionally to the axial velocity at the channel inlet as described in chapter 4 section 4.2.1. The code is set so that the velocity field obtained for the computational domain of the main section (not the inlet section) could be used over many mixing cycles. Mixing simulations to compare the performance of the staggered herringbone (see chapter 3) and the layered herringbone micromixer were obtained by using only the convective part of the particle tracking code (first term in equation 3.2). This emphasizes the stirring effect of the herringbone grooves. This is valid in the limit of high Pe.

Mixing is evaluated with the nearest neighbour analysis described in chapter 3 section 3.4.2. Numerical residence time distributions are obtained with the procedure described in chapter 4 section 4.2.1.

7.4 Results and Discussion

7.4.1 Residence Time Distributions

The numerical and experimental RTDs for the glass layered herringbone channel are shown in figure 7.4. It was found that there was disagreement for the average residence time between experiments and modelling. The RTD for the layered herringbone microchannel is narrower compared to a rectangular channel of the same dimensions as demonstrated in figure 7.4.

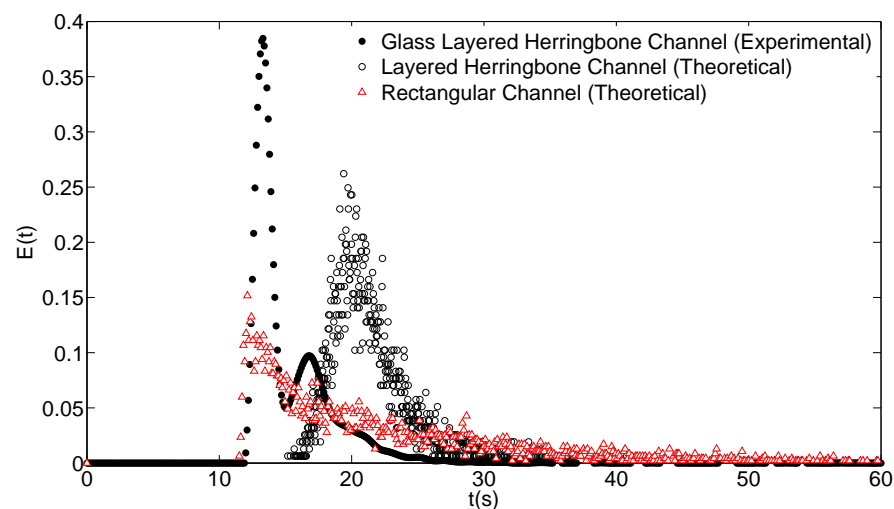


FIGURE 7.4: Experimental and numerical RTD for the glass layered herringbone configuration and comparison with a rectangular channel. $Pe = 10^4$, $Re = 10^1$

Flow maldistribution was thought to be partly responsible for the disagreement between the measured and calculated mean residence times. Confocal fluorescence microscopy was used to investigate this further. Acridine orange and water were pumped to the two inlets of the chip at equal flowrates. The stream of acridine orange splitted in two and entered as two streams on the sides of the channel, while water entered through the middle (see figure 7.3e).

Figure 7.5 shows two cross-sectional pictures, one at the entrance of the herringbone section, and the other after 1.5 cycles. The signal from the top channel is

captured clearly by the microscope. On the other hand, the signal from the bottom channel is weak, as if there was no dye. This was thought to be evidence of flow maldistribution. However, in a following experiment (not shown), the chip was completely filled with dye. In those experiments no signal could be obtained from the bottom channel (unless the chip was flipped over).

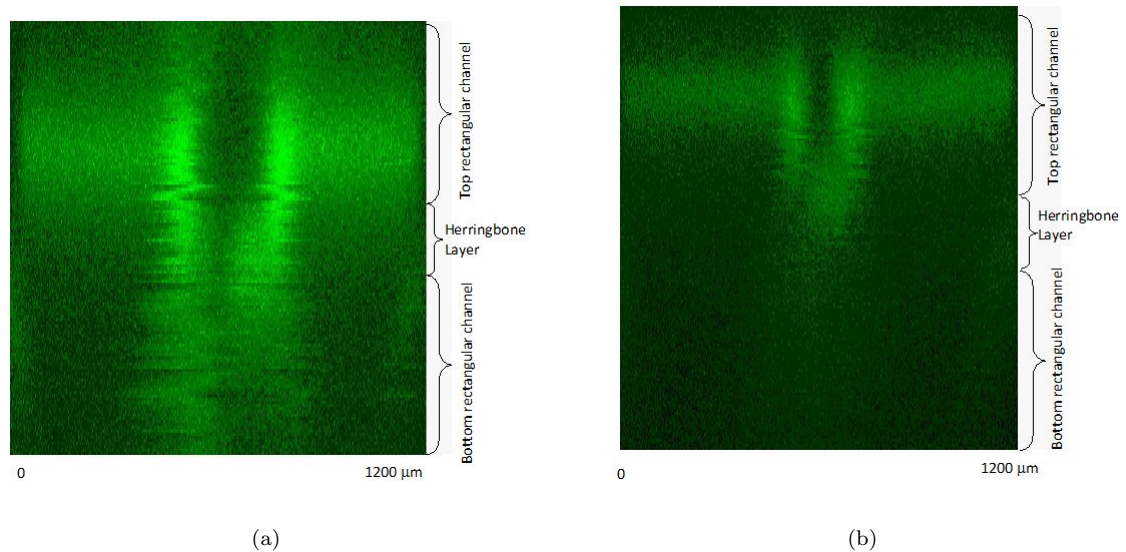


FIGURE 7.5: Cross-sectional picture obtained with confocal microscopy. a) Entrance of herringbone section, b) 1.5th cycle.

Figure 7.6 shows the normalised intensity profile as a function of channel depth for both the top and bottom channels. The laser of the confocal microscope scans from top to bottom. It can be argued that both channels have the same depth because absorption profiles are similar. This rules out the possibility of flow maldistribution due to manufacturing inaccuracies. There seems to be a problem with the quality of the confocal measurements, also evidenced by high fluorescence intensity at intermediate locations. It is believed that light scattering, possibly due to roughness, caused by the middle layer containing the herringbone structures, may be responsible for the poor signal received from the bottom channel.

In order to minimise flow maldistribution, the wall dividing the top and bottom channels (the herringbone layer where no herringbone structures are present) in

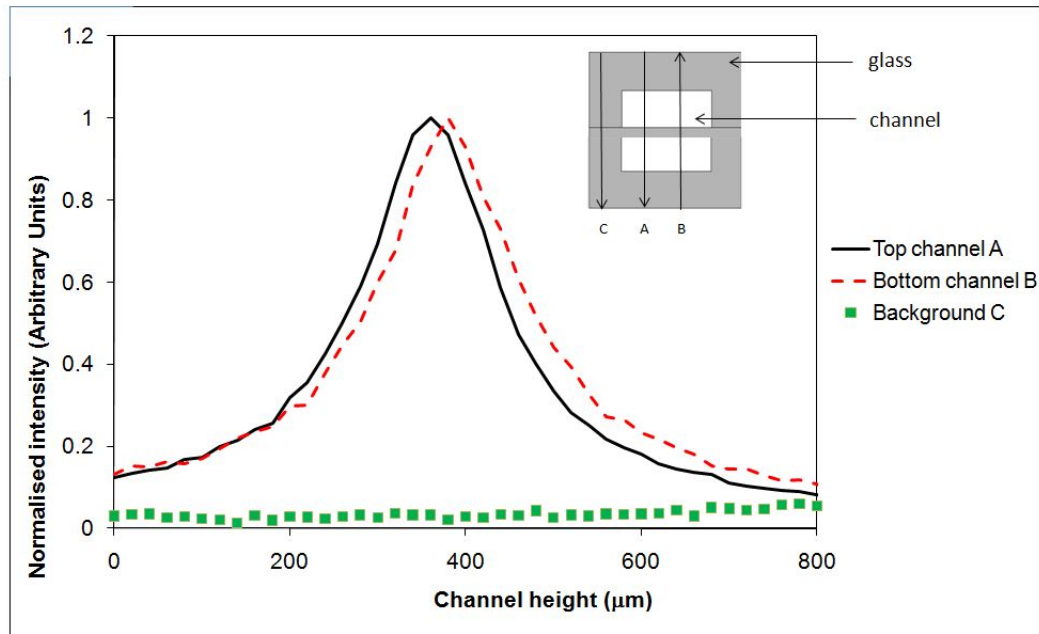


FIGURE 7.6: Normalised fluorescence intensity profiles as a function of channel depth for top and bottom channels.

the acrylic layered herringbone channel is removed so that there is direct communication between top and bottom channels. The experimental mean residence times obtained from the acrylic layered herringbone channel agree well with the ones calculated from particle tracking data indicating that there is no maldistribution (see table 7.2).

TABLE 7.2: Dimensions of the different geometries studied.

	FOTURAN	Acrylic	
	$Pe \approx 10^4$	$Pe \approx 10^4$	$Pe \approx 10^3$
τ_{hyd} (s)	21.0	30.78	307.8
t_{meap} (s)	15.28	25.91	300.16
t_{mtheo} (s)	21.33	31.78	307.30

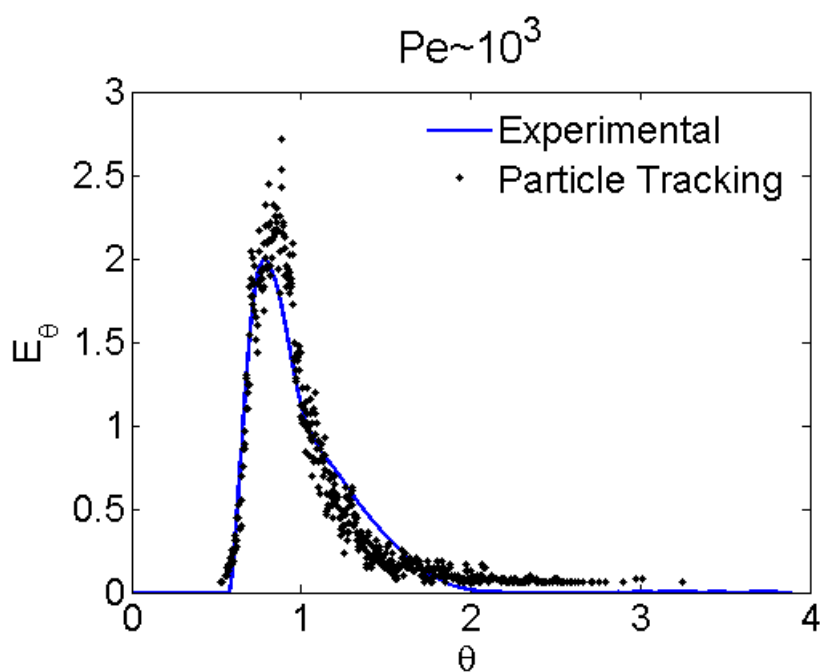
Two experiments with $Pe = 3 \times 10^3$ and $Pe = 3 \times 10^4$ ($Re=3.3$ and $Re=33.3$ respectively) were performed by changing the flowrate within the device. The mean residence times for both the glass and acrylic layered herringbone channel at high Peclet numbers are smaller than the expected hydraulic time. It was found by Williams et al. [162] that at Reynolds number higher than 30, recirculations within

the grooves appeared. This could explain the lower residence time observed experimentally for $Re=33.3$. Figure 7.7 shows the RTDs for the acrylic layered herringbone channel. It can be seen that experiments and simulations are in excellent agreement. We can also see that the RTD is not distorted when the flowrate is increased as would be expected for an unstructured rectangular channel. This results has been pointed out by Cantu-Perez et al. [26] where it was found that for a staggered herringbone channel, increasing the flowrate (increasing Pe) did not have a great impact on the RTD.

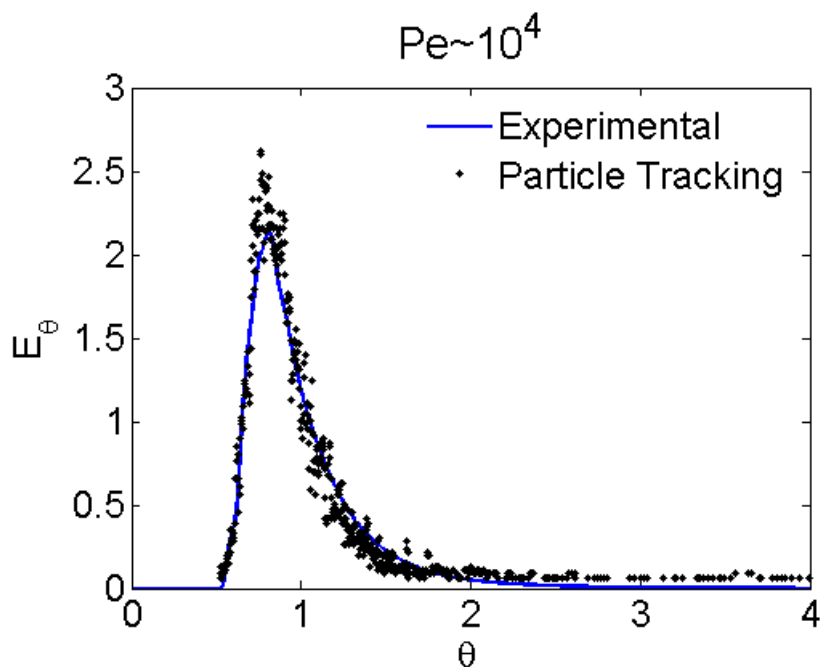
7.4.2 Mixing

Mixing simulations for the layered herringbone channel have been performed to identify differences against the staggered herringbone channel. In these simulations, in order to highlight the stirring effect of the grooves, the inlet section of the mixer was omitted (figure 7.3e), and only the geometry with herringbone structures was considered. For the layered herringbone channel the full geometry was simulated (with no symmetry plane), so that the effect of having grooves with no floor could be studied. Figure 7.8 shows the distributions of the tracer particles over the cross-section of the channel for the SHM and the layered configuration after 5 herringbone cycles for a mixing ratio 1:1 with the inlets side by side. The effect of diffusion was not considered in this simulation.

The layered herringbone channel gives qualitatively similar mixing results to the standard herringbone mixer (SHM) see (figure 7.8). After 5 cycles the herringbone structures for both geometries were able to transport fluid from the right side of the channel to the left. A high concentration of particles near the channel centre is seen, indicating poor mixing characteristics in this zone. This is consistent with the stretching calculations shown in chapter 3 section 3.5.4 where it was shown that regions of low stretching (bad micromixing) were found near the centre



(a)



(b)

FIGURE 7.7: Residence time distribution comparison between experiments and particle tracking for the acrylic layered herringbone channel. a) $Pe = 3 \times 10^3$ b) $Pe = 3 \times 10^4$. Flowrates were 2 and 0.2 ml/min. The diffusion coefficient of the dye used was $1.3 \times 10^{-9} m^2/s$

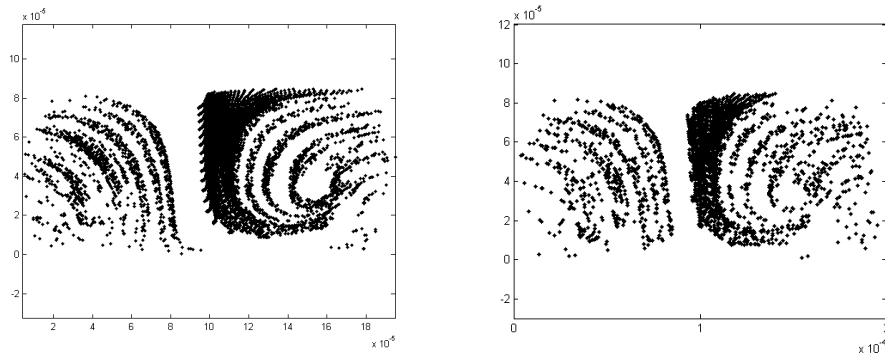


FIGURE 7.8: Cross-sectional particle distribution profiles after 5 cycles for the layered herringbone (left) and the floor herringbone structure (right)

of the channel. It is also seen that the layered herringbone geometry gives a slightly better performance than the herringbone channel indicated by the reduced distance between the fluid layers.

Figure 7.9 shows the calculation of percentage of mixing as function of number of cycles via the nearest neighbour analysis as described in Chapter 3 section 3.4.2. The layered herringbone microchannels give a higher %mixing than the standard SHM. This is due to the absence of the groove floor which eliminates the no-slip boundary condition, increasing the flowrate within the grooves.

Figure 7.10 shows the velocity in the z coordinate (vertical axis) at the top channel/groove interface. Negative values indicate fluid going into the groove and positive ones fluid coming out of the groove. The figure shows that the layered herringbone configuration has a larger area with negative values (at the groove apex) with similar absolute numbers as the SHM. Furthermore, the regions of positive velocity for the layered herringbone are closer to the channel wall and are higher in magnitude than the ones for the SHM. This indicates that the layered herringbone induces stronger transverse movement than the SHM.

Confocal mixing experiments were done to evaluate the mixing quality of the layered herringbone channel. It was shown in section 7.4.1 that the confocal microscope was unable to get signal from both top and bottom channels. If only

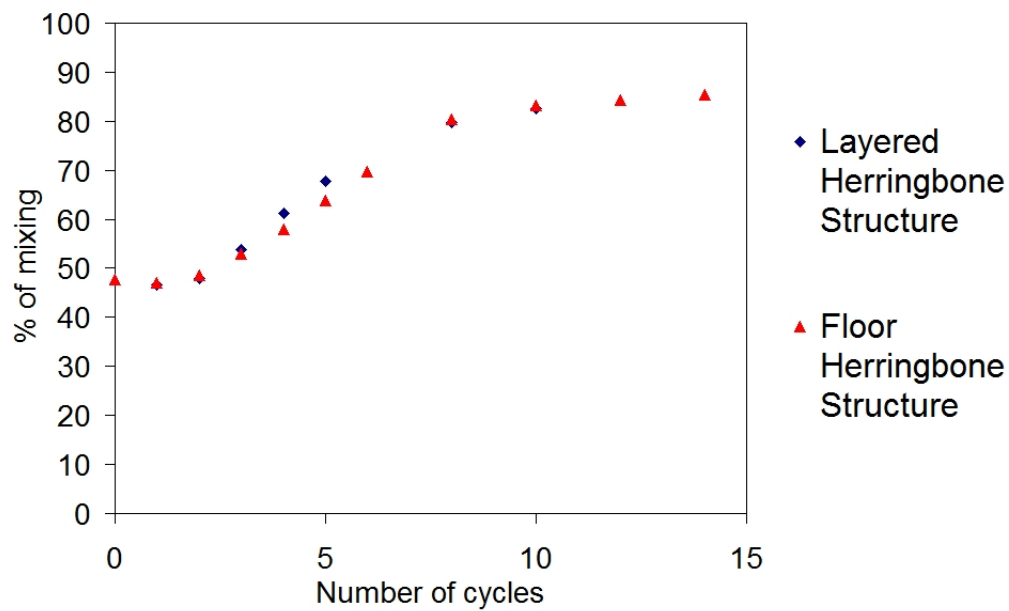


FIGURE 7.9: Percentage of mixing calculated via the nearest neighbour analysis

the top channel is considered, the experimental mixing graphs can be compared to the ones obtained via numerical simulations and particle tracking. Most of the mixing investigations in microchannels have considered a 1:1 ratio with the inlets flowing side by side. It was shown in chapter 3 that for the staggered herringbone channel, putting one of the inlets in the middle results in lower mixing lengths. In this study both experiments and model were carried out with one of the fluids in the centre of the channel. Figure 7.11 shows the comparison between experimental and numerical mixing results.

The experimental mixing graphs and the theoretical results are in reasonable agreement. On both the experiments and simulations, the dye (or particles) originally placed in the centre of the channel is being transported to the sides. Also the thickness of the dye stream in the centre is reduced as it flows through the channel. Numerical simulations seem to slightly underpredict the stirring behaviour of the herringbone structures. This is evidenced by the thickness of the fluid layer in the middle. After 1.5 and 3 cycles the thickness of the fluid layer in the experiments is smaller than in the simulations. This numerical underprediction of the

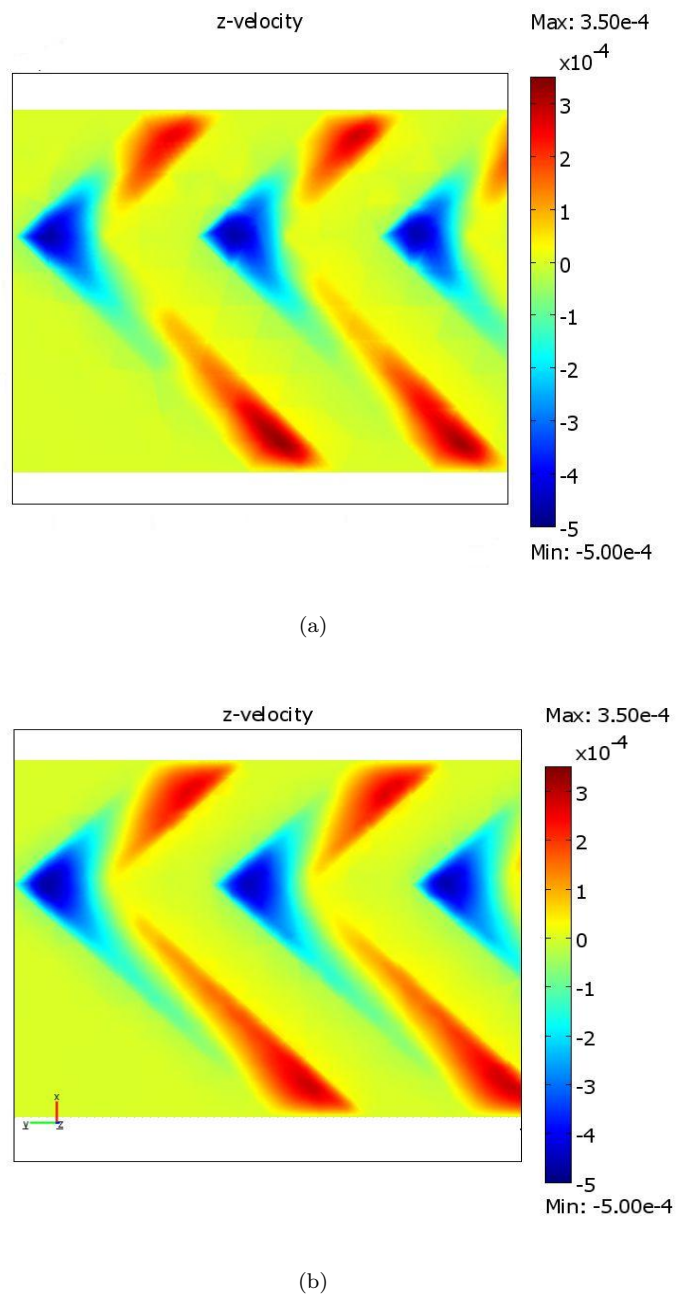


FIGURE 7.10: Vertical z-velocity at the top channel/groove interface (x-y plane) for the layered (a) and floor (b) herringbone configuration.

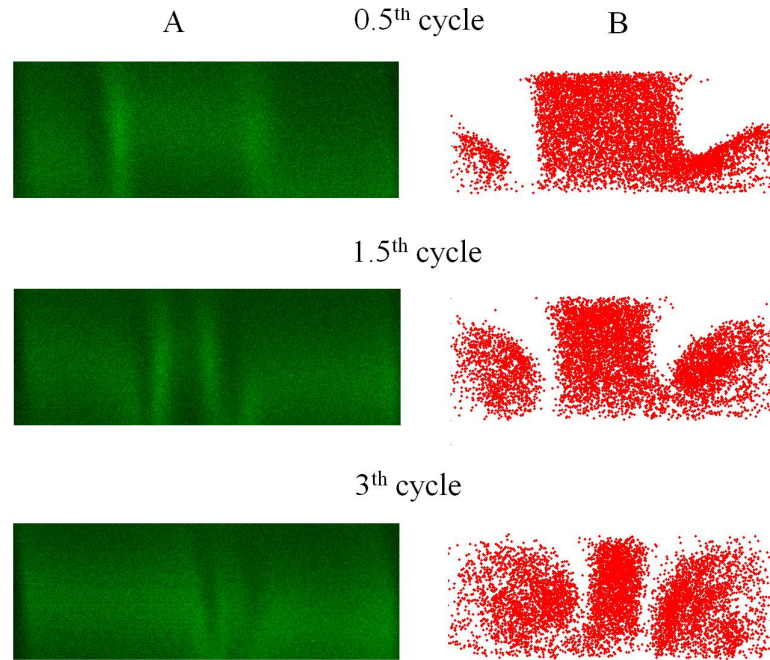


FIGURE 7.11: a) Experimental cross-sectional mixing pictures obtained by confocal microscopy at three different lengths. b) Simulated mixing pictures at three different lengths. $Pe = 10^4$

stirring capabilities of the herringbone structures were also found for the staggered herringbone micromixer in Kee and Gavriilidis [74].

The mixing capabilities of the layered herringbone channel are further shown in figure 7.12. Before the herringbone structures, the dye originally placed on the sides of the channels remain there. However after the first half cycle, it is seen that the dye streams that were originally at the sides of the channel are now closer to each other, reducing diffusion distance and improving mixing.

Mixing simulations were performed for the layered herringbone channel and compared with the capillary T-mixer and the silicon/glass T-mixer as described in section 7.3.1. In order to verify the computational procedure, the results from Engler et al. [42] were reproduced. The mixing characteristics of a $600 \mu\text{m} \times 300 \mu\text{m}$ (width x height) T-mixer have been studied for different Reynolds numbers. Three different regimes can be identified as shown on figure 7.13. The results are in qualitative agreement with the ones shown by Engler et al. [42]. At low Reynolds

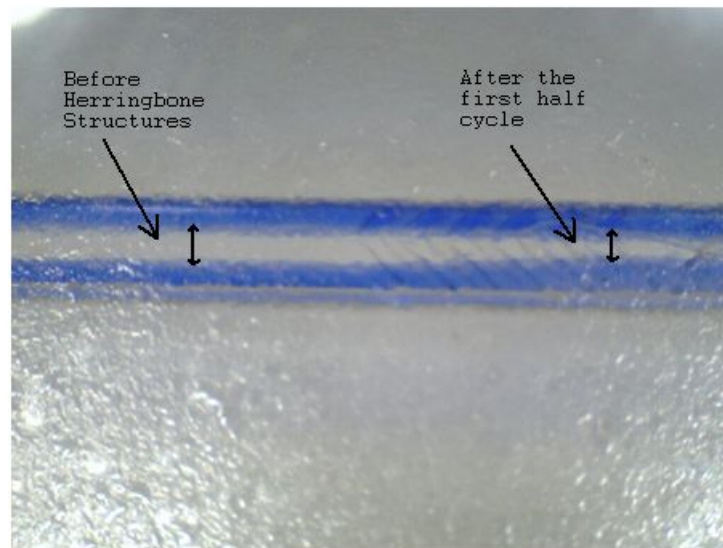
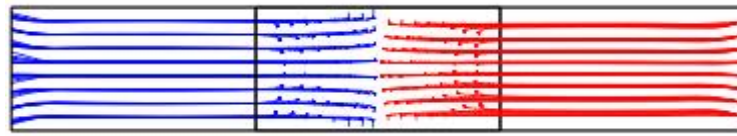


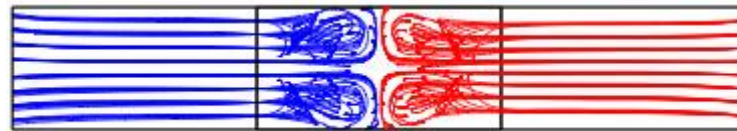
FIGURE 7.12: A) Experimental mixing pictures for the glass layered herringbone channel obtained by microscopy. The picture is seen from the top of the reactor. $Pe = 10^4$

numbers ($Re=7$) the streamlines meet at the T-junction and they flow parallel to each other without bending; this is called the stratified regime. At intermediate Reynolds ($Re=70$) the vortex flow regime is present. Vortices are generated and fluids rotate but without crossing of streamlines to the opposite wall. At higher Reynolds numbers ($Re=200$) the streamlines no longer meet at the T-junction. They cross to the other side of the channel improving mixing efficiency. This is called the engulfment regime. All the experimental conditions considered here fall under the stratified flow regime.

The comparison between mixing simulations and experimental values obtained via the Villermoux-Dushman reaction are not straightforward. Since the quality of mixing measured depends on the amount of iodine formed, and this in turn depends on how good the mixing is within the first seconds (due to the high reaction rate), it seems more appropriate to compare the mixing quality of all geometries at a certain residence time, rather than length. The residence time selected must be related to the reaction time. Guichardon et al. [55] showed that the kinetics for reaction (ii) shown in section 7.2.2 follow fifth order kinetics. If



(a) Stratified flow Re=7



(b) Vortex flow Re=70



(c) Engulfment flow Re=200

FIGURE 7.13: Streamlines inside a $600 \times 300 \mu\text{m}$ (width x height T-mixer) for different Reynolds numbers. In the centre of each figure is the main channel and left and right are the inlets.

the mass balance for the Iodate ion (IO_3^-) is combined with the reaction rate, and the concentration of (H^+) is considered to be in excess, the reaction time would change with conversion of (IO_3^-) according to the following equation (see appendix E for derivation):

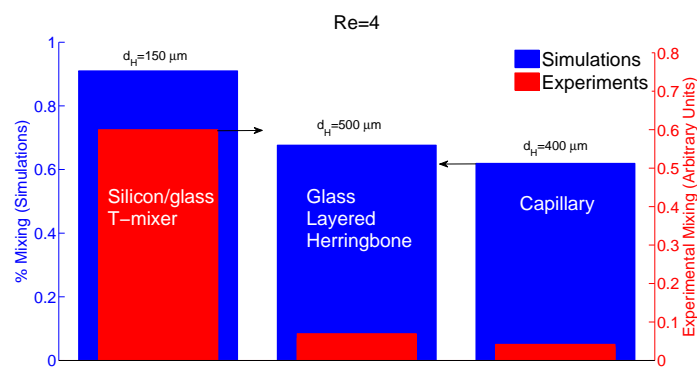
$$t \propto C_1 \left[\frac{1 - (1 - X)^4}{(1 - X)^4} \right] \quad (7.1)$$

where C_1 is constant including the reaction constant and initial concentration for IO_3^- and H^+ . The reaction time to achieve 50% conversion is 6ms and for 90% is 4.9s. 550ms has been selected as the residence time for the theoretical comparison

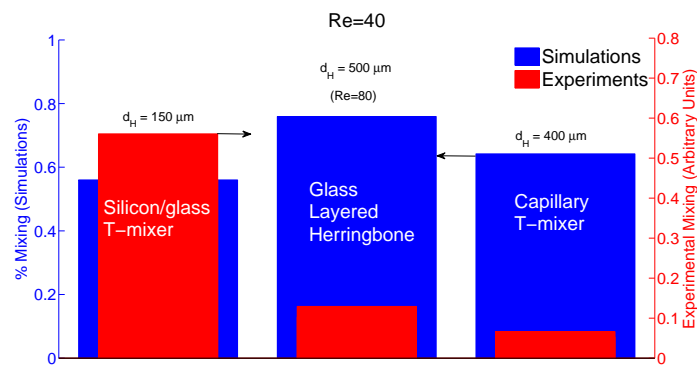
of the different mixers. This residence time ensures that over 80% of the initial reactant has been converted into product. In addition tracking the particles for a longer time would be computationally intensive.

Figure 7.14 shows the UV-vis absorption values and the numerically obtained percentage of mixing for the different geometries considered for two Reynolds numbers. The low Reynolds number is 4 for all geometries (hydraulic diameter is used as the characteristic dimension) and the high is 40 for both T-mixer (silicon/glass and PEEK tee) and 80 for the layered herringbone. For low Reynolds numbers it can be seen that the best mixer is the T-mixer with $d_H = 150\mu m$, followed by the layered herringbone and the PEEK mixing Tee. Both mixing and simulations rank the geometries in that order (T-mixer/layered herringbone/PEEK mixing Tee) as can be seen in figure 7.14a. The main difference is that the experimental results show that the T-mixer has a much stronger performance than the other two, whereas the simulations only show a slight difference. This discrepancy may be attributed to the fact mentioned earlier about the difficulty of analyzing theoretically the quality of mixing via the Villermaux-Dushman reaction.

For high Reynolds numbers there is a discrepancy between experiments and simulations. While experimentally the ranking was the same as for low Re (silicon/glass T-mixer/glass layered/capillary T-mixer), simulations showed that the T-mixer had the worst performance (see figure 7.14b). It is seen from the simulations results that the mixing characteristics of the T-mixer were worsened with an increase in Re. This is expected because when the flowrate is increased, the time spent in the $600 \times 300 \mu m$ region will increase relative to the time spent in the $100 \times 300 \mu m$ region. Note that this is due to constant residence time used in the calculations. Although experimentally, this behaviour was also seen, it was very subtle. For the capillary and the layered herringbone channel, increasing the Reynolds number actually results in an increase in mixing efficiency (contrary to what would be expected). The reason for this, is that for both cases the inlet part



(a)



(b)

FIGURE 7.14: Mixing quality for the different geometries evaluated experimentally via the Villiermaux-Dushman reaction. Theoretical mixing evaluation was done with particle tracking methods and the nearest neighbour analysis at a fixed residence time of 550ms.

of the device has the worst mixing characteristics. On the PEEK mixing tee the diameter of the tee is $500\mu\text{m}$ whereas the capillary attached to it is $400\mu\text{m}$. On the layered herringbone channel, there are no herringbone structures on the first 7mm of length, so the mixing characteristics on this part of the device are quite poor. By increasing the Reynolds number (increasing flowrate), the time spent on the zone of poor mixing characteristics is reduced with a consequent reduction in Iodine formation.

7.5 Conclusions

A layered herringbone channel was analysed in terms of mixing and residence time distributions. The residence time distribution for the layered structure was calculated both numerically and experimentally and it was found to be narrower as compared to a rectangular channel. Transverse velocity components that homogenise the flow are responsible for the improved behaviour. In addition the layered herringbone channel was compared to a one with herringbone placed on the microchannel floor. It was found that both geometries had similar stirring capabilities. Mixing for the layered herringbone channel was compared with a $100\mu\text{m}$ silicon/glass T-mixer and a $500\mu\text{m}$ PEEK mixing tee with $400\mu\text{m}$ with capillaries attached to it, both theoretically and experimentally. Experimentally the T-mixer was found to have the best mixing characteristics, followed by the layered herringbone and the capillary tube. Although the layered herringbone channel showed very strong stirring capabilities, the mixing performance was hindered by the fact that the first part of the mixer did not have any herringbone structures. The use of a layered configuration provides the opportunity of having two channels with improved transverse mixing characteristics with a single set of herringbones. This may reduce the microfabrication costs and opens the possibility for new applications where the middle layer can be used both to improve mixing in the bulk, and as a contact area between two different flows.

Chapter 8

Hydrodynamics and Reaction Studies in a Layered Herringbone Channel

8.1 Introduction

In this chapter, layered herringbone channels which give rise to chaotic flow, improved mixing and narrower RTDs than channels subject to laminar flow are investigated. The amount of intermediate is measured experimentally for a reaction of the type $A \xrightarrow{k_1} B \xrightarrow{k_2} C$. The results are compared with a rectangular channel of similar dimensions. The effect of residence time distributions on the product mixture is evaluated. The theoretical conversion for this reaction is also calculated using the reaction kinetics (first order) and the residence time distributions obtained via CFD calculations and particle tracking methods. For other reaction orders it is not possible to calculate conversion exclusively from the kinetics and the RTDs; however, upper and lower bounds can be obtained with the assumption of a contacting model [45]. The RTDs for the layered herringbone channel are

fitted to an axial dispersion model exchanging mass with a dead volume (ADEM model). The parameters of the model are also calculated exclusively from hydrodynamic data obtained from the CFD calculations and from turbulent theory. This procedure would eliminate the need of particle tracking calculations which require high computational time.

8.2 Experimental Methodology

8.2.1 Description of Reactors

The layered herringbone geometry considered in this chapter is the same as the one studied in chapter 7 shown in figure 7.1a and c, while its dimensions are shown in table 8.1.

TABLE 8.1: Dimensions of the different geometries studied.

	Layered channel	Herringbone	Rectangular Channel
Width (w)	4mm		4mm
Height (h)	1mm		2mm
Groove width (g_w)	700 μ m		-
Groove depth (g_d)	1mm		-
Ridge width (r_w)	1.3mm		-
Angle (θ)	45 \angle		-
Volume	2.9 ml		2.6 ml

8.2.2 Description of Model Reaction

The conversion for first order reaction systems can be predicted by knowing only the reaction constants and the residence time distribution. The successive reaction of epinephrine in alkaline solution with dissolved oxygen can be described as [24]:



where EP is epinephrine ($C_9H_{13}NO_3$), THI (trihydroxyindole) ($C_8H_7NO_3$) is a fluorescent intermediate and the final product is the oxidized form of THI which does not show fluorescence. For the experimental reaction studies, a stock solution 0.01M epinephrine hydrochloride was prepared from epinephrine hydrochloride standard and 0.01M HCl (Sigma-Aldrich). The stock solution was kept in a refrigerator, and solutions for the experiments were prepared by dilution. A concentration of 1×10^{-4} M (obtained by diluting the stock solution with deionised water) was found suitable in order to obtain a strong fluorescence signal at small residence times (of the order of minutes). The maximum excitation and emission wave length was found to be 410 and 510nm respectively [24]. Excitation was done with a 405nm fibre coupled with a LED light source (LLS-405, Sandhouse Design). An in-house built fluorescence detector is used for the measurement of the concentration of the intermediate. The fluorescence signal was detected using a TAOS TSL250R (Farnell, UK) light to voltage sensor. The voltage was acquired using a National Instruments PCI-6010 card and the data displayed and collected using a program written in Labview.

The kinetics of the reaction were experimentally obtained by monitoring the fluorescence intensity of the intermediate as a function of time in a 1cm diameter glass cylinder batch reactor. 1 ml of both epinephrine and sodium hydroxide were taken from stock solutions with 1 ml plastic syringes and were placed in the batch reactor. The reactor was agitated for 10 seconds to ensure complete mixing of the reactants. If *THI* is the intermediate, then the concentration of *THI* as a function of time can be described by [88]:

$$C_{THI} = C_{EP}^0 \frac{k_1}{k_2 - k_1} (e^{-k_1 t} - e^{-k_2 t}) \quad (8.2)$$

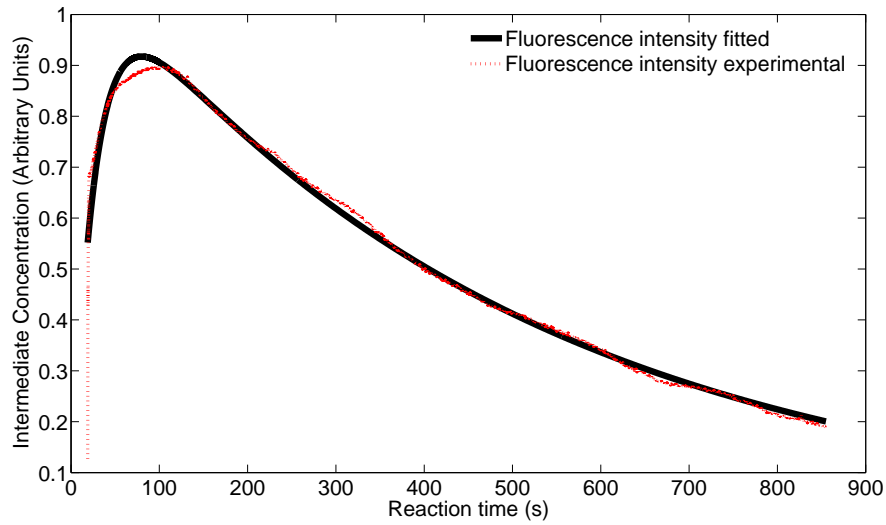


FIGURE 8.1: Experimental and fitted fluorescence kinetic curves for the reaction of epinephrine in NaOH 1M.

If the concentration C_{THI} is replaced by the intensity of the fluorescence signal (S_{THI}), the reaction constants k_1 and k_2 along with C_{EP}^0 can be obtained with the *fminsearch* function in MATLAB. Figure 8.1 shows the experimental kinetic curve along with the fitted one obtained with equation (8.2). The reaction constants were found to be $k_1 = 0.03913s^{-1}$, $k_2 = 0.00203s^{-1}$.

8.3 Theoretical Methodology

8.3.1 Theoretical Approach for RTD Calculations

Two different theoretical approaches were employed for the calculation of the RTD. The first one is completely numerical, relying on the solution of the Navier-Stokes equations and a particle tracking algorithm. The second one is based on a hydrodynamic model with adjustable parameters. The model parameters can be obtained by fitting them from an RTD calculated via particle tracking methods

or exclusively from hydrodynamic data (velocities) obtained from the solutions of the Navier-Stokes and continuity equations

8.3.1.1 Numerical Particle Tracking Method

The Navier-Stokes and the continuity equations, are solved simultaneously with the fluid dynamics module in COMSOL Multiphysics 3.5 for the layered herringbone and rectangular channel with the dimensions shown in table 8.1. A mesh consisting of 44,631 number of elements and 183,046 degrees of freedom is used to execute the simulations in Windows XP with Pentium IV 3.00 GHz CPU and 2 GB of RAM. At this number of elements the solution was found to be mesh independent. The solution is exported to MATLAB and a particle tracking algorithm with a random walk type diffusion step is used to obtain the positions of the particles details of this numerical procedure can be found in chapter 3, sections 3.3.1 and 3.3.2.

The fluid properties of water were used for all simulations with density $\rho = 1000\text{kg}/\text{m}^3$ and viscosity $\mu = 0.001\text{Pa}\cdot\text{s}$. For RTD calculations, 4400 particles are distributed proportionally to the axial velocity at the channel inlet as described in chapter 4 section 4.2.1. RTDs are obtained by analysing the numerical data as described in chapter 4, sections 4.2.1 and 4.3.2. Note that in some of the equations the experimental light intensity ($I(t)$) must be replaced by the number of particles arriving at the channel exit at time t_i .

In addition the Axial Dispersion Exchanging mass with a dead zone model (ADEM) described in chapter 4 section 4.2.2 is used to fit the numerical RTDs.

8.3.1.2 ADEM Model Parameters from Hydrodynamic Data

In chapter 4 it was shown that the residence time distribution for a staggered herringbone channel can be fitted to a model of axial dispersion exchanging mass with a stagnant zone (ADEM). The model has three parameters that need to be calculated, the fraction of volume subject to axial dispersion f , the axial dispersion coefficient D_{ax} and the mass transfer coefficient between the flowing volume and the dead zone K . As shown by Cantu-Perez et al. [26], the parameter $(1 - f)$ can be approximated by the volume fraction occupied by the grooves. From a mass balance within the groove one obtains:

$$\underbrace{Av_g C}_{\text{mass in}} - \underbrace{Av_g C^*}_{\text{mass out}} = \frac{\partial VC^*}{\partial t} \quad (8.3)$$

$$Av_g (C - C^*) = V \frac{\partial C^*}{\partial t} \quad (8.4)$$

$$Av_g (C - C^*) = Ag_d \frac{\partial C^*}{\partial t} \quad (8.5)$$

$$\frac{v_g}{g_d} (C - C^*) = \frac{\partial C^*}{\partial t} \quad (8.6)$$

where A is the open area of the groove parallel to the channel (y) axis, V is the total volume of the groove, v_g is the average vertical velocity inside the groove, and g_d is the groove depth. From (8.6), the mass transfer coefficient K can be obtained as $\frac{v_g}{g_d}$. In order to compare the mass transfer coefficient obtained from hydrodynamic data, with the one obtained from the solution of equations (4.4), (4.5), the value $\frac{v_g}{g_d}$ needs to be multiplied by $(1 - f)$. Note that in order for equation (8.6) to be equivalent to equation (4.5) both sides of the equation need to be multiplied by $(1 - f)$. Therefore the value of K obtained from equation (4.5) is equal to $(1 - f) \frac{v_g}{g_d}$.

The axial dispersion coefficient can be obtained with the expression suggested by Dutta et al. [39] for a rectangular channel with arbitrary aspect ratio:

$$D_{ax} = D + \frac{h^2 U_m^2}{210D} g \quad (8.7)$$

where D is the molecular diffusion, h is the channel height, U_m is the mean axial velocity and g is a number depending on the aspect ratio of the channel (5 for this case). In order to use equation (8.7) for the layered herringbone channel, D must be replaced by an effective diffusion coefficient that includes the stirring effect caused by the grooves. In the section 8.3.2 a procedure to obtain an effective diffusion coefficient based on Taylor's turbulent theory is presented [147].

8.3.2 Calculation of D_{eff} with Turbulent Theory

The procedure to calculate the eddy diffusivity value described in chapter 6 section 6.4.1 is used here to replace the effect of the herringbone structures with a D_{eff} averaged over width and height of the main channel and obtain an axial dispersion coefficient by replacing D with D_{eff} in equation 8.7.

The convective flow that the herringbone structure induces in the vertical direction, can be described in a similar fashion as the transport of eddies in turbulent flow. Thus, an overall eddy diffusivity coefficient for one cycle of the layered herringbone structure can be obtained by calculating the integral in equation (6.9) and multiplying by the average velocity as shown in equation (6.11). First the Navier-Stokes and continuity equations are solved in Comsol Multiphysics 3.5 as described in chapter 3 section 3.3.1 for the geometry shown in figure ??a (1 cycle). The solution is exported to Matlab where a code gets a value of the velocity in the

vertical direction ($\overline{u_z}$) averaged over the width. Rather than calculating an arithmetic average of the vertical velocity over the width, a weighted average according to the axial velocity is calculated (an analog of the mixing cup concentration).

$$\overline{u_z} = \frac{\int_0^Y \int_0^X u_z u_y(x, y, z) dx dy}{\int_0^Y \int_0^X u_y(x, y, z) dx dy} \quad (8.8)$$

where u_y is the axial velocity as a function of width and height, X and Y are the channel width and the cycle length respectively. This procedure is used to replace the effect of the herringbone structures with a D_{eff} averaged over width and height of the main channel and obtain an axial dispersion coefficient with equation (8.7) by replacing D with D_{eff} .

8.3.3 Theoretical Calculation of Reaction Yields

Since the absorbance values obtained from the experiments are related to the concentration by an unknown multiplier, one needs a way of converting these values to meaningful concentrations so that comparisons can be done between different reactors and operating conditions. First the theoretical intermediate concentration for the given calculations is calculated. Once a profile of the concentration as a function of mean residence time is obtained, the maximum experimental concentration value is assumed to be the same as the equivalent theoretical concentration value at that particular residence time. The remaining experimental values are then rescaled accordingly so that they all have values in the same range as the theoretical ones.

The theoretical concentration is obtained in two different ways. If the reactants are assumed to be premixed then the concentration can be calculated as:

$$\overline{C_{THI}} = \int_0^{\infty} C_{THI}(t)E(t)dt \quad (8.9)$$

where $\overline{C_{THI}}$ is the mean concentration of intermediate and $x(t)$ is the yield of THI at time t . For this particular reaction C_{THI} is calculated with equation (8.2). The reaction constants used are the ones obtained from the curve fitting in figure 8.1. The RTDs were obtained from particle tracking data as described in section 8.3.1.1.

Both reactors also considered the case when the reactants were unmixed at the inlet. The theoretical concentration for this particular case required the solution of the convection-diffusion-reaction equations in Comsol Multiphysics 3.5. The Navier-Stokes and continuity equations are solved as described in section 8.3.1.1. Three convection-diffusion-reaction modules are added to the geometry. The three concentrations solved for represent epinephrine, THI and NaOH. The velocities obtained from the solution of the Navier-Stokes and continuity equations are used as input to these modules. Zero flux boundary conditions are applied to all walls. At the channel inlet, initial concentration for epinephrine and sodium hydroxide are implemented. The experimental reactor has three inlets, the middle one is where the epinephrine is fed, the other two are fed with sodium hydroxide. This is implemented in Comsol by having an initial concentration as a function of channel width. The simulated geometry is as the experimental reactor, 4mm width and 2mm height. To ensure that the simulation could be solved in Windows XP with Pentium IV 3.00 GHz CPU and 2GB RAM computer, the length of the simulated reactor was 2.8cm. To obtain results for greater lengths more geometries were added to the simulation. Instead of having an initial concentration at the channel inlet as described earlier, the outlet concentration of the previous geometry is used as the inlet for the next one. The properties used for the simulations were density=1000 kg/m³ viscosity=0.001 Pa.s, all diffusion coefficients were 1x10⁻⁹.

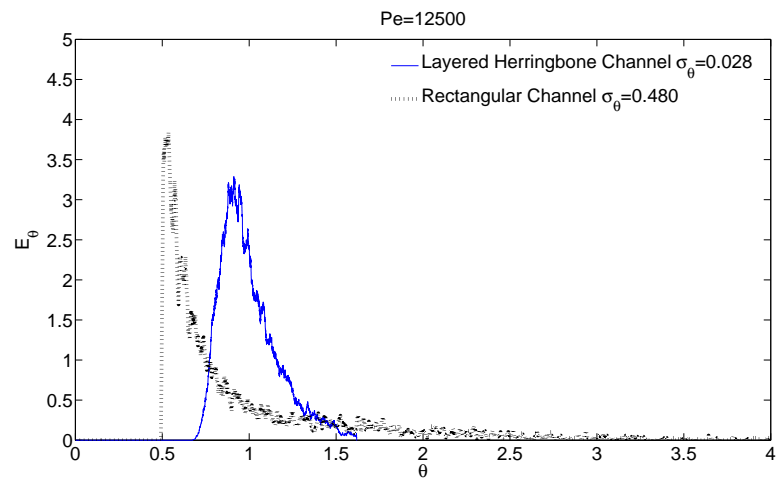
8.4 Results and Discussion

8.4.1 Residence Time Distributions

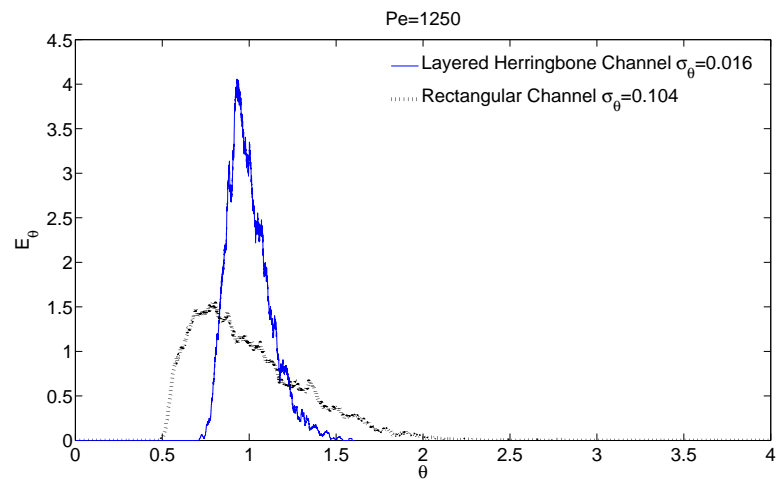
In previous work [26], we have validated the particle tracking algorithm against analytical solutions and experimental data. The numerical RTDs for the layered herringbone and the rectangular channel are shown in figure 8.2 for two Peclet numbers ($Pe = \frac{ud}{D}$) where d is the characteristic dimension of the channel, in this case the channel width was used. It can be seen that the RTD for the layered herringbone microchannel is narrower compared to a rectangular channel of similar dimensions. At high Peclet numbers convection dominates over diffusion and the differences in the RTDs are large. This is evident from the calculated variances. At $Pe=1250$, the variance for the rectangular channel is around 17 times bigger than the one for the the layered herringbone. However at lower Pe , mass transfer by diffusion becomes important and the differences in the RTDs between the rectangular channel and the layered herringbone one are smaller. The variance for the rectangular channel in this case is about 6 times that of the layered herringbone channel. This result was also found for a staggered herringbone channel [26]. Note also that the RTD for a layered herringbone channel does not change much with Pe . It has been shown that when secondary flows are present, the RTD remains independent of Pe [26, 154]

8.4.2 Theoretical and Experimental Reactor Performance for a Consecutive Reaction

The experimental results for the production of THI as a function of hydraulic residence time ($\frac{V}{Q}$) for both geometries are shown in figure 8.3. The maximum concentration of intermediate for the rectangular channel occurs at longer mean



(a)



(b)

FIGURE 8.2: Dimensionless RTD for a layered herringbone and a rectangular channel for two different Peclet numbers a) $Pe=12500$, $Re=12.5$ b) $Pe=1250$, $Re=1.25$. The dimensions of the simulated channels are shown in table 8.1

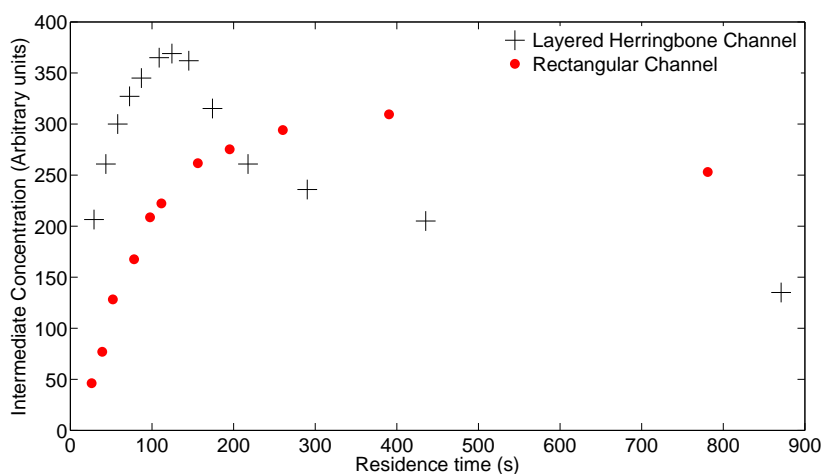


FIGURE 8.3: Experimental concentration of the intermediate in a consecutive reaction for a layered herringbone and a rectangular channel reactor.

residence times (approx 400s) than for the layered herringbone channel (approx 100s). It is also seen that the maximum amount of intermediate formed was higher for the layered herringbone channel than for the rectangular one. Note however, that the intermediate concentrations are shown in arbitrary units and in order to have a better comparison one needs to rescale these values. In section 8.3.3 a procedure to rescale the experimental concentration values using theoretical concentrations was presented. For the case when reactants are unmixed at the inlet, the full convection-diffusion-reaction simulations are used for the rescaling of the experimental values. For theoretical calculations, when the reactants are premixed, equation (8.8) is used with RTDs obtained from particle tracking.

Figure 8.4 shows the rescaled experimental concentrations as a function of mean residence time. It can be seen that the maximum intermediate concentration is higher (about 40%) for the layered herringbone channel than for the rectangular channel. Once the maximum is obtained, the decrease in the intermediate concentration is sharper for the layered herringbone than for the rectangular channel. In addition the maximum concentration is achieved at lower residence times than the rectangular channel. This results indicates that the reactor volume needed to

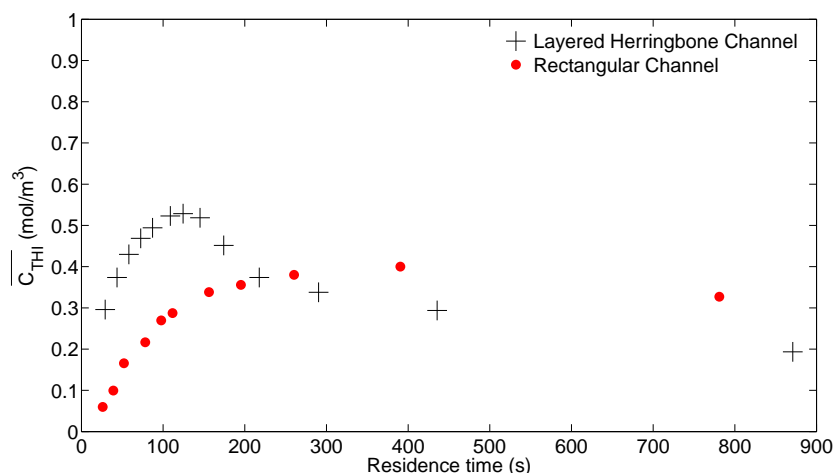
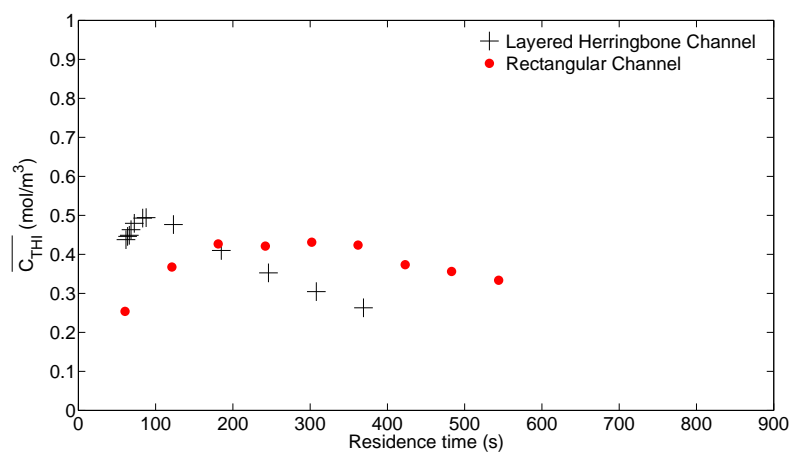


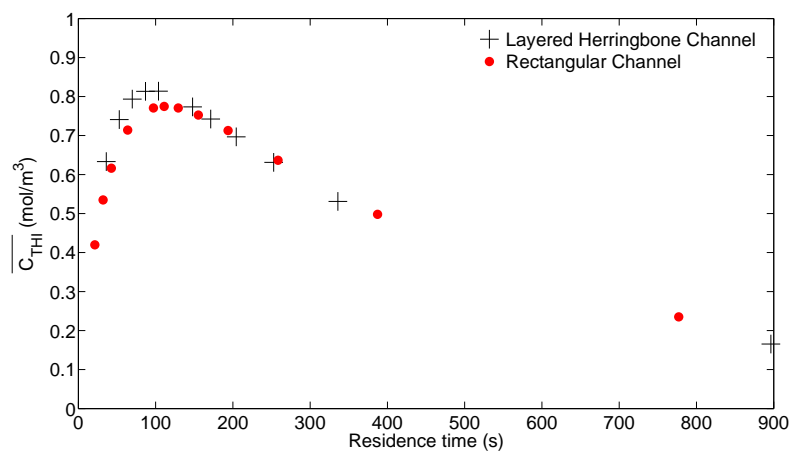
FIGURE 8.4: Rescaled experimental concentration of the intermediate in a consecutive reaction for a layered herringbone and a rectangular channel reactor.

maximise the intermediate is lower for the layered herringbone configuration.

Figure 8.5 shows the theoretical intermediate concentration for reactants unmixed and premixed at the channel inlet. For the case with reactants unmixed (figure 8.5a) the layered herringbone shows a higher maximum concentration of intermediate than the rectangular channel and it is also obtained at earlier times as also shown in the experimental graphs figures 8.3 and 8.4. When the reactants are premixed (figure 8.5b), the differences in the reactors are more subtle. The layered herringbone channel shows only a slightly higher maximum intermediate concentration as compared to a rectangular channel. Although the maximum for the layered herringbone channel was obtained earlier than the rectangular one, the differences are smaller than for the case when the reactants are not premixed. The performance improvement of the layered herringbone channel seems to be mostly due to its enhanced mixing characteristics and to a lesser extent to its improved RTD behaviour. The flowrates studied in this section corresponded to Peclet numbers in the range of 1250 to 39000 (Reynolds 1 to 39).



(a)



(b)

FIGURE 8.5: Theoretical concentration of the intermediate in a consecutive reaction for a layered herringbone and a rectangular channel reactor. a) with reactants unmixed before the reactor inlet, b) with reactants premixed before the reactor inlet.

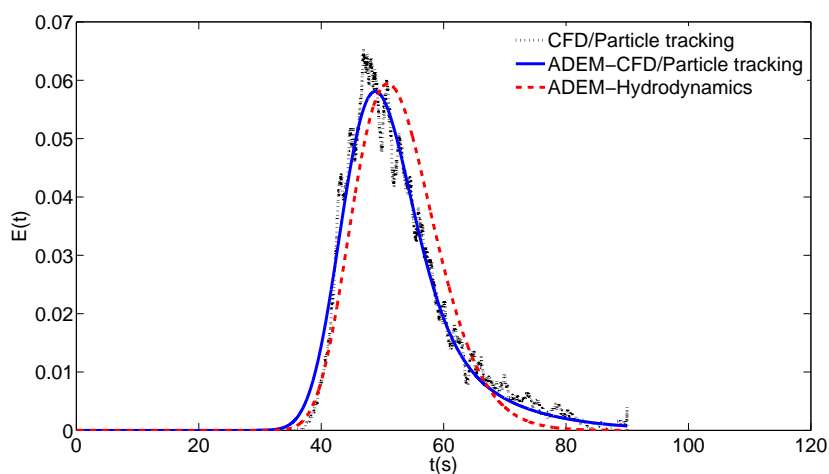


FIGURE 8.6: Residence time distributions for the layered herringbone channel for a flowrate of 4 ml/min. RTDs were obtained by CFD/Particle tracking methods and with the ADEM model with the parameters fitted from the particle tracking data or from the hydrodynamics obtained from CFD calculations.

8.4.3 Comparison of ADEM Model Parameters Obtained from CFD/Particle Tracking and Hydrodynamic Data

Since only the reaction constants and the RTD are needed for the calculation of the intermediate concentration (assuming that the reactants are completely mixed at the entrance), if a mathematical model can be fitted to the RTD, both the theoretical and experimental efforts can be greatly reduced. The suggested approach is to predict the model parameters only with hydrodynamic data, without the need of measuring the RTD either experimentally or by CFD/Particle tracking algorithms. In this section, the ADEM model is used to obtain theoretical RTDs. Two approaches are employed to obtain the ADEM model parameters: a) CFD/Particle tracking algorithms and b) hydrodynamic data utilising velocities obtained from CFD and the turbulence diffusion concept as suggested in section 8.3.2. The residence time distributions obtained from particle tracking data and from the ADEM model are shown in figure 8.6.

The RTD obtained from the ADEM-Hydrodynamic approach deviates from the

one obtained from ADEM-CFD/Particle tracking. The deviation occurs mainly at the tail of the curve because of different mass transfer coefficients (K) obtained by the two models. The ADEM/Hydrodynamic approach gives higher mass transfer coefficients than the ADEM-CFD/Particle tracking and this results in shorter tails for the former. Table 8.2 shows the model parameters obtained from the ADEM-Hydrodynamic and the ADEM-CFD/Particle tracking methods.

The prediction of the axial dispersion coefficient, D_{ax} , and the fraction of fluid subject to plug flow, f , from hydrodynamic data, agree well with the fitted values from RTDs obtained from CFD/Particle tracking data; the results are within 14%. This indicates that the stirring effect of the herringbone structures can be captured satisfactorily by an effective diffusion coefficient as suggested in section 8.3.2. However, large discrepancies are found for the calculation of the mass transfer coefficient K . The value obtained from hydrodynamic data is about 4 times bigger than the one fitted to CFD/Particle tracking. A possible explanation is that whereas the value calculated from hydrodynamics, considers that the dead zone is only constituted by the volume of the grooves, dead zones can also be present in the corners of the channels [12].

TABLE 8.2: Parameters for the model of axial dispersion exchanging mass with a dead zone (ADEM) obtained by two different approaches.

	Parameters fitted to CFD/Particle tracking	Parameters calculated from hydrodynamics
f (fraction of fluid subject to axial dispersion)	0.88	0.82
K (mass transfer coefficient 1/s)	0.035	0.15
D_{ax} (Axial dispersion coefficient m^2/s)	8.9×10^{-6}	1.03×10^{-5}
v_g (Velocity inside the groove m/s)	-	4.33×10^{-4}
E_D (Eddy Diffusivity m^2/s)	-	1.63×10^{-7}
D_{eff} (Effective Diffusivity m^2/s)	-	1.64×10^{-7}

The results of C_{THI} concentration as a function of EP conversion calculated from equation (8.9) are shown in figure 8.7. The RTDs used for the calculations were obtained from the CFD/Particle tracking simulations, or from the ADEM model either with parameters fitted to CFD/Particle tracking or calculated from hydrodynamic data.

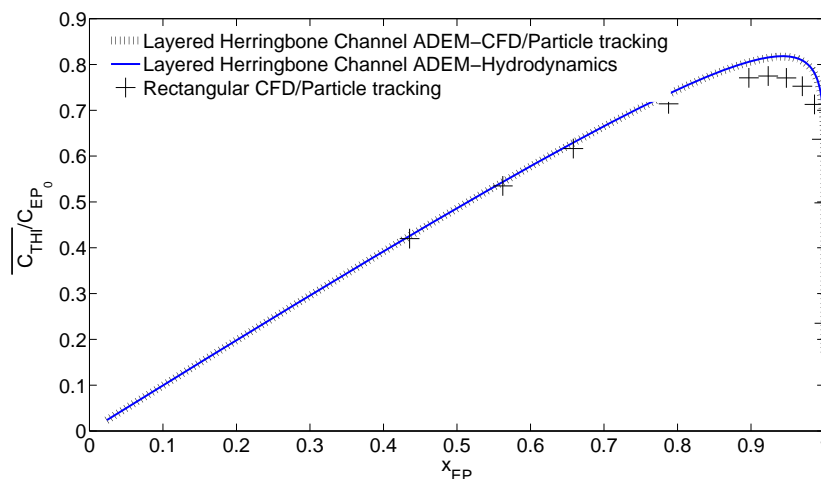


FIGURE 8.7: Theoretical intermediate THI concentration for the reaction (8.1) as a function of EP conversion for the layered herringbone and for the rectangular channel. The RTDs needed for the calculation of concentrations were obtained by the ADEM-CFD/Particle tracking, ADEM-Hydrodynamics and the CFD/Particle tracking methods.

It can be seen that the curves for the layered herringbone channel do not change regardless of the method used for calculating the parameters of the ADEM model. It was also found that using the RTDs calculated from particle tracking data did not change the intermediate concentration vs. reactant conversion behaviour (not shown). This is an interesting result because the parameters for the ADEM model were obtained at a flowrate of 4 ml/min, $t_m = 53s$. The fitted parameters were used for the calculation of RTDs at different mean residence times. This procedure is only an approximation since the parameters fitted for a 4 ml/min flowrate will not be the same compared to a 0.4 ml/min one. Diffusion becomes increasingly important as the flowrate decreases and the parameters needed for the ADEM

model K and D_{ax} are both dependent on diffusion. However, as explained in section 8.4.1, the RTD for the layered herringbone channel is practically independent of Pe (of flowrate in this case) thus the variation of D_{ax} and K is not expected to be large. At low conversions the behaviour of the rectangular channel is similar to the layered herringbone channel. Differences on the intermediate concentration can only be seen at high conversions. This indicates that the effect of the RTD in this particular case is not significant.

8.5 Conclusions

The effect of reactor channel geometry on the product yield of an intermediate for a consecutive reaction was studied both theoretically and experimentally for a layered herringbone channel and a rectangular channel of similar dimensions. Residence time distributions calculated numerically via CFD and particle tracking methods were found to be narrower for the layered herringbone configuration as compared to the rectangular one. Both experiments and theoretical calculations showed that the yield of the intermediate product in a consecutive reaction was maximised in the layered herringbone channel as compared to a rectangular one. Experiments showed that when the reactants are not premixed before the reactor inlet, the maximum concentration of intermediate in a layered herringbone channel was increased by 40% compared to a rectangular channel thanks to its improved mixing characteristics and narrow RTD. In addition, the maximum concentration for the layered herringbone channel was obtained at smaller mean residence times, which indicates that reaction volume could be decreased. When the reactants were premixed before the inlet only the effect of residence time distribution affects the maximum amount of intermediate produced and the time at which this happens. The differences between the two reactors operating under this condition are subtle, as found by simulations. This indicates that the impact of

good mixing on reaction performance is more important than the effect of narrow RTD. The model of axial dispersion exchanging mass with a dead zone was used for the modelling of the RTD. The model parameters could be calculated exclusively from hydrodynamic data obtained from CFD calculations without the need of CFD/Particle tracking simulations. The model parameters were obtained by applying turbulence theory concepts (eddy diffusivity) to replace the stirring effect of the herringbone grooves with an effective diffusion coefficient. It was shown that the residence time distributions obtained from turbulence theory agreed well with the full CFD/Particle tracking simulations. Thus, the calculation of the concentration of the intermediate in a consecutive reaction can be simplified with the use of this method. The use of a layered configuration provides the opportunity of having two channels with improved reaction performance with a single set of herringbones. This may reduce the microfabrication costs and opens the possibility for new applications where the middle layer with the herringbone structures can be used both to improve reaction in the bulk, and as a contact area between two different flows.

Chapter 9

Conclusions and Future Work

Chapter 3 focused on the analysis on the quality of mixing for the staggered herringbone micromixer (SHM) for different flow ratios and injection locations. It was found that the injection location played a significant role on the quality of mixing. An analysis on the stirring intensity of the mixer (stretching calculations) showed that the regions with the strongest mixing characteristics are located close to the herringbone asymmetry and the channel bottom. When fluids were placed on the centre of the channel, the herringbone grooves transported material from poor to good mixing regions. When designing micromixers it is necessary to be able to predict the mixing length or time for a given set of conditions (density, viscosity, diffusivity etc.). This was addressed in this investigation and three different methods for the calculation of the mixing length were evaluated. However, the analysis done in chapter 3 is valid only for the conditions simulated, a more general framework is needed in order to predict mixing times for different conditions or geometries. There have been efforts to provide general guidelines for efficient micromixer design [104, 161]. Future investigations should take into account the flow ratio and injection location which effectively translates to an initial average striation thickness.

Mixing investigations both theoretical and experimental, were also included in chapter 7 for the layered herringbone channel. Experimental investigations were done with Villiermaux-Dushman reaction and with confocal microscopy. Although the Villiermaux-Dushman for the characterisation of mixing efficiency has been extensively used [40, 48, 82], there is still debate as to whether mixing times can be achieved with this method [22, 83]. Confocal microscopy is a useful tool that can give insight into the stirring capabilities of micromixers, however quantitative characterisation can be difficult due to resolution issues. Improved techniques for the quantitative characterisation of micromixers are still needed.

Also in chapter 7 a brief discussion of the different convective regimes found in a T-mixer was included. T-junctions have been found to be efficient mixers at intermediate Reynolds numbers at the so-called engulfment regime. Although there have been efforts at predicting the onset of the engulfment regime as a function of different parameters [42, 140] there is still room for work on this topic. The characteristics of the pulsating regime described in Kockmann [80] have only been briefly studied.

Chapter 4 presented an experimental and numerical study of residence time distributions (RTDs) on channels with and without herringbone structures. It was found that at high Peclet numbers the channels with herringbone structures yielded narrower RTDs than unstructured rectangular channels. On the other hand when the Peclet number decreased ($Pe < 10^2$) the differences were drastically reduced. It was also found that the RTD for herringbone channels was almost unaffected when the Peclet number increased (at $Pe > 10^4$). This opens the possibility of increasing the dimensions of the herringbone channel or increasing flowrate which would have a positive impact in terms of productivity and/or energy consumption. Similar studies were done for the layered herringbone channel in chapter 7 and for

microstructured plate reactors in chapter 5. It was found that a single set of see-through herringbone structures could provide two rectangular channels with similar mixing and RTD characteristics than a standard herringbone channel. Mixing studies have received considerable attention by the research community. However reaction studies under strong convective components have only been briefly addressed.

Chapter 8 studied the effect of a layered herringbone channel in the performance of a consecutive reaction both theoretically and experimentally. Residence time distributions were obtained numerically in order to predict the conversion of the first order reaction. It was found that the RTD could be fitted to the axial dispersion exchanging mass with a dead zone model (ADEM). The parameters of the model were obtained both from RTD simulations and from hydrodynamic data obtained from the simulations. It was found that the parameters obtained from the hydrodynamics were very close to the actual ones (the ones from the full RTD simulations). This simplifies the numerical procedure and may help in modeling more complicated mechanisms.

In chapter 6 an analysis on mass transfer to reactive wall for different microchannel configurations was presented. Two proposed geometries, an alternated herringbone and flow inversion structure, were compared to the staggered herringbone channel. Although both of the proposed geometries gave mass transfer coefficients at least double the ones for the staggered herringbone, the alternated herringbone showed superior performance because the pressure drop was kept low. The eddy diffusivity concept from turbulence theory was successfully used to replace the stirring effect of the herringbone grooves. It was used to model the experimental studies on CO_2 absorption in a falling film microreactor with herringbone grooves on the liquid side. The agreement between simulations and experiments was satisfactory. The use of the eddy diffusivity concept may allow for simulation

of more complicated systems and may in part fill the gap mentioned before on the investigation of reactions under strong convective flows.

Although a lot of research efforts have been directed towards the design and characterisation of novel equipment mainly for mixing purposes, there have not been a lot of interest in using them for other applications such as heat/mass transfer and reaction. For example, in this thesis the layered herringbone channel was studied in terms of mixing RTDs and reaction. However one interesting application would be to use the herringbone layer as a mean of contact between two phases for example for liquid-liquid extraction. The herringbone layer would be useful both for the separation of the phases and to stir the liquid phases and intensify the extraction. Also, although mass transfer has been studied to a wall opposite to the herringbone structures, it would be interesting to study the effect on mass transfer to the actual herringbones. Fluid is constantly entering and leaving the grooves and it could potentially intensify even further mass transfer processes.

In general the field of microreaction technology has reached a state where its advantages have been clearly demonstrated. The high surface to volume ratios enhance heat and mass transfer and can potentially lead to higher yields in reactions due to controlled conditions. In addition, new reaction pathways traditionally unsafe in macroscopic equipment could be explored in microreactors because they are safer due to the low inventories involved. It is time that these advantages are translated to pilot and even production scale chemical plants. The challenge lies not on the design of new pieces of equipment (although lots of room is still there for research) but on real applications of the existing microengineered devices into chemical plants. Therefore, efforts on topics such as fluid mal-distribution, numbering up, manifold design, along with applications of microchannels to processes will probably be more frequent in the coming years.

Appendix A

Particle Tracking Algorithm

Implemented in Matlab

This computer program tracks the positions of massless particles in Matlab. It utilises a velocity field exported from Comsol Multiphysics.

```
1 function M = postpart(fem, varargin)
3
4 % THIS HAS BEEN MODIFIED SO THAT IT DOESN'T TAKE UP SO MUCH MEMORY AS
5 % PREVIOUS VERSIONS ALSO IT HAS BEEN MODIFIED TO TAKE INTO ACCOUNT
6 % MOLECULAR DIFFUSSION AS DESCRIBED IN STROOCK "MASS TRANSFER TO
7     REACTIVE
8 % BOUNDARIES
9 %POSTPART Post processing particle plot function.
10 % POSTPART(FEM,...) is the general particle plot function. It can
11 display
12 % a FEM solution in several different ways. The function works per
13 % automatically on a time-dependent or stationary FEM struct with
14 an
```

```

13 % incompressible Navier–Stokes application mode and at least one (u
    ,v,w) boundary.
    %
15 % M = POSTPART(FEM,...) additionally return handles to the drawn
    objects.
    %
17 % Valid property/value pairs include:
    %
19 % Property      2D  3D  Value/{Default}      Description
    %
    

---


21 % Anim           X  X  'on' | {'off'}      Make Matlab movie
    % Cmap           X  X  string {'bgcmyk'}  Particle color map
23 % Convexpr       X  X  cell-string {fem.dim} Convection
    expression
    % Image         X  X  string      Save image as name (
    jpeg)
25 % Npart         X      integer {10}      Number of inserted
    % boundary      particles per
27 % Odefun        X  X  string      Name of ODE function
    % Partcont      X  X  'on' | {'off'}    Continous particle
    insertion
29 % Partline      X      'on' | {'off'}    Plot line between
    % groups      particle streams/
31 % Partscoord    X  X  Coordinate vector  Initial position of
    % inserted particles
33 % Scheme        X  X  {1} | 2 | 3      Employed ODE
    integration scheme
    % Stol         X  X  integer {1}      Particle line length
    tolerance
35 % T           X  X  vector      Times to use in the

```

```
%                                     {fem.sol.tlist/1:10}  time stepping
algorithm
37 %  Wless          X  X  {'on'} | 'off'          Use weightless
particles
%  Wdata          X  X  cell{2,1,1,1,0,-10,0} Particle data
39 %
%  The property Anim controls if an Matlab movie should be made of
the figures.
41 %
%  Cmap gives the colors used for the different particle streams/
groups. The input
43 %  should be a string of valid color identifiers.
%
45 %  Convexpr gives the expression that should be evaluated to move
the particles.
%  The fem struct is searched by default for 'Incompressible Navier-
Stokes '
47 %  application modes and the corresponding dependent variables are
used.
%
49 %  If the property Image is specified, Jpeg images will be saved in
the working
%  directory with the name ['input' number in squence '.jpg '].
51 %
%  Npart can either be a single integer designating the number of
particles that
53 %  will be evenly distributed over each boundary. The particles will
be grouped
%  according to boundary and each successive insertion of new
particles will be
55 %  designated a new group. Npart can also be a vector of values
between 0 and 1
%  which designate the positions on each parametrized boundary the
particle
```

```
57 % streams/groups are.
%
59 % Odefun specifys the function that will be evaluated when Wless is
% 'on'.
%
61 % If Partcont is active new particles will be inserted at each time
% step.
%
63 % The Partline property plots lines between the particle groups/
% segments.
%
65 % Partscoord can be a vector designating starting positions of the
% particles.
%
67 % The Scheme property controls the ODE integration scheme employed.
% Valid
% inputs are:
69 % 1 - first order explicit forward Euler scheme.
% 2 - second order explicit scheme, from Taylor expansion.
71 % 3 - second order Runge-Kutta scheme, Heuns method.
%
73 % The property Stol controls at which point the plotted lines
% should be removed
% if Partline is active.
75 %
% The property T is a vector of times that should be evaluated.
% This is set to
77 % fem.sol.t per default.
%
79 % The property Wless controls if the mass of the particles should
% be considered.
% If Wless is active the particles meerely follows the flow-field,
% otherwise
81 % the system:
```

```

%
83 %       $mp \cdot d(v_i)/dt = (mp - mf) \cdot g_i - 6 \cdot \pi \cdot r_p \cdot \mu \cdot (v_i - u_i)$ 
%
85 %      will be integrated, where 'mp' is the mass of the particle, 'mf'
%      the mass of the
%      fluid that the particle has displaced, 'ui' the velocity of the
%      particle in the
87 %      xi-direction, 'vi' the velocity of the fluid, 'rp' the radius of
%      the particle, 'gi'
%      the gravity, and 'miu' the dynamic viscosity of the fluid.
89 %
%      Wdata should be used in conjunction with the property Wless to
%      specify the data
91 %      of the particles and fluid. Input is a cell vector with the
%      following entries:
%      { Particle mass, Mass of fluid displaced of particle, Dynamic
%      fluid viscosity, ...
93 %      Particle radius, gravitational acceleration in x-direction,
%      gravitational acceleration in y-direction(, gravitational
%      acceleration in z-direction)}
%
95 %      See also POSTPLOT, MESH PLOT, POSTANIM, POSTARROW, POSTARROWBND,
%      POSTCONT,
%      POSTCROSSPLOT, POSTCONT, POSTEVAL, POSTFLOW, POSTISO, POSTLIN,
%      POSTMOVIE,
97 %      POSTSLICE, POSTSURF, POSTTET
%
99 %      Shu-Ren Hysing 16-July-2002.
%      Copyright (c) 1994-2002 by COMSOL AB
101
crossz=0;
103
[got, val] = l_pvpars(fem, varargin);
105

```

```

if got.partscoord
107   pStartCoord = val.partscoord;
else
109   edgCoord    = l_getedgcoord(fem);    % Find velocity boundaries.
       pStartCoord = l_getpstartcoord(edgCoord, val.npart);    % Get
           starting particle coordinates.
111 end

113
% Startup phase.
115 if val.partcont
       if length(val.npart)==1    % Create total particle vector.
117   pCoord = zeros(size(fem.fem{1}.mesh.p,1), size(pStartCoord,2),
           length(val.t)*size(pStartCoord,3))+NaN;
       else
119   pCoord = zeros(size(fem.fem{1}.mesh.p,1), length(val.t)*size(
           pStartCoord,2), size(pStartCoord,3))+NaN;
       end
121   pCoord(:,1:size(pStartCoord,2),1:size(pStartCoord,3)) = pStartCoord
           ;
       else %no partcont
123   pCoord      = pStartCoord;
       pStartCoord = [];
125 end

127 if val.wless    % Weightless particles.

129   cExpr    = strcat('','',val.convexpr,'','','); %not input hence u,v,w
       args    = ['fem,', [cExpr{:}]]; %args = fem, 'u', 'v', 'w',
131   args    = args(1:end-1); %args = fem, 'u', 'v', 'w'
       p0Coord = pCoord; % for Taylor series?
133
       else    % Particles with mass.
135   p0Coord = pCoord;

```

```

vPart = pCoord;
137 vPart(~isnan(pCoord)) = 0;
cExpr = strcat('''',val.convexpr,'''');
139 args = ['fem',',[cExpr{:}]];
odefun1 = 'l_pforcefunc';
141 odefun2 = 'l_pvelfunc';
if val.scheme == 2
143     val.scheme = 3;
end
145 end

147
% modY(1,:)=pCoord(2,:);
149 % cycle(1,:) = [(0.01006-modY(1,:))/0.001516] ;
%
%           numcycle(1,:) = [1 + floor(cycle(1,:))];
151 %           modY2(1,:)= [(modY(1,:)+((numcycle(1,:)-1)
%           *0.001516))];
% pCoord(2,:)=modY2(1,:);
153
155
157
159
% Main loop.
161 for i=1:length(val.t)
    l_bgrplot(fem,val,i) % Background plot.
163 hold on

165 %     xbound=pCoord(1,:)>200e-6;
%     crossx=find(xbound);
167 % pCoord(1,crossx)=200e-6;
% %

```



```

169 % xbound2=pCoord(1,:) < 0;
    % crossx2=find(xbound2);
171 % pCoord(1,crossx2)=0;
    % % yy=y(3,:);
173 % % velz =eval([odefun,'(t(i),yy,','args,')']);
    %
175 % zbound=p0Coord(3,:) > 85e-6;
    % crossz=find(zbound);
177 % crosszpos=[pCoord(1,crossz),pCoord(2,crossz)];
    % pC0oord(3,crossz)=85e-6;
179
181
    %
183 % zbound2=pCoord(3,:) < 0;
    % crossz2=find(zbound2);
185 % pCoord(3,crossz2)=0;
    %%%%%%%%%%%%%%%%%%%%%%%%%%%%%%%%%%%%%%%%%%%%%%%%%%%%%%%%%%%%%%%%%%%%%%%%%%
187 %Dat as cell array
    % Dat = cell(1,length(val.t));
189 if i >= 2
        notnumbid=isnan(pCoord(3,:));
191 notnumb=find(notnumbid);
        pCoord(3,notnumb)=M{1,i-1}(3,notnumb);
193 pCoord(2,notnumb)=M{1,i-1}(2,notnumb);
        pCoord(1,notnumb)=M{1,i-1}(1,notnumb);
195
        notnumbid=isnan(pCoord(2,:));
197 notnumb=find(notnumbid);
        pCoord(3,notnumb)=M{1,i-1}(3,notnumb);
199 pCoord(2,notnumb)=M{1,i-1}(2,notnumb);
        pCoord(1,notnumb)=M{1,i-1}(1,notnumb);
201
        notnumbid=isnan(pCoord(1,:));

```

```

203     notnumb=find(notnumbid);
        pCoord(3,notnumb)=M{1,i-1}(3,notnumb);
205     pCoord(2,notnumb)=M{1,i-1}(2,notnumb);
        pCoord(1,notnumb)=M{1,i-1}(1,notnumb);
207
209
211
213 end % End if
        % M{1,i} = pCoord(:, :) ;
215 %
        %
217 % rt=find(pCoord(2,:) <= 0.00248);
        % if sum(rt) > 54000
219 M{1,i} = pCoord(:, :) ;
        % end
221
223 % ans=pCoord(2,:) <= 0.005512;
        % ans2=sum(ans);
225 % %if ans2 > 2000
        % if i > 6250
227 % M2{1,i} = pCoord(:, :) ;
        % end
229
        %Dat as 3D array
231 %Dat(:, :, i)=pCoord(:, :) ;
%%%%%%%%%%%%%%%%%%%%%%%%%%%%%%%%%%%%%%%%%%%%%%%%%%%%%%%%%%%%%%%%%%%%%%%%%%
233 l_partplot(pCoord, val.cmap) % Particle marker plot.
235 if val.partline

```

```

    l_sgmplot(pCoord, val.cmap, val.stol) % Particle stream/group
    line plot.
237 end

239 % Take one time step.
    if val.wless
241     if got.nocycle
        tmp = pCoord;
243     [pCoord, crossz] = l_odesolve2(val.odefun, args, val, pCoord,
        p0Coord, fem, i, crossz);
        p0Coord = tmp; %this is coordinate from before odesolve, i.e.
        old pCoord
245 %     crossz = l_odesolve2(val.odefun, args, val, pCoord, p0Coord,
        fem, i, crossz);
        else
247     tmp = pCoord;
        pCoord = l_odesolve(val.odefun, args, val, pCoord, p0Coord, fem, i
        );
249     p0Coord = tmp; %this is coordinate from before odesolve, i.e.
        old pCoord
        end
251
    else
253     vPart = l_odesolve(odefun1, {args, vPart, pCoord}, val, vPart, [], fem
        , i);
        pCoord = l_odesolve(odefun2, {args, vPart, pCoord}, val, pCoord, [],
        fem, i);
255 end %wless

257 %This line gives the particles that are lost through the upper
        boundary
        %(the roof)
259 %for reaction kinetics we include the probability of leaving at the
        top

```

```

    %boundary
261 %   if rand<=0.1
    %   rt=find(pCoord(2,:) <=0.00248);
263 %   if sum(rt)>54000
        M{2,i}=crossz(:,:);
265 %   end
    %   end
267
    if val.partcont
269        % Add new particles.
        if length(val.npart)==1
271            pCoord(:, :, i+1) = pStartCoord;
            p0Coord(:, :, i+1) = pStartCoord;
273        else
            pCoord = [pStartCoord pCoord];
275            p0Coord = [pStartCoord p0Coord];
        end
277        if ~val.wless
            if length(val.npart)==1
279                vPart(:, :, i+1) = zeros(size(pStartCoord));
            else
281                vPart(:, 1:size(pStartCoord,2)*(i+1), :) = [zeros(size(
                    pStartCoord)) vPart(:, 1:size(pStartCoord,2)*i, :)];
            end
283        end
    end
285    drawnow
    hold off
287 %%%%%%%%%%%%%%%%%%%%%%%%%%%%%%%%%%%%%%%%%%%%%%%%%%%%%%%%%%%%%%%%%%%%%%%%%%
    if val.anim
289        M(i) = getframe(gcf);
    % else
291        %Cell array
    %   M(1,i) = Dat(1,i) ;

```

```

293
    %3D Array
295    %M(:, :, i) = Dat(:, :, i) ;
    end
297 %%%%%%%%%%%%%%%%%%%%%%%%%%%%%%%%%%%%%%%%%%%%%%%%%%%%%%%%%%%%%%%%%%%%%%%%%
    if got.image
299    l_imsave([val.image repmat('0',1,4-length(int2str(i))) int2str(i)
        '.jpg'],800,600,'jpeg');
    end
301 end %for i

303

305 %%%%%%%%%%%%%%%%%%%%%%%%%%%%%%%%%%%%%%%%%%%%%%%%%%%%%%%%%%%%%%%%%%%%%%%%%
    %ONLY IF PARTICLE STARTING COORDINATES ARE NOT SPECIFIED
307 function edgCoord = l_getedgcoord(fem)
    % Returns a cell with end coordinates for all dirichlet
309 % velocity boundaries in each cell.

311 % Gets the indexes to the boundaries.
    bndind = []; % Vector of integers representing the starting places
        for the particles.
313 for i=1:length(fem.appl)
    if strcmp((fem.fem{1}.appl{i}.mode.class),{'FlNavierStokes'})
315    for j=1:length(fem.fem{1}.appl{i}.bnd.type)
        if strcmp(fem.fem{1}.appl{i}.bnd.type{j},{'uv','uvw'})
317    bndind = [bndind find(fem.fem{1}.appl{i}.bnd.ind==j)]; %this
        value is 2
        end
319    end
    end
321 end
    if isempty(bndind)
323    bndind = 1;

```

```

end
325 % HOLD – LEAVE UNMODIFIED AS STARTCOORD WILL BE SPECIFIED
    % Find end coordinates for the velocity boundaries.
327 edgCoord = cell(1,length(bndind));
    for i=1:length(bndind)
329     if size(fem.mesh.p,1)==2
        edgind = fem.mesh.e([1 2],find(fem.mesh.e(5,:)==bndind(i)));
331     edgCoord{i} = fem.mesh.p(:,find(sparse(edgind,ones(size(edgind)),1,max(edgind(:),1)==1)));
        else
333     edgind = fem.mesh.e([1 2 3],find(fem.mesh.e(10,:)==bndind(i)));
        edgCoord{i} = fem.mesh.p(:,unique(edgind));
335     end
    end
end
337
%%%%%%%%%%%%%%%%%%%%%%%%%%%%%%%%%%%%%%%%%%%%%%%%%%%%%%%%%%%%%%%%%%%%%%%%%%
339 %ONLY IF PARTICLE STARTING COORDINATES ARE NOT SPECIFIED
    function pStartCoord = l_getpstartcoord(edgCoord,nPart)
341 % Create starting particle coordinate matrix. Output
    % is a three dimensional matrix with rows corresponding
343 % to x, y, (and z) –indexes, columns corresponding
    % to point numbers, and depth corresponding to particle
345 % stream group/cluster number.

347 if size(edgCoord{1},1)==2
    if length(nPart)==1
349     pStartCoord = zeros(2,nPart,length(edgCoord));
        for i=1:length(edgCoord)
351     % Distribute 'npart' particles evenly over each boundary.
        xCoord = linspace(min(edgCoord{i}(1),edgCoord{i}(3)),max(
edgCoord{i}(1),edgCoord{i}(3)),nPart+2);
353     yCoord = linspace(min(edgCoord{i}(2),edgCoord{i}(4)),max(
edgCoord{i}(2),edgCoord{i}(4)),nPart+2);

```

```

355     % Handle horizontal and vertical boundaries.
        if length(xCoord)>nPart
357         xCoord = xCoord(2:end-1);
        end
359     if length(yCoord)>nPart
        yCoord = yCoord(2:end-1);
361     end
        % Each boundary constitutes a particle stream/cluster group.
363     pStartCoord(:, :, i) = [xCoord ; yCoord];
        end
365 else
        % Distribute particles at parametrized positions in 'nPart' over
        each boundary.
367     idx = 1; % Each particle initial position constitutes a
        particle stream/cluster group.
        pStartCoord = zeros(2,1,length(edgCoord)*length(nPart));
369     for i=1:length(edgCoord)
        for j=1:length(nPart)
371         xCoord = min(edgCoord{i}(1),edgCoord{i}(3))+abs(edgCoord{i}
        ){1}-edgCoord{i}(3))*nPart(j);
        yCoord = min(edgCoord{i}(2),edgCoord{i}(4))+abs(edgCoord{i}
        ){2}-edgCoord{i}(4))*nPart(j);
373         pStartCoord(:, :, idx) = [xCoord ; yCoord];
        idx = idx+1;
375     end
        end
377 end
else
379     for i=1:length(edgCoord)
        pStartCoord(:, :, i) = edgCoord{i};
381     end
    % edgCoord{1}(1:2,:) = 0.8*edgCoord{1}(1:2,:); % Tmp. stuff for
        laminar_static_mixer plot.

```



```

409 function l_partplot(pCoord,cmap)
    % Plots the particles as markers.
411 %repmat=Replicate and tile an array

413 %B = repmat(A,m,n) creates a large matrix B consisting of an m-by-n
    tiling of copies of A. The statement repmat(A,n) creates an n-by-n
    tiling.

415 cmap = repmat(cmap,1,ceil(size(pCoord,3)/length(cmap)));

417 for nGrp = 1:size(pCoord,3)
    if size(pCoord,1)==2
419     notNaN = ~isnan(pCoord(1,:,nGrp))&~isnan(pCoord(2,:,nGrp));
        plot(pCoord(1,notNaN,nGrp), ...
421         pCoord(2,notNaN,nGrp), 'o', 'markersize',2, 'markeredgecolor',
        cmap(nGrp), 'markerfacecolor',cmap(nGrp))
    else
423     notNaN = ~isnan(pCoord(1,:,nGrp))&~isnan(pCoord(2,:,nGrp))&~isnan
        (pCoord(3,:,nGrp));
        plot3(pCoord(1,notNaN,nGrp), ...
425         pCoord(2,notNaN,nGrp), ...
        pCoord(3,notNaN,nGrp), ...
427         'marker','o','markersize',2.1,'markeredgecolor',cmap(nGrp),
        'markerfacecolor',cmap(nGrp),'linestyle','none')
    end
429 end

431 axis equal
    axis off
433
    %%%%%%%%%%%%%%%%%%%%%%%%%%%%%%%%%%%%%%%%%%%%%%%%%%%%%%%%%%%%%%%%%%%%%%%%%%
435 function l_sgmsplot(pCoord,cmap,stol)

```

```

437 % Plot interconnecting lines between particles in each particle
      stream/cluster.

439 cmap = repmat(cmap,1,ceil(size(pCoord,3)/length(cmap)));

441 for nGrp=1:size(pCoord,3)
      ixSgms = find(sqrt(sum((pCoord(:,1:end-1,nGrp)-pCoord(:,2:end,nGrp)
          ).^2)) <= stol);
443 sgms = sort(fastsetop('setxor',ixSgms,ixSgms+1));
      sgms = reshape(sgms,2,size(sgms,2)/2);
445 for j = 1:size(sgms,2)
          plot(pCoord(1,sgms(1,j):sgms(2,j),nGrp), ...
447             pCoord(2,sgms(1,j):sgms(2,j),nGrp),'color',cmap(nGrp))
      end
449 end

451 %%%%%%%%%%%%%%%%%%%%%%%%%%%%%%%%%%%%%%%%%%%%%%%%%%%%%%%%%%%%%%%%%%%%%%%%%

453 function y = l_odesolve(odefun, args, val, y, y0, fem, i)
      % Solve ODE one step.

455
      t = val.t;
457 alg = val.scheme;

459 % Reshape input matrix if needed.
      yDim1 = size(y,1);
461 if length(size(y)) > 2
          yDim3 = size(y,3);
463 y = reshape(y,yDim1,size(y,2)*yDim3);
          y0 = reshape(y0,yDim1,size(y0,2)*yDim3);
465 else
          yDim3 = 0;
467 end

```

```

469 % Check for NaN entries.
    if yDim1 == 2
471     UseInd = ~isnan(y(1,:)) & ~isnan(y(2,:));
    else
473     UseInd = ~isnan(y(1,:)) & ~isnan(y(2,:)) & ~isnan(y(3,:));
    end
475
    % Determine the time step.
477 if i >= length(t)
        deltat = t(i)-t(i-1);
479 else
        deltat = t(i+1)-t(i);
481 end

483 % Integrate one time step.
    if iscell(args)
485     funinp = {val.wdata, args{2:end}, UseInd};
        args = [args{1}, 'funinp'];
487 end

489
    switch alg
491     case 1 % First order explicit forward Euler.
        ycalc = ycalc+deltat*eval([odefun, '(t(i),ycalc, ', args, ')']);
493     case 2 % Second order explicit by Taylor expansion.
        ycalc0 = y0(:, UseInd);
495         if i == 1
            ycalc = ycalc+deltat*eval([odefun, '(t(i),ycalc, ', args, ')']);
497         else
            ycalc = ycalc+deltat*0.5*(3*eval([odefun, '(t(i),ycalc, ', args, ')
            ']) - eval([odefun, '(t(i-1),ycalc0, ', args, ')']));
499         end
        case 3 % Fourth Order Runge Kutta
501         yn(:, :) = y(:, UseInd);

```

```

if i < length(t)
503     y1(:, :) = eval([odefun, '(t(i), yn(:, :), ', args, ') ']);
        k1 = deltat*y1(:, :);
505
        y2(:, :) = eval([odefun, '(t(i)+0.5*deltat, yn(:, :)+0.5*k1(:, :), ',
args, ') ']);
507     k2 = deltat*y2(:, :);

509     y3(:, :) = eval([odefun, '(t(i)+0.5*deltat, yn(:, :)+0.5*k2(:, :), ',
args, ') ']);
        k3 = deltat*y3(:, :);
511
        y4(:, :) = eval([odefun, '(t(i)+deltat, yn(:, :)+k3(:, :), ', args, ') ']);
        ;
513     k4 = deltat*y4(:, :);

515     yn2 = yn(:, :) + (1/6)*(k1(:, :)+2*k2(:, :)+2*k3(:, :)+k4(:, :));

517     else %need to check this section!
        y1(:, :) = eval([odefun, '(t(i), yn(:, :), ', args, ') ']);
519     k1 = deltat*y1(:, :);

521     y2(:, :) = y1(:, :);
        k2 = deltat*y2(:, :);
523
        y3(:, :) = y1(:, :);
525     k3 = deltat*y3(:, :);

527     y4(:, :) = y1(:, :);
        k4 = deltat*y4(:, :);
529

        yn2(:, :) = yn(:, :) + (1/6)*(k1(:, :)+2*k2(:, :)+2*k3(:, :)+k4(:, :));
531
end %if
```

```

533 end %Switch

535 y(:,UseInd) = yn2(:,:);

537 % Reshape output according to input.
    if yDim3 > 0
539     y = reshape(y,yDim1, size(y,2)/yDim3,yDim3);
    end
541
%%%%%%%%%%%%%%%%%%%%%%%%%%%%%%%%%%%%%%%%%%%%%%%%%%%%%%%%%%%%%%%%%%%%%%%%%%
543
    function [y, crossz] = l_odesolve2(odefun, args, val, y, y0, fem, i, crossz)
545 % Solve ODE one step.

547 t = val.t;
    alg = val.scheme;
549
    % Reshape input matrix if needed.
551 yDim1 = size(y,1);
    if length(size(y)) > 2
553     yDim3 = size(y,3);
        y = reshape(y,yDim1, size(y,2)*yDim3);
555     y0 = reshape(y0,yDim1, size(y0,2)*yDim3);
    else
557     yDim3 = 0;
    end
559

561 D=1e-11;

563 y(1,:) = y(1,:) + randn(1,10253)*sqrt(2*D*.01);
    y(2,:) = y(2,:) + randn(1,10253)*sqrt(2*D*.01);
565 y(3,:) = y(3,:) + randn(1,10253)*sqrt(2*D*0.01);
    %

```

```

567 % % This part reflects particles that have cross boundary
    % xbound=y(1,:)>200e-6;
569 % crossx=find(xbound);
    % y(1,crossx)=200e-6;
571 % %
    % xbound2=y(1,:)<0;
573 % crossx2=find(xbound2);
    % y(1,crossx2)=0;
575 % % yy=y(3,:);
    % % velz =eval([odefun,'(t(i),yy,','args,')']);
577 %
579
    %
581 % zbound2=y(3,:)<0;
    % crossz2=find(zbound2);
583 % y(3,crossz2)=0;
585 if i>1
    % oldcrossz=crossz;
587 %
    % AA=zeros(1,10500);
589 % BB=zeros(1,10500);
    % AA(:,oldcrossz)=oldcrossz;
591
593 zbound=y(3,:)>85e-6;
    crossz=find(zbound);%zbound;
595 %BB(:,crossz)=crossz;
    %partcrossed=find(AA~=BB);% & AA>0);
597 %y(3,crossz)=85e-6;
599 %for reaction rates that requires probability
    % if rand<=0.1

```

```
601 %crossz=partcrossed;
    % end
603
605 else
    zbound=y(3,:)>85e-6;
607 crossz=find(zbound);%zbound;
    %y(3,crossz)=85e-6;
609 %partcrossed=crossz;

611
    end
613

615 % Check for NaN entries.
    if yDim1 == 2
617     UseInd = ~isnan(y(1,:)) & ~isnan(y(2,:));
    else
619     UseInd = ~isnan(y(1,:)) & ~isnan(y(2,:)) & ~isnan(y(3,:));
    end
621
    % Determine the time step.
623 if i >= length(t)
        deltat = t(i)-t(i-1);
625 else
        deltat = t(i+1)-t(i);
627 end

629 % Integrate one time step.
    if iscell(args)
631     funinp = {val.wdata, args{2:end}, UseInd};
        args = [args{1}, 'funinp'];
633 end
```

```

635 % Modify Y coord for uvw data
    uvwCoord(:, :) = y(:, UseInd) ;
637 modY(1, :) = uvwCoord(2, :) ;
    Ystart = 0.01006; %val.partscoord(2,1) ; %if all particles located
        at same Y boundary
639 cycle1 = val.cycle1 ;

641
        cycle(1, :) = [(Ystart - modY(1, :))/cycle1] ;
643 numcycle(1, :) = [1 + floor(cycle(1, :))];
    modY2(1, :) = [(modY(1, :) + ((numcycle(1, :) - 1) * cycle1))];
645
        uvwCoord2(1, :) = uvwCoord(1, :);
647 uvwCoord2(2, :) = modY2(1, :);
        uvwCoord2(3, :) = uvwCoord(3, :);
649

651 switch alg
    case 1 % First order explicit forward Euler.
653 ycalc = ycalc + deltata*eval([odefun, '(t(i), ycalc, ', args, ')']);
        case 2 % Second order explicit by Taylor expansion.
655 ycalc0 = y0(:, UseInd);
        if i == 1
657 ycalc = ycalc + deltata*eval([odefun, '(t(i), ycalc, ', args, ')']);
            else
659 ycalc = ycalc + deltata*0.5*(3*eval([odefun, '(t(i), ycalc, ', args,
                ')']) - eval([odefun, '(t(i-1), ycalc0, ', args, ')']));
            end
661 case 3 % Fourth Order Runge Kutta
        if i < length(t)
663 y1(:, :) = eval([odefun, '(t(i), uvwCoord2(:, :), ', args, ')']);
            k1(:, :) = deltata*y1(:, :) ;
665 %%%%%%%%%%%%%%%%%%%%%%%%%%%%%%%%%%%%%%%%%%%%%%%%%%%%%%%%%%%%%%%%%%%%%%%%%%%
                modk2(1, :) = [uvwCoord2(2, :) + 0.5*k1(2, :)] ;

```



```

667         k2cycle(1,:) = [(Ystart-modk2(1,:))/cycle1] ;
           numcyclek2(1,:) = [1+floor(k2cycle(1,:))];
669         k2coord(1,:) = [modk2(1, :)+(numcyclek2(1, :)-1)*cycle1];

671         k2uvwCoord(1,:) = [uvwCoord2(1, :)+0.5*k1(1, :)] ;
           k2uvwCoord(2,:) = [k2coord(1, :)] ;
673         k2uvwCoord(3,:) = [uvwCoord2(3, :)+0.5*k1(3, :)] ;

675         y2(:, :) = eval([odefun, '(t(i)+0.5*deltat, k2uvwCoord, ', args, ')',
           ]);
           k2(:, :) = deltat*y2(:, :);
677 %%%%%%%%%%%%%%%%%%%%%%%%%%%%%%%%%%%%%%%%%%%%%%%%%%%%%%%%%%%%%%%%%%%%%%%%%%
           modk3(1,:) = [uvwCoord2(2, :)+0.5*k2(2, :)] ;
679         k3cycle(1,:) = [(Ystart-modk3(1,:))/cycle1] ;
           numcyclek3(1,:) = [1+floor(k3cycle(1,:))];
681         k3coord(1,:) = [modk3(1, :)+(numcyclek3(1, :)-1)*cycle1];

683         k3uvwCoord(1,:) = [uvwCoord2(1, :)+0.5*k2(1, :)] ;
           k3uvwCoord(2,:) = [k3coord(1, :)] ;
685         k3uvwCoord(3,:) = [uvwCoord2(3, :)+0.5*k2(3, :)] ;

687         y3(:, :) = eval([odefun, '(t(i)+0.5*deltat, k3uvwCoord, ', args, ')',
           ]);
           k3(:, :) = deltat*y3(:, :);
689 %%%%%%%%%%%%%%%%%%%%%%%%%%%%%%%%%%%%%%%%%%%%%%%%%%%%%%%%%%%%%%%%%%%%%%%%%%
           modk4(1,:) = [uvwCoord2(2, :)+k3(2, :)] ;
691         k4cycle(1,:) = [(Ystart-modk4(1,:))/cycle1] ;
           numcyclek4(1,:) = [1+floor(k4cycle(1,:))];
693         k4coord(1,:) = [modk4(1, :)+(numcyclek4(1, :)-1)*cycle1];

695         k4uvwCoord(1,:) = [uvwCoord2(1, :)+k3(1, :)] ;
           k4uvwCoord(2,:) = [k4coord(1, :)] ;
697         k4uvwCoord(3,:) = [uvwCoord2(3, :)+k3(3, :)] ;

```

```

699     y4(:, :) = eval([odefun, '(t(i)+deltat, k4uvwCoord, ', args, ') ']);
       k4(:, :) = deltat*y4(:, :);
701 %%%%%%%%%%%%%%%%%%%%%%%%%%%%%%%%%%%%%%%%%%%%%%%%%%%%%%%%%%%%%%%%%%%%%%%%%%
       yn(:, :) = uvwCoord(:, :) + (1/6)*(k1(:, :) + 2*k2(:, :) + 2*k3(:, :) + k4
       (:, :));
703
       else
705     y1(:, :) = eval([odefun, '(t(i), uvwCoord2(:, :), ', args, ') ']);
       k1(:, :) = deltat*y1(:, :);
707
       y2=y1;
709     k2(:, :) = deltat*y2(:, :);
711
       y3=y1;
       k3(:, :) = deltat*y3(:, :);
713
       y4=y1;
715     k4(:, :) = deltat*y4(:, :);
717
       yn(:, :) = uvwCoord(:, :) + (1/6)*(k1+2*k2+2*k3+k4);
       end %if
719     end %Switch
721
       y(:, UseInd) = yn(:, :);
723 %       xbound=y(1, :)>200e-6;
       % crossx=find(xbound);
725 % y(1, crossx)=200e-6;
       % %
727 % xbound2=y(1, :)<0;
       % crossx2=find(xbound2);
729 % y(1, crossx2)=0;
       % % yy=y(3, :);
731 % % velz =eval([odefun, '(t(i), yy, ', args, ') ']);

```

```

%
733 % zbound=y(3,:)>85e-6;
    % crossz=find(zbound);
735 % y(3,crossz)=85e-6;
    %
737 % zbound2=y(3,:)<0;
    % crossz2=find(zbound2);
739 % y(3,crossz2)=0;

741 % zbound2=y(3,:)>85e-6;
    % crossz2=find(zbound2);%zbound;
743 % y(3,crossz)=85e-6;
    % crossz=find(zbound | zbound2);
745

747 % Reshape output according to input.
    if yDim3 > 0
749     y = reshape(y,yDim1, size(y,2)/yDim3,yDim3);
    end
751 %Diffusion constant

753

755 %%%%%%%%%%%%%%%%%%%%%%%%%%%%%%%%%%%%%%%%%%%%%%%%%%%%%%%%%%%%%%%%%%%%%%%%%%

757 function Out = l_postinterp(t,XX,fem,varargin)
    % Get particle convection velocity (weightless particles).
759
    % Check for interpolation indexes into 'fem.sol.tlist'.
761 if fem.sol.jpnr.getType==2 %Blir alltid 0 i 3.0 !!! NOT TYPE 2
        idx = find(fem.sol.tlist==t);
763     if isempty(idx)
            idx = find(fem.sol.tlist>t);
765     if isempty(idx)

```

```

        idx = length(fem.sol.tlist);
767 elseif idx(1)>1
        idx = [idx(1)-1 idx(1)];
769 tstep = ((fem.sol.tlist(idx(2))-t)/(fem.sol.tlist(idx(2))-fem.
sol.tlist(idx(1))));
        else
771 idx = idx(1);
        end % isempty
773 end %isempty
        else %not type2
775 idx = 0;
        end %if fem.sol.jptr.getType
777
        for i=1:length(idx)
779 if idx(i)==0 %YES
            args = {'ext',0}; % Dummy property.args = 'ext'[0]
781 else
            args = {'solnum',idx(i)};
783 end

785 if size(XX,1) == 2
            [Out1 Out2] = postinterp(fem,varargin{1:2},XX,args{:});
787 Out3 = [];
        else
789 [Out1 Out2 Out3] = postinterp(fem,varargin{1:3},XX,args{:});

791 end

793 if i~=2
            Out = [Out1;Out2;Out3];
795 else % Linear interpolation between time steps.
            Out = Out+tstep*[[Out1;Out2;Out3]-Out];
797 end
end
end

```

```

799 %%%%%%%%%%%%%%%%%%%%%%%%%%%%%%%%%%%%%%%%%%%%%%%%%%%%%%%%%%%%%%%%%%%%%%%%%%
801 function Out = l_pforcefunc(t,XX,fem,varargin)
      % Get particle force (Particle with mass).
803
      wdata = varargin{end}{1};
805 massP = wdata{1}; % Mass of the particle.
      massF = wdata{2}; % Mass of the fluid displaced of the particle.
807 miu = wdata{3}; % Dynamic viscosity of the fluid.
      radP = wdata{4}; % Particle radius.
809 grav = repmat([wdata{5:end}]',1,size(XX,2)); % Gravitational
      acceleration vector.

811 % Check for interpolation indexes into 'fem.sol.tlist'.
      if isfield(fem.sol,'tlist')
813     idx = find(fem.sol.tlist==t);
      if isempty(idx)
815     idx = find(fem.sol.tlist>t);
      if isempty(idx)
817     idx = length(fem.sol.tlist);
      elseif idx(1)>1
819     idx = [idx(1)-1 idx(1)];
      tstep = ((fem.sol.tlist(idx(2))-t)/(fem.sol.tlist(idx(2))-fem.
      sol.tlist(idx(1))));
821     else
      idx = idx(1);
823     end
      end
825 else
      idx = 0;
827 end

829 for i=1:length(idx)
      if idx(i)==0

```



```

861 function Out = l_pvelfunc(t,XX,fem, varargin)
    % Get particle velocity (Particle with mass).
863
    if size(XX,1) == 2
865     UseInd = varargin{3}{end};
        Out   = varargin{3}{2};
867 else
        UseInd = varargin{4}{end};
869     Out   = varargin{4}{2};
    end
871 Out = Out(:, UseInd);

873 %%%%%%%%%%%%%%%%%%%%%%%%%%%%%%%%%%%%%%%%%%%%%%%%%%%%%%%%%%%%%%%%%%%%%%%%%%

875 function l_imsave(fname,width,height,imformat,scale,fhandle)
    %L_IMSAVE Save image
877 %
    % L_IMSAVE(FNAME,WIDTH,HEIGHT,IMFORMAT,SCALE,FHANDLE) generates an
879 % image file FNAME for the figure FHANDLE. WIDTH and HEIGHT are
    % given in pixels. IMFORMAT should be 'tiff' or 'jpeg'/'jpeg[nn]'.
881 % SCALE determines font sizes, tick marks etc., in most cases the
    % default value 1 is appropriate.
883 %
    % L_IMSAVE(FNAME) uses the default values WIDTH=800, HEIGHT=600,
885 % IMFORMAT='tiff', SCALE=1 and FHANDLE=gcf.
    %
887 % See also PRINT.

889 % P. Persson, 5-8-98.
    % Copyright (c) 1994-99 by COMSOL AB
891 % $Revision: 1.2 $ $Date: 1999/04/14 16:14:58 $

893 if nargin<1, error('No filename given'); end;
    if nargin<2, width=800; end;

```

```

895 if nargin<3, height=600; end;
    if nargin<4, imformat='tiff'; end;
897 if nargin<5, scale=1; end;
    if nargin<6, fhandle=gcf; end;
899
    res=min(width,height)*0.2*scale;
901
    set(gcf,'PaperUnits','inches');
903 set(gcf,'PaperPosition',[0 0 width/res height/res]);
    print(['-r' int2str(res)], ['-d' imformat], ['-f' num2str(fhandle)],
        fname);
905
    %%%%%%%%%%%%%%%%%%%%%%%%%%%%%%%%%%%%%%%%%%%%%%%%%%%%%%%%%%%%%%%%%%%%%%%%%%
907
function [got, val] = l_pvparse(fem, varargin)
909
    varargin = varargin{1};
911
for i=1:2:(length(varargin)-1)
913     varargin{i}=lower(varargin{i});
end
915
if any(strcmp('anim', varargin))
917     got.anim = 1;
        val.anim = any(strcmp('on', varargin{find(strcmp('anim', varargin))
            +1}));
919 else
        got.anim = 0;
921     val.anim = 0;
end
923 if any(strcmp('cmap', varargin))
        got.cmap = 1;
925     val.cmap = varargin{find(strcmp('cmap', varargin))+1};
else

```



```
927 got.cmap = 0;
    val.cmap = 'bgrcmyk';
929 end
    if any(strcmp('convexpr', varargin))
931 got.convexpr = 1;
        val.convexpr = varargin{find(strcmp('convexpr', varargin))+1};
933 else
        got.convexpr = 0;
935 for i=1:length(fem.fem{1}.appl)
            if any(strcmp(class(fem.fem{1}.appl{i}.mode), {'flpdens2d', '
                flpdecns2d', 'flpdens3d'}))
937                val.convexpr = fem.fem{1}.appl{i}.dim(1:end-1);
                    else
939                        cDim = {'u' 'v' 'w'};
                            val.convexpr = cDim(1:size(fem.fem{1}.mesh.p,1));
941                    end
                end
943 end
    if any(strcmp('image', varargin))
945 got.image = 1;
        val.image = varargin{find(strcmp('image', varargin))+1};
947 else
        got.image = 0;
949 val.image = 'tmp';
    end
951 if any(strcmp('scheme', varargin))
        got.scheme = 1;
953 val.scheme = varargin{find(strcmp('scheme', varargin))+1};
    else
955 got.scheme = 0;
        val.scheme = 1;
957 end
    if any(strcmp('npart', varargin))
959 got.npart = 1;
```

```
    val.npart = varargin{find(strcmp('npart', varargin))+1};
961 else
    got.npart = 0;
963 val.npart = 10;
    end
965 if any(strcmp('partcont', varargin))
    got.partcont = 1;
967 val.partcont = any(strcmp('on', varargin{find(strcmp('partcont',
    varargin))+1}));
    else
969 got.partcont = 0;
    val.partcont = 0;
971 end
    if any(strcmp('partline', varargin))
973 got.partline = 1;
    val.partline = any(strcmp('on', varargin{find(strcmp('partline',
    varargin))+1}));
975 else
    got.partline = 0;
977 val.partline = 0;
    end
979 if any(strcmp('partscoord', varargin))
    got.partscoord = 1;
981 val.partscoord = varargin{find(strcmp('partscoord', varargin))+1};
    else
983 got.partscoord = 0;
    val.partscoord = [];
985 end
    if any(strcmp('stol', varargin))
987 got.stol = 1;
    val.stol = varargin{find(strcmp('stol', varargin))+1};
989 else
    got.stol = 0;
991 val.stol = 1;
```

```
end
993 if any(strcmp('t',varargin))
    got.t = 1;
995     val.t = varargin{find(strcmp('t',varargin))+1};
    else
997     got.t = 0;
        if isfield(fem.sol,'tlist')
999         val.t = fem.sol.tlist;
            else
1001         val.t = 1:10;
                end
1003 end
    if any(strcmp('wless',varargin))
1005     got.wless = 1;
        val.wless = any(strcmp('on',varargin{find(strcmp('wless',varargin))
            +1}));
1007 else
        got.wless = 0;
1009     val.wless = 1;
            end
1011 if any(strcmp('wdata',varargin))
        got.wdata = 1;
1013     val.wdata = varargin{find(strcmp('wdata',varargin))+1};
            else
1015     got.wdata = 0;
        val.wdata = {2,1,1,1,0,-10};
1017     if size(fem.fem{1}.mesh.p,1)==3
        val.wdata = [{2,1,1,1,0,-10} {0}];
1019     end
1021 % Set number of mixing cycles: default value is taken as 1
1023 if any(strcmp('nocycle',varargin))
        got.nocycle = 1;
```

```
1025     val.nocycle = varargin{find(strcmp('nocycle',varargin))+1};
      else
1027     got.nocycle = 0;
         val.nocycle = 1;
1029 end

1031 if any(strcmp('odefun',varargin))
         got.odefun = 1;
1033     val.odefun = varargin{find(strcmp('odefun',varargin))+1};
      else
1035     got.odefun = 0;
         val.odefun = 'l_postinterp';
1037 end

1039 % Set length per cycle:default value is taken as 0.002
         if any(strcmp('cyclel',varargin))
1041     got.cyclel = 1;
         val.cyclel = varargin{find(strcmp('cyclel',varargin))+1};
1043 else
         got.cyclel = 0;
1045     val.cyclel =0.002;
      end
1047

1049 end
```

Appendix B

Further Calculations for Residence Time Distributions

The velocity field has been obtained for three different cases one with 10842, 21136, 40475 number of elements. Figure B.1 shows the magnitude of the axial velocity as a function of channel width for two different channel heights, one at a middle height (0.35mm) and the other at 0.69mm (close to the top wall).

It is seen that at a middle height, all cases show the same profile. However for cases close to the wall a finer mesh is needed. The case with 10842 number of

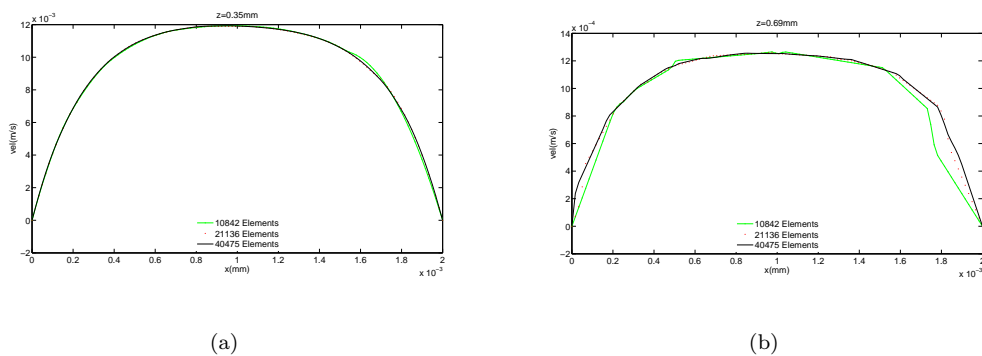


FIGURE B.1: Magnitude of axial velocity as function of channel width for two different channel heights.

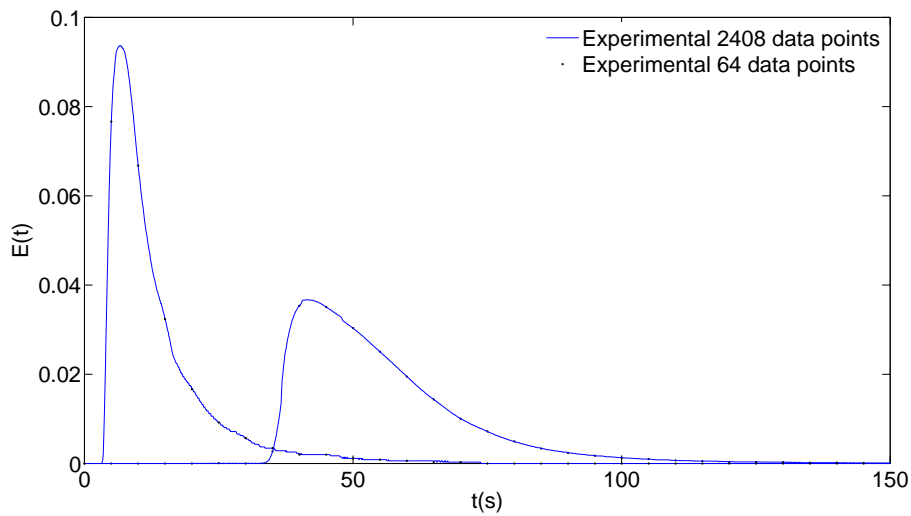


FIGURE B.2: Experimental comparison of inlet and outlet of the reactor with different experimental points.

elements is insufficient to resolve the velocity field at that region. When the mesh is refined to 21136 and to 40475 number of elements the solutions does not change significantly, and it can be considered to be mesh independent. In order to have a high degree of accuracy, without requiring a long computational time a mesh with 34582 number of elements was used.

The number of experimental data points for all cases was greater than 2000 (sampling interval 0.1s). Figure B.2 shows the experimental measured concentration of the tracer at the inlet and outlet of the reactor. The data acquired from the experimental sensor contains 2408 points. A smaller sample has been taken from this data to evaluate the feasibility of using the deconvolution procedure with a smaller sample (64 data values).

Figure B.3 shows the power spectrum vs. frequency for both cases (2408 and 64 points). It can be seen from the graph that the case for 64 points the number of samples is not enough to resolve the high frequency components and we need to sample more often. For the case of 2408 points we can see that maximum resolvable frequency increases from 0.62 to 31 which is well above the highest

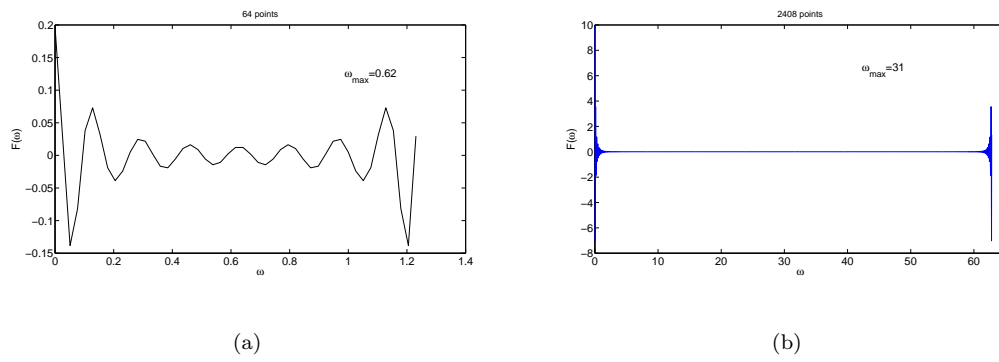


FIGURE B.3: Magnitude of axial velocity as function of channel width for two different channel heights.

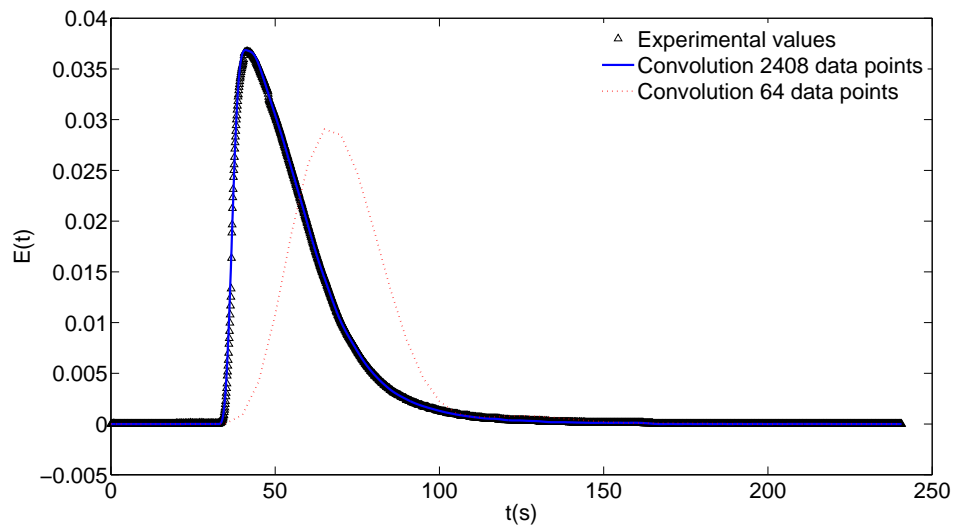


FIGURE B.4: Experimental comparison of inlet and outlet of the reactor with different experimental points.

frequency occurring in the signal. In this case the signal is said to be bandwidth-limited and the sampled data are sufficient to characterise $F(\omega)$.

When we convolute again the RTD with the input signal we must get the measured output. For the case of 2408 points the convoluted and measured output overlap each other as shown in figure B.4. However for the cases with 64 points it is not possible to reconstruct the output data by convoluting the RTD and the input.

The negative frequencies are produce last in the data structure. Sample data from 0 to $N/2$ contain the positive structures, whereas samples $N/2+1$ to $N-1$

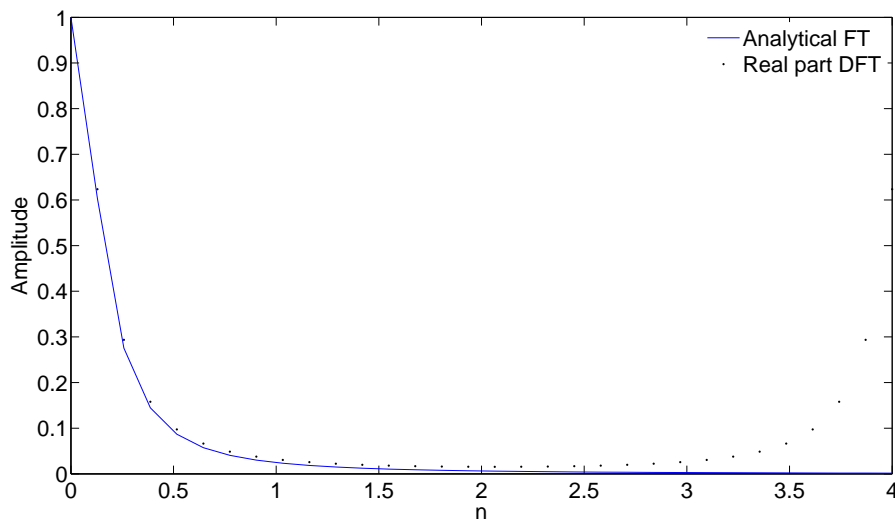


FIGURE B.5: Experimental comparison of inlet and outlet of the reactor with different experimental points.

contain the negative frequency values. In order to test the validity of the process we have calculated the Discrete and the Continuous Fourier Transform for the function $f(t) = e^{-t}$. Figure B.5, shows both the continuous and the discrete Fourier transform for $f(t)$ as a function of the number of sample n . The DFT is symmetrical around $N/2$.

If we were given data computed from the continuous Fourier transform, in order to use the FFT algorithm we will need to obtain the data from $N/2+1$ to $N-1$ by mirroring the data obtained from 0 to $N/2$ (for the imaginary part the data would also need to change sign). Once the data is in the correct structure (positive frequency values first) the Inverse Discrete Fourier Transform (using `ifft` in Matlab) can be used to retrieve the original data. Figure B.6 Shows the Inverse Discrete Fourier Transform obtained both from the Continuous Fourier Transform using analytical equations, and with the FFT algorithm using sampled data from the original $f(t) = e^{-t}$. It can be seen that both cases agree well with the original function $f(t)$. The thing to keep in mind is that data obtained from continuous Fourier Transform needs to be rearranged in order to be used in the FFT algorithm. More details of the procedure detailed here can be found in Beers [16].

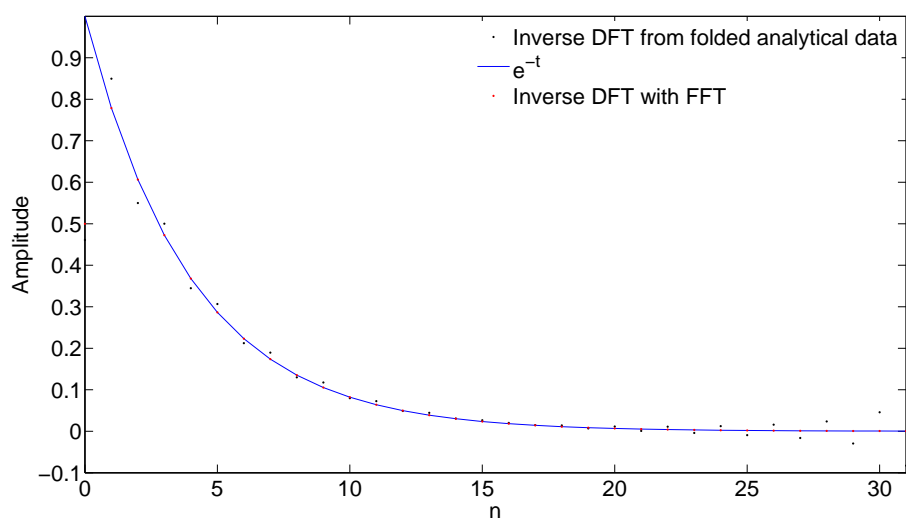


FIGURE B.6: Experimental comparison of inlet and outlet of the reactor with different experimental points.

Appendix C

Example for Experimental RTD calculations with Fourier Transform

This appendix shows an example on how to convert the experimental impulse-response data, into the residence time distribution.

- Create a text file with the input and output experimental data. The experimental apparatus will most likely give non-zero results (noise) before and after the actual response (the main curve). It is recommended to make these values zero, as this noise can create problems on the deconvolution process. Name the files injection.txt and L2.txt respectively
- Change the values of the variables time step, dt and the filter parameters $b1$ and $b2$ in the attached Matlab program deconvolutiong.m.
- Change the values of the filter parameters until the graph “convoluted outlet” is equal to “outlet”.

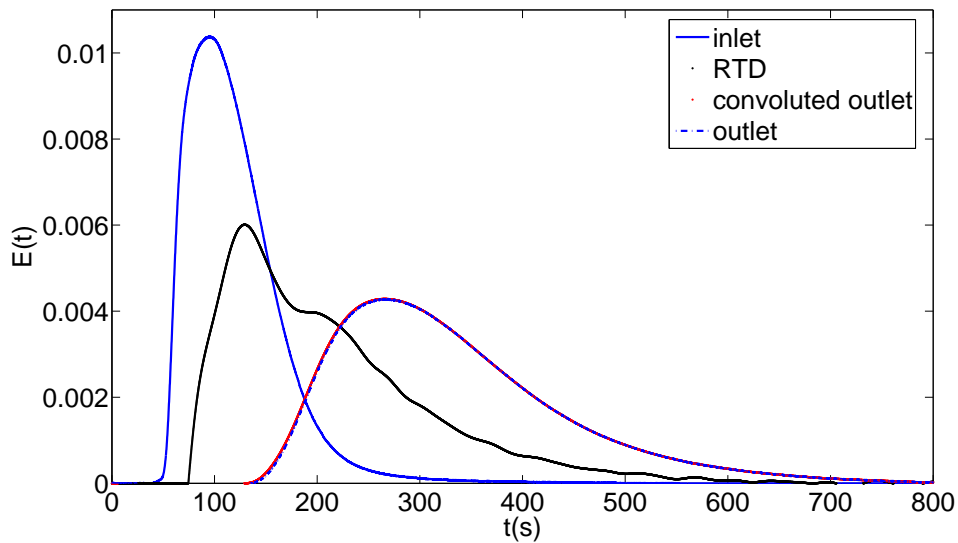


FIGURE C.1: Example of an RTD obtained by deconvolution from inlet and outlet impulse-response data. The convoluted signal $E(t) * Inlet(t)$ is also included to assess the validity of the convolution process.

Figure C.1 shows the graph of the inlet and outlet experimental data, along with the RTD and the convoluted outlet.

The Matlab program takes the experimental data in files injection.txt and L2.txt and performs the deconvolution using the Fast Fourier Transform. The deconvolution procedure is accompanied with a drastic increase in noise, therefore a numerical filter must be applied to obtain meaningful results.

This is the computer program that obtains the RTD from input and output experimental data.

```

1
  %for deconvolution
3
  %injection= input
5 %L2= outlet
7 load('L2.txt')
  load('injection.txt')
9

```

```

%b1 and b2 are values that need to be optimised so the values shown
  here
11 %are a first guess
    dt=0.1;
13 b1=4;
    b2=0.005;
15
    %These commands are to make the lengths of injection and outlet equal
      so
17 %that deconvolution can be applied

19 a1=length(injection);
    a2=length(L2);
21
    injection2=zeros(1,a2);
23 injection2(1,1:a1)=injection;

25 %Command to do deconvolution
    Edeconv=ifft((fft(L2))./(fft(injection2')));
27 %a and b are parameters for the filter command

29 [a,b]=butter(b1,b2);
    RTD=filtfilt(a,b,Edeconv);
31 time=linspace(0,length(L2)/10-dt,length(L2));
    %Econv=ifft((fft(ABC2)).*(fft(injection2')));
33
    %Data needs to be scaled with the time step (due to the numerical
      nature of
35 %the Fourier Transform
    RTDg=RTD/dt;
37
    %remove noise from data
39 RTDgood=RTDg;
    RTDgood(1:745,1)=0;

```

```
41 RTDmod=RTDgood*dt ;
43 %Check that deconvolution is good. You need to convolute the RTD with
    the
    %inlet in order to get the outlet
45
    outcon=ifft (( fft (RTDmod)) .* ( fft (injection2 ')) );
47
    plot (time ,injection2 );
49 hold on
    plot (time ,RTDgood, 'k. ');
51 plot (time ,outcon, 'r. ');
    plot (time ,L2);
53
    legend('inlet ', 'RTD', 'convoluted outlet ', 'outlet ')
```

Appendix D

Geometry Configuration for Layered Herringbone Channel

This appendix, shows the geometry configuration for the layered herringbone channel studied in chapter 7. Figure D.1 shows the layers used on the construction of the glass layered herringbone channel. The same idea is used for the acrylic one, but with different dimensions. All the patterns are etch through the entire thickness of the layer. The layer shown in figure D.1b has a thickness of $510 \mu\text{m}$ whereas layer D.1c is $370 \mu\text{m}$ thick. The dimensions are shown table 7.1

Figure D.2 shows the order on how the layers are stacked.

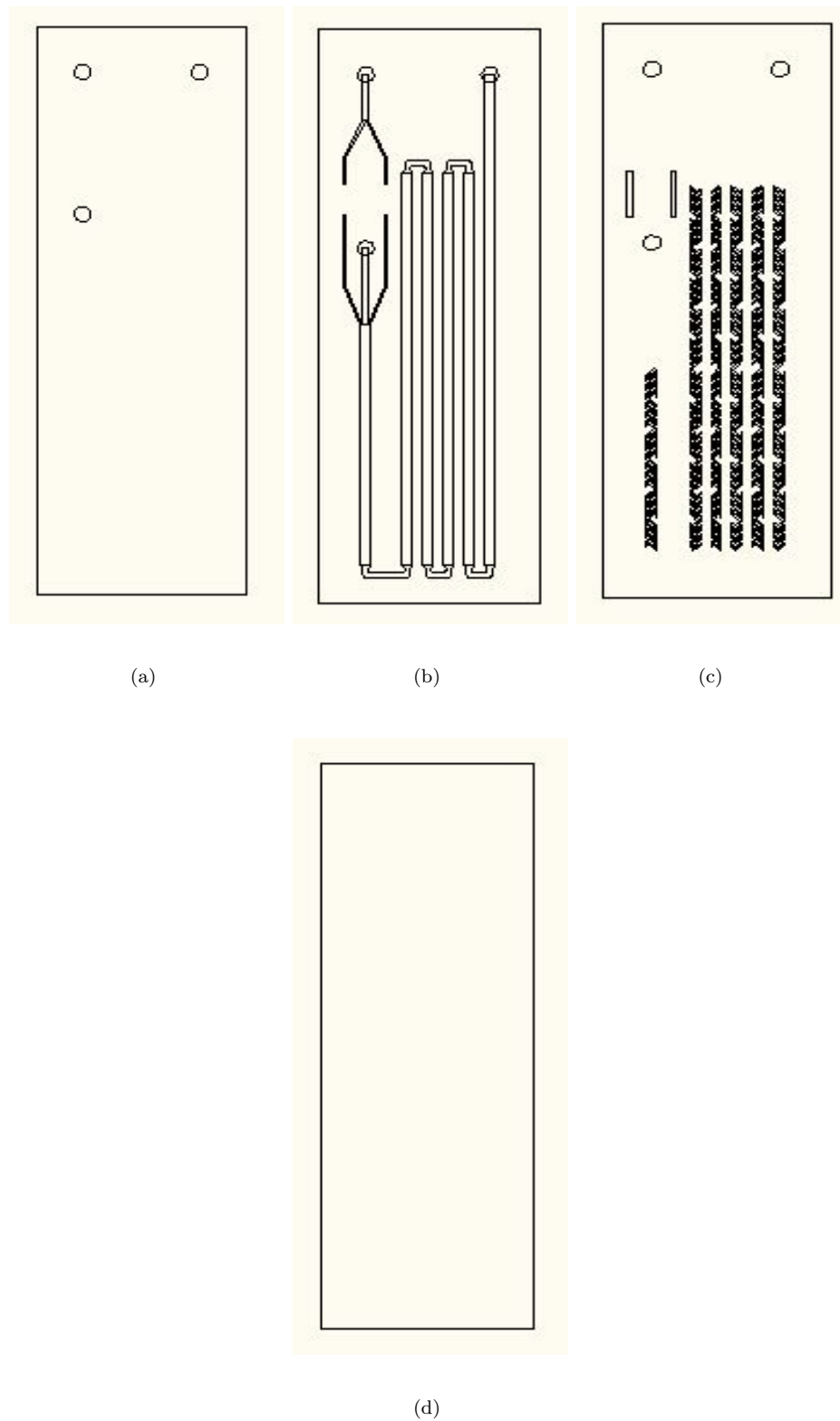


FIGURE D.1: Layers used to fabricate the glass layered herringbone channel. a) shows the top layer with the inlet and outlet ports. b) shows the layer with the main channel, two of these are used: one above and one below the herringbone layer. c) shows the herringbone layer that goes in between the main channels. d) is the bottom layer used for sealing.

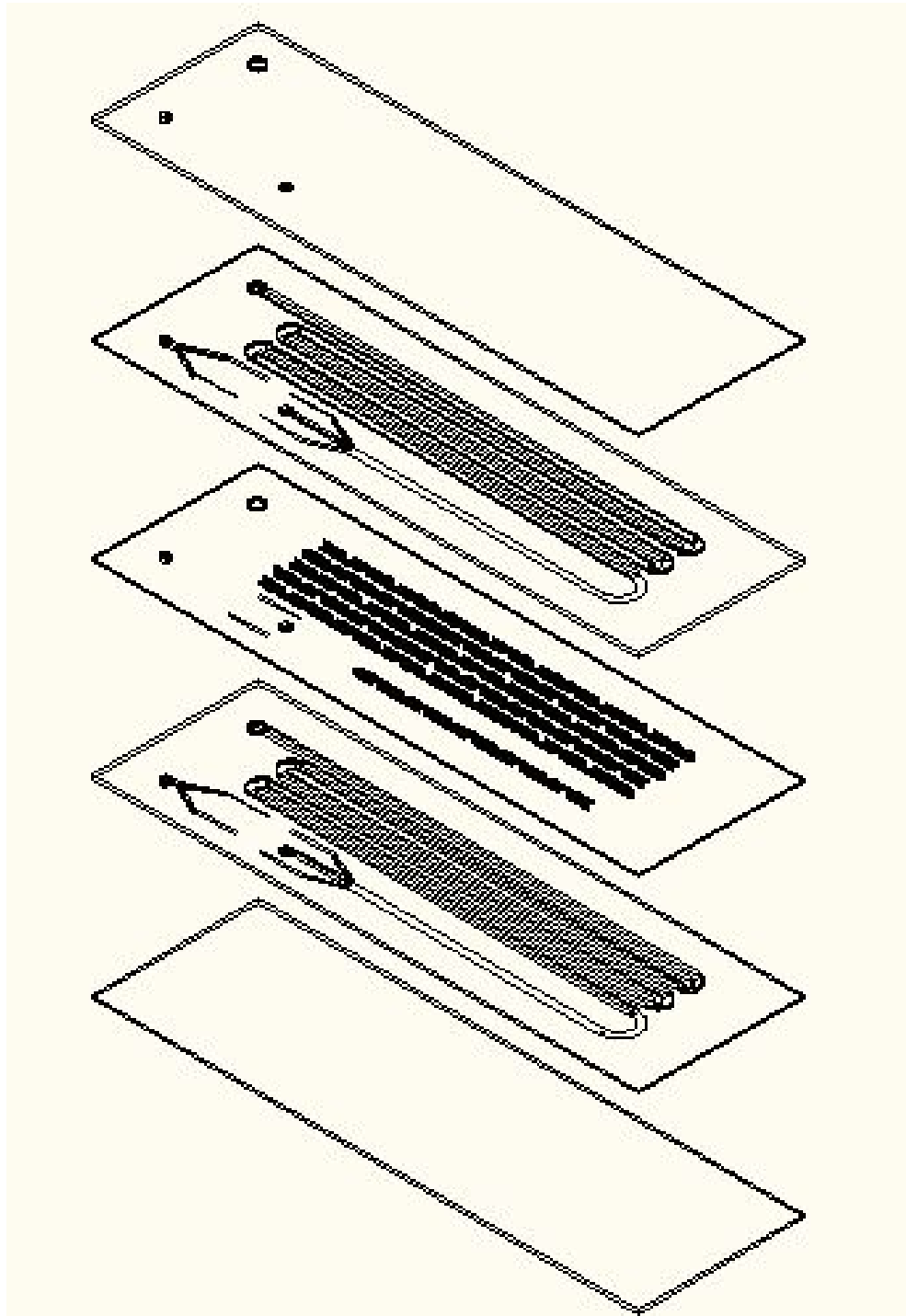


FIGURE D.2: Order of stacking of the layers for the glass layered herringbone channel

Appendix E

Derivation of mixing time equation

A mass balance for the IO_3^- ion gives:

$$\frac{\partial C_{IO_3^-}}{\partial t} = kC_I^2 C_{IO_3^-} C_H^2 \quad (\text{E.1})$$

in terms of conversion this gives:

$$\frac{\partial(C_{IO_3^-}(1-x))}{\partial t} = kC_I^2 C_{IO_3^-} C_H^2 \quad (\text{E.2})$$

$$-C_{IO_3^-} \frac{\partial x}{\partial t} = k \left[(5C_{IO_3^-} - 5C_{IO_3^-} x)^2 C_{IO_3^-} (1-x) (6C_{IO_3^-} - 6C_{IO_3^-} x)^2 \right] \quad (\text{E.3})$$

$$-C_{IO_3^-} \frac{\partial x}{\partial t} = k5^2 6^2 C_{IO_3^-}^5 (1-x)^5 \quad (\text{E.4})$$

solving for t gives:

$$t = C_1 \int_0^X \frac{dx}{(1-x)^5} \quad (\text{E.5})$$

$$t = C_1 \left[\frac{1 - (1-X)^4}{(1-X)^4} \right] \quad (\text{E.6})$$

where:

$$C_1 = \frac{1}{3600 C_{IO_3^-} k} \quad (\text{E.7})$$

Bibliography

- [1] Adeosun, J. and Lawal, A. (2005). Mass transfer enhancement in microchannel reactors by reorientation of fluid interfaces and stretching. *Sensors & Actuators: B. Chemical*, 110(1):101–111.
- [2] Adeosun, J. and Lawal, A. (2009). Numerical and experimental studies of mixing characteristics in a T-junction microchannel using residence-time distribution. *Chemical Engineering Science*, 64(10):2422–2432.
- [3] Ahmed, T. and Semmens, M. (1992). Use of sealed end hollow fibers for bubbleless membrane aeration: experimental studies. *Journal of Membrane Science*, 69(1-2):1–10.
- [4] Al-Rawashdeh, M., Hessel, V., Löb, P., Mevissen, K., and Schönfeld, F. (2008). Pseudo 3-D simulation of a falling film microreactor based on realistic channel and film profiles. *Chemical Engineering Science*, 63(21):5149–5159.
- [5] Ananthakrishnan, V., Gill, W., and Barduhn, A. (1965). Laminar dispersion in capillaries. *AIChE Journal*, 11:1063.
- [6] Ansari, M. and Kim, K. (2007). Shape optimization of a micromixer with staggered herringbone groove. *Chemical Engineering Science*, 62(23):6687–6695.
- [7] Aoki, N., Hasebe, S., and Mae, K. (2004). Mixing in microreactors: effectiveness of lamination segments as a form of feed on product distribution for multiple reactions. *Chemical Engineering Journal*, 101(1-3):323–331.

-
- [8] Aoki, N., Hasebe, S., and Mae, K. (2006). Geometric design of fluid segments in microreactors using dimensionless numbers. *AIChE Journal*, 52(4):1502–1515.
- [9] Aref, H. (1984). Stirring by chaotic advection. *Journal of Fluid Mechanics*, 143(1):21.
- [10] Aris, R. (1956). On the dispersion of a solute in a fluid flowing through a tube. *Proceedings of the Royal Society of London. Series A, Mathematical and Physical Sciences*, pages 67–77.
- [11] Aubin, J., Fletcher, D., Bertrand, J., and Xuereb, C. (2003). Characterization of the mixing quality in micromixers. *Chemical Engineering & Technology*, 26(12).
- [12] Aubin, J., Fletcher, D., and Xuereb, C. (2005). Design of micromixers using CFD modelling. *Chemical Engineering Science*, 60(8-9):2503–2516.
- [13] Aubin, J., Prat, L., Xuereb, C., and Gourdon, C. (2009). Effect of microchannel aspect ratio on residence time distributions and the axial dispersion coefficient. *Chemical Engineering and Processing: Process Intensification*, 48(1):554–559.
- [14] Balakotaiah, V., Gupta, N., and West, D. (2000). A simplified model for analyzing catalytic reactions in short monoliths. *Chemical Engineering Science*, 55(22):5367–5383.
- [15] Balakotaiah, V. and West, D. (2002). Shape normalization and analysis of the mass transfer controlled regime in catalytic monoliths. *Chemical Engineering Science*, 57(8):1269–1286.
- [16] Beers, K. (2007). *Numerical Methods for Chemical Engineering: Applications in Matlab®*. Cambridge University Press.

- [17] Bennett, P. and Wiggins, C. (2003). Computational study of mixing microchannel flows. In *American Physical Society, Annual, APS Meeting Abstracts*, volume 1.
- [18] Bernard, A., Michel, B., and Delamarche, E. (2001). Micromosaic immunoassays. *Analytical Chemistry*, 73(1):8–12.
- [19] Bessoth, F., deMello, A., and Manz, A. (1999). Microstructure for efficient continuous flow mixing. *Analytical Communications*, 36(6):213–215.
- [20] Bošković, D. and Loebbecke, S. (2008). Modelling of the residence time distribution in micromixers. *Chemical Engineering Journal*, 135:138–146.
- [21] Bothe, D., Stemich, C., and Warnecke, H. (2006). Fluid mixing in a T-shaped micro-mixer. *Chemical Engineering Science*, 61(9):2950–2958.
- [22] Bourne, J. (2008). Comments on the iodide/iodate method for characterising micromixing. *Chemical Engineering Journal*.
- [23] Burns, J. and Jachuck, R. (2005). Determination of liquid–solid mass transfer coefficients for a spinning disc reactor using a limiting current technique. *International Journal of Heat and Mass Transfer*, 48(12):2540–2547.
- [24] Cai, R., Liu, Z., Ma, W., and Wu, X. (1999). Kinetic analysis of consecutive reactions using a non-linear least-squares error-compensation algorithm. *The Analyst*, 124(5):751–754.
- [25] Camesasca, M., Kaufman, M., and Manas-Zloczower, I. (2006). Staggered passive micromixers with fractal surface patterning. *Journal of Micromechanics and Microengineering*, 16(11):2298–2311.
- [26] Cantu-Perez, A., Barrass, S., and Gavriilidis, A. (2010). Residence time distributions in microchannels: Comparison between channels with herringbone structures and a rectangular channel. *Chemical Engineering Journal*, 160(3):834–844.

- [27] Casey, E., Glennon, B., and Hamer, G. (1999). Oxygen Mass Transfer Characteristics in a Membrane-Aerated Biofilm Reactor. *Biotechnology and Bioengineering*, 62(2):183–192.
- [28] Castelain, C., Berger, D., Legentilhomme, P., Mokrani, A., and Peerhossaini, H. (2000). Experimental and numerical characterisation of mixing in a steady spatially chaotic flow by means of residence time distribution measurements. *International Journal of Heat and Mass Transfer*, 43(19):3687–3700.
- [29] Castelain, C., Mokrani, A., Legentilhomme, P., and Peerhossaini, H. (1997). Residence time distribution in twisted pipe flows: helically coiled system and chaotic system. *Experiments in Fluids*, 22(5):359–368.
- [30] Cerbelli, S., Alvarez, M., and Muzzio, F. (2002). Prediction and quantification of micromixing intensities in laminar flows. *AIChE Journal*, 48(4):686–700.
- [31] Chang, M., Chen, F., and Fang, N. (2006). Analysis of membraneless fuel cell using laminar flow in a Y-shaped microchannel. *Journal of Power Sources*, 159(2):810–816.
- [32] Chen, Z., Bown, M., OSullivan, B., MacInnes, J., Allen, R., Mulder, M., Blom, M., and vant Oever, R. (2009). Performance analysis of a folding flow micromixer. *Microfluidics and Nanofluidics*, 6(6):763–774.
- [33] Choban, E., Markoski, L., Wieckowski, A., and Kenis, P. (2004). Microfluidic fuel cell based on laminar flow. *Journal of Power Sources*, 128(1):54–60.
- [34] Cohen, J., Westly, D., Pechenik, A., and Abruña, H. (2005). Fabrication and preliminary testing of a planar membraneless microchannel fuel cell. *Journal of Power Sources*, 139(1-2):96–105.
- [35] Cussler, E. (1997). *Diffusion: Mass Transfer in Fluid Systems*. Cambridge University Press.

- [36] Danckwerts, P. (1951). Significance of Liquid-Film Coefficients in Gas Absorption. *Industrial & Engineering Chemistry*, 43(6):1460–1467.
- [37] Danckwerts, P. (1952). The definition and measurement of some characteristics of mixtures. *Applied Scientific Research*, 3:279–296.
- [38] Danckwerts, P. (1953). Continuous flow systems:: Distribution of residence times. *Chemical Engineering Science*, 2(1):1–13.
- [39] Dutta, D., Ramachandran, A., and Leighton, D. (2006). Effect of channel geometry on solute dispersion in pressure-driven microfluidic systems. *Microfluidics and Nanofluidics*, 2(4):275–290.
- [40] Ehrfeld, W., Golbig, K., Hessel, V., Lowe, H., and Richter, T. (1999). Characterization of mixing in micromixers by a test reaction: single mixing units and mixer arrays. *Industrial & Engineering Chemistry Research*, 38(3):1075–1082.
- [41] Ehrfeld, W., Hessel, V., and Löwe, H. (2000). *Microreactors: New technology for modern chemistry*. Vch Verlagsgesellschaft Mbh.
- [42] Engler, M., Kockmann, N., Kiefer, T., and Woias, P. (2004). Numerical and experimental investigations on liquid mixing in static micromixers. *Chemical Engineering Journal*, 101(1-3):315–322.
- [43] Fahim, M. and Wakao, N. (1982). Parameter estimation from tracer response measurements. *Chemical Engineering Journal*, 25(1).
- [44] Ferrigno, R., Stroock, A., Clark, T., Mayer, M., and Whitesides, G. (2002). Membraneless vanadium redox fuel cell using laminar flow. *Journal of the American Chemical Society*, 124(44):12930–12931.
- [45] Fogler, H. (2001). *Elements of chemical reaction engineering*. Prentice-Hall Englewood Cliffs, NJ.

- [46] Fouqueau, A., Meuwly, M., and Bemish, R. (2007). Adsorption of acridine orange at a C-8, C-18/Water/Acetonitrile interface. *The journal of Physical Chemistry. B, Condensed Matter, Materials, Surfaces, Interfaces & Biophysical*, 111(34):10208–10216.
- [47] Fourcade, E., Wadley, R., Hoefsloot, H., Green, A., and Iedema, P. (2001). CFD calculation of laminar striation thinning in static mixer reactors. *Chemical Engineering Science*, 56(23):6729–6741.
- [48] Fournier, M., Falk, L., and Villermaux, J. (1996). A new parallel competing reaction system for assessing micromixing efficiency Determination of micromixing time by a simple mixing model. *Chemical Engineering Science*, 51(23):5187–5192.
- [49] Gardiner, C. (1983). Handbook of Stochastic Methods for Physics. *Berlin-Haideberg, New York, Spring-Verlag*.
- [50] Gavriilidis, A., Angeli, P., Cao, E., Yeong, K., and Wan, Y. (2002). Technology and applications of microengineered reactors. *Chemical Engineering Research and Design*, 80(1):3–30.
- [51] Gobby, D., Angeli, P., and Gavriilidis, A. (2001). Mixing characteristics of T-type microfluidic mixers. *Journal of Micromechanics and Microengineering*, 11(2):126–132.
- [52] Gogate, P. and Pandit, A. (1999). Survey of measurement techniques for gas–liquid mass transfer coefficient in bioreactors. *Biochemical Engineering Journal*, 4(1):7–15.
- [53] Golden, J., Floyd-Smith, T., Mott, D., and Ligler, F. (2007). Target delivery in a microfluidic immunosensor. *Biosensors and Bioelectronics*, 22(11):2763–2767.

- [54] Gray, B., Jaeggi, D., Mourlas, N., Van Driehuisen, B., Williams, K., Maluf, N., and Kovacs, G. (1999). Novel interconnection technologies for integrated microfluidic systems. *Sensors & Actuators: A. Physical*, 77(1):57–65.
- [55] Guichardon, P., Falk, L., and Villiermaux, J. (2000). Characterisation of micromixing efficiency by the iodide–iodate reaction system. Part II: kinetic study. *Chemical Engineering Science*, 55(19):4245–4253.
- [56] Günther, A., Khan, S., Thalmann, M., Trachsel, F., and Jensen, K. (2004a). Transport and reaction in microscale segmented gas–liquid flow. *Lab on a Chip*, 4(4):278–286.
- [57] Günther, M., Schneider, S., Wagner, J., Gorges, R., Henkel, T., Kielbinski, M., Albert, J., Bierbaum, R., and Köhler, J. (2004b). Characterisation of residence time and residence time distribution in chip reactors with modular arrangements by integrated optical detection. *Chemical Engineering Journal*, 101(1-3):373–378.
- [58] Hassell, D. and Zimmerman, W. (2006). Investigation of the convective motion through a staggered herringbone micromixer at low Reynolds number flow. *Chemical engineering science*, 61(9):2977–2985.
- [59] He, B., Burke, B., Zhang, X., Zhang, R., and Regnier, F. (2001). A picoliter-volume mixer for microfluidic analytical systems. *Analytical Chemistry*, 73(9):1942–1947.
- [60] Hermann, C., Dewes, I., and Schumpe, A. (1995). The estimation of gas solubilities in salt solutions. *Chemical Engineering Science*, 50(10):1673–1675.
- [61] Hermann, R., Walther, N., Maier, U., and Buechs, J. (2001). Optical method for the determination of the oxygen-transfer capacity of small bioreactors based on sulfite oxidation. *Biotechnology and Bioengineering*, 74(5):355–363.

- [62] Hessel, V., Hardt, S., Löwe, H., and Schönfeld, F. (2003). Laminar mixing in different interdigital micromixers: I. Experimental characterization. *AIChE Journal*, 49(3):566–577.
- [63] Hessel, V., Löwe, H., and Schönfeld, F. (2005). Micromixers: a review on passive and active mixing principles. *Chemical Engineering Science*, 60(8-9):2479–2501.
- [64] Higbie, R. (1935). The rate of absorption of a pure gas into a still liquid during a short time of exposure. *Transactions of the American Institute of Chemical Engineers*, 31:365–389.
- [65] Hobbs, D. and Muzzio, F. (1997). The Kenics static mixer: a three-dimensional chaotic flow. *Chemical Engineering Journal*, 67(3):153–166.
- [66] Hobbs, D. and Muzzio, F. (1998a). Optimization of a static mixer using dynamical systems techniques. *Chemical Engineering Science*, 53(18):3199–3213.
- [67] Hobbs, D. and Muzzio, F. (1998b). Reynolds number effects on laminar mixing in the Kenics static mixer. *Chemical Engineering Journal*, 70(2):93–104.
- [68] Holmgren, A. and Andersson, B. (1998). Mass transfer in monolith catalysts—CO oxidation experiments and simulations. *Chemical Engineering Science*, 53(13):2285–2298.
- [69] Hornung, C. and Mackley, M. (2009). The measurement and characterisation of residence time distributions for laminar liquid flow in plastic microcapillary arrays. *Chemical Engineering Science*.
- [70] Howell, P., Mott, D., Fertig, S., Kaplan, C., Golden, J., Oran, E., and Ligler, F. (2005). A microfluidic mixer with grooves placed on the top and bottom of the channel. *Lab on a Chip*, 5(5):524–530.

- [71] Jackman, R., Floyd, T., Ghodssi, R., Schmidt, M., and Jensen, K. (2001). Microfluidic systems with on-line UV detection. *Journal of Micromechanics and Microengineering*, 11:263–269.
- [72] Johnson, T., Ross, D., and Locascio, L. (2002). Rapid microfluidic mixing. *Analytical Chemistry*, 74(1):45–51.
- [73] Kang, T. and Kwon, T. (2004). Colored particle tracking method for mixing analysis of chaotic micromixers. *Journal of Micromechanics and Microengineering*, 14(7):891–899.
- [74] Kee, S. and Gavrilidis, A. (2008). Design and characterisation of the staggered herringbone mixer. *Chemical Engineering Journal*, 142(1):109–121.
- [75] Khinast, J., Bauer, A., Bolz, D., and Panarello, A. (2003). Mass-transfer enhancement by static mixers in a wall-coated catalytic reactor. *Chemical Engineering Science*, 58(3-6):1063–1070.
- [76] Kim, D., Lee, S., Kwon, T., and Lee, S. (2004). A barrier embedded chaotic micromixer. *Journal of Micromechanics and Microengineering*, 14(6):798–805.
- [77] Kirtland, J., McGraw, G., and Stroock, A. (2006). Mass transfer to reactive boundaries from steady three-dimensional flows in microchannels. *Physics of Fluids*, 18:073602.
- [78] Knight, J., Vishwanath, A., Brody, J., and Austin, R. (1998). Hydrodynamic focusing on a silicon chip: mixing nanoliters in microseconds. *Physical Review Letters*, 80(17):3863–3866.
- [79] Koch, M., Chatelain, D., Evans, A., and Brunnschweiler, A. (1998). Two simple micromixers based on silicon. *Journal of Micromechanics and Microengineering*, 8:123–126.

- [80] Kockmann, N. (2007). *Transport Phenomena in Micro Process Engineering*. Springer Verlag.
- [81] Kockmann, N., Engler, M., Haller, D., and Woias, P. (2005). Fluid dynamics and transfer processes in bended microchannels. *Heat Transfer Engineering*, 26(3):71–78.
- [82] Kockmann, N., Kiefer, T., Engler, M., and Woias, P. (2006). Convective mixing and chemical reactions in microchannels with high flow rates. *Sensors & Actuators: B. Chemical*, 117(2):495–508.
- [83] Kölbl, A. (2008). Further comments on the Iodide Iodate Reaction Method for characterising micromixing. *Chemical Engineering Journal*, 145(1):176–177.
- [84] Kolbl, A., Kraut, M., and Schubert, K. (2008). The iodide iodate method to characterize microstructured mixing devices. *AIChE Journal*, 54(3):639–645.
- [85] Kreulen, H., Smolders, C., Versteeg, G., and van Swaaij, W. (1993). Microporous hollow-fibre membrane modules as gas–liquid contactors. Part 1. Physical mass transfer processes. *Journal of Membrane Science*, 78:197–216.
- [86] Kreutzer, M., Bakker, J., Kapteijn, F., Moulijn, J., and Verheijen, P. (2005). Scaling-up multiphase monolith reactors: Linking residence time distribution and feed maldistribution. *Industrial & Engineering Chemistry Research*, 44(14):4898–4913.
- [87] Lee, S., Kim, D., Lee, S., and Kwon, T. (2006). A split and recombination micromixer fabricated in a PDMS three-dimensional structure. *Journal of Micromechanics and Microengineering*, 16(5):1067–1072.
- [88] Levenspiel, O. (1999). Chemical reaction engineering. *Industrial & Engineering Chemistry Research*, 38(11):4140–4143.

- [89] Levenspiel, O., Lai, B., and Chatlynne, C. (1970). Tracer curves and residence time distribution. *Chemical Engineering Science*, 25:1611–1613.
- [90] Levenspiel, O. and Smith, W. (1995). Notes on the Diffusion-Type Model for the Longitudinal Mixing of Fluids in Flow (Reprinted from Chem-Engng-Sci, Vol 6, Pg 227-233, 1957). *Chemical Engineering Science*, 50(24):3891–3896.
- [91] Levenspiel, O. and Turner, J. (1970). The interpretation of residence-time experiments. *Chemical Engineering Science*, 25:1605–1609.
- [92] Levien, K. and Levenspiel, O. (1999). Optimal product distribution from laminar flow reactors: Newtonian and other power-law fluids. *Chemical Engineering Science*, 54(13-14):2453–2458.
- [93] Li, C. and Chen, T. (2005a). Simulation and optimization of chaotic micromixer using lattice Boltzmann method. *Sensors & Actuators: B. Chemical*, 106(2):871–877.
- [94] Li, F., Meindersma, W., de Haan, A., and Reith, T. (2004). Experimental validation of CFD mass transfer simulations in flat channels with non-woven net spacers. *Journal of Membrane Science*, 232(1-2):19–30.
- [95] Li, J. and Chen, B. (2005b). Review of CO₂ absorption using chemical solvents in hollow fiber membrane contactors. *Separation and Purification Technology*, 41(2):109–122.
- [96] Li, K. and Teo, W. (1998). Use of permeation and absorption methods for CO₂ removal in hollow fibre membrane modules. *Separation and Purification Technology*, 13(1):79–88.
- [97] Liu, M., Peskin, R., Muzzio, F., and Leong, C. (1994). Structure of the stretching field in chaotic cavity flows. *AIChE Journal*, 40(8):1273–1286.

- [98] Liu, R., Stremmer, M., Sharp, K., Olsen, M., Santiago, J., Adrian, R., Aref, H., and Beebe, D. (2000). Passive mixing in a three-dimensional serpentine microchannel. *Journal of Microelectromechanical Systems*, 9(2):190–197.
- [99] Liu, Y., Kim, B., and Sung, H. (2004). Two-fluid mixing in a microchannel. *International Journal of Heat and Fluid Flow*, 25(6):986–995.
- [100] Lohse, S., Kohnen, B., Janasek, D., Dittrich, P., Franzke, J., and Agar, D. (2008). A novel method for determining residence time distribution in intricately structured microreactors. *Lab on a Chip*, 8(3):431–438.
- [101] Lopez, M. and Graham, M. (2008). Enhancement of mixing and adsorption in microfluidic devices by shear-induced diffusion and topography-induced secondary flow. *Physics of Fluids*, 20:053304.
- [102] Lu, H., Koo, L., Wang, W., Lauffenburger, D., Griffith, L., and Jensen, K. (2004). Microfluidic shear devices for quantitative analysis of cell adhesion. *Analytical Chemistry*, 76(18):5257–5264.
- [103] Lynn, N. and Dandy, D. (2007). Geometrical optimization of helical flow in grooved micromixers. *Lab on a Chip*, 7(5):580–587.
- [104] MacInnes, J., Vikhansky, A., and Allen, R. (2007). Numerical characterisation of folding flow microchannel mixers. *Chemical Engineering Science*, 62(10):2718–2727.
- [105] Maier, U. and Büchs, J. (2001). Characterisation of the gas–liquid mass transfer in shaking bioreactors. *Biochemical Engineering Journal*, 7(2):99–106.
- [106] Manz, A., Graber, N., and Widmer, H. (1990). Miniaturized total chemical analysis systems: a novel concept for chemical sensing. *Sensors and actuators B: Chemical*, 1(1-6):244–248.

- [107] Mengeaud, V., Josserand, J., and Girault, H. (2002). Mixing processes in a zigzag microchannel: finite element simulations and optical study. *Analytical Chemistry*, 74(16):4279–4286.
- [108] Michelsen, M. and Ostergaard, K. (1970). The use of residence time distribution data for estimation of parameters in the axial dispersion model. *Chemical Engineering Science*, 25:583.
- [109] Mills, P. and Dudukovic, M. (1989). Convolution and deconvolution of non-ideal tracer response data with application to three-phase packed-beds. *Computers & Chemical Engineering*, 13(8):881–898.
- [110] Mitrovic, B., Le, P., and Papavassiliou, D. (2004). On the Prandtl or Schmidt number dependence of the turbulent heat or mass transfer coefficient. *Chemical Engineering Science*, 59(3):543–555.
- [111] Moulin, P., Rouch, J., Serra, C., Clifton, M., and Aptel, P. (1996). Mass transfer improvement by secondary flows: Dean vortices in coiled tubular membranes. *Journal of Membrane Science*, 114(2):235–244.
- [112] Munson, M. and Yager, P. (2004). Simple quantitative optical method for monitoring the extent of mixing applied to a novel microfluidic mixer. *Analytica Chimica Acta*, 507(1):63–71.
- [113] Muzzio, F., Swanson, P., and Ottino, J. (1991). The statistics of stretching and stirring in chaotic flows. *Physics of Fluids A: Fluid Dynamics*, 3:822.
- [114] Myszka, D., Morton, T., Doyle, M., and Chaiken, I. (1997). Kinetic analysis of a protein antigen-antibody interaction limited by mass transport on an optical biosensor. *Biophysical chemistry*, 64(1-3):127–137.
- [115] Nauman, E. (1979). Enhancement of heat transfer and thermal homogeneity with motionless mixers. *AIChE Journal*, 25(2):246–258.

- [116] Nauman, E. and Buffham, B. (1983). *Mixing in Continuous Flow Systems*. John Wiley & Sons Inc.
- [117] Nguyen, N. and Wu, Z. (2005). Micromixers: a review. *Journal of Micromechanics and Microengineering*, 15(2).
- [118] Niu, X. and Lee, Y. (2003). Efficient spatial-temporal chaotic mixing in microchannels. *Journal of Micromechanics and Microengineering*, 13(3):454–462.
- [119] Ottino, J. and Wiggins, S. (2004). Introduction: mixing in microfluidics. *Philosophical Transactions of the Royal Society A: Mathematical, Physical and Engineering Sciences*, 362(1818):923–935.
- [120] Ozbek, B. and Gayik, S. (2001). The studies on the oxygen mass transfer coefficient in a bioreactor. *Process Biochemistry*, 36(8):729–41.
- [121] Panić, S., Loebbecke, S., Tuercke, T., Antes, J., and Bošković, D. (2004). Experimental approaches to a better understanding of mixing performance of microfluidic devices. *Chemical Engineering Journal*, 101(1-3):409–419.
- [122] Park, S., Kim, J., Park, J., Chung, S., Chung, C., and Chang, J. (2004). Rapid three-dimensional passive rotation micromixer using the breakup process. *Journal of Micromechanics and Microengineering*, 14(1):6–14.
- [123] Pohorecki, R. and Moniuk, W. (1988). Kinetics of reaction between carbon dioxide and hydroxyl ions in aqueous electrolyte solutions. *Chemical engineering science*, 43(7):1677–1684.
- [124] Qi, Z. and Cussler, E. (1985). Microporous hollow fibers for gas absorption. I. Mass transfer in the liquid. *Journal of Membrane Science*, 23(3):321–332.
- [125] Rangwala, H. (1996). Absorption of carbon dioxide into aqueous solutions using hollow fiber membrane contactors. *Journal of Membrane Science*, 112(2):229–240.

- [126] Rinker, E., Sami, S., and Sandall, O. (1995). Kinetics and modelling of carbon dioxide absorption into aqueous solutions of N-methyldiethanolamine. *Chemical Engineering Science*, 50(5):755–768.
- [127] Roberge, D., Ducry, L., Bieler, N., Cretton, P., and Zimmermann, B. (2005). Microreactor technology: A revolution for the fine chemical and pharmaceutical industries? *Chemical Engineering & Technology*, 28(3):318–323.
- [128] Salman, W., Angeli, P., and Gavriilidis, A. (2005). Sample pulse broadening in Taylor flow microchannels for screening applications. *Chemical Engineering & Technology*, 28(4).
- [129] Salman, W., Gavriilidis, A., and Angeli, P. (2007). Axial mass transfer in Taylor flow through circular microchannels. *AIChE Journal*, 53(6).
- [130] Saxena, A. and Nigam, K. (2004). Coiled configuration for flow inversion and its effect on residence time distribution. *AIChE Journal*, 30(3):363–368.
- [131] Schönfeld, F. and Hardt, S. (2004). Simulation of helical flows in microchannels. *AIChE Journal*, 50(4):771–778.
- [132] Schönfeld, F., Hessel, V., and Hofmann, C. (2004). An optimised split-and-recombine micro-mixer with uniform chaotic mixing. *Lab on a Chip*, 4(1):65–69.
- [133] Schwesinger, N., Frank, T., and Wurmus, H. (1996). A modular microfluid system with an integrated micromixer. *Journal of Micromechanics and Micro-engineering*, 6:99–102.
- [134] Shaw, D. and Hanratty, T. (1977). Turbulent mass transfer rates to a wall for large Schmidt numbers. *AIChE Journal*, 23(1).
- [135] Sherwood, T., Pigford, R., and Wilke, C. (1975). *Mass Transfer*. McGraw-Hill, New York.

- [136] Shrivastava, A., Kumar, S., and Cussler, E. (2008). Predicting the effect of membrane spacers on mass transfer. *Journal of Membrane Science*, 323(2):247–256.
- [137] Sieder, E. and Tate, G. (1936). Heat Transfer and Pressure Drop of Liquids in Tubes. *Industrial & Engineering Chemistry*, 28(12):1429–1435.
- [138] Sikavitsas, V., Nitsche, J., and Mountziaris, T. (2002). Transport and kinetic processes underlying biomolecular interactions in the BIACORE optical biosensor. *Biotechnology Progress*, 18(4):885–897.
- [139] Skelland, A. (1974). *Diffusional Mass Transfer*. Wiley.
- [140] Soleymani, A., Yousefi, H., and Turunen, I. (2008). Dimensionless number for identification of flow patterns inside a T-micromixer. *Chemical Engineering Science*, 63(21):5291–5297.
- [141] Son, J. and Hanratty, T. (1967). Limiting relation for the eddy diffusivity close to a wall. *AIChE Journal*, 13(4).
- [142] Song, H. and Han, S. (2005). A general correlation for pressure drop in a Kenics static mixer. *Chemical Engineering Science*, 60(21):5696–5704.
- [143] Stroock, A., Dertinger, S., Ajdari, A., Mezic, I., Stone, H., and Whitesides, G. (2002). Chaotic mixer for microchannels. *Science*, 295(5555):647–651.
- [144] Stroock, A. and McGraw, G. (2004). Investigation of the staggered heringbone mixer with a simple analytical model. *Philosophical Transactions: Mathematical, Physical and Engineering Sciences*, pages 971–986.
- [145] Stropky, D., Pougatch, K., Nowak, P., Salcudean, M., Pagori, P., Gartshore, I., and Yuan, J. (2007). RTD (residence time distribution) predictions in large mechanically aerated lagoons. *Water Science Technology*, 55(11):29–36.

- [146] Swanson, P. and Ottino, J. (1990). A comparative computational and experimental study of chaotic mixing of viscous fluids. *Journal of Fluid Mechanics Digital Archive*, 213:227–249.
- [147] Taylor, G. (1935). Statistical Theory of Turbulence. *Proceedings of the Royal Society of London. Series A, Mathematical and Physical Sciences*, pages 421–444.
- [148] Taylor, G. (1953). Dispersion of soluble matter in solvent flowing slowly through a tube. *Proceedings of the Royal Society of London. Series A, Mathematical and Physical Sciences*, pages 186–203.
- [149] Tobias, C., Eisenberg, M., and Wilke, C. (1952). Diffusion and Convection in Electrolysis A Theoretical Review. *Journal of The Electrochemical Society*, 99:359C.
- [150] Trachsel, F., Günther, A., Khan, S., and Jensen, K. (2005). Measurement of residence time distribution in microfluidic systems. *Chemical Engineering Science*, 60(21):5729–5737.
- [151] Tribe, L., Briens, C., and Margaritis, A. (1995). Determination of the volumetric mass transfer coefficient ($k(L) a$) using the dynamic “gas out-gas in” method: Analysis of errors caused by dissolved oxygen probes. *Biotechnology and Bioengineering*, 46(4):388–92.
- [152] Van Swaaij, W., Charpentier, J., and Villiermaux, J. (1969). Residence time distribution in the liquid phase of trickle flow in packed columns. *Chemical Engineering Science*, 24:1083.
- [153] Vashisth, S. and Nigam, K. (2008). Liquid-Phase Residence Time Distribution for Two-Phase Flow in Coiled Flow Inverter. *Industrial & Engineering Chemistry Research*, 47(10):3630–3638.

- [154] Vikhansky, A. (2008). Effect of diffusion on residence time distribution in chaotic channel flow. *Chemical Engineering Science*, 63(7):1866–1870.
- [155] Wakao, N. and Kaguei, S. (1982). *Heat and Mass Transfer in Packed Beds*. Gordon & Breach, London.
- [156] Walter, S., Malmberg, S., Schmidt, B., and Liauw, M. (2005). Mass transfer limitations in microchannel reactors. *Catalysis Today*, 110(1-2):15–25.
- [157] Wang, H., Iovenitti, P., Harvey, E., and Masood, S. (2002). Optimizing layout of obstacles for enhanced mixing in microchannels. *Smart Materials and Structures*, 11:662–667.
- [158] Wang, H., Iovenitti, P., Harvey, E., and Masood, S. (2003). Numerical investigation of mixing in microchannels with patterned grooves. *Journal of Micromechanics and Microengineering*, 13(6):801–808.
- [159] Wang, R., Li, D., and Liang, D. (2004). Modeling of CO₂ capture by three typical amine solutions in hollow fiber membrane contactors. *Chemical Engineering & Processing*, 43(7):849–856.
- [160] Wen, C. and Fan, L. (1975). *Models for Flow Systems and Chemical Reactors*. Marcel Dekker, New York.
- [161] Wiggins, S. and Ottino, J. (2004). Foundations of chaotic mixing. *Philosophical Transactions-Royal Society of London Series A Mathematical Physical and Engineering Sciences*, pages 937–970.
- [162] Williams, M., Longmuir, K., and Yager, P. (2008). A practical guide to the staggered herringbone mixer. *Lab on a Chip*, 8(7):1121–1129.
- [163] Wong, S., Bryant, P., Ward, M., and Wharton, C. (2003). Investigation of mixing in a cross-shaped micromixer with static mixing elements for reaction kinetics studies. *Sensors & Actuators: B. Chemical*, 95(1-3):414–424.

-
- [164] Wong, S., Ward, M., and Wharton, C. (2004). Micro T-mixer as a rapid mixing micromixer. *Sensors & Actuators: B. Chemical*, 100(3):359–379.
- [165] Xia, Y. and Whitesides, G. (1998). Soft lithography. *Annual Review of Materials Science*, 28(1):153–184.
- [166] Yang, J., Huang, K., and Lin, Y. (2005). Geometric effects on fluid mixing in passive grooved micromixers. *Lab on a Chip*, 5(10):1140–1147.
- [167] Yang, J., Huang, K., Tung, K., Hu, I., et al. (2007). A chaotic micromixer modulated by constructive vortex agitation. *Journal of Micromechanics and Microengineering*, 17:2084–2092.
- [168] Yoon, S., Fichtl, G., and Kenis, P. (2006). Active control of the depletion boundary layers in microfluidic electrochemical reactors. *Lab on a Chip*, 6(12):1516–1524.
- [169] Zanfır, M., Gavriilidis, A., Wille, C., and Hessel, V. (2005). Carbon dioxide absorption in a falling film microstructured reactor: experiments and modeling. *Industrial & Engineering Chemistry Research*, 44(6):1742–1751.
- [170] Ziegenbalg, D., Löb, P., Al-Rawashdeh, M., Kralisch, D., Hessel, V., and Schönfeld, f. (2010). Use of smart interfaces to improve the liquid-sided mass transport in a falling film microreactor. *Chemical Engineering Science*, Corrected Proof.